X-RAY BIOMECHANICAL IMAGING AND DIGITAL VOLUME CORRELATION OF BONE: FROM REGENERATION TO STRUCTURE

Marta Peña Fernández

The thesis is submitted in partial fulfilment of the requirements for the award of the degree of

DOCTOR OF PHILOSOPHY

of the

University of Portsmouth

December 2018

Whilst registered as a candidate for the above degree, I have not been registered for any other research award. The results and conclusions embodied in this thesis are the work of the named candidate and have not been submitted for any other academic award.

Marta Peña Fernández

October 2018

Word count: ~54,000

A ellas, las mujeres de mi vida.

Por ser, estar, confiar.

“If I have seen further it is by standing on the shoulders of Giants”

Isaac Newton, 1676

CONTENTS LIST

Acknowledgements

During the past three years I have been lucky enough to spend time, collaborate and discuss with many people, without whom this project would not have been possible. Now it is the moment to express my most sincere gratitude to them.

I would like to start by deeply thanking my supervisor Dr. Gianluca Tozzi for giving me the opportunity to work with him, making me fall in love with science and research. His passion for his work was a never-ending source of inspiration; every meeting was full of new ideas, projects and stimulating discussions. I will always appreciate his dedication, encouragement and his ever-open office door over all these years. I am not less thankful to Gianluca for his patience and understanding when things were not working as expected, for always pushing me forward to successfully complete each project, for believing in my work. Without his guidance and support my PhD journey would have been a different story.

I am extremely thankful to Dr. Enrico Dall'Ara, who has always provided fruitful and constructive comments and feedback to this work, improving the quality of every piece he revised. I would also like to thank Dr. Dave Hollis for always looking for an answer to my difficult questions. In addition, I want to express my gratitude to Dr. Alexander Kao, who has always had his door open for discussing new ideas, methods and experiments.

I have had the privilege to conduct part of my experiments in I13-2 beamline at Diamond Light Source and it is a pleasure for me to acknowledge Dr. Andrew Bodey and Dr. Kazimir Wanelik for sharing their knowledge and for the important support during and after beamtimes. The always valuable feedback from Andrew was of great help to improve this work and without any doubts, beamtime was more fun with him around.

I am thankful to Mr. Colin Lupton, who has always been willing to help and share new ideas and past stories. I am also truly grateful to Dr. Hom Dhakal and Mr. Robert Elliott, who have always had kind words of support and encouragement to me. I would like to thank Ian and Darren, for their much appreciated good mornings and evenings every day. In addition, I am thankful to Prof. Gordon Blunn, Prof. Asa Barber, Dr. Martino Pani and Dr. Marta Roldo for supporting and contributing to this work in different ways.

There are several colleagues to whom I am grateful: Tim, Saúl, Samuel, Roxane, Arianna, Alberto, for the always welcome science and non-science chats. A especial thanks go to Katerina Karali, with whom I share countless coffees and talks during the past years.

In the course of this years some people have been my very close companions and I owe them a lot. My colleagues, my friends, Marco Curto, Hayder Murad and Ahmed Ahmed, who took care of me over the past three years and with whom I have shared discussions about everything and nothing, innumerable coffees, hugs and laughs. Marco, who started this adventure with me; Hayder, who has always believed in me; Ahmed, with whom I spent long and late hours working side by side. All this has definitely had an enormous contribution to the outcome of this project. Thank you, guys.

This section would certainaly not be complete if I omit to thank my girl-friends, Aleksandra, Fuen and María. I arrived to Portsmouth three years ago I have been extremely lucky not only to work in what I love but also to find friends for life. Aleksandra, Fuen, I want to thank you both for always understanding my busy days and never leave my side, for your patient and caring. I would like to especially thank María, who despite the distance has always stood by my side. Girls, you are a very important part of this work. Gracias, amigas.

Hace ya cuatro años dedicí dejar mi ciudad, mi Sevilla, buscando una oportunidad en lo que me apasiona. Nada hubiera sido posible sin mi famila, a la que estaré eternamente agradecida, a la que nunca he dejado de echar de menos. A mi padre, por su continuo apoyo y cariño, por los abrazos en cada reencuentro y despedida. A mis hermanos, Jose y Javi, y mi casi-hermano Will, gracias por ser mis compañeros de por vida, gracias por quererme, por hacerme reír, por estar conmigo a pesar de la distancia. Mis chicos, os quiero.

Finalmemente, esta tesis está dedicada a las tres mujeres de mi vida, por su fuerza y valentía, por hacer de mí la mujer que hoy soy. Mamá, Yaya, Marijuli, nunca podré agradeceros lo suficiente todo el apoyo y amor que me habéis dado. Gracias por siempre confiar y creer en mí, incluso cuando yo misma no lo hago. Gracias por cuidarme, por quererme, por estar siempre conmigo incluso a miles de kilómetros. Gracias por cada abrazo y sonrisa en nuestros reencuentros; gracias por compartir lágirmas en las despedidas. Sin vosotras nada de esto hubiera sido posible. Sois mis personas, incondicionales, con todo lo que eso significa.

Marta Peña Fernández

December 2018

Abstract

Bone as such displays an intrinsic regenerative potential following fracture; however, this capacity is limited with large bone defects that cannot heal spontaneously. The management of critical-sized bone defects remains a major clinical and socioeconomic need; thus, osteoregenerative biomaterials are constantly under development aiming at promoting and enhancing bone healing. Measuring the biomechanical response of regenerated bone at different dimensional scales is crucial in order to assess its mechanical performance and overall structural response, ultimately validating different treatments applied to restore bone within the defect site.

The major aim of this PhD project was to combine high-resolution X-ray micro-computed tomography (microCT) biomechanical imaging and digital volume correlation (DVC) to newly formed bone structures in order to provide a detailed characterisation of bone formation, mechanical competence and deformation mechanisms at tissue level following use of different biomaterials in critical-sized bone defects. A methodological approach was developed to extract full-field deformation of bone at tissue level based on synchrotron radiation (SR)-microCT. This was achieved through an optimisation of image postprocessing and DVC settings that provided reliable displacement and strain measurements at tissue level to investigate the micromechanics of trabecular bone structures and bone-biomaterial systems. In addition, the effect of SR on bone integrity was assessed and experimental protocols were established for a safer and more reliable application of *in situ* SR-microCT experiments aiming at minimising the irradiation-induced tissue damage.

The defined methods were then used for the investigation of the micromechanics of bone-biomaterial systems and newly formed bone *in vivo* after the application of osteoconductive and osteoinductive biomaterials. Microdamage initiation and propagation at the bone-biomaterial interface was identified, indicating that the resorption rate and osteoinduction properties of bone grafts may be as beneficial as the original stiffness of the scaffolds for an efficient micromechanics *in vivo*. Furthermore, the mechanical adaptation of bone structure at an early stage of bone regeneration was demonstrated irrespective of the implanted biomaterial in the bone defect.

In conclusion, the experimental approaches herein presented have shown to be advantageous for investigating the local mechanics of bone tissue during the healing process in relation to the regeneration achieved *in vivo* for a variety of biomaterials. Moreover, results suggest that enhanced osteoinductive biomaterials offering a controlled release of growth factors could be successfully adopted for the treatment of critical-sized bone defects.

Resumen

El tejido óseo presenta un gran potencial de regeneración tras su fractura; sin embargo, esta capacidad está limitada en defectos óseos de gran tamaño que no pueden regenerarse por sí mismos. El tratamiento de defectos de tamaño crítico continúa siendo un gran problema clínico y socioeconómico, por tanto, biomateriales osteoregenerativos se encuentran constantemente en desarrollo con el objetivo de promover la reparación ósea. La evaluación de la respuesta biomecánica del hueso regenerado en varias escalas dimensionales es decisiva para valorar la competencia mecánica y la respuesta general de la estructura ósea, validando así los tratamientos aplicados para restaurar el hueso en el lugar del defecto.

El principal objetivo de esta tesis es la combinación de microtomografía computarizada (microCT), ensayos biomecánicos y correlación digital de volúmenes (DVC) en estructuras óseas recientemente constituidas para proporcionar una caracterización detallada de la formación ósea, la competencia mecánica y los mecanismos de deformación a nivel tisular tras la aplicación de diferentes biomateriales en defectos óseos de tamaño crítico. Para este propósito se ha desarrollado una metodología para la obtención del campo completo de deformaciones en el tejido óseo basado en microCT mediante radiación sincrotrón (SR). Dicha metodología se ha logrado mediante una optimización del postproceso de imágenes y los parámetros de la DVC, proporcionando medidas fiables de desplazamiento y deformaciones a nivel tisular para la posterior investigación de la micromecánica de estructuras de hueso trabecular y sistemas hueso-biomaterial. Asimismo, se ha evaluado el efecto de la SR en la integridad del tejido óseo, estableciendo protocolos experimentales para una aplicación más segura y responsable de experimentos *in situ* basados en microCT mediante SR, con el objetivo de reducir el daño inducido en el tejido óseo por irradiación.

Los métodos definidos se han usado en la investigación de la micromecánica de sistemas integrados por hueso y biomateriales, así como estructuras óseas recién formadas *in vivo* tras la aplicación de biomateriales osteoconductores y osteoinductores. Se ha identificado el inicio y la progresión del daño en la interfase entre hueso y biomaterial, indicando que el grado de resorción y las propiedades osteoinductivas de los injertos óseos pueden ser más favorables que la rigidez inicial del implante para una mecánica eficiente *in vivo*. Igualmente, se ha demostrado la adaptación mecánica de la estructura ósea en la etapa temprana de regeneración, independiente del biomaterial implantado en el defecto óseo.

Finalmente, se ha mostrado que las estrategias experimentales presentadas son beneficiosas para la investigación de las propiedades mecánicas locales en el tejido óseo durante el proceso de reparación en relación con la regeneración conseguida *in vivo* por la acción de biomateriales. Los resultados presentados sugieren que los biomateriales osteoinductivos mejorados que promueven una liberación controlada de factores de crecimiento podrían adoptarse en el tratamiento de defectos óseos de tamaño crítico satisfactoriamente.

Chapter 1. Introduction

1.1. Thesis motivation

Bone displays a unique capability to regenerate itself as part of physiological remodelling or in response to injury [1,2]. Opposite to other adult tissues that heal with the production of scar tissue, bone defects and fractures heal with new bone formation, which is continuously remodelled until the original site of injury is no longer observed [3]. However, not all fractures heal spontaneously, as the self-healing capacity of bone becomes more difficult with large bone defects [4]. Those defects are common and occur in many clinical situations including high-grade open fractures with bone loss, high-energy trauma, infection requiring debridement of bone and resection of bone tumours [5–7]. Bone is the second tissue transplantation worldwide, coming right after blood transfusion [8,9]. More than 2.2. million bone grafting procedures are performed annually worldwide in order to repair bone defects in orthopaedics, neurosurgery and dentistry [10,11]. This is even more important with the expected ageing society and the increase in activity up to older age, meaning that the number of patients undergoing these procedures will raise, as well as the associated costs in treating those patients [12,13]. Despite the profound clinical and economic impact, the treatments of bone defects remain controversial, especially when the defect is critical sized [5,7].

Clinically, the most common strategy to treat critical-sized bone defects is the use of autografts (i.e. harvesting bone form another location in the same patient) [14,15]. While biologically ideal, allografts present important limitations such as limited supply and donor site complications [16,17]. Grafts from bone banks or other animal species are still subjected to risks, such as immunological reactions or disease transmission [18,19]. To address these drawbacks, numerous alternatives have been brought by the emergence of novel tissue engineering strategies during the past decades [20,21]. Consequently, the use of natural grafts in bone grafting procedures have shifted towards synthetic bone substitutes and biological factors [9]. Among those alternatives, calcium phosphate based biomaterials and bone morphogenetic proteins (BMPs) are most widely used, often combined [9,22–25]. Whereas synthetic bone substitutes are generally only osteoconductive and mainly being applied in reconstruction of large defects, bone morphogenetic proteins are basically osteoinductive, with the capability of enhancing the fracture healing [25,26].

One of the main gaps in the field of biomaterials for bone regeneration concerns the successful translation of the product design into clinical practice. In fact, different experimental methodologies are being used to test such materials and compositions in terms of biocompatibility and bioactivity *in vitro*, as well as the characterisation of bone regeneration and biomaterial resorption *in vivo* [27–31]. However, a multidisciplinary approach involving the standardisation of *in vitro* and *in vivo* performance of biomaterials and consequent regenerated bone quality is still missing. In that context, the application of *in vitro* testing protocols to newly formed bone produced *in vivo* and harvested from the defect sites at selected time points would benefit the translation of biomaterials design (i.e.

biocompatibility, bioactivity) into the osteoregeneration that can be achieved *in vivo*. Particularly, a comprehensive biomechanical evaluation of the bone regeneration process following different applied treatments will provide novel and essential information on the ability of those materials in producing bone that is comparable with the native tissue that they are meant to replace. This approach will therefore benefit the translation into clinic and the improvement of bone tissue regeneration strategies, which will ultimately replace the autogenous graft in several clinical situations, reducing cost, time and surgeries complications [12,13].

Biomechanical testing can be used to determine a number of parameters to mechanically characterise the integrity of bone (i.e. stiffness, strength) and provide information on global bone failure [32–36]. However, when an understanding of the relationships between microstructure and mechanics is needed, direct mechanical tests are not sufficient. The combination of mechanical testing and X-ray micro-computed tomography (microCT), known as *in situ* microCT, has allowed the direct three-dimensional (3D) evaluation of bone deformation and has enhanced the knowledge of how the microstructure influences bone damage [37–39]. Additionally, in conjunction to digital volume correlation (DVC), full-field displacement and strain measurements within the internal bone volume can be analysed [40,41]. In fact, DVC remains the only experimental-based method able to provide 3D strain distribution in bone. However, despite its extensive use in bone mechanics (i.e. trabecular bone [42], cortical bone [43], whole bones [44,45]), the application to newly formed bone induced *in vivo*, following different tissue engineering strategies has never been proposed.

In order to provide a detailed characterisation of bone regeneration and its deformation under different loading scenarios, high-resolution microCT images are needed. Only then, *ex vivo* bone-biomaterial interfaces during the healing process and/or remodelling of woven bone could be resolved in sufficient detail. Conventional laboratory-based X-ray microCT systems are a useful tool to assess bone density, mineralisation and microarchitecture [46,47]. However, the evaluation of smaller features within the tissue, such as osteocyte lacunae, bone-biomaterial interfaces and microcracks cannot be properly resolved without the requirement of long acquisition times. This represents a significant problem when X-ray imaging is combined with *in situ* mechanical experiments and multiple tomographic datasets are to be collected. In this perspective, high-energy synchrotron radiation (SR)-microCT has become a powerful technique able to combine fast imaging and high spatial resolution to resolve small features within the bone tissue [48–50]. Moreover, DVC applied to laboratory-based microCT systems cannot provide precise strain measurement within the tissue, but only if several bone structural units (BSUs) are included [51]. DVC based on SR-microCT high resolution images has recently shown great potential for the computation of reliable measurements within the BSUs [51,52], which would ultimately benefit the translation of full-field strain measurements from apparent to tissue level within bone structures. However, the application of DVC to investigate 3D displacement and strain measurements at tissue level is

still very recent; thus, there is a clear need to define a methodological approach to provide accurate and precise full-field measurements obtained from high-resolution images. This is particularly important for regenerated bone, with or without the presence of biomaterials, which needs to provide mechanical stability within the defect site. A reliable estimation of the internal distribution of local properties (i.e. displacements and strains) will allow the characterisation of such highly heterogeneous bone constructs.

Therefore, an evaluation of the initiation and progression of microdamage in newly formed bone, and bone-biomaterial interfaces could be better investigated when combining *in situ* SR-microCT mechanics and DVC. This will enhance the understanding of the osteoregeneration and biomechanical competence that novel biomaterials may induce *in vivo*, allowing to better predict the long-term bone healing process following bone tissue engineering strategies. Unfortunately, the high flux density of synchrotron X-ray radiation induces damage in bone tissue as a consequence of collagen degradation [53,54]. Therefore, prior to the application of *in situ* SR-microCT mechanics to newly regenerated bone structures, it remains essential to define some guidelines in order to preserve bone tissue integrity during such experiments.

1.2. Specific aims

The ultimate goal of this thesis is to combine X-ray biomechanical imaging and digital volume correlation (DVC) to newly regenerated bone structures in order to provide a deeper insight on bone regeneration, mechanical competence and deformation mechanisms following different tissue engineering strategies. Distinct biomaterials implanted in critical-sized bone defects are known to influence the bone healing process, and consequently, the achieved newly formed bone morphometry, mineralisation and mechanics. Thus, the design of novel biomaterials will benefit from the 3D *ex vivo* structural and mechanical analysis herein presented. In short, *in situ* microCT mechanics and DVC will be applied, for the first time, to newly formed bone produced *in vivo* in critical bone defects following the implantation of osteoregenerative biomaterials. To do so, a mandatory step will be to define a comprehensive methodological approach, able to determine the reliability of DVC at tissue level based on high-resolution microCT images. Additionally, experimental protocols will be fine-tuned for the application of *in situ* SR-microCT mechanics to bone tissue aiming at minimising the irradiation-induced damage. Finally, the developed methodological approach will be used to investigate the micromechanics of bone-biomaterial systems and newly formed bone *in vivo*.

Specifically, the following three aims are defined:

Aim 1: Development of a methodological approach for full-field strain investigation of bone at tissue level.

Aim 2: Establishment of experimental protocols able to preserve bone tissue integrity during *in situ* SR-microCT mechanics.

Aim 3: Investigation of three-dimensional deformation mechanisms of bone-biomaterial systems and new regenerated bone produced *in vivo*, following implantation of osteoregenerative biomaterials.

1.3. Outline of the thesis

The thesis is structured into six chapters. In addition to the current chapter in which thesis motivation and specific aims are presented, the content of the subsequent chapters is as follow:

- **Chapter 2** provides the required scientific background for this thesis. Firstly, bone as an organ is described with regards to its morphology, composition and development in normal conditions and following fracture. Further, a short overview of critical-sized bone defects and its clinical relevance in orthopaedics is presented. Most commonly used bone grafts and biomaterials for bone defect repair are reviewed, as well as the different techniques employed to biomechanically evaluate bone regeneration process. High-resolution X-ray imaging is then introduced, together with the generic principles of X-ray computed tomography (CT) and the description and experimental setup for both laboratory- and synchrotron-based microCT systems. Finally, the experimental approaches employed for the mechanical characterisation of bone regeneration, *in situ* mechanical testing and DVC, are described together with the state-of-the-art in the application to bone mechanics.

- **Chapter 3** describes the DVC approach used in the course of this PhD project. A detailed description of its application to SR-microCT images of trabecular bone and bone-biomaterial systems is presented, together with the operating principles of the DVC algorithm. An optimisation of image post-processing and DVC settings is performed in order to enhance DVC-computed displacements/strains based on 'zero-strain' repeated SR-microCT scans, providing reliable full-field measurements at tissue level.

- **Chapter 4** contains two methodological approaches aiming at preserving bone tissue integrity during *in situ* SR-microCT experiments. Firstly, the effect of SR X-ray radiation on the mechanical integrity of trabecular bone is assessed using *in situ* mechanical testing and DVC following variable exposure times to SR irradiation. Additionally, a simulation of the radiation dose delivered to bone specimens is computed to assess the combination of local irradiation and mechanical strain concentration on bone-induced damage. Secondly, a proof-of-concept methodology in presented based on the determination of DVC-computed residual strains in cortical and trabecular bone specimens exposed to SR irradiation either at room temperature or 0°C. The effect of the environmental temperature during *in situ* SR-microCT studies on bone tissue integrity is assessed, as well as the characterisation of irradiation-induced microcracks in the tissue.

- **Chapter 5** presents the application of *in situ* X-ray biomechanical imaging and DVC for the investigation of the 3D deformation mechanisms in newly regenerated bone following the implantation of osteoregenerative biomaterials in critical-sized bone defects *in vivo* (ovine model). Specifically, the first section of the chapter describes the full-field strain distribution at the bone-biomaterial interface, in relation to the newly formed bone produced *in vivo* after the implantation of osteoconductive commercial grafts in the defect site. DVC is applied to high-resolution SR-microCT images to evaluate the internal strain and microdamage evolution of bone-biomaterial systems under step-wise compression. The second section of the chapter presents a detailed analysis of the 3D internal strain for bone regeneration in bone defects treated *in vivo* with osteoinductive biomaterials. High-resolution microCT, *in situ* step-wise compression and DVC are combined to evaluate the bone mineral density distribution, morphometry and load transfer response following different treatments.

- **Chapter 6** includes the overall synthesis of the thesis. The thesis content is summarised with its major research contributions and findings. The societal impact of the research is discussed together with the limitations of the presented work. Finally, the chapter is concluded with an outlook on future work.

References

[1] A. Oryan, S. Monazzah, A. Bigham-Sadegh, Bone injury and fracture healing biology., Biomed. Environ. Sci. 28 (2015) 57–71. doi:10.3967/bes2015.006.

[2] D.J. Hadjidakis, I.I. Androulakis, Bone Remodeling, Ann. N. Y. Acad. Sci. 1092 (2006) 385–396. doi:10.1196/annals.1365.035.

[3] R. Marsell, T.A. Einhorn, The biology of fracture healing, Injury. 42 (2011) 551–555. doi:10.1016/j.injury.2011.03.031.

[1] E. Roddy, M.R. DeBaun, A. Daoud-Gray, Y.P. Yang, M.J. Gardner, Treatment of critical-sized bone defects: clinical and tissue engineering perspectives, Eur. J. Orthop. Surg. Traumatol. 28 (2018) 351–362. doi:10.1007/s00590-017-2063-0.

[5] E.H. Schemitsch, Size Matters: Defining Critical in Bone Defect Size!, J. Orthop. Trauma. 31 (2017) S20–S22. doi:10.1097/BOT.0000000000000978.

[6] A. Nauth, M.D. McKee, T.A. Einhorn, J.T. Watson, R. Li, E.H. Schemitsch, Managing bone defects., J. Orthop. Trauma. 25 (2011) 462–466. doi:10.1097/BOT.0b013e318224caf0.

[7] A. Nauth, E. Schemitsch, B. Norris, Z. Nollin, J.T. Watson, Critical-Size Bone Defects, J. Orthop. Trauma. 32 (2018) S7–S11. doi:10.1097/BOT.0000000000001115.

[8] V. Campana, G. Milano, E. Pagano, M. Barba, C. Cicione, G. Salonna, W. Lattanzi, G. Logroscino, Bone substitutes in orthopaedic surgery: from basic science to clinical practice, J. Mater. Sci. Mater. Med. 25 (2014) 2445–2461. doi:10.1007/s10856-014-5240-2.

[9] W. Wang, K.W.K. Yeung, Bone grafts and biomaterials substitutes for bone defect repair: A review, Bioact. Mater. 2 (2017) 224–247. doi:https://doi.org/10.1016/j.bioactmat.2017.05.007.

[10] P. V. Giannoudis, H. Dinopoulos, E. Tsiridis, Bone substitutes: An update, Injury. 36 (2005) S20–S27. doi:10.1016/j.injury.2005.07.029.

[11] M.-P. Ginebra, M. Espanol, Y. Maazouz, V. Bergez, D. Pastorino, Bioceramics and bone healing, EFORT Open Rev. 3 (2018) 173–183. doi:10.1302/2058-5241.3.170056.

[12] T. Winkler, F.A. Sass, G.N. Duda, K. Schmidt-Bleek, A review of biomaterials in bone defect healing, remaining shortcomings and future opportunities for bone tissue engineering, Bone Joint Res. 7 (2018) 232–243. doi:10.1302/2046-3758.73.BJR-2017-0270.R1.

[13] V. Martin, A. Bettencourt, Bone regeneration: Biomaterials as local delivery systems with improved osteoinductive properties, Mater. Sci. Eng. C. 82 (2018) 363–371. doi:10.1016/j.msec.2017.04.038.

[14] J.F. Keating, A.H.R.W. Simpson, C.M. Robinson, The management of fractures with bone loss., J. Bone Joint Surg. Br. 87 (2005) 142–150.

[15] M.K. Sen, T. Miclau, Autologous iliac crest bone graft: Should it still be the gold standard for treating nonunions?, Injury. 38 (2007) 2–7. doi:10.1016/j.injury.2007.02.012.

[16] R. Dimitriou, G.I. Mataliotakis, A.G. Angoules, N.K. Kanakaris, P. V. Giannoudis, Complications following autologous bone graft harvesting from the iliac crest and using the RIA: A systematic review, Injury. 42 (2011) S3–S15. doi:10.1016/j.injury.2011.06.015.

[17] J.C. Banwart, M.A. Asher, R.S. Hassanein, Iliac Crest Bone Graft Harvest Donor Site Morbidity: A Statistical Evaluation, Spine (Phila. Pa. 1976). 20 (1995). https://journals.lww.com/spinejournal/Fulltext/1995/05000/Iliac_Crest_Bone_Graft_Harvest_Donor_Site.12.aspx.

[18] H.J. Mankin, F.J. Hornicek, K.A. Raskin, Infection in Massive Bone Allografts., Clin. Orthop. Relat. Res. 432 (2005). https://journals.lww.com/corr/Fulltext/2005/03000/Infection_in_Massive_Bone_Allografts_.28.aspx.

[19] V. Grover, A. Kapoor, R. Malhotra, S. Sachdeva, Bone allografts: a review of safety and efficacy., Indian J. Dent. Res. 22 (2011) 496. doi:10.4103/0970-9290.87084.

[20] S. Bose, M. Roy, Recent Advances in Bone Tissue Engineering Scaffolds, Trends Biotechnol. 30 (2013) 546–554. doi:10.1016/j.tibtech.2012.07.005.Recent.

[21] F.R.A.J. Rose, ore, R.O.C. Oreffo, Bone tissue engineering: Hope vs hype, Biochem. Biophys. Res. Commun. 292 (2002) 1–7. doi:10.1006/bbrc.2002.6519.

[22] Y. Fillingham, J. Jacobs, Bone grafts and their substitutess, Bone Jt. J. 98–B (2016) 6–9. doi:10.1302/0301-620X.98B1.36350.

[23] T.-M. De Witte, L.E. Fratila-Apachitei, A.A. Zadpoor, N.A. Peppas, Bone tissue engineering via growth factor delivery: from scaffolds to complex matrices, Regen. Biomater. (2018) 197–211. doi:10.1093/rb/rby013.

[24] C.J. Kowalczewski, J.M. Saul, Biomaterials for the delivery of growth factors and other therapeutic agents in tissue engineering approaches to bone regeneration, Front. Pharmacol. 9 (2018) 1–15. doi:10.3389/fphar.2018.00513.

[25] S. Zwingenberger, C. Nich, R.D. Valladares, Z. Yao, M. Stiehler, S.B. Goodman, Recommendations and considerations for the use of biologics in orthopedic surgery, BioDrugs. 26 (2012) 245–256. doi:10.2165/11631680-000000000-00000.

[26] R. Dimitriou, E. Jones, D. McGonagle, P. V. Giannoudis, Bone regeneration: Current concepts and future directions, BMC Med. 9 (2011) 66. doi:10.1186/1741-7015-9-66.

[27] C.P.G. Machado, S.C. Sartoretto, A.T.N.N. Alves, I.B.C. Lima, A.M. Rossi, J.M. Granjeiro, M.D. Calasans-Maia, Histomorphometric evaluation of strontium-containing nanostructured hydroxyapatite as bone substitute in sheep, Braz. Oral Res. 30 (2016) 1–11. doi:10.1590/1807-3107BOR-2016.vol30.0045.

[28] W.R. Walsh, R.A. Oliver, C. Christou, V. Lovric, E.R. Walsh, G.R. Prado, T. Haider, Critical size bone defect healing using collagen-calcium phosphate bone graft materials, PLoS One. 12 (2017) 1–21. doi:10.1371/journal.pone.0168883.

[29] Z. Sheikh, M.N. Abdallah, A.A. Hanafi, S. Misbahuddin, H. Rashid, M. Glogauer, Mechanisms of *in vivo* degradation and resorption of calcium phosphate based biomaterials, Materials (Basel). 8 (2015) 7913–7925. doi:10.3390/ma8115430.

[30] J.J. Li, A. Akey, C.R. Dunstan, M. Vielreicher, O. Friedrich, D. Bell, H. Zreiqat, Effects of material-tissue interactions on bone regeneration outcomes using baghdadite implants in a large animal model, Adv. Healthc. Mater. 1800218 (2018) 1–9. doi:10.1002/adhm.201800218.

[31] P. Wang, L. Zhao, J. Liu, M.D. Weir, X. Zhou, H.H.K. Xu, Bone tissue engineering via nanostructured calcium phosphate biomaterials and stem cells, Bone Res. 2 (2015). doi:10.1038/boneres.2014.17.

[32] C.H. Turner, D.B. Burr, Basic biomechanical measurements of bone: A tutorial, Bone. 14 (1993) 595–608. doi:https://doi.org/10.1016/8756-3282(93)90081-K.

[33] S. Li, E. Demirci, V. V. Silberschmidt, Variability and anisotropy of mechanical behavior of cortical bone in tension and compression, J. Mech. Behav. Biomed. Mater. 21 (2013) 109–120. doi:10.1016/j.jmbbm.2013.02.021.

[34] J.S. Nyman, H. Leng, X. Neil Dong, X. Wang, Differences in the mechanical behavior of cortical bone between compression and tension when subjected to progressive loading, J. Mech. Behav. Biomed. Mater. 2 (2009) 613–619. doi:10.1016/j.jmbbm.2008.11.008.

[35] C. Öhman, M. Baleani, E. Perilli, E. Dall'Ara, S. Tassani, F. Baruffaldi, M. Viceconti, Mechanical testing of cancellous bone from the femoral head: Experimental errors due to off-axis measurements, J. Biomech. 40 (2007) 2426–2433. doi:10.1016/j.jbiomech.2006.11.020.

[36] U. Wolfram, H.J. Wilke, P.K. Zysset, Damage accumulation in vertebral trabecular bone depends on loading mode and direction, J. Biomech. 44 (2011) 1164–1169. doi:10.1016/j.jbiomech.2011.01.018.

[37] R. Müller, S.C. Gerber, W.C. Hayes, Micro-compression: a novel technique for the nondestructive assessment of local bone failure, Technol. Heal. Care. 6 (1998) 433–444. doi:10.1016/S0021-9290(98)80302-3.

[38] A. Nazarian, R. Müller, Time-lapsed microstructural imaging of bone failure behavior, J. Biomech. 37 (2004) 55–65. doi:10.1016/S0021-9290(03)00254-9.

[39] A. Nazarian, B.D. Snyder, D. Zurakowski, R. Müller, Quantitative micro-computed tomography: A non-invasive method to assess equivalent bone mineral density, Bone. 43 (2008) 302–311. doi:10.1016/j.bone.2008.04.009.

[40] B.K. Bay, T.S. Smith, D.P. Fyhrie, M. Saad, Digital volume correlation: Three-dimensional strain mapping using X-ray tomography, Exp. Mech. 39 (1999) 217–226. doi:10.1007/BF02323555.

[41] B.K. Bay, Methods and applications of digital volume correlation, J. Strain Anal. Eng. Des. 43 (2008) 745–760. doi:10.1243/03093247JSA436.

[42] F. Gillard, R. Boardman, M. Mavrogordato, D. Hollis, I. Sinclair, F. Pierron, M. Browne, The application of digital volume correlation (DVC) to study the microstructural behaviour of trabecular bone during compression, J. Mech. Behav. Biomed. Mater. 29 (2014) 480–499. doi:10.1016/j.jmbbm.2013.09.014.

[43] D. Christen, A. Levchuk, S. Schori, P. Schneider, S.K. Boyd, R. Müller, Deformable image registration and 3D strain mapping for the quantitative assessment of cortical bone microdamage, J. Mech. Behav. Biomed. Mater. 8 (2012) 184–193. doi:10.1016/j.jmbbm.2011.12.009.

[44] A.I. Hussein, P.E. Barbone, E.F. Morgan, Digital volume correlation for study of the mechanics of whole bones, Procedia IUTAM. 4 (2012) 116–125. doi:10.1016/j.piutam.2012.05.013.

[45] G. Tozzi, V. Danesi, M. Palanca, L. Cristofolini, Elastic Full-Field Strain Analysis and Microdamage Progression in the Vertebral Body from Digital Volume Correlation, Strain. 52 (2016) 446–455. doi:10.1111/str.12202.

[46] A. Nazarian, J. Muller, D. Zurakowski, R. Müller, B.D. Snyder, Densitometric, morphometric and mechanical distributions in the human proximal femur, J. Biomech. 40 (2007) 2573–2579. doi:10.1016/j.jbiomech.2006.11.022.

[47] M.L. Bouxsein, S.K. Boyd, B.A. Christiansen, R.E. Guldberg, K.J. Jepsen, R. M??ller, Guidelines for assessment of bone microstructure in rodents using micro-computed tomography, J. Bone Miner. Res. (2010). doi:10.1002/jbmr.141.

[48] R. Voide, P. Schneider, M. Stauber, P. Wyss, M. Stampanoni, U. Sennhauser, G.H. van Lenthe, R. Müller, Time-lapsed assessment of microcrack initiation and propagation in murine cortical bone at submicrometer resolution, Bone. 45 (2009) 164–173. doi:10.1016/j.bone.2009.04.248.

[49] P.J. Thurner, P. Wyss, R. Voide, M. Stauber, M. Stampanoni, U. Sennhauser, R. Müller, Time-lapsed investigation of three-dimensional failure and damage accumulation in trabecular bone using synchrotron light, Bone. 39 (2006) 289–299. doi:10.1016/j.bone.2006.01.147.

[50] A. Larrue, A. Rattner, N. Laroche, L. Vico, F. Peyrin, Feasibility of micro-crack detection in human trabecular bone images from 3D synchrotron microtomography, Annu. Int. Conf. IEEE Eng. Med. Biol. - Proc. (2007) 3918–3921. doi:10.1109/IEMBS.2007.4353190.

[51] E. Dall'Ara, M. Peña-Fernández, M. Palanca, M. Giorgi, L. Cristofolini, G. Tozzi, Precision of DVC approaches for strain analysis in bone imaged with μCT at different dimensional levels, Front. Mater. 4:31 (2017). doi:10.3389/fmats.2017.00031.

[52] M. Palanca, A.J. Bodey, M. Giorgi, M. Viceconti, D. Lacroix, L. Cristofolini, E. Dall'Ara, Local displacement and strain uncertainties in different bone types by digital volume correlation of synchrotron microtomograms, J. Biomech. c (2017). doi:10.1016/j.jbiomech.2017.04.007.

[53] H.D. Barth, M.E. Launey, A.A. MacDowell, J.W. Ager, R.O. Ritchie, On the effect of X-ray irradiation on the deformation and fracture behavior of human cortical bone, Bone. 46 (2010) 1475–1485. doi:10.1016/j.bone.2010.02.025.

[54] H.D. Barth, E.A. Zimmermann, E. Schaible, S.Y. Tang, T. Alliston, R.O. Ritchie, Characterization of the effects of x-ray irradiation on the hierarchical structure and mechanical properties of human cortical bone, Biomaterials. 32 (2011) 8892–8904. doi:10.1016/j.biomaterials.2011.08.013.

Chapter 2. Background

2.1. Bone

Bone is the main constituent of the skeletal system, important to the body both mechanically and metabolically, and differs from the other connective tissues forming the skeleton in rigidity and hardness [1]. Mechanically, bone enables the skeleton to maintain the shape of the body, to protect vital organs, to supply the framework for the bone marrow and to transmit the force of muscular contraction from one part of the body to another during movement. Metabolically, the high mineralisation of the bone matrix serves as a reservoir for ions, particularly calcium and phosphate [1,2]. Bone is a unique material, capable of adapting to a variety of environmental stimuli to fulfil specific demands [3,4].

2.1.1. Bone morphology

Bones can be divided in four general categories according to their shape: long bones, short bones, flat bones and irregular bones. The macroscopic morphology of bone is well represented in long bones (Figure 1). A typical adult long bone consists of a central cylindrical shaft (diaphysis) and two wider and rounder ends (epiphyses). The diaphysis and epiphyses are connected by conical regions (metaphysis). Most long bones have their ends wider than their central part, because the ephiphyseal and methapyseal bone supports the articular cartilage that covers the joints at the ends [5].

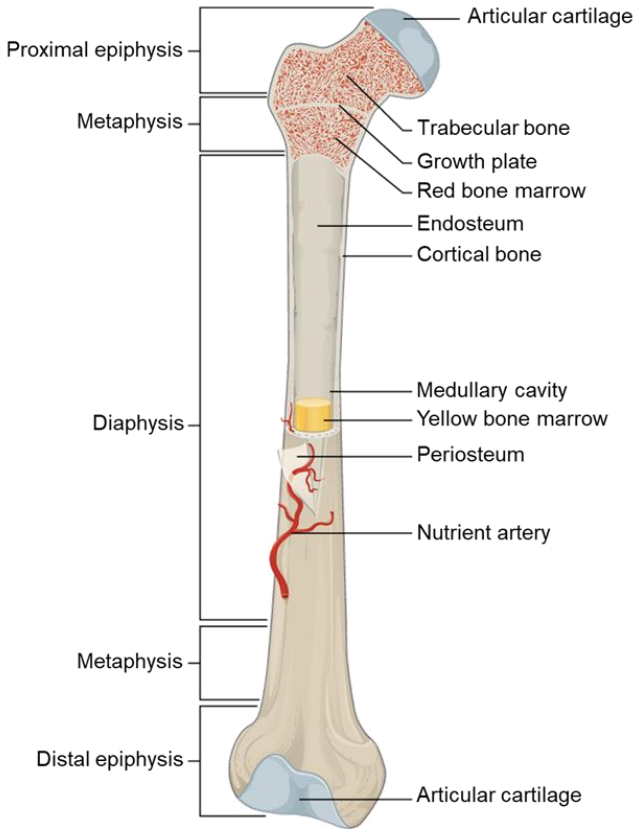

Figure 1. Schematic diagram of a typical long bone (femur). Adapted from [6] under license CC BY 4.0.

At the macroscopic scale, bone tissue is arranged in two architectural forms: cortical or compact bone; and trabecular or cancellous bone. The diaphysis is composed mainly of cortical bone, while the epiphysis and metaphysis contain mostly trabecular bone with a thin shell of cortical bone (Figure 2). During growing, the epiphysis and metaphysis are separated by a plate of cartilage known as the growth plate. The growth plate and the adjacent trabecular bone in the metaphysis constitutes a region where trabecular bone production and longitudinal growth of bone occur. In the adult, the growth plate has been replaced by trabecular bone, which caused the fusion of the epiphysis and metaphysis [1,5].

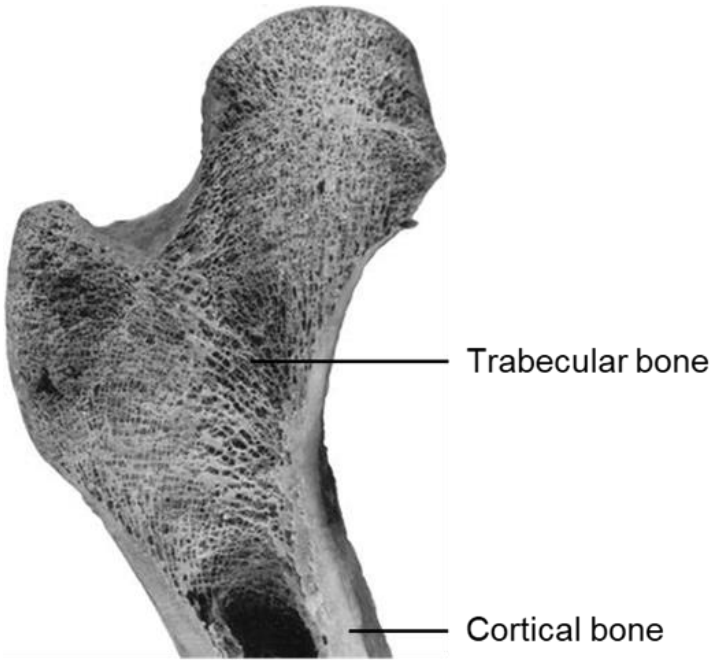

Figure 2. Trabecular and cortical bone distribution in the proximal femur. Adapted from [7] with permission. Copyright (2006) Springer Nature.

Cortical bone is dense and solid with only microscopic channels (i.e. Haversian canals) and an overall porosity of ~10%. Approximately 80% of the adult human skeleton is cortical bone, which forms the outer wall of all bones and which is largely responsible for the supportive and protective function of the skeleton. The remaining 20% of the bone mass is trabecular bone, which is found in the internal parts of the skeleton. Trabecular bone appears as a network of small, interconnected plates and rods called trabeculae, with relatively large spaces between them, having a porosity between 50% and 90% [1,2,5].

The outer surface of most bone is covered by the periosteum, a fibrous connective tissue sheath that surrounds the outer cortical surface of bone and an inner cellular layer of undifferentiated cells. The periosteum protects and aides in bone formation, playing an important role in appositional growth and fracture healing. The inner surface of cortical bone, trabecular bone and the blood vessels canals present in bone are covered by the endosteum. The endosteum is a membranous structure containing blood vessels, osteoblast, osteoclasts and bone-lining cells [1,8].

At the microscopic scale, mammalian bone can be structurally classified into woven and lamellar bone (Figure 3). Woven bone is rapidly deposited during periods of rapid growth or rapid bone production. Its collagen is fine-fibre and oriented almost randomly [9]. It then becomes highly mineralised [10], providing a provisional material that is eventually resorbed and replaced by lamellar bone. Lamellar bone is laid down much more slowly, having a more defined structure, which is built up of a unit layer called lamellae. In the lamellae, the collagen is arranged in thicker bundles than in woven bone [4].

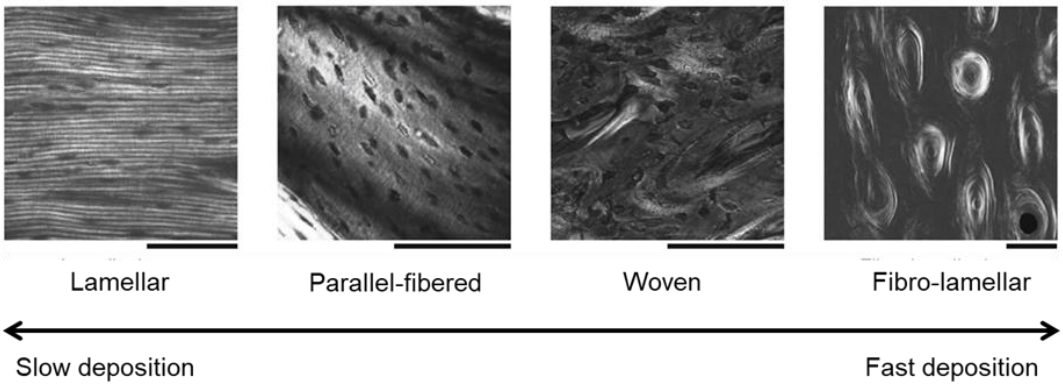

Figure 3. Bone tissue types classified on the basis of collagen fiber matrix organisation [12], imaged in circularly polarised light. Lamellar bone is a slow-forming tissue type characterised by a highly ordered arrangement; the optical distinction of individual layers, or lamellae, is the result of regular changes in the preferred orientation of collagen fiber bundles. Woven bone is a rapidly forming tissue type, characterised by loosely packed collagen fibers coursing in all directions in a more or less random arrangement. Parallel-fibered bone presents an intermediate arrangement in its collagen fiber organisation. Fibro-lamellar bone is classically deposited as in initial framework of fine trabeculae of woven bone; the intervening trabecular spaces are later in-filled by deposition of lamellar bone, forming primary osteons. Scale bar = 0.1 mm. Adapted from [11,12] with permission. Copyright 2016 Elsevier.

The fundamental structural unit of cortical bone is the osteon or Haversian system (Figure 4). At the centre of each osteon there is a small channel, called a Haversian canal, which contains blood vessels and nerve fibres. The osteon itself consists of circular rings of lamellar (concentric lamellae) of mineralised matrix surrounding the central canal. Angular fragments of lamellar bone (interstitial lamellae) may exist between the osteons and these represent former osteons or primary bone. On the periosteum and endosteum of cortical bone, large layers of lamellae (circumferential lamellae) may be found, associated with bone growth on these specific surfaces. Transverse canals (Volkmann canals), connect the Haversian canals allowing the communication between the periosteum and bone marrow. The outer border of each osteon is surrounded by a cement line, which is a thick layer (0.5 – 1 µm) of mineralised matrix, deficient in collagen fibres [13]. Throughout woven and lamellar bone, small cavities (lacunae) containing entrapped bone cells (osteocytes) are visible. Microscopic tubular canals (canaliculi) connect the lacunae to each other and to the Haversian canals [1,2,14].

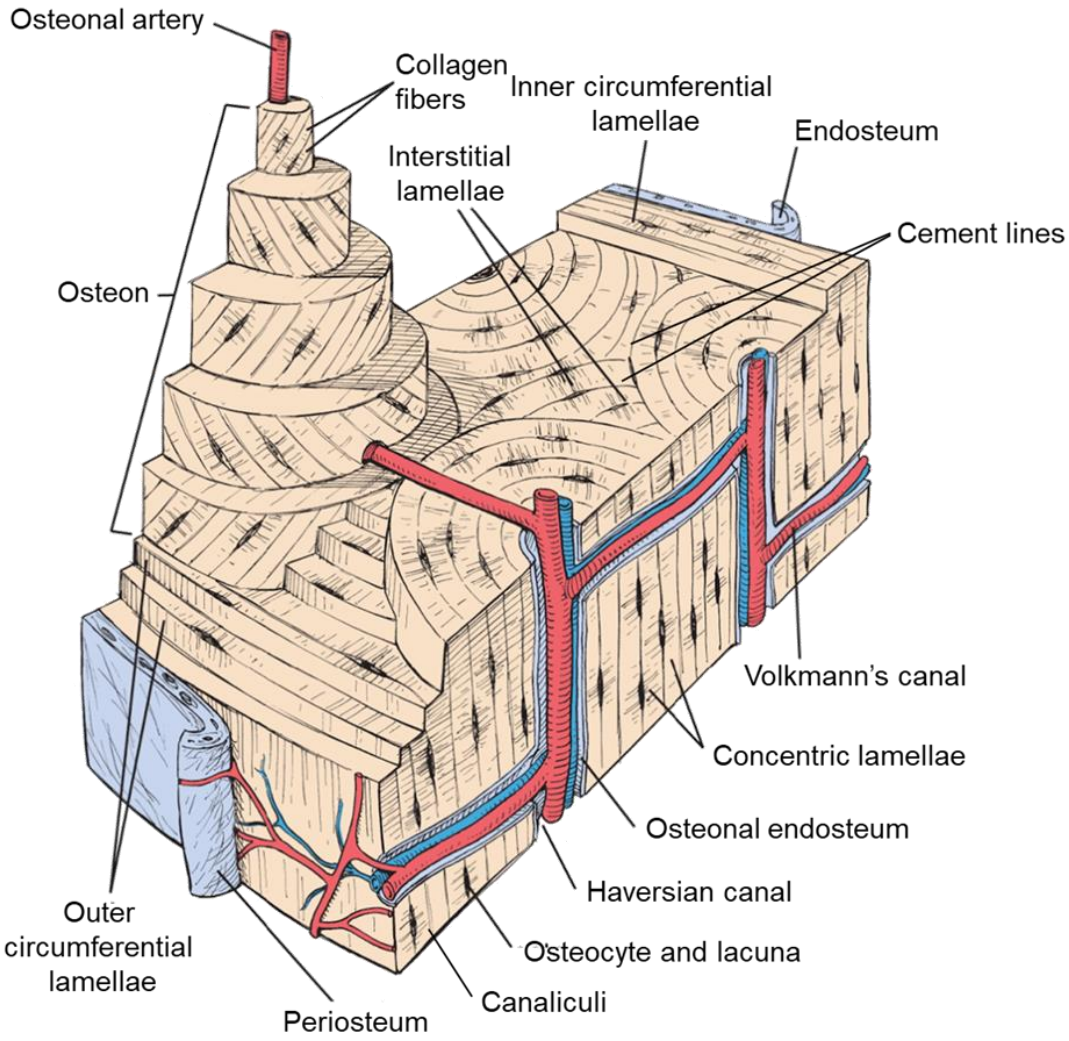

Figure 4. Diagram of a portion of a long bone shaft containing histological details of cortical bone. (Copyright © 2011 Wolters Kluwer Health | Lippincott Williams & Wilkins).

Trabecular bone is characterised by the absence of Haversian systems and its tissue is formed by a mosaic of angular segments of parallel sheets of lamellae, preferentially aligned with the orientation of the trabeculae (Figure 5). The angular grouping of lamellae is called trabecular packet and defines the structural unit of trabecular bone. As in the cortical bone, cement lines hold the trabecular packets together. The density and orientation of trabecular bone is related to the anatomical site and aligned to the loading regime experienced locally [15].

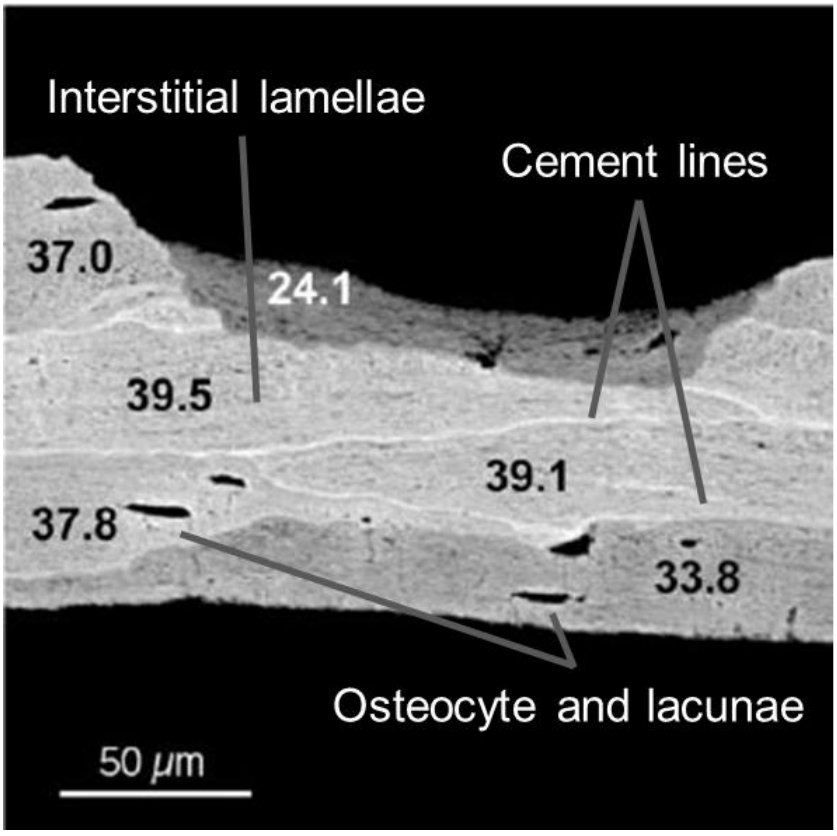

Figure 5. Surface of a sectioned trabecular bone feature viewed by quantitative backscattered imaging. Individual bone packets of different gray-levels, separate by thin bright cement lines, can be seen. The numbers indicate the average mineral content given in volume % within bone packets. The bone packets with the lowest mineral content corresponds to fresh bone formation, to the period of primary mineralisation, whereas others correspond to different time points of secondary mineralisation. Adapted from [16] with permissions. Copyright (2004) Royal Society of Chemistry.

2.1.2. Bone composition

The composition of bone varies with age, anatomical location, health condition and diet. In general, mature healthy bone consist of 50-70 vol% mineral, 20-40 vol% organic matrix, 5-10 vol% water and 1-5 vol% lipids [17]. The mineral phase of bone is usually presented in the form of small crystals in the shape of needles, plates and rods. Bone mineral is mainly impure hydroxyapatite (HA), containing constituents such as carbonate, sodium, potassium, citrate, magnesium, fluoride, and strontium. The organic matrix of bone is primarily composed of type I collagen (90%) and non-collagenous proteins (10%). Collagen aligns and creates three-dimensional frameworks into and onto which mineral crystals form (Figure 6) [17,18].

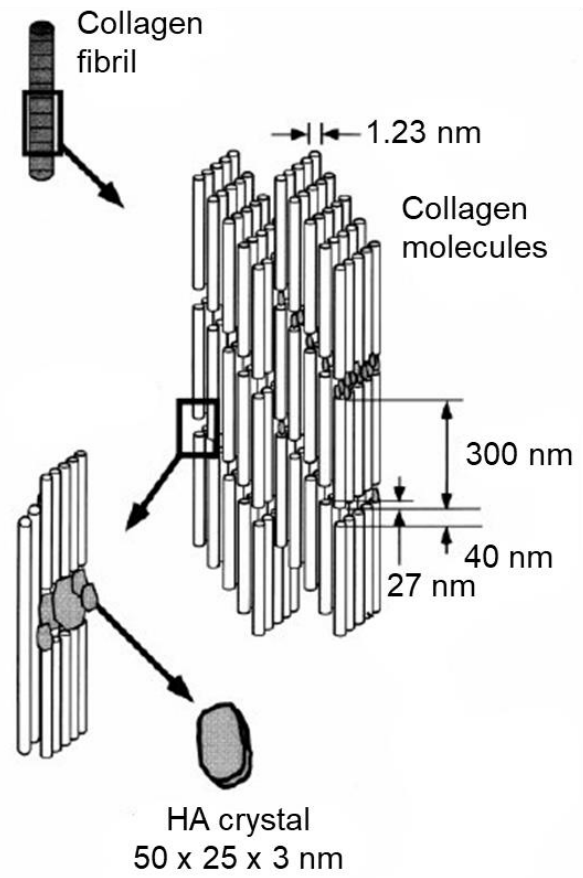

Figure 6. Schematic diagram illustrating the assembly of collagen fibrils and fibers and bone mineral crystals. Adapted from [19] with permission. Copyright (1998) Elsevier.

2.1.3. Bone cells

Bone absorption and remodelling are the primary functions of bone cells, which in turn originate from two cell lines: mesenchymal stem cells (MSCs) and hematopoietic stem cells (HSCs). The major cellular elements of bone include osteoclasts, osteoblasts, osteocytes and bone-lining cells (Figure 7). Osteoblasts are bone-forming cells that secrete several proteins that are present in the bone matrix, such as collagen I, and promote bone mineralisation. Osteoclasts are responsible for bone resorption and they balance the intricate processes of formation, maintenance and destruction of bone tissue. Osteocytes are the most abundant cell type in mature bone and they are formed from osteoblasts that have been entrapped during bone formation. Osteocytes play a key role in homeostatic, morphogenetic, and restructuring processes of bone mass. Additionally, they serve as a mechanical or damage sensor to initiate bone remodelling and repair. Bone-lining cells cover the majority of bone surface and they are derived from inactive osteoblasts. Bone-lining cells are able to release enzymes to remove the layer of osteoids covering the mineralised bone matrix, allowing osteoclasts to attach and begin resorption [1,8,20].

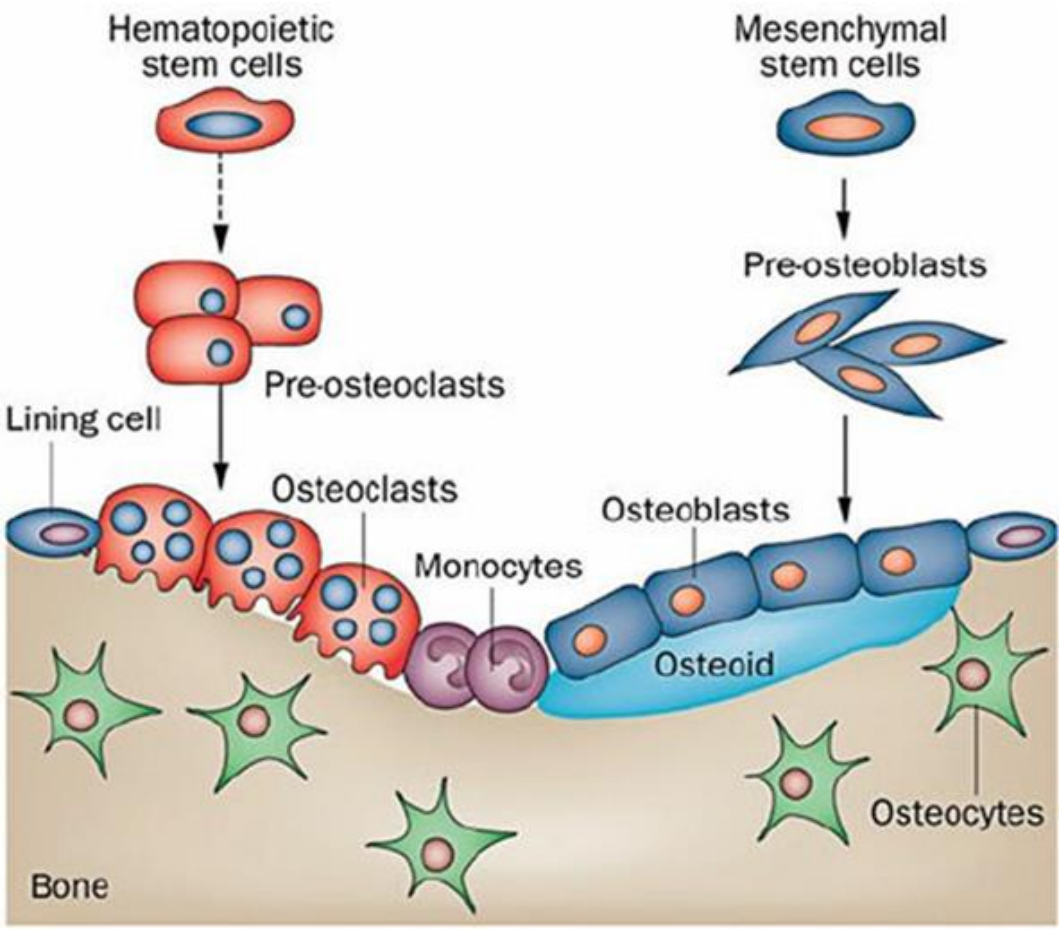

Figure 7. Classification of bone cells based on source, resorption and formation function. Adapted from [21] with permission. Copyright (2012) Springer Nature.

2.1.4. Bone growth, modelling and remodelling

Bone undergoes longitudinal and radial growth, modelling and remodelling during life. Longitudinal and radial growth takes place during childhood and adolescence. Longitudinal growth occurs at the growth plates, where cartilage proliferates in the epiphyseal and metaphyseal areas of long bones, before subsequently undergoing mineralisation to form primary new bone. Longitudinal growth adds new trabecular bone to pre-existing trabeculae and new length of cortical bone to pre-existing cortex, whereas radial growth adds new width by the apposition of sub-periosteal bone to the cortex [5,22].

Growth and modelling go side by side. During growth, periosteal bone is formed faster than endosteal bone removal. Together, modelling leads to an increasing of the outside of cortex and marrow cavity diameters, shaping the ends of long bones and drifting the trabeculae and cortices. Modelling allows not only the development of normal architecture during growth, but also the modulation of the overall bone shape in response to physiological influences or mechanical condition changes [1,23,24].

Bone remodelling is a lifelong process wherein bone is renewed to maintain bone that is mechanically and metabolically competent. Remodelling involves the replacement of

immature (primary) and old bone by resorption, followed by the formation of new lamellar bone. Remodelling serves to remove microdamage, replace dead and hypermineralised bone and adapt the microarchitecture to local stresses. Bone turnover preserves mechanical strength by replacing older, microdamaged bone with newer healthier bone and it also helps to regulate calcium and phosphate homeostasis [22,24,25].

2.1.5. Bone healing

Bone adaptability allows for efficient repair, which in turn helps to prevent bone fracture. However, the emergence of a load exceeding bone strength, or the accumulated damage under cyclic activity of loads (well below bone strength) at a rate that cannot be repaired, unavoidably cause bone fracture [26–28]. Following fracture, bone shows a remarkable ability to build a repair process that not only restores the mechanical integrity, but also the anatomical configuration with little or no evidence of scar tissue formation [29]. This has the advantage that no residual stress concentration remains and the strength of the bone returns to pre-fracture values [26,29,30].

Bone fracture repair occurs either by primary (direct) bone healing, where the fracture gap ossifies via intramembranous bone formation without external callus [29,31,32], or secondary (indirect) bone healing, where a multistage process of tissue regeneration stabilizes the bone with an external callus and repairs the fracture via endochondral ossification [29–34].

Primary bone healing mainly happens when the fracture gap is less than 0.1 mm and the fracture site is rigidly stabilised [35–38]. During primary fracture healing, the fractured cortices repair directly by continuous ossification and subsequent osteonal remodelling with the absence of cartilaginous or connective tissue [29,39].

Secondary fracture healing is the most common form of bone healing and occurs when the fracture edges are less than twice the diameter of the injured bone [38]. In general, secondary bone healing involves a sequence of events such as blood clotting, inflammatory response, fibrocartilage callus formation, intramembranous and endochondral ossification, and bone remodelling (Figure 8) [29,40,41]. During this type of healing bone forms from the periosteum and endosteum to produce hard callus. The fracture haematoma undergoes a process of tissue differentiation through granulation tissue, fibrous tissue, fibrocartilage and hyaline cartilage, which then forms woven bone that remodel to the definitive tissue of lamellar bone [41,42]. These phases involve the coordinated activity of different cell populations that proliferate, differentiate and synthetise extracellular matrix components. This cellular activity is spatially and temporally coordinated by a variety of growth factors and other regulatory molecules [26,29,30,43]. The initial repair is rapid, although the contour of the bone shows the bulge of callus for an extended period of remodelling [29,37].

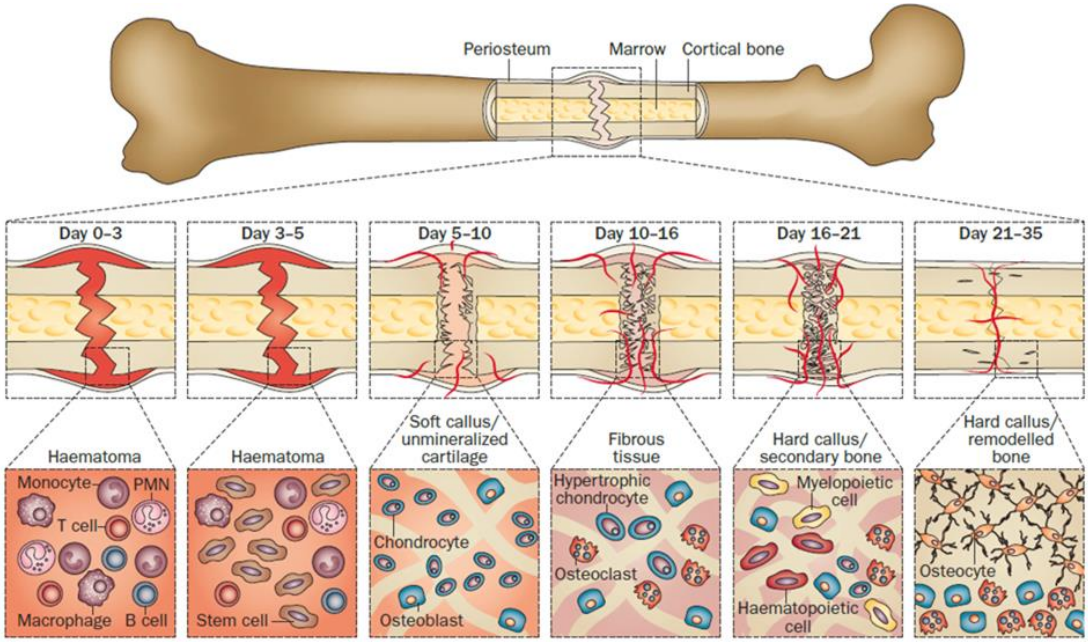

Figure 8. Illustration of a typical process of secondary bone healing showing the biological events and cellular activities at different phases. The time-scale of healing is equivalent to a mouse closed femur fracture fixed with an intramedullary rod. Adapted from [40] with permission. Copyright (2014) Springer Nature.

2.2. Critical-sized bone defects

Despite the intrinsic capacity of bone to regenerate and self-repair as part of physiological remodelling, this ability is limited to small fractures [44]. The native healing potential of bone is occasionally insufficient for reasons such as smoking [45,46], malnutrition [47], congenital disease [48] or large defects resulting from tumour resections [49,50] or trauma [51] and, therefore, therapeutic solutions need to be applied to promote healing [44,52–54].

Bone defects that exceed a size that can naturally heal are known as critical-sized bone defects and represent a specific type of non-union [55,56]. The classical definition of critically sized segmental bone defect is ‘the smallest osseous defect in a particular bone and species of animal that will not heal spontaneously during the lifetime of the animal’ [55] or ‘shows less than 10% bone regeneration during the lifetime of the animal’ [57]. Even if the defect size is not the unique parameter used to define a bone defect as critical [58], it has been found that, in most species, bone loss exceeding two times the diameter of the affected bone is unlikely to result in union despite appropriate stabilization methods [59,60].

The overall incidence of critical-sized bone defects is low. For instance, it is estimated that 10% of bone fractures in the United States result in impaired or incomplete bone healing, known as delayed and non-union, respectively [60–62]. However, the non-union caused by such defects can highly influence the quality of patient’s life, as they frequently lead to secondary complications including morbidity and functional limitations [63,64]. In order for a

large defect to be functionally restored, a surgical intervention is required to attempt bridging the affected area. Bone grafting is one of the most commonly used surgical methods to augment bone regeneration in orthopaedic procedures [65,66]. In fact, of the 20 million people affected by a lack of bone tissue annually worldwide, about 5 million cases require orthopaedic intervention, with grafting procedures representing about 60% of these interventions [67–70]. With an ageing society and an increase in activity even up to older age, an increase in patients affected by non-union fractures is expected, with associated rising costs of €37 billion for 3.5 million osteoporotic fractures in the European Union [71,72]. Thus, from both a quality of life and socio-economic perspectives, bone grafts providing fast and efficient bone restoration following fracture are beneficial [73].

2.3. Bone grafts and biomaterials for bone regeneration

Bone substitutes mainly serve as combined functions of mechanical support and osteoregeneration and they differ in terms of their biological properties such as osteoconduction, osteoinduction and osteogenesis, as well as osteointegration and structural support [66,74]. Osteoconduction refers to the ability to provide an environment capable of hosting osteoblast and osteo-progenitor cells and allow the migration and ingrowth of these cells within the three-dimensional architecture of the graft [75,76]. Osteoinduction describes the process of recruitment, proliferation and differentiation of primitive MSCs into the bone-forming cell lineage (i.e. osteoblasts) by which osteogenesis is induced [77–79]. Osteogenesis means the osteo-differentiation and subsequent new bone formation by donor cells derived from either the host bone or the graft [60,80]. Besides these three properties, bone grafts are sometimes required to provide osteointegration and structural support in order to promote bone tissue formation around the graft without the formation of fibrous tissue [66,74].

The primary approaches to bone grafting include natural and/or synthetic bone grafts [66,74]. More recently, to improve clinical outcomes, tissue engineering strategies have been applied to develop a number of growth-factor-based products [62,69,81].

2.3.1. Natural bone grafts

Natural bone grafts involve autografts and allografts. Autologous bone grafts remain the clinical ‘gold standard’ in orthopaedics [61,82] for bone defect repair because they contain growth factors for osteoinduction, cells for the osteogenesis and the framework for osteoconduction [83]. Autologous means that the bone is removed from the patient’s own body, often from the iliac crest, skullcap, mandible or tibia [82]. Even though autograft transplantation does not lead to immunogenic response [82,84], it presents limited source once a donator area is requited, donor site morbidity [85,86] and it is often associated with high surgical risk and a failure rate up to 30% [87]. One solution to overcome limited supply and donor site morbidity is the use of allogeneic bone sources.

Allografts refer to bone tissue that is harvested from human cadavers that have the advantage of being osteoconductive and osteoinductive, while being available through regional tissue banks in a variety of sizes and shapes [88]. They are considered the best alternative to autografts and have been effectively used in clinical practice in many circumstances [89–93], especially for those patients with poor healing potential, established non-union and extensive comminuted or pulverised fractures [66,83]. The allograft may be machined or customised and it is available in a variety of forms, including cortical, cancellous and highly processed bone derivatives (i.e. demineralised bone matrix) [62,66,74]. However, allograft treatments are associated with risk of rejection and viral transmission [94–97]. While tissue processing and sterilization through freezing or gamma irradiation virtually eliminates the possibility of disease transmissions, irradiation causes a number of adverse effects on tissue properties such as weakening [98–101].

2.3.2. Synthetic bone graft substitutes

The shortage of natural bone grafts and therefore the chance of meeting the demands in an aging population has driven the research on synthetic bone graft substitutes, focusing on finding safer, cheaper and easier biomaterials for bone regeneration. Table 1 summarises the different groups of bone substitutes: natural and synthetic biodegradable polymers, ceramics, including bioglasses, metals and composites, with their advantages and disadvantages. Among them, calcium sulphate, calcium phosphate ceramics and bioactive glass are the most popular synthetic bone substitutes currently available.

Calcium sulphate has been used as bone void filler since the late 1980s [102]. It has resorbable osteoconductive properties due to its three-dimensional structural framework, which is useful for angiogenesis and osteogenesis; however, it lacks osteogenic and osteoinductive properties [103,104]. Calcium sulphate has a rapid resorption rate and weak internal strength, which means that it can only be used to fill small bone defects with rigid internal fixation [88,97]. The ingrowth of vascular and new bone happens in conjunction with the resorption of the graft, which is fully dissolved within 6-12 weeks [74].

Calcium phosphate ceramics, such as tricalcium phosphate (TCP) and hydroxyapatite (HA) are constituted by calcium hydroxyapatites, in a chemical composition similar to the mineral phase of calcified tissues [105]. They are usually produced by sintering at high temperatures with the exclusion of water vapor and moulded by high pressure compaction. They are commonly commercialised as porous implants, non-porous dense implants and granular particles with pores [97]. Due to their excellent osteoconductive properties, calcium phosphate ceramics have been experimented extensively in clinical studies [106–109]. The osteoconductive properties of these materials depend on the pore size, porosity and degradation potential of the bone substitute, which is strictly related to the calcium-to-phosphate ratio [66,105,110]. The optimal pore dimension for ingrowth of new bone is between 150 and 500 μm in size (macroporosity), and both HA and TCP ceramics offer a

suitable macroporous structure to enhance new bone ingrowth [111–113]. Calcium phosphates generally provide limited biomechanical support due to their low tensile and shear resistance [105,114]. TCP ceramics are useful for filling bone defects caused by trauma and benign tumours but they are not indicated in large bone defects due to their unpredictable biodegradation profile (from months to years) [115]. HA has been used successfully in larger bone defects; however, the difficulty in implantation, the long time required for complete integration and replacement by newly formed bone and the inability to fill irregular gaps limit its use [66,116].

Table 1. Bone grafting materials used for bone repair and regeneration: advantages and disadvantages. Adapted from [79] with permission. Copyright (2015) Elsevier.

Bone grafting materials		**Advantages**	**Disadvantages**
Polymers	Natural	–Biodegradability – Biocompatibility – Bioactivity – Unlimited source (some of them)	– Low mechanical strength – High rates of degradation – High batch to batch variations
	Synthetic	– Biodegradability – Biocompatibility – Versatility	– Low mechanical strength – High local concentration of acidic degradation products
Ceramics	Calcium-sulphate and phosphate Bioglasses	– Biocompatibility – Biodegradability – Bioactivity – Osteoconductivity – Osteoinductivity (subject to structural and chemical properties)	– Brittleness – Low fracture strength – Degradation rates difficult to predict
Metals		– Excellent mechanical properties (high strength and wear resistance, ductility) – Biocompatibility	– Lack of tissue adherence – Corrosion – Risk of toxicity due to release of metal ions
Composites		– Combination of the above	– Combination of the above

Bioactive glass, also known as bioglass, refers to a group of synthetic silicate-based ceramics constituted by sodium oxide, calcium oxide, silicon dioxide, phosphorous pentoxide, potassium oxide, magnesium oxide and boric oxide [117,118]. The key component, silicate, constitutes ~50% of its weight [119]. The optimised constitution of the bioglass lead to a strong physical bonding between the bioglass and the host bone [120,121]. Bioglasses display mainly osteoconductive properties and have few osteoinductive properties [79]. Additionally, the porosity and relative fast resorption rate in

the first two weeks of implantation allow the ingrowth of neo-vascularization following the deposition of new bone [122]. Like the other ceramics, the mechanical properties of bioglass are reported to be weak and brittle [66,105]. Hence, it has been mainly applied for craniofacial reconstructive surgery [123], dental trauma [118] and orthopaedic surgery, when combined with growth factors [124].

2.3.3. Growth factors on bone regeneration

Most bone graft substitutes, especially ceramics, do not possess any osteoinductive properties and their ability to enhance bone healing mainly relies on their osteoconductivity [79]. To improve the clinical outcomes of biomaterials as bone grafts substitutes, new strategies rely on the application of osteoinductive compounds, such as growth factors, with osteoconductive carriers [62,69,81]. Growth factors play an essential role in bone regeneration, providing signals at the bone injury site and allowing progenitors and inflammatory cells to migrate and initiate the healing process [78,125,126]. The main families of growth factors involved in bone regeneration include fibroblast growth factors (FGFs), bone morphogenetic proteins (BMPs), vascular endothelial growth factors (VEGFs) and insulin-like growth factors (IGFs) [127]. Particular attention has been given to bone morphogenetic proteins (BMP), especially BMP-2 and BMP-7, which have been approved for clinical use in the US and Europe and present superior osteoinductive properties [128]. BMPs play an important role in the initiation of the bone fracture repair process and primarily act by triggering osteogenic differentiation of osteoprogenitors and MSCs recruited to the injured site [129,130]. BMP-2 is able to induce osteoblastic differentiation from MSCs and BMP-7 can directly promote angiogenesis [88]. Growth factors need to reach the injured site without loss of bioactivity and remain in the target location over the healing time-frame [131]. Therefore, efficient carriers for the delivery of growth factors are needed, able to control their release kinetics in order to optimise tissue formation [132]. Additionally, an optimal carrier must allow site-specific delivery of growth factors, have an ideal porosity to promote enhanced infiltration of cells, posterior vascular in-growth and should be easy to manufacture without losing bioactivity [131,133,134].

Collagen is marked as the ‘gold standard’ delivery system for BMPs, being the main organic component of bone and providing a structural matrix for bone regeneration. It can be used as a film, gel or sponge to provide osteoconductive properties that, together with its high affinity to BMPs, results in an ideal carrier for bone defect treatments [135,136]. Therefore, absorbable collagen sponges were among the first carriers for BMP-2 [137]. However, they present a number of drawbacks as their positioning is often difficult and secondary displacement may occur [138]. Collagen is quickly degraded *in vivo*, causing voids to develop within the new bone matrix due to its inability to provide a structure that lasts long enough to sustain cell migration [139]. Additionally, the use of collagen sponges is associated with an initial burst release of BMP-2 into the local environment [140], leading to

heterotrophic bone formation and activation of osteoclasts in the surrounding environment at high BMP-2 concentration, which may cause bone resorption [141,142].

Alternative carriers for the delivery of BMPs include synthetic polymers such as polycaprolactone (PCL), polyethylene glycol (PEG), polylactic-co-glycolic acid (PLGA) and natural polymers such as chitosan, silk fibroin, alginate, gelatin and hyaluronan, as well as composite materials combining the polymers with ceramics such as HA and TCP [62,69,81]. Additionally, micro- and nano-particle based delivery systems have been extensively used for a more precise and localised delivery and sustained release of BMPs [70,143]. Despite the intense research on the field, there are still major limitations in the use of biomaterials-mediated delivery of growth factors, mainly related to the inadequate release profiles of the compounds [144] In fact, the rapid burst release of the BMPs often results in an inefficient strategy at longer healing times [145] and therefore, there is a clinical need for an optimal delivery system that provides a more reliable spatiotemporal control.

2.4. Bone biomechanics

The major function of bone is to form the skeleton, which provides support for the body and protection for vital organs. The mechanical properties of bone are influenced by its quantity, distribution and quality. Since bone is a dynamic tissue, structure and composition can adapt over time to withstand the forces imposed upon it [146]. The most commonly used experimental approaches for characterising the mechanical properties of bone can be divided based on four hierarchical levels (Figure 9, Table 2): whole bone, tissue, microscale and nanoscale testing [147].

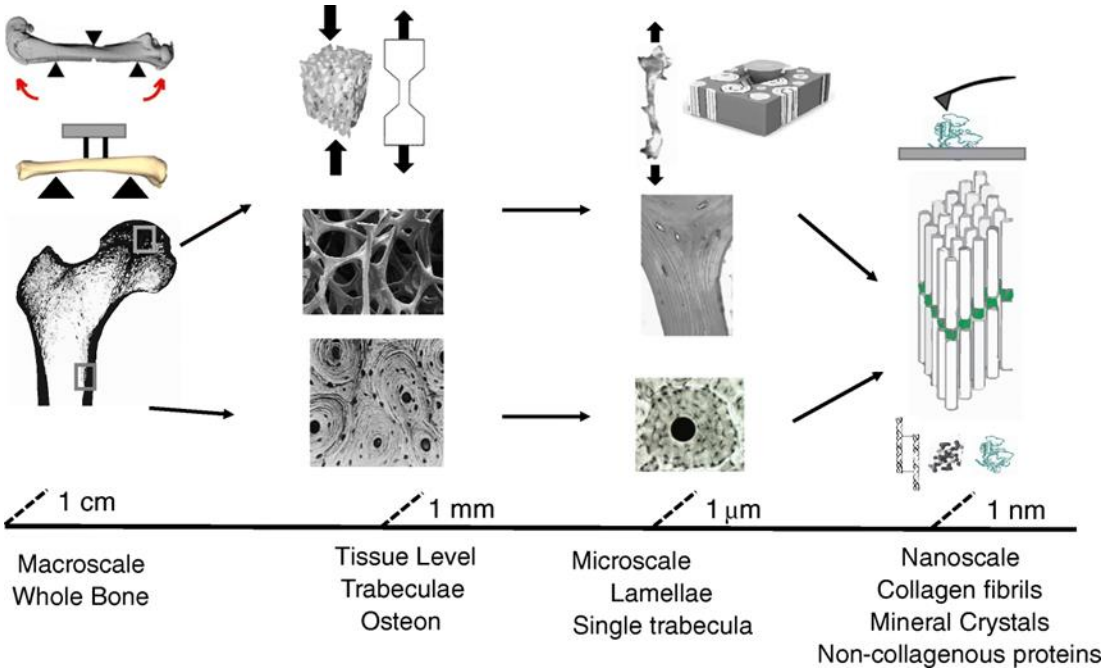

Figure 9. Schematic of bone structural hierarchy with the commonly used mechanical characterization technique at each length scale. Adapted from [147] with permission. Copyright (2018) Springer Nature.

Table 2. Summary of mechanical characterization techniques with outcome variables based on length scale and type of specimens. Adapted from [147] with permission. Copyright (2018) Springer Nature.

Length scale	Type of specimen	Mechanical testing mode	Outcome variables
Whole bones	Long bones, vertebra	Bending, tension, compression, torsion, compression	Extrinsic mechanical properties (i.e., structural stiffness, max load, work to fracture, fracture load)
Tissue	Cortical beam, dumbbell, dog bone, single-edged notched specimen (SEB), cancellous cores	Tension, compression, torsion, bending fatigue, compression (static or cyclic)	Intrinsic mechanical properties (i.e., Young's modulus, yield, fatigue and ultimate strength, fracture toughness)
Micro	Cortical bone cubes up to 5 mm thick, cortical or trabecular bone slices	Microscratch, microindentation, reference point indentation	Material level properties (i.e. fracture toughness, hardness, modulus (elastic and reduced), elastic work, total work, total indentation distance, indentation distance increase)
Nano	Cortical or trabecular bone specimen 2–3 mm thick, cortical or trabecular bone slices	Nanoindentation, *in situ* testing (tension, compression, bending)	Material level properties (i.e., hardness, modulus, fibril strain, mineral stress)

The outcome mechanical properties from the above mentioned tests are influenced by the amount, distribution and composition of bone tissue, as well as the interactions between the primary constituents [19]. The mechanical properties of bone vary widely from cancellous to cortical bone (Table 3). Nevertheless, a good description of bone mechanics is important for the characterisation of bone and bone-biomaterial interactions in critical-sized bone defects. This is of fundamental importance for bone tissue engineering strategies aiming at promoting bone regeneration with the correct mechanical properties to match that of the host bone [148,149].

2.4.1. Biomechanical evaluation of bone regeneration

In the field of orthopaedics, it is vital to evaluate the *in vivo* competence of the regenerated bone in order to validate the different treatments used for bone regeneration in critical bone defects. Traditionally, the *in vivo* performance of the biomaterials used for bone augmentation in terms of new bone formation, remodelling, biomaterial resorption and local biological effects is assessed using microCT and histology at selected end-points. Bone formation and biomaterial resorption can be examined in great detail using *in vivo* microCT, providing a unique insight of the implantation site at different time points. However, *in vivo* microCT resolution is limited [150] and a quantitative analysis remains difficult. Therefore, *ex vivo* analysis of new regenerated bone are commonly used to evaluate the efficacy of new biomaterials in bone defects healing.

Table 3. Mechanical properties of Trabecular and Cortical bone tissue. Elastic modulus reported in GPa mean (standard deviation when available). Adapted from [1].

Bone type	Testing technique	Trabecular bone	Cortical bone
Human distal femur	Buckling	8.69 (3.17)	
Human proximal tibia	Inelastic buckling	11.38 (wet)	
Human proximal tibia	Experiments and 2D finite element modeling	1.30	
Bovine femur Human tibia	Finite-element model	1.4–5.0	
Bovine femur Human femur	Ultrasonic method, bone cubes	10.9 (1.6) 12.7 (2.0)	
Human iliac crests	Three-point bending	3.81	4.89
Dry human femur Fresh human tibia	Cantilever bending with finite-element analysis	7.8 (5.4)	
Bovine femur	Tensile testing	1.0	
Bovine tibia PMMA composites	Ultrasonic test extrapolation	8.9	
Human vertebra (L3)	Three-dimensional structure model	3.8	
Human tibia	Three-point bending	4.59 (1.60)	5.44 (1.25)
Human tibia	Four-point bending	5.72 (1.27)	6.75 (1.00)
Human tibia	Tensile test (dry) Ultrasonic test	10.4 (3.5) 14.8 (1.4)	18.6 (3.5) 20.7 (1.9)
Porcine femur	Microindentation Nanoindentation	5.9 (4.3) 21.5 (2.1)	11.6 (9.5) 16.4 (1.3)
Human vertebra Human tibia (osteon/interstitial)	Nanoindentation	13.4 (2.0)	22.5 (1.3) (osteon) 25.8 (0.7) (interstitial)
Human femur	Nanoindentation (dry) Acoustic microscopy	18.14 (1.7) 17.50 (1.12)	20.02 (0.27) 17.73 (0.22)
Human femur	Nanoindentation (wet)	11.4 (5.6) (neck)	19.1 (5.4) (diaphysis: osteon) 21.2 (5.3) (diaphysis: interstitial) 15.8 (5.3) (neck: osteon) 17.5 (5.3) (neck: interstitial)
Human vertebra	Micro-CT image-based finite-element models	5.7 (1.6)	
Human vertebra	Micro-CT image-based finite-element models	6.6 (1.1)	
Bovine tibia	Micro-CT image-based finite-element models	17.3 (2.62)	
Human vertebra	Four-point bending	2.11 (1.89)	2.50 (1.58)

Ex vivo evaluation of bone regeneration is conducted at one unique time point, after the animal used for the critical bone defect model is sacrificed and they usually involve histology, scanning electron microscopy (SEM) and microCT investigations [110,151–155]. The three techniques are complimentary and together provide a deep vision on bone formation in the defect site. Histological analysis is a useful tool to understand the cell-mediated processes involved in the new bone formation and biomaterial degradation, as well as the biological effects of the biomaterials on the newly formed tissue, such as inflammatory response or soft

tissue presence. The high resolution of SEM images provides a detailed characterisation of the bone-biomaterial interactions, as well as the bone formation processes involved during bone healing and the different fibrillar organization within the previous defect site. However, SEM is restricted to sample sectioning and only surface analysis can be conducted. Very recently, Li et al. [152] used, for the first time, focused ion beam scanning electron microscopy (FIB-SEM) to evaluate the bone-biomaterial interaction at the nanoscale along the defect site. Although FIB-SEM allows volumetric information of the analysed region by compiling all sections together, it is a destructive technique and therefore, lot of attention has been given to microCT imaging, which allows for a 3D investigation in a non-destructive way of the implantation site. Furthermore, microCT analysis supports the quantification of the different tissue density components present in the defect site (i.e. newly formed bone, remaining biomaterials), as well as a 3D morphological analysis of the regenerated bone [156–160].

As stated above, a biomechanical characterisation of the new bone during the healing process is of fundamental importance to demonstrate the ability of the different treatments to restore new bone with biological and mechanical properties that are comparable to the initial native tissue. However, little research has focused on the *ex vivo* mechanical competence of bone reconstructions after implantation of biomaterials. In particular, traditional mechanical tests such as indentation and micro-indentation at different locations through the defect areas have been used to measure the stress at failure [161] and yield strength [156], respectively. Whereas indentation tests provided the mechanical strength of the healing defect size including both newly formed bone and remaining biomaterial [161], micro-indentation allowed for the characterization of the mechanical properties of the new regenerated bone tissue only [156]. Despite those data are extremely beneficial for the biomechanical evaluation of different biomaterials, they only provided local material properties and the deformation mechanisms at the implantation site under load could not be investigated.

The development of image-guided failure assessment (IGFA) by Müller et al. in the late 90s [162] allowed to monitor and evaluate, for the first time, the 3D deformation of bone at the microscopic level, as well as to determine how bone microstructure influences bone failure. However, a quantification of the full-field mechanical response was only possible with the introduction of digital volume correlation (DVC) by Bay et al. in 1999 [163]. A combination of high-resolution X-Ray imaging, *in situ* mechanical testing and DVC can be therefore considered a powerful tool to evaluate the mechanical response of newly formed bone during the osteoregeneration process, providing a better understanding of the efficacy of novel biomaterials to induce bone formation with mechanical properties resembling those of native bone tissue.

2.5. High-resolution X-ray imaging

X-ray imaging is particularly well suited for the hierarchical analysis of bone microstructure. X-ray computed tomography (CT) is a widely used technique for the analysis and quantification of bone structure in 3D, as it provides multiscale imaging with resolutions ranging from few millimetres to 100 nanometres (Figure 10), allowing to resolve bone structure from organ to cellular level [164]. At the microstructural level, X-ray microCT has been extensively used for the analysis of bone microarchitecture not only in healthy bone but also to better understand different diseases and their treatments, tissue engineering strategies and novel biomaterials [164,165].

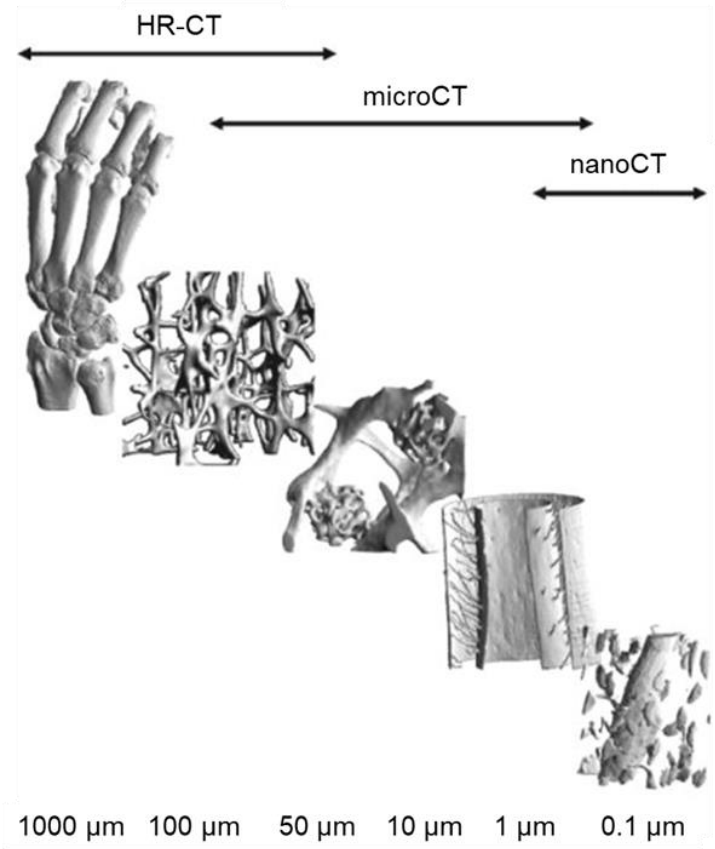

Figure 10. Hierarchical imaging using multiscale computed tomography (CT). The technique can be used on a large scale with different resolutions. The images show from left to right, human hand, trabecular bone structure, microcallus, murine cortical bone surface of a femur with internal vasculature and capillary in bone surrounded by osteocyte lacunae. Adapted from [166] with permission. Copyright (2008) Springer Nature.

Traditional laboratory-based microCT systems can achieve nominal resolution below 1 µm (Table 4), allowing the visualisation of ultrastructural features such as the canal network and osteocyte lacunae. The X-ray radiation used in those systems is polychromatic, and the beam diverges in a fan-like or conical shape. However, for achieving the highest resolutions (below 5 µm), long acquisition times are typically required to obtain a signal-to-noise-ratio (SNR) that is sufficient to resolve those specific features [165,167]. The combination of synchrotron radiation (SR) and CT techniques allows the fast acquisition of 3D images at

high spatial resolution (below 1 µm) (Table 4), able to resolve bone structure at tissue and cellular level. Synchrotron radiation has several advantages over conventional laboratory systems by providing monochromatic X-rays at a much higher photon flux. This property becomes particularly important for sub-micrometre spatial resolution imaging, limiting scan times while achieving high SNR [167,168]. The main drawback of SR-microCT imaging is in the limited access to SR sources. Moreover, the SR dose for typical SR-microCT experiments is usually high and even though no damage leading to detrimental effects of the bone microstructure is expected [169,170], it cannot be considered as a non-invasive technique. In fact, high SR doses can alter the mechanical properties of bone [169,171,172]; thus, special consideration is needed when performing mechanical tests in combination with SR-microCT imaging.

Table 4. Summary of characteristics of microCT systems with the typical values used in this PhD project.

microCT system	Equipment	Objective	Pixel size (µm)	X-rays
Laboratory microCT	Zeiss Versa 510/520	0.4X	~4-5	Micro-focus tungsten target laboratory source
		4X	~1-2	60-110 kV/ Polychromatic X-rays (>~10 keV)
		20X	~0.4-0.5	Peaks in spectrum at ~10-12keV and ~60keV
SR-microCT	DLS- I13-2	2X	2.6	5-35 keV/ monochromatic or polychromatic
		4X	0.81	Parallel beam, high brilliance, coherent

2.5.1. X-ray CT principles

The basic principle of CT is the interaction of X-ray radiation with matter. As an X-ray penetrates an object, it is exponentially attenuated according to the material along its path. The attenuation depends not only on the material but also on the energy spectrum of the X-ray source. Attenuation of monoenergetic X-rays is described by the Beer-Lambert law [173]:

$$I = I_0 \cdot e^{-\mu t}$$

Where I_0 is the X-ray intensity before reaching the object; I is the X-ray intensity after passing through the object; μ is the X-ray attenuation coefficient; and t is the thickness of the absorbing material.

X-ray CT is based on the data acquisition and data processing of individual projections (X-rays radiographs) recorded from different viewing directions that are combined using a reconstruction algorithm to compute the internal structure of the object of interest. In microCT, these projections are usually taken in a configuration in which the source and detector are at a fixed position and the object is rotated around its long axis (Figure 11). The source is mostly either a microfocus X-ray for lab-based systems or an insertion device in

SR-based systems and the detector is normally based on a CCD camera with a phospholayer to convert X-ray to visible light [166]. The two-dimensional projections can then be used to reconstruct a 3D image.

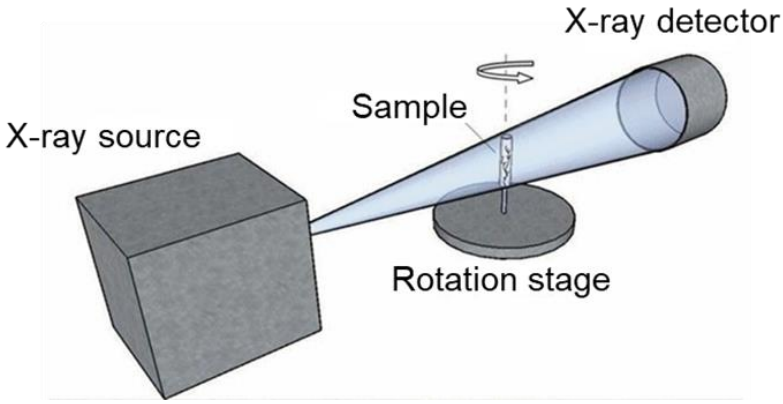

Figure 11. MicroCT system general configuration. Adapted from [167] with permission. Copyright (2015) IEEE.

Image reconstruction is used to compute the internal structural information from the projection images. The standard method of reconstructing microCT slices is a filtered back-projection [174,175]. The starting point is always an empty image matrix (i.e. a defined range of computer memory that contains only zeros at starting values). Each projection value is added to all the pictures elements in the computer memory along the direction in which it has been measured. In general, each detail in the object (represented in the attenuation profile) does not only contribute to the pixel value at the desired image point, but to the entire image as well. As a result, an unsharped image is obtained. To avoid the unsharpening, each projection has to be convolved before back-projection with a mathematical function, the convolution kernel. This constitutes a pointwise multiplication of the convolution kernel with the attenuation profile and addition of the resulting values. In essence, it represents a high-pass filtering procedure, which generates over- and under-shoots at object boundaries. Convolution additionally offers the possibility to influence image characteristics by the choice and design of the convolution kernel – from soft or smoothing to sharp or edge enhancing.

During image acquisition artifacts and partial volume effect intrinsic to the experimental apparatus and to the X-ray source can appear, obscuring details of interest and introducing errors during image reconstruction [176]. Among these errors, motion artefacts, ring artefacts, aliasing and beam hardening are common [166,176].

- Motion artefacts: If the object moves or rotates during the measurement, the projections do not fit together at the reconstruction, resulting in distortion of the object and tails enclosing it.
- Ring artefacts: Defective pixels in the CCD, defects in the scintillator or dust in the detector system may cause rings or half-rings around the rotation centre of the reconstructed images.

- Aliasing: It appears as streaks in the end images at the corner of objects as a result of insufficient number of projections. The number of projections is a trade-off between image quality and measurement time.
- Beam hardening: As a polychromatic beam passes through an object, the X-rays with lower energies are more easily attenuated than the higher energy X-rays, for this reason a beam will preferentially lose the lower end of its spectrum. This increase in mean energy is defined as beam hardening, which is the most common artefact encountered in CT imaging and causes an object to appear brighter at its edges than at the centre.

If imaging low atomic numbers, attenuation contrast does not provide sufficient contrast between the material (i.e. cortical bone matrix) and the features that need to be distinguished (i.e. lacuno-canalicular network, cement lines) [168,177,178]. As an alternative, contrast can be obtained from the phase shift of the X-rays as they pass through the object. This mode is called 'phase-contrast' [179,180]. In-line phase contrast takes advantage of image magnification when the sample is placed after the focus of X-ray focusing optics, creating a projection microscopy setup. The detector is mounted on a translation stage allowing to set up the geometrical magnification, which is a function of the beam divergence after the X-ray source, the source-to-sample distance, and the source-to-detector distance. Letting the beam propagate after interaction with the object creates not only a magnification effect but also strong phase contrast between different materials with similar attenuation coefficients. In-line phase contrast exploits the Fresnel diffraction of X-rays to enhance the visibility of edges and boundaries within an object. Phase retrieval procedures normally require at least two measurements of the intensity, taken at two different distances from the source [181], with the extent of phase contrast increasing with distance [179,180]. The 2D phase maps are retrieved following a holographic reconstruction approach [182], separating the object information from the defocused X-ray projections, which is employed for subsequent CT reconstruction to provide the 3D representation of the sample.

2.5.2. Laboratory-based X-ray microCT

In standard laboratory systems the X-ray radiation is created by focusing an electron beam, generated by a filament, on a target in a vacuum chamber. The X-rays (photons) produced have a broad spectrum which is controlled by the applied voltage as well as the target material, typically tungsten. Most of the modern lab-based microCT systems operate in a cone-beam geometry, in which the resolution of the system is defined by the pixel size of the detector, as well as the source spot size (size of the region on the target material from which X-rays are generated). The source spot size limits the resolution for large geometrical magnification, with spot sizes of ~1 μm being typical for higher-resolution microCT systems (Table 4). For some systems, the pixel size of the detector is controlled by using optical magnification between the scintillator (fluorescent material) and charge-coupled device, which converts the visible light (X-rays) to and electric signal (Figure 12). Phase contrast can be achieved using the in-line/propagation based method, which is manifested as an edge-

enhancement around sharp boundaries within the object and which increases with the distance between the object and the detector [180].

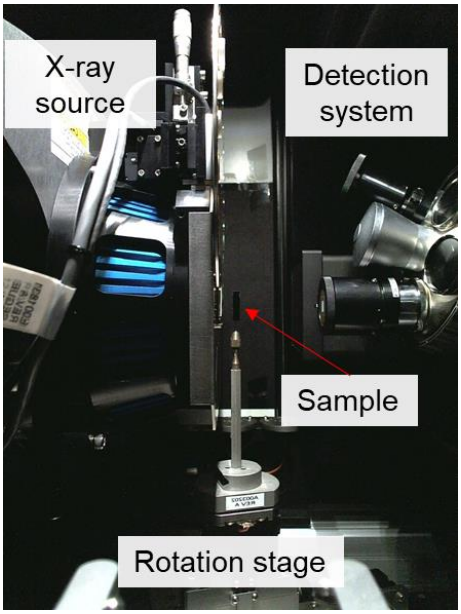

Figure 12. Zeiss Versa 510 setup for microCT imaging. The detector system incorporates optical magnification of a scintillator to achieve sub-micron pixel size.

2.5.3. Synchrotron radiation X-ray microCT

Synchrotron radiation from a third-generation source offer high flux and high coherence, with the ability to tune the X-ray spectrum to a monochromatic beam [183]. X-rays are produced when electron in the storage ring are forced to move in curved paths by bending magnets or insertion devices. The high flux enables rapid tomography data collection, so that dynamic experiments can be conducted [184]. The parallel beam geometry also facilitates *in situ* experiments since a large distance between sample and detector can be maintained without loss of intensity. Sub-micron imaging can be achieved with high resolution detectors, which employ optical magnification of scintillator screens. Phase contrast can be obtained via the in-line method or a variety of other techniques [185].

A synchrotron X-ray source consists of three components: the linear accelerator, the booster and the storage ring (Figure 13), which produce the intense synchrotron light required for experiments. Electrons are generated in the electron gun by heating high voltage cathode which will increase the thermal energy of the electrons to break away from the surface. There electrons are accelerated to almost the speed of light by two particle accelerators, namely the linear accelerator and the booster. Once the energy of the electrons reaches ~ 3 GeV (energy required to produce the whole spectrum of electromagnetic radiation – nearly the speed of light) they are transferred into the storage ring. The storage ring is a polygon, consisting of specially designed magnets called insertion devices, which are usually inserted in the straight parts of the storage rings and a radio frequency voltage source to deflect the electrons around the bends or re-accelerate the electron in the straight sections,

respectively. There are mainly two types of insertion devices: wigglers and undulators. The storage ring is maintained in a high vacuum condition, with a pressure approximately one million times lower than atmospheric pressure. Synchrotron light is emitted when the electrons travel at a relativistic speed and undulate within the powerful magnetic field inside the storage ring [186].

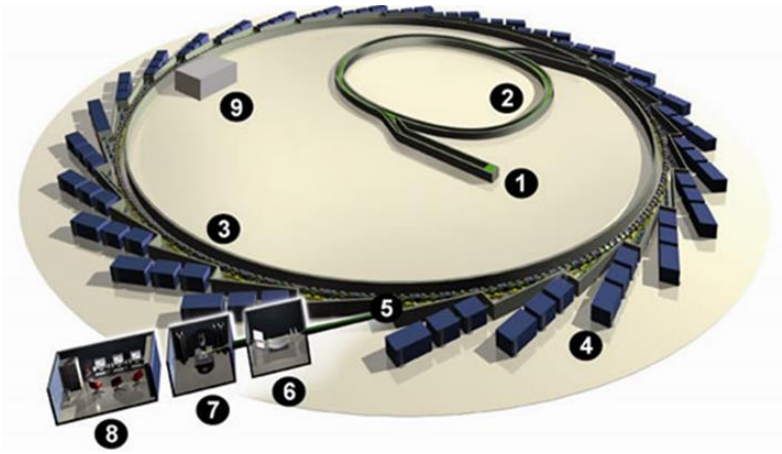

Figure 13. Layout of Diamond Light Source synchrotron third generation facility. (1) Linear accelerator. (2) Booster. (3) Storage ring. (4) Beamline. (5) Front-end. (6) Optics hutch. (7) Experimental hutch. (8) Control cabin. (9) Radiofrequency cavity [187]. Copyright (2018) Diamond Light Source.

The synchrotron light is then guided to the beamlines, which are usually tailored by appropriate optics and apertures to meet the need of the experiments. Each beamline is made up of three basic compartments: the front-end, the optic hutch, and the experimental station downstream (Figure 13). The front-end is fitted to the storage ring and connects to it at a tangent, passing through the main concrete shielding wall into the optics hutch. It contains vacuum isolation valves and/or beryllium or diamond windows to protect the storage ring from vacuum mishaps on the beamline, with cooled apertures to limit the horizontal extent of the beam. Most importantly, it contains thick metal safety shutters that prevent X-rays from passing further down the beamline when closed.

The beam transport typically consists of one or more beryllium or diamond windows, to isolate the beamline vacuum from that of the storage ring and evacuated beam pipes to conduct the beam into the experimental station. Along the beam path, between the storage ring and the experimental station, there may be one or more optics enclosures, which contain a sequence of X-ray optical devices such as a monochromator, used to filter the synchrotron light and focusing mirrors, used to focus the X-rays down to hundreds of a millimetre.

The experimental station for hard X-ray experiments is typically a steel or steel/lead enclosure. The experimenter has access to the station to change samples and align equipment as long as the shutters are closed. When ready for data collection, the station is interlocked to prevent access and the safety shutters are opened. The experimental station

contains manipulators to position the sample, optics to view the sample and detectors to measure the fluorescent, scattered or diffracted X-rays. The details of the actual setup depend entirely on the type of experiment to be performed.

2.5.4. The Diamond-Manchester Imaging Branchline (I13-2) at Diamond Light Source

Diamond Light Source (DLS) is a third-generation synchrotron facility (3 GeV, 300 mA) in the UK, which runs in top-up injection mode: the electron beam current in the storage ring is kept constant by small, frequent 'topping-up' of electrons from the injection system. At 250 metres in length, I13 is Diamond's longest beamline [188–190]. It comprises two branchlines that provide complementary X-ray imaging techniques (Figure 14). The branchlines run simultaneously and independently from each other. I13-2, performs real-space imaging and tomography in the 8-30 keV energy range. Absorption and in-line phase contrast imaging are both available. Imaging can be conducted with both pink and monochromatic light. Typically, monochromatic beams are used in synchrotron beamlines to avoid the beam-hardening artifacts. However, the monochromator on a synchrotron beamline typically transmits less than 0.1% of the beam, which means that the flux on the sample is greatly decreased and the data collection time increases. Monochromatic beams are therefore generally unsuitable for dynamic studies. The term 'pink beam' refers to the fact that a monochromator is not used, but rather the X-ray beam is reflected from a grazing incidence mirror. The mirror only reflects energies below a certain threshold, which depends on the mirror coating and grazing incidence angle. The result is a tunable broad bandwidth, with an X-ray flux that is more than 1000 times that of a monochromatic beam [191]. Flux at I13 is over a million times higher than that of a laboratory X-ray source. Monochromatic light represents a single wavelength which may be chosen according the sample. The partially coherent radiation at the I13-2 enables contrast enhancement at the edges of structures. This 'in-line phase contrast imaging' is particularly useful for biomedical applications in which absorption contrast between structures is weak [180].

The experimental setup at I13-2 (Figure 15) consists of a sample and detector stage placed on a vibration isolated table. The distance between both can be freely changed, modulating the edge-enhanced contrast in the radiographs. The spatial resolution depends on the detector system. The X-ray active layer of a scintillation screen transforms the X-rays into visible light. This image is then projected through a microscope optics, adapted to the screen on the chip of the CCD camera. The camera (pco.edge 5.5, PCO AG, Germany), with 2560 x 2160 pixels and a pixel size of 6.5 µm, is coupled to a visual light microscope, which is equipped with a revolving nosepiece accommodating lenses of varying magnification (1.25X, 2X, 4X, 10X). Together with a 2X relay lens, the effective pixel size varies between 325 nm and 2.6 µm, providing a field of view between 0.83 x 0.70 µmm^2 and 6.7 x 5.6 mm^2, respectively

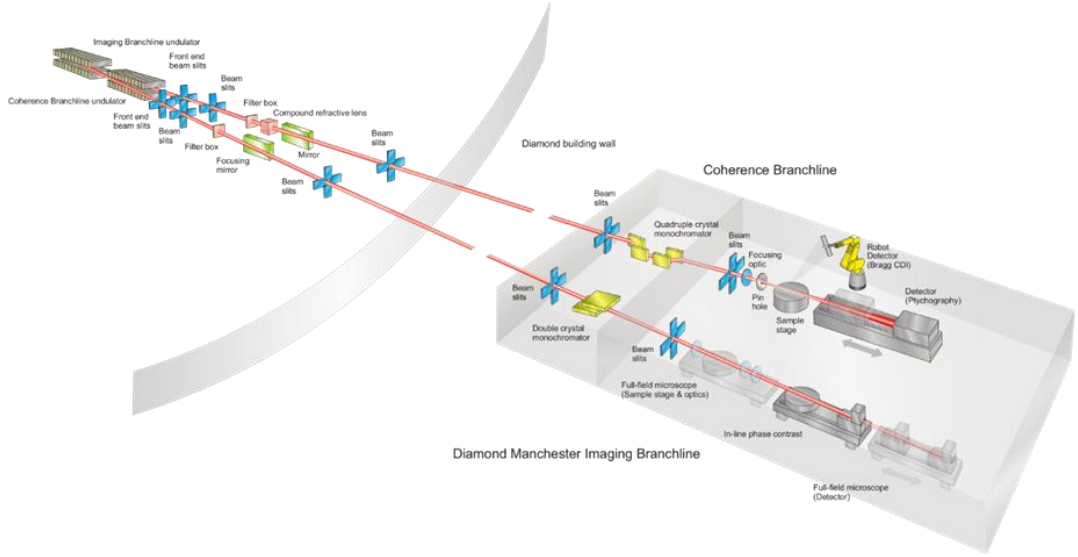

Figure 14. Schematic of I13 beamline at DLS. Adapted from [192] under license CC BY.

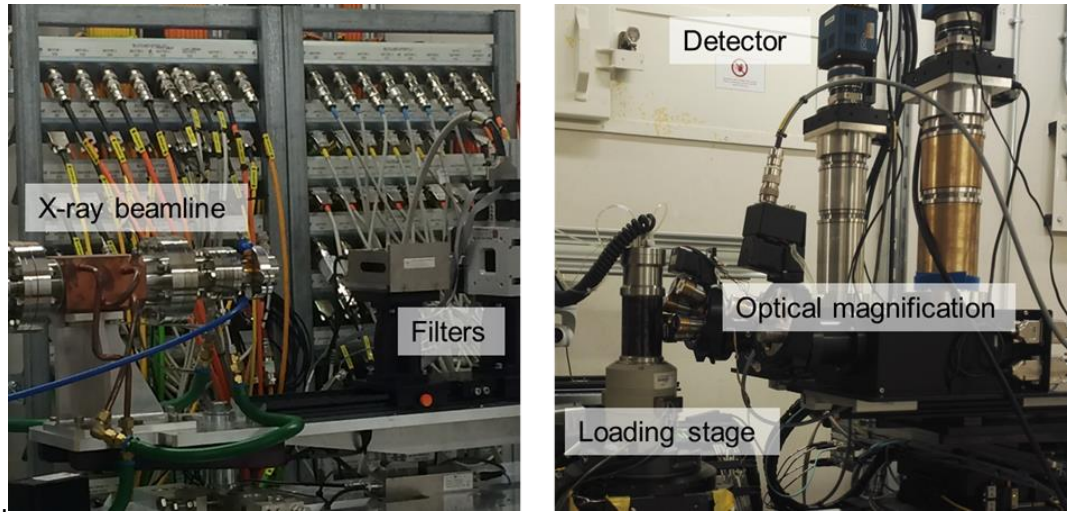

Figure 15. Instrumentation of the Diamond-Manchester Imaging Branchline (I13-2) at DLS.

2.6. *In situ* mechanics and digital volume correlation

2.6.1. *In situ* microCT mechanical testing

Because of its non-destructive nature, microCT is an ideal technique to perform not only static measurements of bone microstructure but also to conduct measurements under increasing applied load or other temporal events (4D evaluations) to investigate bone deformation mechanisms, fracture initiation and propagation or damage accumulation in a 3D manner (Figure 16). *In situ* microCT mechanics, also known as Image Guided Failure Assessment (IGFA) involves the use of a micromechanical loading device to perform step-wise mechanical testing (i.e. compression, tension, bending), and a microCT system to image the specimens in a given deformed state [193]. When the mechanical testing setup is

positioned inside the microCT chamber the experiments can be performed *in situ* and images can be acquired under load, without repositioning of the specimens. Generally, a first image is acquired in an undeformed state (0% deformation). Consequently, the specimen is loaded (i.e. displacement control) until the desired deformation level in the elastic or plastic region is achieved. Following each loading step the specimens are allowed to relax for a given time prior to image acquisition to reduce the time-depended phenomena during stress relaxation [194–196]. The obtained stress-strain curves typically present discontinuities due to the time-lapsed nature of the testing method [193]. Measurements corresponding to each compression step are stored in 3D image arrays and after 3D reconstruction, failure initiation and progression as well as local structural and architectural differences in the specimens, can be monitored. Since its development, the combination of *in situ* mechanical testing and microCT has been widely used to characterise trabecular bone, cortical bone and bone-biomaterial systems under different loading scenarios, in healthy and pathological bone and various dimensional scales [193,194,197–200].

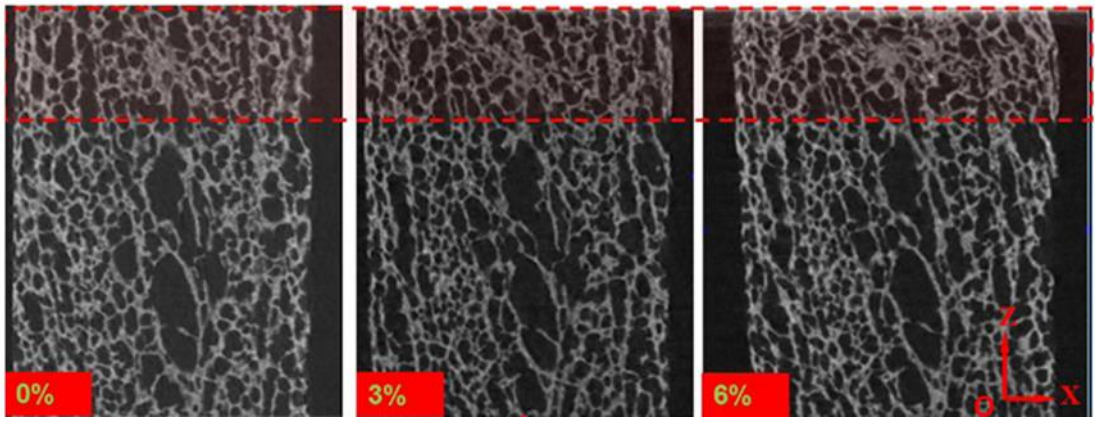

Figure 16. Trabecular bone structure in a two-plate compression testing experiment at different applied compression levels. Localised strain, particularly near the top end (dashed box) is evident. Adapted from [201] with permission. Copyright (2013) Elsevier.

2.6.2. Digital volume correlation

Despite time-lapsed mechanical testing and microCT imaging revealed important 3D visual information on the deformation of bone structures, a quantification of the full-field displacement and strain was only achieved with the development of digital volume correlation (DVC). DVC is a 3D-extension of the 2D digital image correlation (DIC) technique, a widely employed method for measurement of in-plane full-field displacement and strain fields in a variety of materials subjected to mechanical or thermal loads [202–206]. For a given material sample under applied load, DIC provides a surface measurement of deformation or strain, whereas DVC is able to provide full-field displacement and strain fields throughout the interior of the sample in 3D [163,207]. Generally, DVC methods can be described in three main steps (Figure 17): (1) generation of volumetric images of samples in both unloaded and loaded conditions; (2) measurement of a discrete displacement field

throughout the sample by a correlation procedure; (3) calculation of the strain tensor field from the displacement vector field.

High-resolution X-ray microCT remains the main imaging modality used in the development of DVC, although not the unique [208]. Some researchers have also employed confocal microscopy [209,210], micro-magnetic resonance imaging (microMRI) [211,212] or optical coherence tomography (OCT) [213,214]. With any of those imaging modalities, tomograms are generated in both an undeformed (reference) and deformed (target) state, either whilst under load (i.e. *in situ* microCT mechanical testing) or following specific temporal events. DVC was firstly applied to microCT images of trabecular bone tissue subjected to uniaxial compression load [207] and has since then been successfully applied to trabecular bone [215], cortical bone [216], whole bones [196,217] and bone-cement composites [195,198].

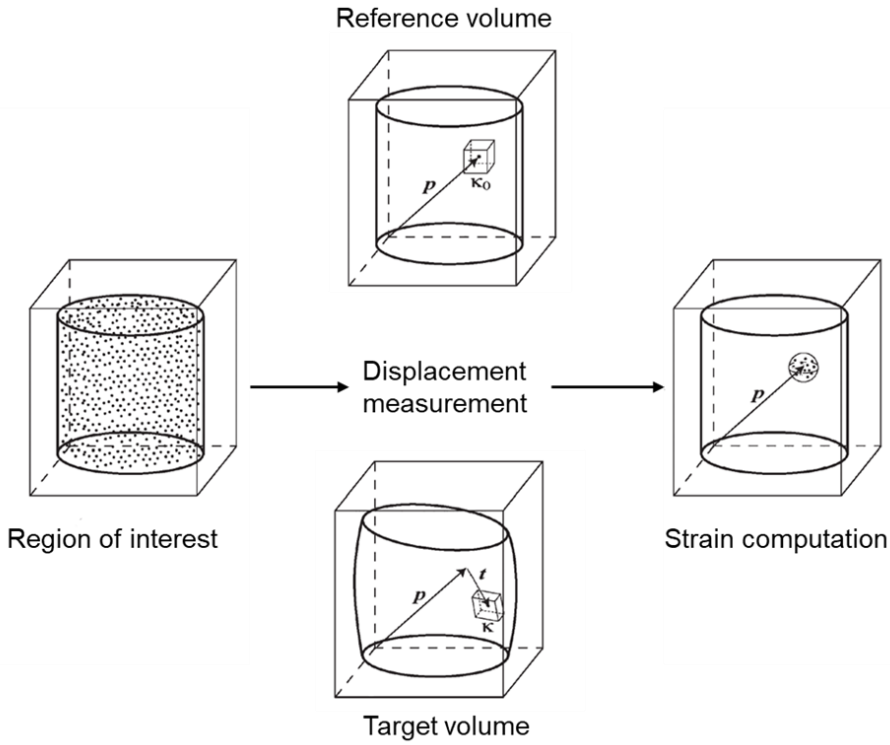

Figure 17. The overall digital volume correlation algorithm involves: (1) specification of a region of interest populated with measurement locations; (2) displacement measurement at each location by correlation of reference and target volumes; and (3) strain computation at each point by estimation of the surrounding deformation gradients. A sub-volume κ_0, centered at a single point location p, is extracted from the reference volume. The correlation process estimates the displacement vector t that better matches the sub-volume in the reference state, κ_0, with its correspondent sub-volume in the target volume, κ. Adapted from [207] with permission. Copyright (2008) SAGE Publications.

The fundamentals of DVC technique rely on the measurement of a discrete displacement vector field by correlation of image volumes of a sample in a reference and target state, based on the natural variations in image grey-level intensity, which are given by the characteristics of the material texture, within the image volumes. Within the reference image, a grid of points of interests is defined, where the displacements values are sought. The

discrete measurement points may be either user-defined and evenly distributed throughout the volume, else generated through meshing techniques [218].

In the early developments of DVC, local approaches were implemented in which a sub-volume can be defined and extracted from the reference image and registered with its counterpart in the deformed configuration (Figure 18a). The sub-volume is typically cubic and is sized with respect to the underlying material texture scale. Local approaches have the advantage of enabling an easy and efficient implementation, however, when discontinuities arise, they are less appropriate per se [219] as the sub-volumes are registered independently [201,215]. As an alternative, global approaches (Figure 18b), in which the whole 3D image is analysed by using elements (i.e. 8-noded cubes) to form a mesh, enforced a spatial regularization; thus, the displacement field is assumed to be continuous [219]. The fact that continuity is enforced allows the measurement uncertainty to be reduced in comparison with the same discretization in which the nodes are not shared [219–221].

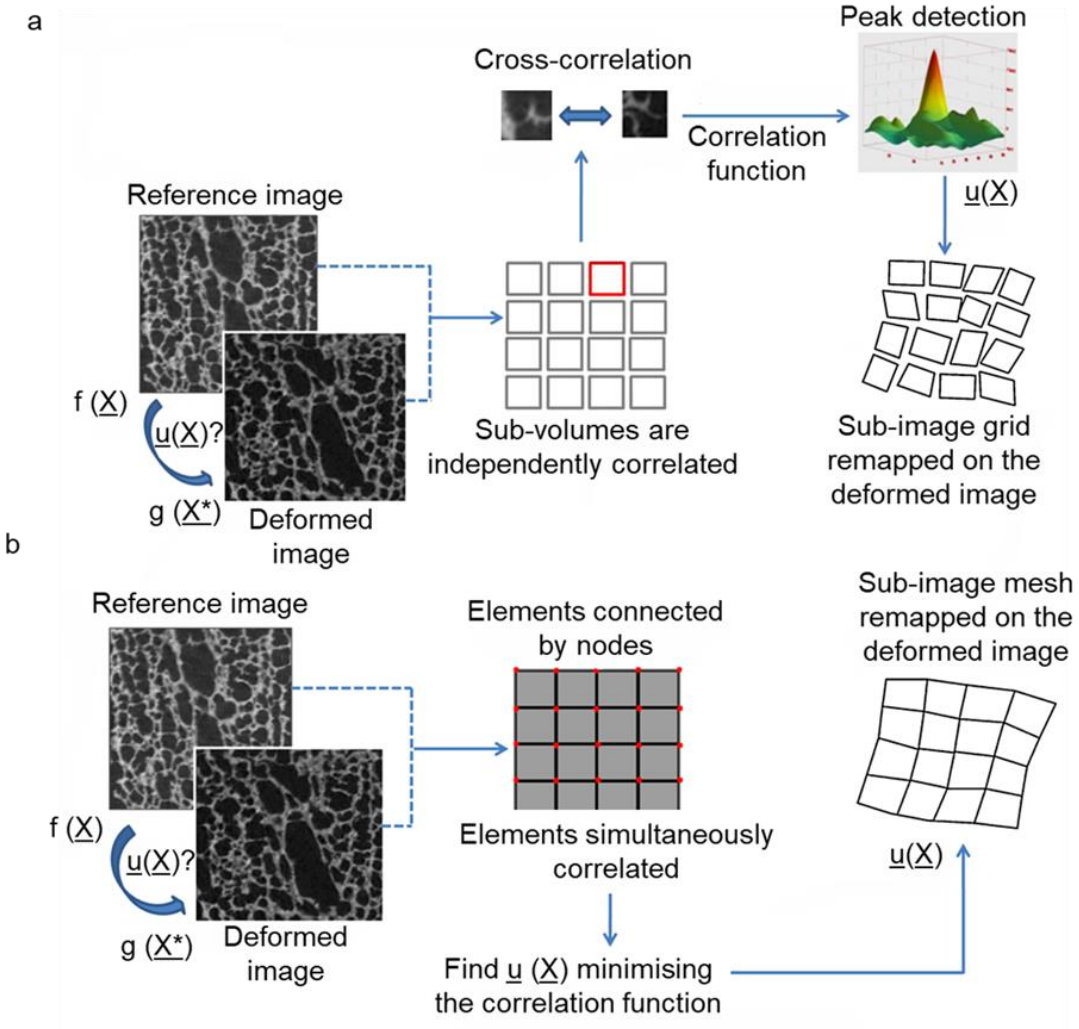

Figure 18. Differences between a local (a) and global (b) DVC approach. X and X* refers to the coordinates (in voxels) of a point in the reference and the deformed state, respectively; u(X) is the sought displacement field; f and g are the grey levels of the reference and deformed volumes. Adapted from [201] with permission. Copyright (2013) Elsevier.

The DVC method then determines the deformation required to best correlate the reference (unloaded) image with the target (loaded) image. The correlation requires the undeformed volume to undergo a deformation characterised by an affine transformation. The main transformation of interest is translation, as this provides the estimate of the displacement vector. The remaining transformations (rotation, normal strain, shear strain) may be invoked to improve correlation accuracy when the associated modes are significant over the sub-volumes [222–224]. The mapping of the reference feature to the corresponding position within the target image requires the definition of an objective or correlation function, which quantifies the degree of matching between the undeformed and deformed configurations. The sum-of-squares correlation coefficient (SSCC), cross-correlation (CC), normalised cross-correlation (NCC), zero-mean normalised cross-correlation (ZNCC) and mutual information are typical functions used as objective functions [207,219,224–226]. The affine transformations applied to the reference may result in sub-voxel deformations. Thus, interpolation is required to estimate image data between voxel locations. Tricubic spline interpolation has proven adequate and is prevalent within the literature [207,224,227,228]. Finally, the strain measurements can be estimated by differentiation of the displacement vector field. The displacement data may be first smoothed and filtered before estimating the gradient deformation tensor [163,222,223].

The accuracy and precision of the DVC in measuring the displacements depend on the quality of the input images and such errors in displacements can be amplified for the strain field, once differentiated. DVC algorithms showed errors in the displacement measurements of a fraction of voxel (precision of 0.0004–0.115 voxels) [218]. Nevertheless, a compromise must always be accepted between the precision of the DVC measurements and the measurement spatial resolution [221,229,230]. In fact, the larger is the sub-volume/element size, which represents the spatial resolution of the measurement, the lower are the random errors associated with the measurement. There is no single optimal solution for all cases, but an adaptation of the method for different bone structures and image resolutions is required [221]. Moreover, considering that there is no other measurement technique that allows evaluating the 3D bone deformations within heterogeneous structures, the precision of the method is typically estimated by registering repeated scans of the same undeformed specimen (“zero-strain” condition) [163,218,225]. It is up to the individual researchers, depending on the specific application, to determine the magnitude of measurement error that they are willing to accept.

References

[1] S. Cowin, J. Telega, Bone Mechanics Handbook, 2nd Edition. -, 2003. doi:10.1115/1.1579463.

[2] J.D. Currey, Bones, Princeton University Press, 2002.

[3] J.D. Currey, How well are bones designed to resist fracture?, J. Bone Miner. Res. 18 (2003) 591–598. doi:10.1359/jbmr.2003.18.4.591.

[4] J.D. Currey, The many adaptations of bone, J. Biomech. 36 (2003) 1487–1495. doi:10.1016/S0021-9290(03)00124-6.

[5] L. Weiss, Cell and Tissue Biology: A Textbook of Histology, Lippincott Williams & Wilkins, 1988. https://books.google.co.uk/books?id=ssxpAAAAMAAJ.

[6] B.Q. Le, V. Nurcombe, S.M.K. Cool, C.A. van Blitterswijk, J. de Boer, V.L.S. LaPointe, The Components of bone and what they can teach us about regeneration, Materials (Basel). 11 (2017) 1–16. doi:10.3390/ma11010014.

[7] S.H. Patel, K.P. Murphy, Fractures of the proximal femur: Correlates of radiological evidence of osteoporosis, Skeletal Radiol. 35 (2006) 202–211. doi:10.1007/s00256-005-0065-1.

[8] B. Clarke, Normal bone anatomy and physiology., Clin. J. Am. Soc. Nephrol. 3 Suppl 3 (2008) 131–139. doi:10.2215/CJN.04151206.

[9] S. Weiner, W. Traub, H.D. Wagner, Lamellar bone: structure– function relations., J. Struct. Biol. 126 (1999) 241–255.

[10] J.J. Pritchard, General anatomy and histology of bone, in: G.H. Bourne (Ed.), Biochem. Physiol. Bone, Academic Press, 1956: pp. 1–25. doi:https://doi.org/10.1016/C2013-0-12533-0.

[11] H.M. Goldman, S.C. McFarlin, D.M.L. Cooper, C.D.L. Thomas, J.G. Clement, Ontogenetic patterning of cortical bone microstructure and geometry at the human mid-shaft femur, Anat. Rec. 292 (2009) 48–64. doi:10.1002/ar.20778.

[12] S.C. McFarlin, C.J. Terranova, A.L. Zihlman, T.G. Bromage, Primary bone microanatomy records developmental aspects of life history in catarrhine primates, J. Hum. Evol. 92 (2016) 60–79. doi:10.1016/j.jhevol.2015.12.004.

[13] S. Nobakhti, G. Limbert, P.J. Thurner, Cement lines and interlamellar areas in compact bone as strain amplifiers - Contributors to elasticity, fracture toughness and mechanotransduction, J. Mech. Behav. Biomed. Mater. 29 (2014) 235–251. doi:10.1016/j.jmbbm.2013.09.011.

[14] A.M. Parfitt, C.H.E. Mathews, A.R. Villanueva, M. Kleerekoper, B. Frame, D.S. Rao, Relationships between Surface , Volume , and Thickness of Iliac Trabecular Bone in Aging and in Osteoporosis., J. Clin. Invest. 72 (1983) 1396–1409.

[15] R. Oftadeh, M. Perez-Viloria, J.C. Villa-Camacho, A. Vaziri, A. Nazarian, Biomechanics and Mechanobiology of Trabecular Bone: A Review., J. Biomech. Eng. 137 (2015) 1–15. doi:10.1115/1.4029176.

[16] P. Fratzl, H.S. Gupta, E.P. Paschalis, P. Roschger, Structure and mechanical quality of the collagen–mineral nano-composite in bone, J. Mater. Chem. 14 (2004) 2115–2123. doi:10.1039/B402005G.

[17] J.A. Gokhale, A.L. Boskey, P.G. Robey, The Biochemistry of Bone, in: R. Marcus, D. Feldman, J.B.T.-O. (Second E. Kelsey (Eds.), Osteoporosis, Academic Press, San Diego, 2001: pp. 107–188. doi:https://doi.org/10.1016/B978-012470862-4/50005-2.

[18] J.P. Gorski, Is all bone the same? Distinctive distributions and properties of non-collagenous matrix proteins in Lamellar vs. Woven bone imply the existence of different underlying osteogenic mechanisms, Crit. Rev. Oral Biol. Med. 9 (1998) 201–223. doi:10.1177/10454411980090020401.

[19] J.Y. Rho, L. Kuhn-Spearing, P. Zioupos, Mechanical properties and the hierarchical structure of bone, Med. Eng. Phys. 20 (1998) 92–102. doi:10.1016/S1350-4533(98)00007-1.

[20] U. Kini, B.N. Nandeesh, Physiology of Bone Formation, Remodeling, and Metabolism, in: I. Fogelman, G. Gnanasegaran, H. van der Wall (Eds.), Radionucl. Hybrid Bone Imaging, Springer Berlin Heidelberg, Berlin, Heidelberg, 2012: pp. 29–57. doi:10.1007/978-3-642-02400-9_2.

[21] J.B. Lian, G.S. Stein, A.J. Van Wijnen, J.L. Stein, M.Q. Hassan, MicroRNA control of bone formation and homeostasis, 8 (2013) 212–227. doi:10.1038/nrendo.2011.234.MicroRNA.

[22] R. Baron, Anatomy and Ultrastructure of Bone - Histogenesis, Growth and Remodeling, in: L.J. De Groot, G. Chrousos, K. Dungan, K.R. Feingold, A. Grossman, J.M. Hershman, C. Koch, M. Korbonits, R. McLachlan, M. New, J. Purnell, R. Rebar, F. Singer, A. Vinik (Eds.), South Dartmouth (MA), 2000.

[23] H.M. Frost, Wolff's Law and bone's structural adaptations to mechanical usage: an overview for clinicians, Angle Orthod. 64 (1994) 175–188.

[24] H.M. Frost, Skeletal structural adaptations to mechanical usage (SATMU): 1. Redefining Wolff's Law: The bone modeling problem, Anat. Rec. 226 (1990) 403–413. doi:10.1002/ar.1092260402.

[25] R.. B. Martin, Toward a unifying theory of bone remodeling, Bone. 26 (2000) 1–6. doi:10.1016/S8756-3282(99)00241-0.

[26] M. Doblaré, J.M. García, M.J. Gómez, Modelling bone tissue fracture and healing: A review, Eng. Fract. Mech. 71 (2004) 1809–1840. doi:10.1016/j.engfracmech.2003.08.003.

[27] D.R. Carter, Mechanical loading histories and cortical bone remodeling., Calcif. Tissue Int. 36 Suppl 1 (1984) S19-24.

[28] A.D. Martin, R.G. McCulloch, Bone dynamics: Stress, strain and fracture, J. Sports Sci. 5 (1987) 155–163. doi:10.1080/02640418708729773.

[29] R. Marsell, T.A. Einhorn, The biology of fracture healing, Injury. 42 (2011) 551–555. doi:10.1016/j.injury.2011.03.031.

[30] A. Oryan, S. Monazzah, A. Bigham-Sadegh, Bone injury and fracture healing biology., Biomed. Environ. Sci. 28 (2015) 57–71. doi:10.3967/bes2015.006.

[31] L. Claes, S. Recknagel, A. Ignatius, Fracture healing under healthy and inflammatory conditions, Nat. Rev. Rheumatol. 8 (2012) 133. http://dx.doi.org/10.1038/nrrheum.2012.1.

[32] M.S. Ghiasi, J. Chen, A. Vaziri, E.K. Rodriguez, A. Nazarian, Bone fracture healing in mechanobiological modeling: A review of principles and methods, Bone Reports. 6 (2017) 87–100. doi:10.1016/j.bonr.2017.03.002.

[33] L.C. Gerstenfeld, Y.M. Alkhiary, E.A. Krall, F.H. Nicholls, S.N. Stapleton, J.L. Fitch, M. Bauer, R. Kayal, D.T. Graves, K.J. Jepsen, T.A. Einhorn, Three-dimensional reconstruction of fracture callus morphogenesis, J. Histochem. Cytochem. 54 (2006) 1215–1228. doi:10.1369/jhc.6A6959.2006.

[34] A.E. Goodship, J.L. Cunningham, J. Kenwright, Strain rate and timing of stimulation in mechanical modulation of fracture healing., Clin. Orthop. Relat. Res. (1998) S105-15.

[35] M. Jagodzinski, C. Krettek, Effect of mechanical stability on fracture healing — an update Michael, Injury. 38 (2007) 53–60. doi:10.1016/j.injury.2007.02.005.

[36] T. Savaridas, R.J. Wallace, a Y. Muir, D.M. Salter, a H.R.W. Simpson, The development of a novel model of direct fracture healing in the rat., Bone Joint Res. 1 (2012) 289–96. doi:10.1302/2046-3758.111.2000087.

[37] F. Shapiro, Cortical bone repair. The relationship of the lacunar-canalicular system and intercellular gap junctions to the repair process., J. Bone Joint Surg. Am. 70 (1988) 1067–1081.

[38] J.J. Sela, I.A. Bab, Healing of Bone Fracture: General Concepts, in: J.J. Sela, I.A. Bab (Eds.), Princ. Bone Regen., Springer-Verlag New York, 2012: pp. 1–8. doi:10.1007/978-1-4614-2059-0.

[39] R.E. Kaderly, Primary bone healing., Semin. Vet. Med. Surg. (Small Anim). 6 (1991) 21–25.

[40] T.A. Einhorn, L.C. Gerstenfeld, Fracture healing: Mechanisms and interventions, Nat. Rev. Rheumatol. 11 (2015) 45–54. doi:10.1038/nrrheum.2014.164.

[41] A.M. Phillips, Overview of the fracture healing cascade, Injury. 36 (2005) S5–S7. doi:10.1016/j.injury.2005.07.027.

[42] A.A. White, M.M. Panjabi, W.O. Southwick, The four biomechanical stages of fracture repair., J. Bone Joint Surg. Am. 59 (1977) 188–192.

[43] T.A. Einhorn, The cell and molecular biology of fracture healing., Clin. Orthop. Relat. Res. (1998) S7-21.

[44] P. V. Giannoudis, T.A. Einhorn, D. Marsh, Fracture healing: The diamond concept, Injury. 38 (2007) 3–6. doi:10.1016/S0020-1383(08)70003-2.

[45] R.A. Patel, R.F. Wilson, P.A. Patel, R.M. Palmer, The effect of smoking on bone healing: A systematic review., Bone Joint Res. 2 (2013) 102–11. doi:10.1302/2046-3758.26.2000142.

[46] D.P. Taormina, B.S. Shulman, R. Karia, A.B. Spitzer, S.R. Konda, K.A. Egol, Older Age Does Not Affect Healing Time and Functional Outcomes After Fracture Nonunion Surgery, Geriatr. Orthop. Surg. Rehabil. 5 (2014) 116–121. doi:10.1177/2151458514532811.

[47] J. Alvear, C. Artaza, S. Guerrero, S. Muzzo, Physical growth and bone energy malnutrition, (1986) 257–262.

[48] H. Shah, M. Rousset, F. Canavese, Congenital pseudarthrosis of the tibia: Management and complications, Indian J. Orthop. 46 (2012) 616–626. doi:10.4103/0019-5413.104184.

[49] H. Qu, W. Guo, R. Yang, D. Li, S. Tang, Y. Yang, S. Dong, J. Zang, Reconstruction of segmental bone defect of long bones after tumor resection by devitalized tumor-bearing bone, World J. Surg. Oncol. 13 (2015) 1–7. doi:10.1186/s12957-015-0694-3.

[50] C. Delloye, P. de Nayer, N. Allington, E. Munting, L. Coutelier, A. Vincent, Massive bone allografts in large skeletal defects after tumor surgery: a clinical and microradiographic evaluation, Arch. Orthop. Trauma. Surg. 107 (1987) 31–41. doi:10.1007/BF00463522.

[51] F.R. Nusbickel, P.C. Dell, M.P. McAndrew, M.M. Moore, Vascularized autografts for reconstruction of skeletal defects following lower extremity trauma. A review, Clin. Orthop. Relat. Res. (1989) 65—70. http://europepmc.org/abstract/MED/2656034.

[52] J. Salgado, O.P. Coutinho, R.L. Reis, Bone Tissue Engineering : State of the Art and Future Trends, Macromol. Biosci. 4 (2004) 743–765. doi:10.1002/mabi.200400026.

[53] A.R. Amini, C.T. Laurencin, S.P. Nukavarapu, Bone Tissue Engineering: Recent Advances and Challenges, Crit. Rev. Biomed. Eng. 40 (2012) 363–408. http://www.ncbi.nlm.nih.gov/pmc/articles/PMC3766369/.

[54] F.R.A.J. Rose, ore, R.O.C. Oreffo, Bone tissue engineering: Hope vs hype, Biochem. Biophys. Res. Commun. 292 (2002) 1–7. doi:10.1006/bbrc.2002.6519.

[55] J.P. Schmitz, J.O. Hollinger, The critical size defect as an experimental model for craniomandibulofacial nonunions., Clin. Orthop. Relat. Res. (1986) 299–308.

[56] P.P. Spicer, J.D. Kretlow, S. Young, J.A. Jansen, F.K. Kasper, A.G. Mikos, Evaluation of bone regeneration using the rat critical size calvarial defect., Nat. Protoc. 7 (2012) 1918–1929. doi:10.1038/nprot.2012.113.

[57] Z. Gugala, S. Gogolewski, Regeneration of segmental diaphyseal defects in sheep tibiae using resorbable polymeric membranes: a preliminary study., J. Orthop. Trauma. 13 (1999) 187–195.

[58] N.G. Lasanianos, N.K. Kanakaris, P. V. Giannoudis, Current management of long bone large segmental defects, Orthop. Trauma. 24 (2010) 149–163. doi:10.1016/j.mporth.2009.10.003.

[59] Z. Gugala, R.W. Lindsey, S. Gogolewski, New approaches in the treatment of critical-size segmental defects in long bones, Macromol. Symp. 253 (2007) 147–161. doi:10.1002/masy.200750722.

[60] E. Roddy, M.R. DeBaun, A. Daoud-Gray, Y.P. Yang, M.J. Gardner, Treatment of critical-sized bone defects: clinical and tissue engineering perspectives, Eur. J. Orthop. Surg. Traumatol. 28 (2018) 351–362. doi:10.1007/s00590-017-2063-0.

[61] J.F. Keating, A.H.R.W. Simpson, C.M. Robinson, The management of fractures with bone loss., J. Bone Joint Surg. Br. 87 (2005) 142–150.

[62] C.J. Kowalczewski, J.M. Saul, Biomaterials for the delivery of growth factors and other therapeutic agents in tissue engineering approaches to bone regeneration, Front. Pharmacol. 9 (2018) 1–15. doi:10.3389/fphar.2018.00513.

[63] S.S. Tseng, M.A. Lee, A.H. Reddi, Nonunions and the potential of stem cells in fracture-healing., J. Bone Joint Surg. Am. 90 Suppl 1 (2008) 92–98. doi:10.2106/JBJS.G.01192.

[64] M.S. Virk, J.R. Lieberman, Biologic adjuvants for fracture healing, Arthritis Res. Ther. 14 (2012). doi:10.1186/ar4053.

[65] R. Dimitriou, E. Jones, D. McGonagle, P. V. Giannoudis, Bone regeneration: Current concepts and future directions, BMC Med. 9 (2011) 66. doi:10.1186/1741-7015-9-66.

[66] W. Wang, K.W.K. Yeung, Bone grafts and biomaterials substitutes for bone defect repair: A review, Bioact. Mater. 2 (2017) 224–247. doi:https://doi.org/10.1016/j.bioactmat.2017.05.007.

[67] P. Habibovic, (*) Strategic Directions in Osteoinduction and Biomimetics., Tissue Eng. Part A. 23 (2017) 1295–1296. doi:10.1089/ten.TEA.2017.0430.

[68] E. Nyberg, C. Holmes, T. Witham, W.L. Grayson, Growth factor-eluting technologies for bone tissue engineering, Drug Deliv. Transl. Res. 6 (2016) 184–194. doi:10.1007/s13346-015-0233-3.

[69] T.-M. De Witte, L.E. Fratila-Apachitei, A.A. Zadpoor, N.A. Peppas, Bone tissue engineering via growth factor delivery: from scaffolds to complex matrices, Regen. Biomater. (2018) 197–211. doi:10.1093/rb/rby013.

[70] M. Mohammadi, S.A. Mousavi Shaegh, M. Alibolandi, M.H. Ebrahimzadeh, A. Tamayol, M.R. Jaafari, M. Ramezani, Micro and nanotechnologies for bone regeneration: Recent advances and emerging designs, J. Control. Release. 274 (2018) 35–55. doi:10.1016/j.jconrel.2018.01.032.

[71] E. Hernlund, A. Svedbom, M. Ivergård, J. Compston, C. Cooper, J. Stenmark, E. V. McCloskey, B. Jönsson, J.A. Kanis, Osteoporosis in the European Union: Medical management, epidemiology and economic burden: A report prepared in collaboration with the International Osteoporosis Foundation (IOF) and the European Federation of Pharmaceutical Industry Associations (EFPIA), Arch. Osteoporos. 8 (2013). doi:10.1007/s11657-013-0136-1.

[72] T. Winkler, F.A. Sass, G.N. Duda, K. Schmidt-Bleek, A review of biomaterials in bone defect healing, remaining shortcomings and future opportunities for bone tissue engineering, Bone Joint Res. 7 (2018) 232–243. doi:10.1302/2046-3758.73.BJR-2017-0270.R1.

[73] J.C. Reichert, S. Saifzadeh, M.E. Wullschleger, D.R. Epari, M.A. Schütz, G.N. Duda, H. Schell, M. van Griensven, H. Redl, D.W. Hutmacher, The challenge of establishing preclinical models for segmental bone defect research, Biomaterials. 30 (2009) 2149–2163. doi:10.1016/j.biomaterials.2008.12.050.

[74] Y. Fillingham, J. Jacobs, Bone grafts and their substitutess, Bone Jt. J. 98–B (2016) 6–9. doi:10.1302/0301-620X.98B1.36350.

[75] S.N. Khan, F.P.J. Cammisa, H.S. Sandhu, A.D. Diwan, F.P. Girardi, J.M. Lane, The biology of bone grafting., J. Am. Acad. Orthop. Surg. 13 (2005) 77–86.

[76] T. Albrektsson, C. Johansson, Osteoinduction, osteoconduction and osseointegration, Eur. Spine J. 10 (2001) S96–S101. doi:10.1007/s005860100282.

[77] M.R. Urist, Bone: formation by autoinduction., Science. 150 (1965) 893–899.

[78] A.M.C. Barradas, H. Yuan, C.A. van Blitterswijk, P. Habibovic, Osteoinductive biomaterials: current knowledge of properties, experimental models and biological mechanisms., Eur. Cell. Mater. 21 (2011) 407–429. doi:10.22203/eCM.v021a31.

[79] E. Garcia-Gareta, M.J. Coathup, G.W. Blunn, E. García-Gareta, M.J. Coathup, G.W. Blunn, Osteoinduction of bone grafting materials for bone repair and regeneration, Bone. 81 (2015) 112–121. doi:10.1016/j.bone.2015.07.007.

[80] R. Dimitriou, E. Tsiridis, P. V. Giannoudis, Current concepts of molecular aspects of bone healing, Injury. 36 (2005) 1392–1404. doi:10.1016/j.injury.2005.07.019.

[81] V. Martin, A. Bettencourt, Bone regeneration: Biomaterials as local delivery systems with improved osteoinductive properties, Mater. Sci. Eng. C. 82 (2018) 363–371. doi:10.1016/j.msec.2017.04.038.

[82] M.K. Sen, T. Miclau, Autologous iliac crest bone graft: Should it still be the gold standard for treating nonunions?, Injury. 38 (2007) 2–7. doi:10.1016/j.injury.2007.02.012.

[83] V.M. Goldberg, S. Akhavan, Biology of Bone Grafts BT - Bone Regeneration and Repair: Biology and Clinical Applications, in: J.R. Lieberman, G.E. Friedlaender (Eds.), Humana Press, Totowa, NJ, 2005: pp. 57–65. doi:10.1385/1-59259-863-3:057.

[84] T.W. Bauer, G.F. Muschler, Bone graft materials. An overview of the basic science., Clin. Orthop. Relat. Res. (2000) 10–27.

[85] J.C. Banwart, M.A. Asher, R.S. Hassanein, Iliac Crest Bone Graft Harvest Donor Site Morbidity: A Statistical Evaluation, Spine (Phila. Pa. 1976). 20 (1995). https://journals.lww.com/spinejournal/Fulltext/1995/05000/Iliac_Crest_Bone_Graft_Harvest_Donor_Site.12.aspx.

[86] E.M. Younger, M.W. Chapman, Morbidity at bone graft donor sites., J. Orthop. Trauma. 3 (1989) 192–195.

[87] J.A. Goulet, L.E. Senunas, G.L. DeSilva, M.L. Greenfield, Autogenous iliac crest bone graft. Complications and functional assessment., Clin. Orthop. Relat. Res. (1997) 76–81.

[88] T.T. Roberts, A.J. Rosenbaum, T.T. Roberts, A.J. Rosenbaum, T.T. Roberts, A.J. Rosenbaum, Bone grafts , bone substitutes and orthobiologics The bridge between basic science and clinical advancements in fracture healing, Organogenesis. 8 (2012) 114–124. doi:10.4161/org.23306.

[89] B.W. Schreurs, T.J. Slooff, P. Buma, J.W. Gardeniers, R. Huiskes, Acetabular reconstruction with impacted morsellised cancellous bone graft and cement. A 10- to 15-year follow-up of 60 revision arthroplasties., J. Bone Joint Surg. Br. 80 (1998) 391–395.

[90] T. Azuma, H. Yasuda, K. Okagaki, K. Sakai, Compressed allograft chips for acetabular reconstruction in revision hip arthroplasty., J. Bone Joint Surg. Br. 76 (1994) 740–744.

[91] D.J. Berry, M.E. Muller, Revision arthroplasty using an anti-protrusio cage for massive acetabular bone deficiency., J. Bone Joint Surg. Br. 74 (1992) 711–715.

[92] T.J. Gill, J.B. Sledge, M.E. Muller, The Burch-Schneider anti-protrusio cage in revision total hip arthroplasty: indications, principles and long-term results., J. Bone Joint Surg. Br. 80 (1998) 946–953.

[93] G.A. Gie, L. Linder, R.S. Ling, J.P. Simon, T.J. Slooff, A.J. Timperley, Impacted cancellous allografts and cement for revision total hip arthroplasty., J. Bone Joint Surg. Br. 75 (1993) 14–21.

[94] V. Grover, A. Kapoor, R. Malhotra, S. Sachdeva, Bone allografts: a review of safety and efficacy., Indian J. Dent. Res. 22 (2011) 496. doi:10.4103/0970-9290.87084.

[95] B.E. Buck, T.I. Malinin, M.D. Brown, Bone transplantation and human immunodeficiency virus. An estimate of risk of acquired immunodeficiency syndrome (AIDS)., Clin. Orthop. Relat. Res. (1989) 129–136.

[96] K.U. Lewandrowski, V. Rebmann, M. Passler, G. Schollmeier, A. Ekkernkamp, H. Grosse-Wilde, W.W. Tomford, Immune response to perforated and partially demineralized bone allografts., J. Orthop. Sci. 6 (2001) 545–555. doi:10.1007/s007760100011.

[97] J.S. Carson, M.P.G. Bostrom, Synthetic bone scaffolds and fracture repair., Injury. 38 Suppl 1 (2007) S33-7. doi:10.1016/j.injury.2007.02.008.

[98] H. Nguyen, D.A.F. Morgan, M.R. Forwood, Sterilization of allograft bone: Effects of gamma irradiation on allograft biology and biomechanics, Cell Tissue Bank. 8 (2007) 93–105. doi:10.1007/s10561-006-9020-1.

[99] A.J. Hamer, I. Stockley, R.A. Elson, Changes in allograft bone irradiated at different temperatures, J Bone Jt. Surg. 81 (1999) 342–4. doi:10.1302/0301-620X.81B2.9083.

[100] L. Vastel, A. Meunier, H. Siney, L. Sedel, J.P. Courpied, Effect of different sterilization processing methods on the mechanical properties of human cancellous bone allografts, Biomaterials. 25 (2004) 2105–2110. doi:10.1016/j.biomaterials.2003.08.067.

[101] R. Singh, D. Singh, A. Singh, Radiation sterilization of tissue allografts: A review, World J. Radiol. 8 (2016) 355. doi:10.4329/wjr.v8.i4.355.

[102] H. Dreesmann, Ueber Knochenplombirung1, DMW-Deutsche Med. Wochenschr. 19 (1892) 445–446.

[103] C. Yashavantha Kumar, K.B. Nalini, J. Menon, D.K. Patro, B.H. Banerji, Calcium sulfate as bone graft substitute in the treatment of osseous bone defects, a prospective study, J. Clin. Diagnostic Res. 7 (2013) 2926–2928. doi:10.7860/JCDR/2013/6404.3791.

[104] M. V Thomas, D.A. Puleo, M. Al-Sabbagh, Calcium sulfate: a review., J. Long. Term. Eff. Med. Implants. 15 (2005) 599–607.

[105] S. Zwingenberger, C. Nich, R.D. Valladares, Z. Yao, M. Stiehler, S.B. Goodman, Recommendations and considerations for the use of biologics in orthopedic surgery, BioDrugs. 26 (2012) 245–256. doi:10.2165/11631680-000000000-00000.

[106] C. Schwartz, R. Bordei, Biphasic phospho-calcium ceramics used as bone substitutes are efficient in the management of severe acetabular bone loss in revision total hip arthroplasties, Eur. J. Orthop. Surg. Traumatol. 15 (2005) 191–196. doi:10.1007/s00590-005-0244-8.

[107] C. Nich, L. Sedel, Bone substitution in revision hip replacement, Int. Orthop. 30 (2006) 525–531. doi:10.1007/s00264-006-0135-6.

[108] R.D.A. Gaasbeek, H.G. Toonen, R.J. Van Heerwaarden, P. Buma, Mechanism of bone incorporation of β-TCP bone substitute in open wedge tibial osteotomy in patients, Biomaterials. 26 (2005) 6713–6719. doi:10.1016/j.biomaterials.2005.04.056.

[109] J.H. Scheer, L.E. Adolfsson, Tricalcium phosphate bone substitute in corrective osteotomy of the distal radius, Injury. 40 (2009) 262–267. doi:10.1016/j.injury.2008.08.013.

[110] Z. Sheikh, M.N. Abdallah, A.A. Hanafi, S. Misbahuddin, H. Rashid, M. Glogauer, Mechanisms of in vivo degradation and resorption of calcium phosphate based biomaterials, Materials (Basel). 8 (2015) 7913–7925. doi:10.3390/ma8115430.

[111] P.S. Eggli, W. Muller, R.K. Schenk, Porous hydroxyapatite and tricalcium phosphate cylinders with two different pore size ranges implanted in the cancellous bone of rabbits. A comparative histomorphometric and histologic study of bony ingrowth and implant substitution., Clin. Orthop. Relat. Res. (1988) 127–138.

[112] J.C. Le Huec, T. Schaeverbeke, D. Clement, J. Faber, A. Le Rebeller, Influence of porosity on the mechanical resistance of hydroxyapatite ceramics under compressive stress, Biomaterials. 16 (1995) 113–118. doi:10.1016/0142-9612(95)98272-G.

[113] M. Bohner, F. Baumgart, Theoretical model to determine the effects of geometrical factors on the resorption of calcium phosphate bone substitutes, Biomaterials. 25 (2004) 3569–3582. doi:10.1016/j.biomaterials.2003.10.032.

[114] R.W. Bucholz, A. Carlton, R.E. Holmes, Hydroxyapatite and tricalcium phosphate bone graft substitutes., Orthop. Clin. North Am. 18 (1987) 323–334.

[115] C.G. Finkemeier, Bone-grafting and bone-graft substitutes., J. Bone Joint Surg. Am. 84–A (2002) 454–464.

[116] A.J. Tonino, B.C.H. Van Der Wal, I.C. Heyligers, B. Grimm, Bone remodeling and hydroxyapatite resorption in coated primary hip prostheses, Clin. Orthop. Relat. Res. 467 (2009) 478–484. doi:10.1007/s11999-008-0559-y.

[117] L.L. Hench, The story of Bioglass®, J. Mater. Sci. Mater. Med. 17 (2006) 967–978. doi:10.1007/s10856-006-0432-z.

[118] J.R. Jones, Review of bioactive glass: From Hench to hybrids, Acta Biomater. 9 (2013) 4457–4486. doi:10.1016/j.actbio.2015.07.019.

[119] L.L. Hench, N. Roki, M.B. Fenn, Bioactive glasses: Importance of structure and properties in bone regeneration, J. Mol. Struct. 1073 (2014) 24–30. doi:10.1016/j.molstruc.2014.03.066.

[120] L.L. Hench, H.A. Paschall, Direct chemical bond of bioactive glass-ceramic materials to bone and muscle, J. Biomed. Mater. Res. 7 (1973) 25–42. doi:10.1002/jbm.820070304.

[121] V. V Välimäki, H.T. Aro, Molecular basis for action of bioactive glasses as bone graft substitute., Scand. J. Surg. 95 (2006) 95–102. http://www.ncbi.nlm.nih.gov/pubmed/16821652.

[122] T. Kurien, R.G. Pearson, B.E. Scammell, Bone graft substitutes currently available in orthopaedic practice: The evidence for their use, Bone Jt. J. 95 B (2013) 583–597. doi:10.1302/0301-620X.95B5.30286.

[123] M.R. Azenha, S.A. de Lacerda, H.F. Marão, O.P. Filho, O.M. Filho, Evaluation of Crystallized Biosilicate in the Reconstruction of Calvarial Defects, J. Maxillofac. Oral Surg. 14 (2015) 659–665. doi:10.1007/s12663-015-0755-8.

[124] W.C. Liu, I.S. Robu, R. Patel, M.C. Leu, M. Velez, T.M. Gabriel Chu, The effects of 3D bioactive glass scaffolds and BMP-2 on bone formation in rat femoral critical size defects and adjacent bones, Biomed. Mater. 9 (2014). doi:10.1088/1748-6041/9/4/045013.

[125] F. Akter, Chapter 2 - Principles of Tissue Engineering, in: F.B.T.-T.E.M.E. Akter (Ed.), Academic Press, 2016: pp. 3–16. doi:https://doi.org/10.1016/B978-0-12-805361-4.00002-3.

[126] S.T. Yoon, S.D. Boden, Osteoinductive molecules in orthopaedics: basic science and preclinical studies., Clin. Orthop. Relat. Res. (2002) 33–43.

[127] H.S. Azevedo, I. Pashkuleva, Biomimetic supramolecular designs for the controlled release of growth factors in bone regeneration, Adv. Drug Deliv. Rev. 94 (2015) 63–76. doi:10.1016/j.addr.2015.08.003.

[128] G.B. Bishop, T.A. Einhorn, Current and future clinical applications of bone morphogenetic proteins in orthopaedic trauma surgery, Int. Orthop. 31 (2007) 721–727. doi:10.1007/s00264-007-0424-8.

[129] P.C. Bessa, M. Casal, R.L. Reis, Bone morphogenetic proteins in tissue engineering: the road from the laboratory to the clinic, part I (basic concepts), J. Tissue Eng. Regen. Med. 2 (2008) 1–13. doi:10.1002/term.63.

[130] J.A. Spector, J.S. Luchs, B.J. Mehrara, J.A. Greenwald, L.P. Smith, M.T. Longaker, Expression of bone morphogenetic proteins during membranous bone healing., Plast. Reconstr. Surg. 107 (2001) 124–134.

[131] F.M. Chen, M. Zhang, Z.F. Wu, Toward delivery of multiple growth factors in tissue engineering, Biomaterials. 31 (2010) 6279–6308. doi:10.1016/j.biomaterials.2010.04.053.

[132] M.A. Fernandez-Yague, S.A. Abbah, L. McNamara, D.I. Zeugolis, A. Pandit, M.J. Biggs, Biomimetic approaches in bone tissue engineering: Integrating biological and physicomechanical strategies, Adv. Drug Deliv. Rev. 84 (2015) 1–29. doi:10.1016/j.addr.2014.09.005.

[133] A.R. Shrivats, M.C. McDermott, J.O. Hollinger, Bone tissue engineering: State of the union, Drug Discov. Today. 19 (2014) 781–786. doi:10.1016/j.drudis.2014.04.010.

[134] T.N. Vo, F.K. Kasper, A.G. Mikos, Strategies for controlled delivery of growth factors and cells for bone regeneration, Adv. Drug Deliv. Rev. 64 (2012) 1292–1309. doi:10.1016/j.addr.2012.01.016.

[135] M. Geiger, R.H. Li, W. Friess, Collagen sponges for bone regeneration with rhBMP-2, Adv. Drug Deliv. Rev. 55 (2003) 1613–1629. doi:10.1016/j.addr.2003.08.010.

[136] J.D. Boerckel, Y.M. Kolambkar, K.M. Dupont, B.A. Uhrig, E.A. Phelps, H.Y. Stevens, A.J. García, R.E. Guldberg, Effects of protein dose and delivery system on BMP-mediated bone regeneration, Biomaterials. 32 (2011) 5241–5251. doi:10.1016/j.biomaterials.2011.03.063.

[137] M. Nevins, C. Kirker-Head, M. Nevins, J.A. Wozney, R. Palmer, D. Graham, Bone formation in the goat maxillary sinus induced by absorbable collagen sponge implants impregnated with recombinant human bone morphogenetic protein-2., Int. J. Periodontics Restorative Dent. 16 (1996) 8–19.

[138] G. Schmidmaier, P. Schwabe, B. Wildemann, N.P. Haas, Use of bone morphogenetic proteins for treatment of non-unions and future perspectives, Injury. 38 (2007) S35–S41. doi:10.1016/S0020-1383(08)70007-X.

[139] W. Friess, H. Uludag, S. Foskett, R. Biron, C. Sargeant, Characterization of absorbable collagen sponges as recombinant human bone morphogenetic protein-2 carriers, Int. J. Pharm. 185 (1999) 51–60. doi:10.1016/S0378-5173(99)00128-3.

[140] K. V Brown, B. Li, T. Guda, D.S. Perrien, S.A. Guelcher, J.C. Wenke, Improving bone formation in a rat femur segmental defect by controlling bone morphogenetic protein-2 release., Tissue Eng. Part A. 17 (2011) 1735–1746. doi:10.1089/ten.TEA.2010.0446.

[141] M. Okamoto, J. Murai, H. Yoshikawa, N. Tsumaki, Bone morphogenetic proteins in bone stimulate osteoclasts and osteoblasts during bone development., J. Bone Miner. Res. 21 (2006) 1022–1033. doi:10.1359/jbmr.060411.

[142] S. Suliman, Z. Xing, X. Wu, Y. Xue, T.O. Pedersen, Y. Sun, A.P. Doskeland, J. Nickel, T. Waag, H. Lygre, A. Finne-Wistrand, D. Steinmuller-Nethl, A. Krueger, K. Mustafa, Release and bioactivity of bone morphogenetic protein-2 are affected by scaffold binding techniques in vitro and in vivo., J. Control. Release. 197 (2015) 148–157. doi:10.1016/j.jconrel.2014.11.003.

[143] M. Mousa, N.D. Evans, R.O.C. Oreffo, J.I. Dawson, Clay nanoparticles for regenerative medicine and biomaterial design: A review of clay bioactivity, Biomaterials. 159 (2018) 204–214. doi:10.1016/j.biomaterials.2017.12.024.

[144] C.M. Cowan, T. Aghaloo, Y.-F. Chou, B. Walder, X. Zhang, C. Soo, K. Ting, B. Wu, MicroCT Evaluation of Three-Dimensional Mineralization in Response to BMP-2 Doses In Vitro and in Critical Sized Rat Calvarial Defects, Tissue Eng. 13 (2007) 501–512. doi:10.1089/ten.2006.0141.

[145] B. Vaibhav, P. Nilesh, S. Vikram, C. Anshul, Bone morphogenic protein and its application in trauma cases: A current concept update, Injury. 38 (2007) 1227–1235. doi:10.1016/j.injury.2006.12.012.

[146] S.R. Goodyear, R.M. Aspden, Mechanical properties of bone ex vivo., Methods Mol. Biol. (2012). doi:10.1007/978-1-61779-415-5_35.

[147] S. Bailey, D. Vashishth, Mechanical Characterization of Bone: State of the Art in Experimental Approaches—What Types of Experiments Do People Do and How Does One Interpret the Results?, Curr. Osteoporos. Rep. 16 (2018) 423–433. doi:10.1007/s11914-018-0454-8.

[148] S. Bose, M. Roy, Recent Advances in Bone Tissue Engineering Scaffolds, Trends Biotechnol. 30 (2013) 546–554. doi:10.1016/j.tibtech.2012.07.005.Recent.

[149] M.M. Stevens, Biomaterials for bone tissue engineering, Mater. Today. 11 (2008) 18–25. doi:https://doi.org/10.1016/S1369-7021(08)70086-5.

[150] G.H. van Lenthe, R. Müller, CT-based visualization and quantification of bone microstructure in vivo, IBMS Bonekey. 5 (2008) 410–425. doi:10.1138/20080348.

[151] C.P.G. Machado, S.C. Sartoretto, A.T.N.N. Alves, I.B.C. Lima, A.M. Rossi, J.M. Granjeiro, M.D. Calasans-Maia, Histomorphometric evaluation of strontium-containing nanostructured hydroxyapatite as bone substitute in sheep, Braz. Oral Res. 30 (2016) 1–11. doi:10.1590/1807-3107BOR-2016.vol30.0045.

[152] J.J. Li, A. Akey, C.R. Dunstan, M. Vielreicher, O. Friedrich, D. Bell, H. Zreiqat, Effects of material-tissue interactions on bone regeneration outcomes using baghdadite implants in a large animal model, Adv. Healthc. Mater. 1800218 (2018) 1–9. doi:10.1002/adhm.201800218.

[153] W.R. Walsh, R.A. Oliver, C. Christou, V. Lovric, E.R. Walsh, G.R. Prado, T. Haider, Critical size bone defect healing using collagen-calcium phosphate bone graft materials, PLoS One. 12 (2017) 1–21. doi:10.1371/journal.pone.0168883.

[154] M. Coathup, N. Smith, C. Kingsley, T. Buckland, R. Dattani, G.P. Ascroft, G. Blunn, Impaction grafting with a bone-graft substitute in a sheep model of revision hip

replacement, J. Bone Jt. Surg. - Br. Vol. 90–B (2008) 246–253. doi:10.1302/0301-620X.90B2.19675.

[155] P. Wang, L. Zhao, J. Liu, M.D. Weir, X. Zhou, H.H.K. Xu, Bone tissue engineering via nanostructured calcium phosphate biomaterials and stem cells, Bone Res. 2 (2015). doi:10.1038/boneres.2014.17.

[156] O. Gauthier, R. Müller, D. Von Stechow, B. Lamy, P. Weiss, J.M. Bouler, E. Aguado, G. Daculsi, In vivo bone regeneration with injectable calcium phosphate biomaterial: A three-dimensional micro-computed tomographic, biomechanical and SEM study, Biomaterials. 26 (2005) 5444–5453. doi:10.1016/j.biomaterials.2005.01.072.

[157] A. Cahyanto, K. Tsuru, K. Ishikawa, Effect of setting atmosphere on apatite cement resorption: An in vitro and in vivo study, J. Mech. Behav. Biomed. Mater. 88 (2018) 463–469. doi:10.1016/j.jmbbm.2018.08.021.

[158] S. Lewin, A. Barba, C. Persson, J. Franch, M.-P. Ginebra, C. Öhman-Mägi, Evaluation of bone formation in calcium phosphate scaffolds with μ CT-method validation using SEM, Biomed. Mater. 12 (2017) 065005. doi:10.1088/1748-605X/aa801d.

[159] A. Sweedy, M. Bohner, G.H. van Lenthe, G. Baroud, A novel method for segmenting and aligning the pre- and post-implantation scaffolds of resorbable calcium-phosphate bone substitutes, Acta Biomater. 54 (2017) 441–453. doi:10.1016/j.actbio.2017.03.001.

[160] A. Czenek, R. Blanchard, A. Dejaco, Ó.E. Sigurjónsson, G. Örlygsson, P. Gargiulo, C. Hellmich, Quantitative intravoxel analysis of microCT-scanned resorbing ceramic biomaterials-Perspectives for computer-aided biomaterial design, J. Mater. Res. 29 (2014) 2757–2772. doi:10.1557/jmr.2014.326.

[161] E. Tayton, M. Purcell, J.O. Smith, S. Lanham, S.M. Howdle, K.M. Shakesheff, A. Goodship, G. Blunn, D. Fowler, D.G. Dunlop, R.O.C. Oreffo, The scale-up of a tissue engineered porous hydroxyapatite polymer composite scaffold for use in bone repair: An ovine femoral condyle defect study, J. Biomed. Mater. Res. - Part A. 103 (2015) 1346–1356. doi:10.1002/jbm.a.35279.

[162] R. Müller, S.C. Gerber, W.C. Hayes, Micro-compression: a novel technique for the nondestructive assessment of local bone failure, Technol. Heal. Care. 6 (1998) 433–444. doi:10.1016/S0021-9290(98)80302-3.

[163] B.K. Bay, T.S. Smith, D.P. Fyhrie, M. Saad, Digital volume correlation: Three-dimensional strain mapping using X-ray tomography, Exp. Mech. 39 (1999) 217–226. doi:10.1007/BF02323555.

[164] R. Müller, Hierarchical microimaging of bone structure and function, Nat. Rev. Rheumatol. 5 (2009) 373–381. doi:10.1038/nrrheum.2009.107.

[165] P.M. Goggin, K.C. Zygalakis, R.O.C. Oreffo, P. Schneider, High-resolution 3D imaging of osteocytes and computational modelling in mechanobiology: Insights on bone development, ageing, health and disease, Eur. Cells Mater. 31 (2016) 264–295. doi:10.22203/eCM.v031a18.

[166] M. Stauber, R. Müller, Micro-Computed Tomography: A Method for the Non-Destructive Evaluation of the Three-Dimensional Structure of Biological Specimens BT - Osteoporosis: Methods and Protocols, in: J.J. Westendorf (Ed.), Humana Press, Totowa, NJ, 2008: pp. 273–292. doi:10.1007/978-1-59745-104-8_19.

[167] R. Schurch, S.M. Rowland, R.S. Bradley, P.J. Withers, Comparison and combination of imaging techniques for three dimensional analysis of electrical trees, IEEE Trans. Dielectr. Electr. Insul. 22 (2015) 709–719. doi:10.1109/TDEI.2014.004730.

[168] J.A. Núñez, A. Goring, E. Hesse, P.J. Thurner, P. Schneider, C.E. Clarkin, Simultaneous visualisation of calcified bone microstructure and intracortical vasculature using synchrotron X-ray phase contrast-enhanced tomography, Sci. Rep. 7 (2017) 1–9. doi:10.1038/s41598-017-13632-5.

[169] A. Pacureanu, M. Langer, E. Boller, P. Tafforeau, F. Peyrin, Nanoscale imaging of the bone cell network with synchrotron X-ray tomography: optimization of acquisition setup., Med. Phys. 39 (2012) 2229–38. doi:10.1118/1.3697525.

[170] P. Schneider, R. Voide, M. Stampanoni, L.R. Donahue, R. Müller, The importance of the intracortical canal network for murine bone mechanics, Bone. 53 (2013) 120–128. doi:10.1016/j.bone.2012.11.024.

[171] H.D. Barth, M.E. Launey, A.A. MacDowell, J.W. Ager, R.O. Ritchie, On the effect of X-ray irradiation on the deformation and fracture behavior of human cortical bone, Bone. 46 (2010) 1475–1485. doi:10.1016/j.bone.2010.02.025.

[172] H.D. Barth, E.A. Zimmermann, E. Schaible, S.Y. Tang, T. Alliston, R.O. Ritchie, Characterization of the effects of x-ray irradiation on the hierarchical structure and mechanical properties of human cortical bone, Biomaterials. 32 (2011) 8892–8904. doi:10.1016/j.biomaterials.2011.08.013.

[173] F. Swinehart, The Beer-Lambert, J. Chem. Educ. 39 (1962) 333–335. doi:10.1021/ed039p333.

[174] L.A. Feldkamp, L.C. Davis, J.W. Kress, Practical cone-beam algorithm, J. Opt. Soc. Am. A. 1 (1984) 612–619. doi:10.1364/JOSAA.1.000612.

[175] X. Pan, E.Y. Sidky, M. Vannier, Why do commercial CT scanners still employ traditional, filtered back-projection for image reconstruction?, Inverse Probl. 25 (2009). doi:10.1088/0266-5611/25/12/123009.

[176] S.R. Stock, MicroComputed tomography. Methodology and Applications, 2009.

[177] M. Langer, A. Pacureanu, H. Suhonen, Q. Grimal, P. Cloetens, F. Peyrin, X-Ray Phase Nanotomography Resolves the 3D Human Bone Ultrastructure, PLoS One. 7 (2012) 1–7. doi:10.1371/journal.pone.0035691.

[178] T. Frachon, L. Weber, B. Hesse, S. Rit, P. Dong, C. Olivier, F. Peyrin, M. Langer, Dose fractionation in synchrotron radiation x-ray phase micro-tomography., Phys. Med. Biol. 60 (2015) 7543–7566. doi:10.1088/0031-9155/60/19/7543.

[179] P. Cloetens, R. Barrett, J. Baruchel, J.-P. Guigay, M. Schlenker, Phase object in synchrotron radiation hard x-ray imaging, J. Phys. D. Appl. Phys. 29 (1996) 133.

[180] S.C. Mayo, A.W. Stevenson, S.W. Wilkins, In-Line Phase-Contrast X-ray Imaging and Tomography for Materials Science, Materials (Basel). 5 (2012) 937–965. doi:10.3390/ma5050937.

[181] A. Burvall, U. Lundström, P.A. C Takman, D.H. Larsson, H.M. Hertz, A. Barty, K.A. Nugent, D. Paganin, A. Roberts, L.D. Turner, B.B. Dhal, J.P. Hayes, A.P. Mancuso, D. Paterson, R.E. Scholten, C.Q. Tran, A.G. Peele, Phase retrieval in X-ray phase-contrast imaging suitable for tomography On the possibilities of X-ray phase contrast microimaging by coherent high-energy synchrotron radiation, Suetens Fundam. Med. Imaging Phys. Today J. Phys. D Appl. Phys. Rev. Sci. Instrum. Phys. Rev. Lett. J. Phys. D Appl. Phys. Phys. Med. Biol. J. Appl. Phys. 53 (2009) 23–26. doi:10.1364/OE.19.010359.

[182] P. Cloetens, W. Ludwig, J. Baruchel, D. Van Dyck, J. Van Landuyt, J.P. Guigay, M. Schlenker, Holotomography: Quantitative phase tomography with micrometer resolution using hard synchrotron radiation x rays, Appl. Phys. Lett. 75 (1999) 2912–2914. doi:10.1063/1.125225.

[183] C. Kunz, Synchrotron radiation: Third generation sources, J. Phys. Condens. Matter. 13 (2001) 7499–7510. doi:10.1088/0953-8984/13/34/303.

[184] R. Mokso, F. Marone, M. Stampanoni, Real Time Tomography at the Swiss Light Source, AIP Conf. Proc. 1234 (2010) 87–90. doi:10.1063/1.3463356.

[185] E. Maire, P.J. Withers, Quantitative X-ray tomography, Int. Mater. Rev. 59 (2014) 1–43. doi:10.1179/1743280413Y.0000000023.

[186] G. Shenoy, Basic Characteristics of Synchrotron Radiation, 14 (2003).

[187] I. Martin, Bird's eye view of the synchrotron, (2017). https://www.diamond.ac.uk/Science/Machine/Components.html (accessed October 8, 2018).

[188] C. Rau, U. Wagner, Z. Pešić, A. De Fanis, Coherent imaging at the Diamond beamline I13, Phys. Status Solidi Appl. Mater. Sci. 208 (2011) 2522–2525. doi:10.1002/pssa.201184272.

[189] Z.D.P. and A.D.F. and U.W. and C. Rau, Experimental stations at I13 beamline at Diamond Light Source, J. Phys. Conf. Ser. 425 (2013) 182003. http://stacks.iop.org/1742-6596/425/i=18/a=182003.

[190] C. Rau, U. Wagner, Z. Pešić, The Imaging and Coherence Beamline I13 at Diamond, AIP Conf. Proc. 1365 (2011) 132–135. doi:10.1063/1.3625322.

[191] M. Rivers, Synchrotron ' pink beam ' tomography for the study of dynamic processes, SPIE Newsroom. (2016) 1–3. doi:10.1117/2.1201608.006674.

[192] C. Rau, Imaging with Coherent Synchrotron Radiation: X-ray Imaging and Coherence Beamline (I13) at Diamond Light Source, Synchrotron Radiat. News. 30 (2017) 19–25. doi:10.1080/08940886.2017.1364530.

[193] A. Nazarian, R. Müller, Time-lapsed microstructural imaging of bone failure behavior, J. Biomech. 37 (2004) 55–65. doi:10.1016/S0021-9290(03)00254-9.

[194] G. Tozzi, Q.H. Zhang, J. Tong, 3D real-time micromechanical compressive behaviour of bone-cement interface: Experimental and finite element studies, J. Biomech. 45 (2012) 356–363. doi:10.1016/j.jbiomech.2011.10.011.

[195] V. Danesi, G. Tozzi, L. Cristofolini, Application of digital volume correlation to study the efficacy of prophylactic vertebral augmentation, Clin. Biomech. 39 (2016) 14–24. doi:10.1016/j.clinbiomech.2016.07.010.

[196] G. Tozzi, V. Danesi, M. Palanca, L. Cristofolini, Elastic Full-Field Strain Analysis and Microdamage Progression in the Vertebral Body from Digital Volume Correlation, Strain. 52 (2016) 446–455. doi:10.1111/str.12202.

[197] A. Nazarian, M. Stauber, R. Müller, Design and implementation of a novel mechanical testing system for cellular solids, J. Biomed. Mater. Res. - Part B Appl. Biomater. 73 (2005) 400–411. doi:10.1002/jbm.b.30232.

[198] G. Tozzi, Q.H. Zhang, J. Tong, Microdamage assessment of bone-cement interfaces under monotonic and cyclic compression, J. Biomech. 47 (2014) 3466–3474. doi:10.1016/j.jbiomech.2014.09.012.

[199] P.J. Thurner, P. Wyss, R. Voide, M. Stauber, M. Stampanoni, U. Sennhauser, R. Müller, Time-lapsed investigation of three-dimensional failure and damage accumulation in trabecular bone using synchrotron light, Bone. 39 (2006) 289–299. doi:10.1016/j.bone.2006.01.147.

[200] R. Voide, P. Schneider, M. Stauber, P. Wyss, M. Stampanoni, U. Sennhauser, G.H. van Lenthe, R. Müller, Time-lapsed assessment of microcrack initiation and propagation in murine cortical bone at submicrometer resolution, Bone. 45 (2009) 164–173. doi:10.1016/j.bone.2009.04.248.

[201] K. Madi, G. Tozzi, Q.H. Zhang, J. Tong, A. Cossey, A. Au, D. Hollis, F. Hild, Computation of full-field displacements in a scaffold implant using digital volume correlation and finite element analysis, Med. Eng. Phys. 35 (2013) 1298–1312. doi:10.1016/j.medengphy.2013.02.001.

[202] S. Hensley, M. Christensen, S. Small, D. Archer, E. Lakes, R. Rogge, Digital image correlation techniques for strain measurement in a variety of biomechanical test models, Acta Bioeng. Biomech. 19 (2017) 187–195. doi:10.5277/ABB-00785-2016-04.

[203] M. Palanca, G. Tozzi, L. Cristofolini, The use of digital image correlation in the biomechanical area: a review, Int. Biomech. 3 (2015) 1–21. doi:10.1080/23335432.2015.1117395.

[204] Y. Chen, D. Yang, Y. Ma, X. Tan, Z. Shi, T. Li, H. Si, Experimental investigation on the mechanical behavior of bovine bone using digital image correlation technique, Appl. Bionics Biomech. 2015 (2015). doi:10.1155/2015/609132.

[205] F. Hild, S. Roux, Digital image correlation: From displacement measurement to identification of elastic properties - A review, Strain. 42 (2006) 69–80. doi:10.1111/j.1475-1305.2006.00258.x.

[206] B. Pan, K. Qian, H. Xie, A. Asundi, Two-dimensional digital image correlation for in-plane displacement and strain measurement: A review, Meas. Sci. Technol. 20 (2009). doi:10.1088/0957-0233/20/6/062001.

[207] B.K. Bay, Methods and applications of digital volume correlation, J. Strain Anal. Eng. Des. 43 (2008) 745–760. doi:10.1243/03093247JSA436.

[208] N. Lenoir, M. Bornert, J. Desrues, P. Bésuelle, G. Viggiani, Volumetric Digital Image Correlation Applied to X-ray Microtomography Images from Triaxial Compression Tests on Argillaceous Rock, Strain. 43 (2007) 193–205. doi:10.1111/j.1475-1305.2007.00348.x.

[209] B.A. Roeder, K. Kokini, Local, Three-Dimensional Strain Measurements Within Largely Deformed Extracellular Matrix Constructs, J. Biomech. Eng. 126 (2005) 699. doi:10.1115/1.1824127.

[210] C. Franck, S. Hong, S.A. Maskarinec, D.A. Tirrell, G. Ravichandran, Three-dimensional full-field measurements of large deformations in soft materials using confocal microscopy and digital volume correlation, Exp. Mech. 47 (2007) 427–438. doi:10.1007/s11340-007-9037-9.

[211] C.L. Gilchrist, J.Q. Xia, L.A. Setton, E.W. Hsu, High-resolution determination of soft tissue deformations using MRI and first-order texture correlation., IEEE Trans. Med. Imaging. 23 (2004) 546–553.

[212] G.D. O'Connell, W. Johannessen, E.J. Vresilovic, D.M. Elliott, Human internal disc strains in axial compression measured noninvasively using magnetic resonance imaging., Spine (Phila. Pa. 1976). 32 (2007) 2860–2868. doi:10.1097/BRS.0b013e31815b75fb.

[213] J. Fu, F. Pierron, P.D. Ruiz, Elastic stiffness characterization using three-dimensional full-field deformation obtained with optical coherence tomography and digital volume correlation., J. Biomed. Opt. 18 (2013) 121512. doi:10.1117/1.JBO.18.12.121512.

[214] A. Nahas, M. Bauer, S. Roux, A.C. Boccara, 3D static elastography at the micrometer scale using Full Field OCT, Biomed. Opt. Express. 4 (2013) 2138. doi:10.1364/BOE.4.002138.

[215] F. Gillard, R. Boardman, M. Mavrogordato, D. Hollis, I. Sinclair, F. Pierron, M. Browne, The application of digital volume correlation (DVC) to study the microstructural behaviour of trabecular bone during compression, J. Mech. Behav. Biomed. Mater. 29 (2014) 480–499. doi:10.1016/j.jmbbm.2013.09.014.

[216] D. Christen, A. Levchuk, S. Schori, P. Schneider, S.K. Boyd, R. Müller, Deformable image registration and 3D strain mapping for the quantitative assessment of cortical bone microdamage, J. Mech. Behav. Biomed. Mater. 8 (2012) 184–193. doi:10.1016/j.jmbbm.2011.12.009.

[217] A.I. Hussein, P.E. Barbone, E.F. Morgan, Digital volume correlation for study of the mechanics of whole bones, Procedia IUTAM. 4 (2012) 116–125. doi:10.1016/j.piutam.2012.05.013.

[218] B.C. Roberts, E. Perilli, K.J. Reynolds, Application of the digital volume correlation technique for the measurement of displacement and strain fields in bone: A literature review, J. Biomech. 47 (2014) 923–934. doi:10.1016/j.jbiomech.2014.01.001.

[219] H. Leclerc, J.-N. Périé, F. Hild, S. Roux, Digital volume correlation: what are the limits to the spatial resolution?, Mech. Ind. 13 (2012) 361–371. doi:10.1051/meca/2012025.

[220] F. Hild, A. Bouterf, L. Chamoin, H. Leclerc, F. Mathieu, J. Neggers, F. Pled, Z. Tomičević, S. Roux, Toward 4D mechanical correlation, Adv. Model. Simul. Eng. Sci. 3 (2016). doi:10.1186/s40323-016-0070-z.

[221] E. Dall'Ara, M. Peña-Fernández, M. Palanca, M. Giorgi, L. Cristofolini, G. Tozzi, Precision of DVC approaches for strain analysis in bone imaged with μCT at different dimensional levels, Front. Mater. 4:31 (2017). doi:10.3389/fmats.2017.00031.

[222] A. Germaneau, P. Doumalin, J.C. Dupré, Full 3D Measurement of Strain Field by Scattered Light for Analysis of Structures, Exp. Mech. 47 (2007) 523–532. doi:10.1007/s11340-006-9029-1.

[223] A. Germaneau, P. Doumalin, J.C. Dupré, 3D strain field measurement by correlation of volume images using scattered light: Recording of images and choice of marks, Strain. 43 (2007) 207–218. doi:10.1111/j.1475-1305.2007.00340.x.

[224] T.S. Smith, B.K. Bay, M.M. Rashid, Digital Volume Correlation Including Rotational Degrees of Freedom during Minimization, Exp. Mech. 42 (2002) 272–278. doi:10.1177/001448502321548346.

[225] L. Liu, E.F. Morgan, Accuracy and precision of digital volume correlation in quantifying displacements and strains in trabecular bone, J. Biomech. 40 (2007) 3516–3520. doi:10.1016/j.jbiomech.2007.04.019.

[226] M.R. Hardisty, Whole Bone Strain Quantification by Image Registration: A Validation Study, J. Biomech. Eng. 131 (2009) 064502. doi:10.1115/1.3127249.

[227] R. Zauel, Y.N. Yeni, B.K. Bay, X.N. Dong, D.P. Fyhrie, Comparison of the Linear Finite Element Prediction of Deformation and Strain of Human Cancellous Bone to 3D Digital Volume Correlation Measurements, (n.d.). doi:10.1115/1.2146001.

[228] E. Verhulp, B. Van Rietbergen, R. Muller, R. Huiskes, Micro-finite element simulation of trabecular-bone post-yield behaviour--effects of material model, element size and type., Comput. Methods Biomech. Biomed. Engin. 11 (2008) 389–395. doi:10.1080/10255840701848756.

[229] E. Dall'Ara, D. Barber, M. Viceconti, About the inevitable compromise between spatial resolution and accuracy of strain measurement for bone tissue: A 3D zero-strain study, J. Biomech. 47 (2014) 2956–2963. doi:10.1016/j.jbiomech.2014.07.019.

[230] M. Palanca, G. Tozzi, L. Cristofolini, M. Viceconti, E. Dall'Ara, 3D Local Measurements of Bone Strain and Displacement: Comparison of Three Digital Volume Correlation Approaches., J. Biomech. Eng. 137 (2015) 1–14. doi:10.1115/1.4030174.

Chapter 3. Full-field strain measurements at tissue level

3.1. Optimisation of digital volume correlation computation in SR-microCT images

Marta Peña Fernández[1], Asa H Barber[1,2], Gordon W Blunn[3], Gianluca Tozzi[1]

[1] *Zeiss Global Centre, School of Engineering, University of Portsmouth, Portsmouth, UK.*
[2] *School of Engineering, London South Bank University, London, UK.*
[3] *School of Pharmacy and Biomedical Sciences, University of Portsmouth, Portsmouth, UK.*

Published in:

Journal of Microscopy, 2018, doi: 10.1111/jmi.12745

as *"Optimisation of digital volume correlation computation in SR-microCT images of trabecular bone and bone biomaterial systems".*

Abstract

A micromechanical characterisation of biomaterials for bone tissue engineering is essential to understand the quality of the newly regenerated bone, enabling the improvement of tissue regeneration strategies. A combination of micro-computed tomography (microCT) in conjunction with *in situ* mechanical testing and digital volume correlation (DVC) has become a powerful technique to investigate the internal deformation of bone structure at a range of dimensional scales. However, in order to obtain accurate three-dimensional (3D) strain measurement at tissue level, high-resolution images must be acquired, and displacement/strain measurement uncertainties evaluated. The aim of this study was to optimise imaging parameters, image post-processing and DVC settings to enhance computation based on 'zero-strain' repeated high-resolution synchrotron microCT (SR-microCT) scans of trabecular bone and bone-biomaterial systems. Low exposures to SR X-ray radiation were required to minimize irradiation-induced tissue damage, resulting in the need of advanced 3D filters on the reconstructed images to reduce DVC-measured strain errors. Furthermore, the computation of strain values only in the hard phase (i.e. bone, biomaterial) allowed the exclusion of large artifacts localised in the bone marrow. This study demonstrated the suitability of a local DVC approach based on SR-microCT images to investigate the micromechanics of trabecular bone and bone-biomaterial composites at tissue level with a standard deviation of the errors in the region of 100 microstrain after a thorough optimisation of DVC computation.

Keywords: digital volume correlation, synchrotron, microCT, bone, bone-biomaterial, displacement/strain uncertainties.

3.1.1. Introduction

Novel osteoregenerative biomaterials for bone tissue engineering are constantly under development with the aim of favouring optimal bone integration in the defect site up to complete bone formation [1–3]. Synthetic bone grafts substitutes, such as commercial StronBone [4], have shown excellent regenerative properties [1,5,6]. However, to date, the ability of such biomaterials in producing bone that is comparable to the native tissue they are meant to replace is poorly understood and may, therefore, be insufficient to support load-bearing regions. Micromechanical characterisation of bone-biomaterial systems has been extremely beneficial to better understand the overall structural response of such composites [7–9]. Particularly, a significant understanding of the internal microdamage at the bone-biomaterial interface, which could promote further damage to the bone structure, remains partially unexplored [9,10]. This is due to the intrinsic limitations of most experimental techniques, like strain gauges or digital image correlation, limited to two-dimensional surface measurement, while the internal volume response could not be interrogated [11,12].

The recent advances in high-resolution micro-computed tomography (microCT) combined with *in situ* mechanical testing [13,14], has allowed Digital Volume Correlation (DVC) to become a powerful and unique technique to investigate three-dimensional (3D) full-field displacement and strain in bone based on 3D images acquired at different deformation states [12,15,16]. DVC has been extensively used to investigate trabecular bone [17,18], cortical bone [19], whole bones [10,20], biomaterials [21], and bone-biomaterial systems [7,9] under different loading conditions. However, in order to expand the applications of DVC to the study of clinically-relevant issues such as integration of biomaterials and consequent bone formation after bone grafting procedures, it is important to understand the displacement and strain measurement errors (uncertainties) associated with the DVC measurement, and optimising the imaging and DVC settings to minimise these errors. Uncertainties of any specific DVC approach are defined as the differences between the computed measurements obtained by DVC and the nominal applied or expected values, and they are reported in terms of accuracy (mean) and precision (standard deviation). Measurement errors are typically quantified on repeated scans (i.e. in a known deformation field such as ‘zero-strain’) to account for the intrinsic noise of the input images [22,23]. This repeated scan methodology has been already adopted to quantify strain errors associated with bone-biomaterial interfaces (i.e. bone-cement) [24,25]. Specifically, Tozzi et al. [24] focused on images obtained in laboratory microCT systems with a voxel size of 39 μm. The random errors for the strain components were found to be all around or lower than 200 με, for a sub-volume size of 48 voxels, providing measurements approximately every 2 mm. In this sense, the DVC measurement spatial resolution, defined as the smallest distance of computed outputs (i.e. displacements) in relation to the sub-volume of interest, were able to include more bone structural units (BSUs, i.e., trabecula), and enabled the classification of regions at high or low localised strain. However, measurement within BSUs remained unexplored. To

overcome the limitation of laboratory microCT systems, where a strong compromise between strain precision and measurement spatial resolution must be accepted [11,23], synchrotron-based microCT (SR-microCT) has proven to provide strain uncertainties below 200 με for correlations performed with a measurement spatial resolution below 100 μm for both cortical and trabecular bone [26]. In fact, the use of DVC based on SR-microCT high resolution images (~2 μm voxel size), allowed reliable strain measurements within the BSUs [22,26]. However, the performance of DVC based on SR-microCT images on composite biological structures such as bone-biomaterial systems still remains unclear. Recently, Dall'Ara et al. [22] provided an overview of the strain errors associated to several bone structures acquired with different microCT techniques, at different dimensional levels. In that study, the precision of DVC applied to SR-microCT images of bone and bone-biomaterial systems was analysed for the first time, reporting values below 150 με for a measurement spatial resolution close to 150 μm, allowing strain measurement at tissue level. Despite those results were promising to evaluate full-field strain in bone-biomaterial systems, only the precision in terms of displacement and strain was analysed, but the accuracy of the method was not reported. In addition, the optimisation on imaging settings, post-processing and DVC features was also not reported.

The reliability of DVC based on high-resolution SR-microCT images of trabecular bone and bone-biomaterial systems will provide accurate 3D strain measurement at tissue level. Therefore, a better understanding of the micromechanical behaviour of trabecular bone and bone-biomaterials interfaces can be achieved through optimisation of the DVC computation. In this perspective, the main aim of this study was to investigate the effect of image post-processing and DVC settings on the displacement- and strain-measured uncertainties at tissue level based on 'zero-strain' repeated SR-microCT scans, using a local DVC approach, in trabecular bone and bone-biomaterial systems.

3.1.2. Methods

3.1.2.1. Specimen preparation

Cylindrical bone defects (8mm diameter by 14 mm depth) were surgically created in the femur condyles of an adult sheep [27] and four different biomaterials (Actifuse, ApaPore, StronBone, StronBone-P) were implanted under Ethics approval granted by the Royal Veterinary College and in compliance with the United Kingdom Home Office regulations (Animal Scientific Procedure Act [1986]) under the animal project licence number PLL 70/8247. Six weeks after implantation both left and right condyles were harvested and cylindrical samples (4 mm diameter by 18 mm length) were cored from the condyles in proximal-distal direction by drilling with a coring tool. The ends of the cores were trimmed plane and parallel, and end-constraint was achieved by embedding the ends of the samples in poly-methyl-methacrylate (PMMA) endcaps. Approximately, 5 mm of the core was embedded into each endcap to achieve a 2:1 aspect ratio and reduce experimental artifacts

[28]. In total, four bone-biomaterial systems (n=1 p/biomaterial) from the bone defect areas and two trabecular native bone in proximity of the implantation site (n=1 p/condyle) were analysed. Samples were kept frozen at -20° and thawed for around 2 h in saline solution at room temperature before image acquisition.

3.1.2.2. SR-microCT

SR-microCT imaging was performed at the Diamond-Manchester Imaging Branchline I13-2 of Diamond Light Source (DLS), UK, using a filtered (1.3 mm pyrolytic graphite, 3.2 mm aluminium and 60µm steel) partially-coherent polychromatic 'pink' beam (5-35 keV) of parallel geometry with an undulator gap of 5 mm. Sample alignment in the beam was under low dose conditions (0.2 Gy/s). Projections were recorded by a sCMOS (2560 x 2160 pixels) pco.edge 5.5 (PCO AG, Germany) detector, which was coupled to a 500 µm-thick $CdWO_4$ and a visual light microscope. A 1.25X objective lens was used to achieve a total magnification of 2.5X, resulting in an effective voxel size of 2.6 µm and a field of view of 6.7 x 5.6 mm. For each dataset, 1801 projection images were collected over 180 degrees of continuous rotation ('fly scan') [29]. The final projection was not used for reconstruction, but was compared to the first image to check for experimental problems including sample deformation and bulk movements [30]. The exposure time was set to 64 ms per projection, leading to a nominal absorbed radiation dose of 4.7 kGy per scan, therefore minimising SR irradiation-induced damage during image acquisition [31] (Figure 1). The propagation distance (sample to detector) was first set to 50 mm and increased in ~100 mm increments until sufficient in-line phase contrast was gained to visualise the microstructure. The final propagation distance used was 150 mm. The projection images were flat-field and dark-field corrected prior to reconstruction. For each dataset, 40 flat and dark images were collected. Reconstruction was performed at DLS using the in-house software, DAWN [32,33], incorporating ring artefact suppression. Specimens were imaged within a loading stage (CT5000, Deben Ltd, UK) equipped with an environmental chamber and were kept immersed in saline solution during the entire experiment. A small preload (5 N) was applied only to ensure good end-contact prior to imaging and minimise motion artifacts during the scan. Each specimen was scanned twice under the same configuration ('zero-strain' repeated scan) without any repositioning.

3.1.2.3. Image post-processing

Each 3D image dataset consisted of 2160 images (2256 x 2076 pixels) with 32-bit grey-levels. Images were converted to 8-bit grey-scale (0 – 255 counts). The repeated scans for each specimen were first rigidly registered using the rigid registration plugin in Fiji software [34]. Registration was performed minimising the Euclidean distance (corresponding to the square root of summed squares of voxel intensity differences) between the reference and the target image, using an iterative optimisation algorithm (conjugate direction search [35]).

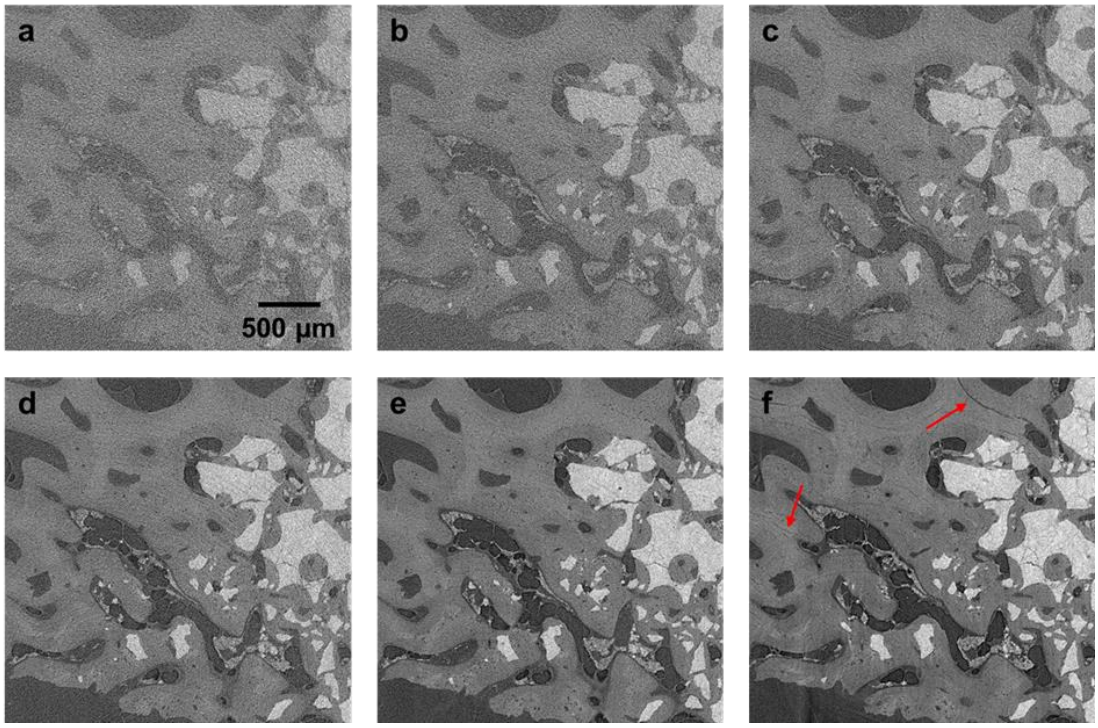

Figure 1. SR-microCT two-dimensional (2D) cross-sections acquired at different exposure times in the same bone-biomaterial system (ApaPore). Increasing the exposure time per projection (from a to f) improved the quality of the images but induced damage in the tissue due to SR X-ray radiation. Red arrows indicate microcracks in the tissue. (a) t_{exp} = 32 ms. (b) t_{exp} = 64 ms. (c) t_{exp} = 128 ms. (d) t_{exp} = 256 ms. (e) t_{exp} = 512 ms. (f) t_{exp} = 1024 ms. (t_{exp}: exposure time per projection). Scale bar is valid for all images.

The algorithm iteratively adjusts the six degrees of freedom (three translational and three rotational parameters) of the rigid transformation to match the target to the reference image. The optimised transformation is then applied to the target image using TransformJ plugin using a cubic spline interpolation [36]. After registration, a volume of interest (VOI) was cropped for each tomogram, consisting of a parallelepiped with side lengths of 1000 voxels (2.6 mm^3). The VOI was set in the centre of the volume for the trabecular bone and manually selected for the bone-biomaterial specimens in order to include the interface. Noise in the images was reduced by applying a 3D filter. To compare the DVC algorithm performance on the filtered images, two different filters were used (Figure 2): a local median filter (radius = 2 pixels) and a non-local means (NLM) filter [37,38], where the variance (sigma) of the noise was automatically estimated for each dataset [39]. The choice of both filters was based on the fact that local smoothing methods aim at noise reduction and at a reconstruction of the main geometrical features, but not at the preservation of details and textures in the images. In that sense, non-local methods have shown to better retain image fine structures [40], therefore DVC results may differ.

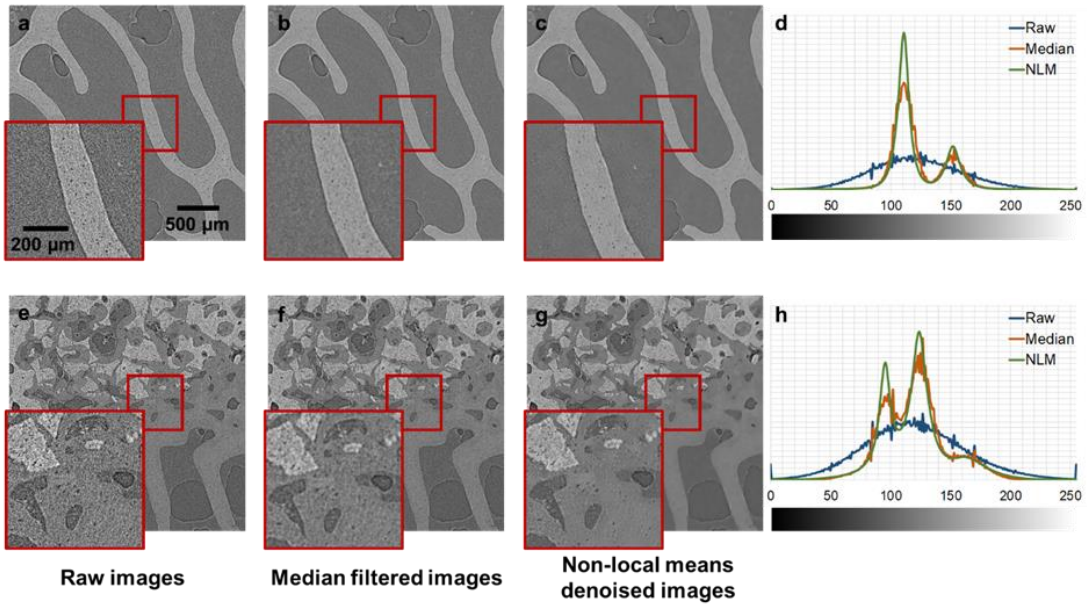

Figure 2. SR-microCT two-dimensional (2D) cross-sections in trabecular bone (a, b, c) and bone-biomaterial interface of Actifuse (e, f, g). The raw images (first column) present a reduced quality due to the low X-ray exposure used. Applying a median filter (second column) and a non-local means filter (third column) resulted in considerable noise reduction. Intensity histograms of trabecular bone (d) and bone-biomaterial (h) showed noise reduction from raw to median and non-local means filtered images. Scale bar is valid for all images.

Additionally, the original SR-microCT images were also masked by setting to zero the grey-scale intensity of non-bone/biomaterial voxels. A binary image (value one for bone-biomaterial voxels and zero elsewhere) was first created from the non-local mean denoised images using an iterative approach. Due to the low exposure used during image acquisition to minimise irradiation-induced damage in the tissue, the quality of the images was considerably low (Figure 1); therefore, a global thresholding can be insufficient for segmenting the mineralised tissue and biomaterial from the soft (i.e. bone marrow) and watery material, due to variations in signal intensity and noise within the same material. The method employed in this study firstly used a global threshold based on Huang's method [41], followed by an iterative approach. The latter consisted on applying three different operations to the binary images as follows: 1) the connected regions in the 3D volume were identified by applying a purifying cycle using BoneJ [42], which locates all particles in the 3D volume and removes all of those, but the largest foreground (bone-biomaterial) and background (bone marrow) particles [43]; 2) a closing cycle, which performs a dilation operation followed by erosion, was applied in order to fill in small holes; 3) an opening cycle, consisting on an erosion operation followed by dilation, was used to remove isolated pixels. The quality of the binary images was checked by visual inspection after each iteration. The iterative process was concluded when no improvements were observed. In this study 6 iterations were selected (Figure 3). Masked images, with the original grey-scale value in the mineralised tissue and biomaterial, and zero elsewhere, were obtained multiplying the filtered image to

the final binary image. For each VOI, the solid volume fraction (SV/TV) was obtained to assess possible correlations with DVC measurements.

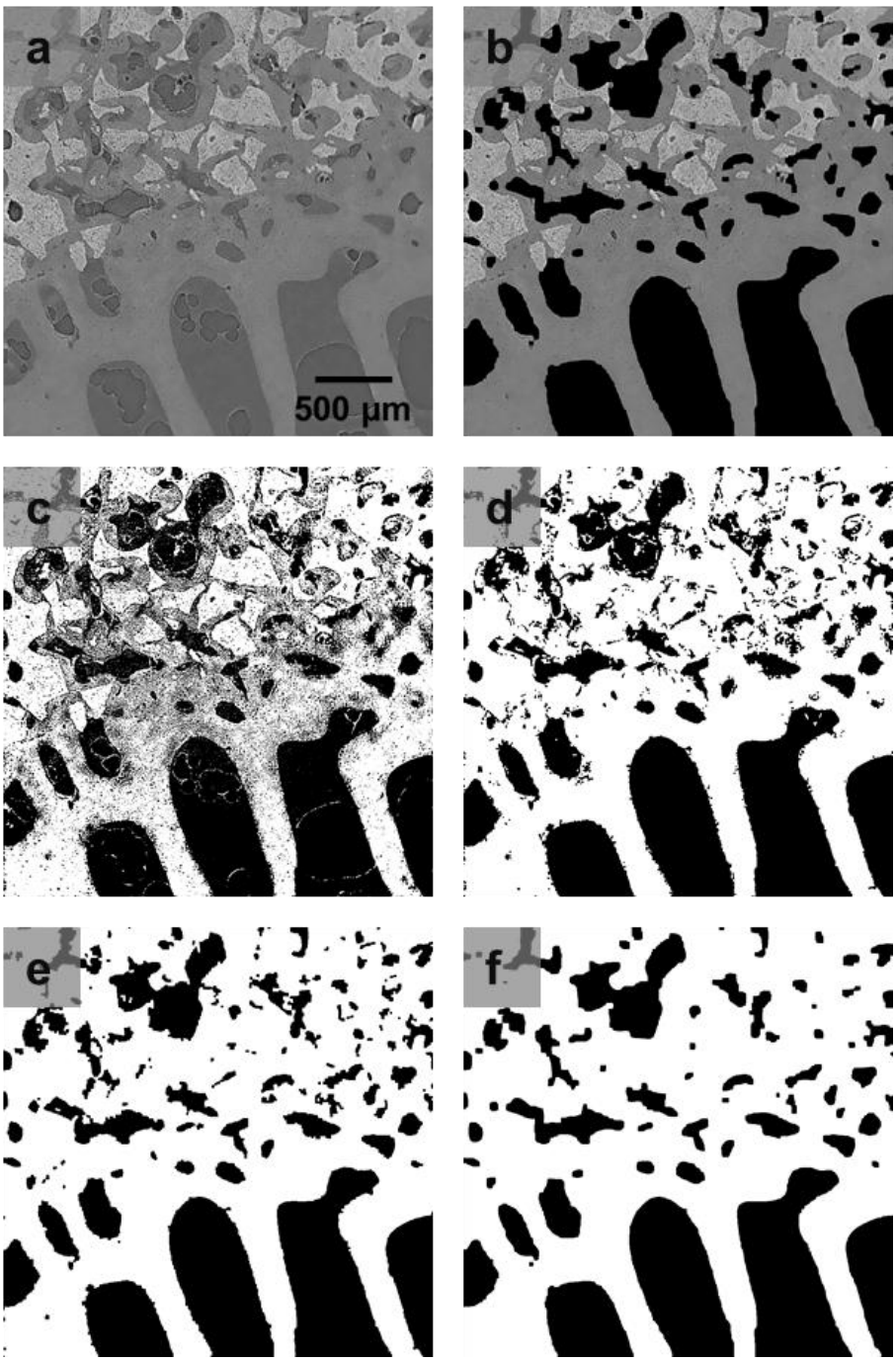

Figure 3. Iterative approach for segmentation of SR-microCT images of bone-biomaterial systems. (a) Non-local means denoised image showing unabsorbed biomaterial (light grey), bone tissue (medium grey) and soft material (dark grey). (b) Final masked image where voxels of the soft phase were set to zero (black) intensity value. (c) Initial segmentation based on Huang's method. Binary images after two (d), four (e) and six (f) iterations. More bone-biomaterial and less marrow/watery material is included in the segmentation as the number of iterations increases. Scale bar is valid for all images.

3.1.2.4. Digital volume corraltion

DVC was performed on the reconstructed tomograms using DaVis 8.4 software (LaVision Ltd., Goettingen, Germany). DVC is a cross-correlation method operating on the intensity values (grey-level) of 3D images. In essence, the measurement volume is divided into smaller sub-volumes and the contrast pattern within the sub-volumes is then tracked from reference to deformed state (local approach [21]) as a discrete function of the grey-levels. The matching between the sub-volumes is achieved via a direct cross-correlation (DC) function [44]. It is called "direct" because it directly sums the products of voxel grey values of the initial and deformed volumes to form the 3D correlation map. The zero-mean normalised correlation coefficient C_{norm} for two sub-volumes A and B with shift $\underline{\boldsymbol{u}} = (u, v, w)$ in the x, y and z direction respectively, and a window of $N\,x\,N\,x\,N$ voxels at point $\underline{\boldsymbol{x_0}} = (x_0, y_0, z_0)$ is computed according to:

$$C_{norm}(\underline{\boldsymbol{u}}) = \sum_{\underline{\boldsymbol{x}}} \frac{\left(A_{\underline{\boldsymbol{x}}} - \langle A \rangle\right)\left(B_{\underline{\boldsymbol{x}}+\underline{\boldsymbol{u}}} - \langle B_{\underline{\boldsymbol{u}}} \rangle\right)}{\sqrt{|A'|^2 \cdot \left|B'_{\underline{\boldsymbol{u}}}\right|^2}} \tag{1}$$

With

$$\langle A \rangle = \sum_{\underline{\boldsymbol{x}}} \frac{A_{\underline{\boldsymbol{x}}}}{N^3}$$

$$\langle B_{\underline{\boldsymbol{u}}} \rangle = \sum_{\underline{\boldsymbol{x}}} \frac{B_{\underline{\boldsymbol{x}}+\underline{\boldsymbol{u}}}}{N^3}$$

$$|A'|^2 = \sum_{\underline{\boldsymbol{x}}} \left[A_{\underline{\boldsymbol{x}}} - \langle A \rangle\right]^2$$

$$\left|B'_{\underline{\boldsymbol{x}}+\underline{\boldsymbol{u}}}\right|^2 = \sum_{\underline{\boldsymbol{x}}} \left[B_{\underline{\boldsymbol{x}}+\underline{\boldsymbol{u}}} - \langle B_{\underline{\boldsymbol{u}}} \rangle\right]^2$$

Where all summations run from $\underline{\boldsymbol{x}} = \underline{\boldsymbol{x_0}} = (x_0, y_0, z_0)$ to $\underline{\boldsymbol{x}} = (x_0 + N - 1, y_0 + N - 1, z_0 + N - 1)$. $A_{\underline{\boldsymbol{x}}}$ is the grey value (intensity) of the voxel $\underline{\boldsymbol{x}} = (x,\ y,\ z)$ in the reference sub-volume A, and consequently $B_{\underline{\boldsymbol{x}}+\underline{\boldsymbol{u}}}$ is the intensity of the voxel at the shifted position $\underline{\boldsymbol{x}} + \underline{\boldsymbol{u}} = (x + u, y + v, z + w)$ in the deformed sub-volume B.

The DaVis software adopts a multi-pass scheme that uses the displacement gradient from the previous pass to deform the sub-volume on the subsequent pass until the highest possible correlation is achieved. This iterative analysis is adapted from particle image velocimetry (PIV) techniques [45]. And can be summarised as follows for a two-pass scheme:

I. First pass: A specific sub-volume of $N\,x\,N\,x\,N$ voxels is chosen, determining the node distribution and spacing. The intensity pattern within each sub-volume in the reference volume V_0 is matched with the corresponding pattern in the shifted volume V_1.

The predictor shift, $\underline{\boldsymbol{u_p}} = (u_p, v_p, w_p)$, is obtained by maximising (1) for each sub-volume, where sub-pixel accuracy is achieved by fitting a Gaussian curve to the correlation peak [46].

II. The calculated displacements describe a mapping function between the intensity pattern contained within each voxel in volume V_0 to its corresponding voxel in volume V_1. Tri-linear interpolation is used to calculate displacements of voxels located between the nodes of the sub-volume. This mapping information is then used to deform the entire shifted volume V_1 to overlay the reference volume V_0. The intensity of each displaced voxel in V_1 at sub-voxel positions is computed using spline interpolation, resulting in a new volume V_2.

III. Second pass: Step I is repeated between the reference volume V_0 and the new shifted volume V_2, to calculate a new correlation map, obtaining a corrector shift $\underline{\boldsymbol{u_c}} = (u_c, v_c, w_c)$.

IV. The sum of predictor and corrector is the desired shift field $\underline{\boldsymbol{u}} = \underline{\boldsymbol{u_p}} + \underline{\boldsymbol{u_c}}$.

The final displacement, $\underline{\boldsymbol{U}} = (U, V, W)$, is therefore a 3D full-field average displacement of the pattern within a specific sub-volume between reference V_0 and deformed V_1 volume. The field of strain components is computed using a centered finite difference (CFD) scheme [47,48]. First, the local gradients in the displacement field, equivalent to the deformation gradient, are calculated by finite differences:

$$\begin{cases} \dfrac{\partial \alpha}{\partial x} = \dfrac{\alpha(x_0 + l, y_0, z_0) - \alpha(x_0 - l, y_0, z_0)}{2l} \\ \dfrac{\partial \alpha}{\partial y} = \dfrac{\alpha(x_0, y_0 + l, z_0) - \alpha(x_0, y_0 - l, z_0)}{2l} \\ \dfrac{\partial \alpha}{\partial z} = \dfrac{\alpha(x_0, y_0, z_0 + l) - \alpha(x_0, y_0 - l, z_0)}{2l} \end{cases} \quad (2)$$

where α $\alpha = (U, V, W)$ and $l\ (= N)$ is the length of the sub-volume. From the deformation gradient, the strain tensor is derived as:

$$E = \begin{bmatrix} E_{xx} & E_{xy} & E_{xz} \\ E_{yx} & E_{yy} & E_{yz} \\ E_{zx} & E_{zzy} & E_{zz} \end{bmatrix} = \begin{bmatrix} \dfrac{\partial U}{\partial x} & \dfrac{1}{2}\left(\dfrac{\partial U}{\partial y} + \dfrac{\partial V}{\partial x}\right) & \dfrac{1}{2}\left(\dfrac{\partial U}{\partial z} + \dfrac{\partial W}{\partial x}\right) \\ \dfrac{1}{2}\left(\dfrac{\partial U}{\partial y} + \dfrac{\partial V}{\partial x}\right) & \dfrac{\partial V}{\partial y} & \dfrac{1}{2}\left(\dfrac{\partial V}{\partial z} + \dfrac{\partial W}{\partial y}\right) \\ \dfrac{1}{2}\left(\dfrac{\partial U}{\partial z} + \dfrac{\partial W}{\partial x}\right) & \dfrac{1}{2}\left(\dfrac{\partial V}{\partial z} + \dfrac{\partial W}{\partial y}\right) & \dfrac{\partial W}{\partial z} \end{bmatrix} \quad (3)$$

Influence of sub-volume size

The DVC technique relies on the internal grey-level texture of the material that can be recognised in the 3D images to correlate a reference sub-volume to a deformed one. The features included within each sub-volume, and therefore the sub-volume size affects DVC

uncertainties [16,17]. A small sub-volume size is typically susceptible to noise effects, whereas large sub-volumes may result in an insufficient spatial resolution [23]. Therefore, the goal is always to choose a sub-volume small enough to capture the essential features of deformation, and still large enough to give accurate results. In order to evaluate the influence of sub-volume size on the DVC displacement/strain uncertainties, seven sub-volume sizes ranging from 16 to 112 voxels, in steps of 16 voxels were investigated. Two passes were performed for each sub-volume size, using the first pass as a predictor for the final computation and therefore, improving the correlation. Moreover, a multi-pass scheme with variable sub-volume sizes was tested. The multi-pass scheme used sub-volumes of 112, 96, 80, 64 and 48 voxels.

Influence of masking

DVC was applied to the raw and masked images to investigate the influence of including the bone marrow regions, usually associated to large strain artefacts due to the lack of a clear pattern distribution, in the correlation algorithm. Two different approaches were considered for DVC computation in the masked images: treating the non-hard areas as a black 'zero-count' region (masked) and creating a threshold-based algorithmic mask using DaVis tools (DaVis-masked). The difference between both approaches lies on the inclusion of regions outside the bone and biomaterial when correlating the 3D images. Whereas the use of masked images allows DVC algorithm to correlate the entire 3D image (bone/biomaterial and black regions (zero intensity)), DaVis-masked allows calculating vectors only in bone and biomaterial areas within the 3D image, as the black regions are ignored (no intensity). Additionally, the minimal fraction of valid pixel (mfvp) can be controlled when using the masking tools in DaVis. This parameter specifies the number of voxels that need to be contained within a sub-volume for the computed vector to be valid; the higher this value the less close calculated vectors are to the mask edges, resulting in a progressive loss of data, since voxels close to the mask edges are not included. It should be highlighted that the resulting vectors are computed in the centre of each sub-volume and not at the centre of mass of the non-zero voxels. To account only for the uncertainties within bone and biomaterial and allow a better comparison between the three different options, the sub-volumes containing all voxels outside the bone and biomaterial areas were ignored for the raw and masked images, and the uncertainties were computed considering only the remaining sub-volumes. The resulting displacement/strain fields were weighted according to the SV/TV for each sub-volume. Additionally, for the raw and masked images, sub-volumes with a correlation coefficient below 0.6 were removed, to avoid large strain artifacts due to poor correlation in some regions. The latter could not be applied to the DaVis-masked images, as the mean correlation coefficient was lower (below 0.56), and any filtering of the data would lead to insufficient correlated sub-volumes.

Evaluation of DVC uncertainties

To quantify the level of uncertainties of the DVC measurements, which is associated to imaging conditions, image post-processing and sub-volume size, different scalar indicators were computed for each pair of 'zero-strain' repeated scans. Ideally, the displacements could be considered null; however, in the real experiment the actual displacements were affected by the inevitable unknown micro-movements of the different parts of the image acquisition setup. Therefore, the systematic error for the displacements could not be quantified and only the random errors, computed as the variability of the displacement within each specimen, was calculated [11].

Strain components are computed from the local gradients in the displacement field as shown in equation (3). As the test was based on a 'zero-strain' condition, any non-zero values of strain were considered as error. Random errors for each specimen were calculated as standard deviation for each of the strain components to investigate the presence of any preferential components. Additionally, the mean absolute error (MAER) and standard deviation of the error (SDER) [25] were obtained as:

$$MAER = \frac{1}{n}\sum_{k=1}^{n}\left(\frac{1}{6}\sum_{c=1}^{6}\left|\varepsilon_{c,k}\right|\right) \tag{4}$$

$$SDER = \sqrt{\frac{1}{n}\sum_{k=1}^{n}\left(\frac{1}{6}\sum_{c=1}^{6}\left|\varepsilon_{c,k}\right| - MAER\right)^{2}} \tag{5}$$

Where ε represents the strain; c represent the six independent strain components, k represents the measurement point; and n is the total number of measurement points. MAER and SDER correspond to the indicators formerly known as "accuracy" and "precision", respectively [17]. Additionally, the correlated volume (CV) was assessed as the volume where correlation was successful (> 0.6 for raw and masked images, > 0 for DaVis-mask). The correlated solid volume (CV/SV) was then computed dividing the CV by the SV/TV.

3.1.3. Results

3.1.3.1. Influence of filtering the images

The influence of filtering the images was only assessed on the raw images prior to masking procedures and data screening. The use of a median and NLM filter reduced the noise in the images considerably (Figure 2), as depicted by the intensity histograms of each dataset. Furthermore, filters had a clear impact on the final mean value of the Cnorm, ranging from 0.41 for the raw images to 0.89 (Table 1) in the trabecular bone specimens, and from 0.37 to 0.84 in the bone-biomaterial systems, for the raw and NLMD denoised images, respectively, using a multi-pass scheme with a final sub-volume size of 48 voxels. However, the

improvement of the correlation coefficient was not related to a clear decrease of the measured DVC errors. Whereas filtering the images reduced the displacement random errors in bone-biomaterial systems (from 0.35 µm for the raw images to 0.29 µm using the median filtered images and 0.25 µm for the NLM filtered images), it increased those values for the trabecular bone specimens (from 0.21 µm for the raw images to 0.22 µm using the median filtered images and 0.23 µm for the NLM filtered images). Conversely, the use of a NLM filter was found to improve the strain uncertainties, for both trabecular bone (up to 12% lower errors) and bone-biomaterial specimens (up to 18% improvement), when compared to the use of raw or median filtered images.

Table 1. Correlated solid volume (CV/SV), mean value of the normalized correlation coefficient (C_{norm}), random errors affecting the displacement components, MAER and SDER on the strain measurements for the multi-pass scheme (final sub-volume size of 48 voxels) in trabecular bone and bone-biomaterial specimens analysed with the different filters used (raw images, median filter and NLM filter). Median values are calculated accounting for the total number of specimens for each type.

	Filter	**CV/SV (%)**	**C_{norm}**	**Displacement random errors (µm)**			**Strain uncertainties (µε)**	
				x	y	z	MAER	SDER
Trabecular bone	None	96.6	0.41	0.21	0.19	0.14	387	294
	Median	93.3	0.87	0.22	0.20	0.17	380	273
	NLM	93.0	0.89	0.23	0.21	0.15	376	257
Bone-Biomaterial	None	97.4	0.37	0.35	0.22	0.14	300	215
	Median	96.1	0.73	0.29	0.22	0.15	307	215
	NLM	96.1	0.84	0.11	0.25	0.14	289	175

3.1.3.2. Influence of varying the minimal fraction of valid pixels (mfvp)

The mfvp used for DVC computation applied to the DaVis-masked images had an indirect effect on the CV/SV (Table 2). The CV/SV increased from 55.8% to 86.8% for the trabecular bone and from 83.0% to 93.9% for the bone-biomaterial specimens, for a mfvp of 50% and 30%, respectively. Despite the changes in the CV/SV, the C_{norm} remained nearly constant. Larger error variations were found in the trabecular bone (up to 20% change) compared to the bone-biomaterial systems (less than 10% change) as a function of the mfvp. A visual representation is shown in Figure 4. The number of successfully correlated sub-volumes (colour shaded) increased (higher CV/SV) when decreasing the mfvp.

Table 2. Correlated solid volume (CV/SV), mean normalised correlation coefficient (C_{norm}), random errors affecting the displacement components, MAER and SDER of the strain measurements for the multi-pass pass scheme (final sub-volume size of 48 voxels) using DaVis-masked images in trabecular bone and bone-biomaterial specimens varying the minimal fraction of valid pixel (mfvp) for the computation. Median values are calculated accounting for the total number of specimens for each type.

	mfvp (%)	CV/SV (%)	Cnorm	Displacement random errors (µm)			Strain uncertainties (µε)	
				x	y	z	MAER	SDER
Trabecular bone	50	55.8	0.41	0.42	0.50	0.34	1373	736
	40	74.8	0.42	0.41	0.48	0.29	1308	692
	30	86.8	0.42	0.43	0.44	0.27	1304	670
Bone-Biomaterial	50	83.0	0.56	0.21	0.27	0.16	438	337
	40	90.6	0.56	0.23	0.28	0.16	468	395
	30	93.9	0.56	0.25	0.28	0.16	491	384

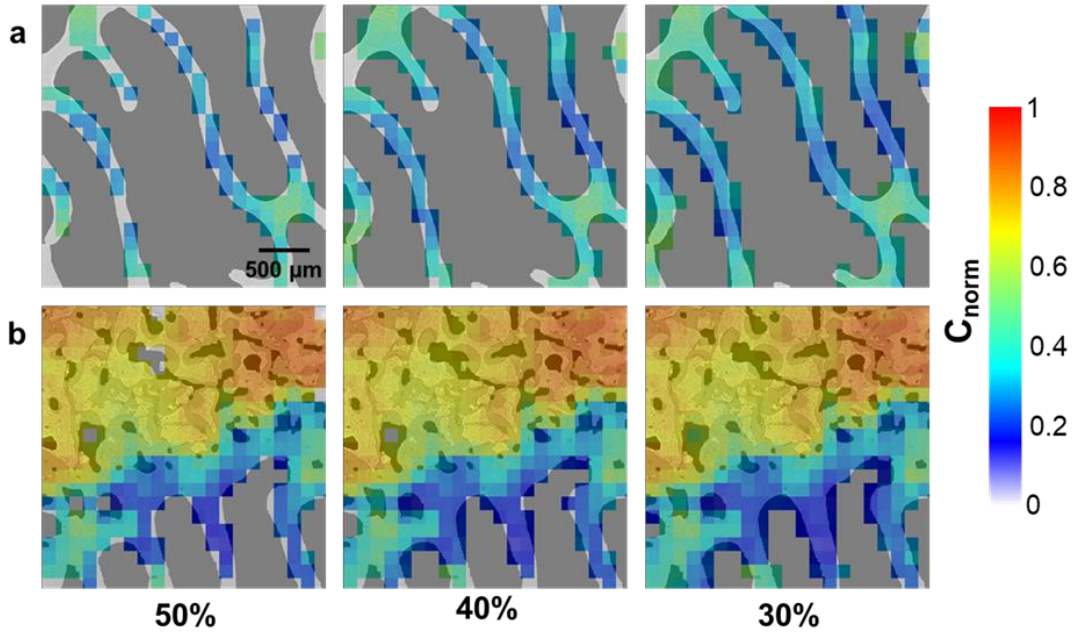

Figure 4. Normalised correlation coefficient (C_{norm}) overlaid to the 2D SR-microCT tomograms showing the influence of varying the minimal fraction of valid pixel (mfvp) from 30% to 50% on the correlated volume for trabecular bone (a) and bone-biomaterial (b) specimens. Areas with a high density of material (top area in b) presents a higher correlation compared to areas of trabecular bone (bottom area in b). Scale bar is valid for all images.

3.1.3.3. Influence of masking

The comparison of masking the images to remove possible artifacts (i.e. bubbles (Figure 2)) in the marrow/saline is presented in Table 3 for the multi-pass scheme with a final sub-volume of 48 voxels. The CV/TV was similar for the three approaches analysed, despite the data was filtered (only sub-volumes with correlation coefficient above 0.6 were considered)

for the raw and masked images. The use of DaVis-masked notably decreased the correlation coefficient compared to the use of raw or masked images (57% in trabecular bone and 38% in bone-biomaterial systems). At the same time, the measured uncertainties in terms of strain and displacements were largest. Both masked and raw images showed a high correlation coefficient, being higher in the masked case (10% improvement in trabecular bone and 13% in bone-biomaterial). Furthermore, displacement random errors, MAER and SDER were lowest using the masked images. When compared to the raw images, the use of masked images reduced the MAER and SDER of 11% and 40 %, respectively, in trabecular bone, and of 13% and 5% in bone-biomaterial. Contrarily, using DaVis-masked the MAER and SDER were enlarged of 82% and 74% in trabecular bone, and of 54% and 72% in bone-biomaterial systems.

Table 3. Correlated solid volume (CV/SV), normalised correlation coefficient (C_{norm}), random errors affecting the displacement components, MAER and SDER of the strain measurements for the multi-pass pass scheme (final sub-volume size of 48 voxels) using raw, masked and DaVis-masked images in trabecular bone and bone-biomaterial specimens. Median values are calculated accounting for the total number of specimens for each type.

	Image	**CV/SV (%)**	**C_{norm}**	**Displacement random errors (µm)**			**Strain uncertainties (µε)**	
				x	y	z	MAER	SDER
Trabecular bone	Raw	92.8	0.89	0.20	0.18	0.13	239	171
	Masked	86.8	0.98	0.15	0.22	0.14	212	101
	DaVis-masked	95.5	0.42	0.43	0.44	0.27	1304	670
Bone-Biomaterial	Raw	94.5	0.79	0.10	0.20	0.15	225	107
	Masked	90.9	0.91	0.08	0.22	0.12	195	102
	DaVis-masked	90.0	0.56	0.25	0.28	0.16	491	384

3.1.3.4. Random errors for the displacement

The random errors affecting each component of the displacement as a function of the sub-volume size are reported in Table 4. They ranged between 0.42 µm and 0.12 µm for the raw images, from 0.54 µm to 0.14 µm for the masked images, and from 0.61 µm to 0.13 µm for the DaVis-masked images in the trabecular bone specimens. Similarly, they ranged between 0.40 µm and 0.08 µm for the raw images, from 0.44 µm to 0.11 µm for the masked images, and from 0.49 µm to 0.08 µm for the DaVis-masked images in the bone-biomaterial systems. Random errors were typically larger for smaller sub-volume sizes. The multi-pass scheme (final sub-volume size of 48 voxels) notably improved the performance in both types of specimens for both raw and masked options, when compared to the results obtained with sub-volumes of 48 voxels, where values were comparable to the case of a sub-volume size

of 112 voxels. Multi-pass in DaVis-masked images did not improve the displacement random errors in all directions when compared to the single-pass scheme (48 voxels).

Table 4. Random errors of the displacements (μm) for the trabecular bone and bone-biomaterial specimens varying the sub-volume size (voxels) for the raw, masked and DaVis-masked images. Median values are calculated accounting for the total number of specimens for each type.

	Sub-volume	Raw			Masked			DaVis-masked		
		x	y	z	x	y	z	x	y	z
Trabecular bone	16	0.35	0.42	0.29	0.38	0.54	0.35	0.61	0.61	0.26
	32	0.32	0.35	0.26	0.35	0.52	0.36	0.54	0.55	0.26
	48	0.31	0.30	0.23	0.32	0.41	0.29	0.50	0.51	0.25
	64	0.26	0.31	0.20	0.28	0.36	0.26	0.53	0.52	0.36
	80	0.25	0.29	0.15	0.24	0.29	0.25	0.40	0.47	0.35
	96	0.24	0.32	0.13	0.23	0.30	0.22	0.40	0.35	0.30
	112	0.20	0.20	0.12	0.21	0.25	0.19	0.21	0.28	0.13
	48 (mp)	0.20	0.18	0.13	0.15	0.22	0.14	0.43	0.44	0.27
Bone-biomaterial	16	0.18	0.40	0.16	0.20	0.44	0.16	0.29	0.49	0.17
	32	0.13	0.33	0.15	0.15	0.38	0.15	0.29	0.43	0.15
	48	0.12	0.28	0.13	0.12	0.36	0.14	0.24	0.37	0.14
	64	0.11	0.24	0.13	0.10	0.32	0.13	0.15	0.30	0.12
	80	0.09	0.23	0.12	0.09	0.29	0.11	0.11	0.23	0.10
	96	0.08	0.21	0.12	0.08	0.23	0.12	0.10	0.20	0.09
	112	0.08	0.19	0.13	0.08	0.22	0.12	0.09	0.18	0.08
	48 (mp)	0.10	0.20	0.13	0.08	0.22	0.12	0.25	0.28	0.16

3.1.3.5. MAER and SDER

To facilitate comparison with published literature, the scalar values MAER and SDER [25] were computed in order to provide a single strain value associated to each specimen. As expected from the results reported in previous studies [22], the measured DVC uncertainties had decreasing tends with respect to the sub-volume size for both types of specimens

(Figure 5). In particular, the median values for MAER and SDER for the bone-biomaterial samples ranged between 671 με to 167 με and 766 με to 42 με for the raw images, between 695 με to 154 με and 679 με to 44 με for the masked images, and between 1525 με to 208 με and 1354 με to 71 με for the DaVis-masked images, respectively; using sub-volumes sizes ranging from 16 to 112 voxels. The errors for bone-biomaterial were lower than those obtained for the trabecular bone specimens. The median values of MAER and SDER for the bone-biomaterial specimens ranged between 671 με to 167 με and 766 με to 42 με for the raw images, between 695 με to 154 με and 679 με to 44 με for the masked images, and between 1525 με to 208 με and 1354 με to 71 με for the DaVis-masked images, respectively; for the same sub-volumes. As for the displacement random errors, the use of DaVis-masked considerably enlarged the measured strain uncertainties. The multi-pass scheme (final sub-volume size of 48 voxels) notably improved the performance in both types of specimens when compared to the results obtained with sub-volumes of 48 voxels for both MAER and SDER.

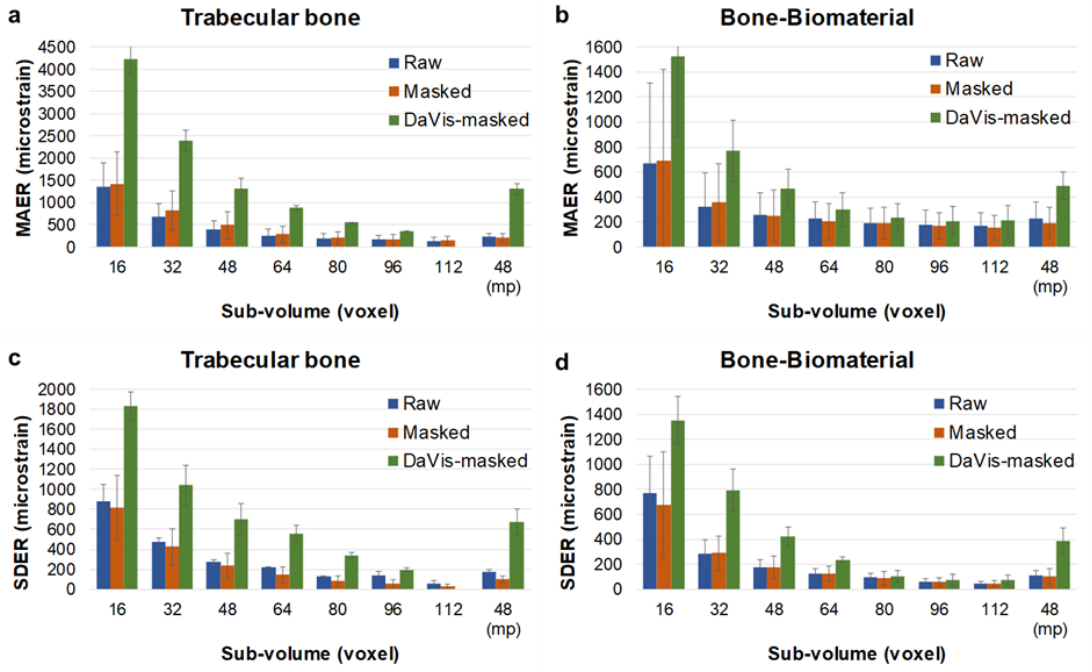

Figure 5. MAER (top) and SDER (bottom) for and trabecular bone (left) and bone-biomaterial systems (right), for raw, masked and DaVis-masked images (blue, orange and green bars, respectively) as a function of the sub-volume size. Results for the multi-pass (mp) scheme are also shown. Bars represent the median value, while error bars represent the standard deviation between the number of specimens of each type.

3.1.3.6. Random errors for each strain component

Increasing the sub-volume size reduced the random error of each strain component for both types of specimens and the different mask-based options used. As found for the displacement random errors, MAER and SDER, the bone-biomaterial systems were less affected when compared to the trabecular bone specimens. Consistently with previous results, the use of DaVis-masked images produced higher random errors for all strain

components and they are not reported in this section. Furthermore, the use of masked images and multi-pass scheme reduced the uncertainties for both types of specimens when compared to raw images and single-pass schemes (Figure 6). For a final sub-volume of 48 voxels using a single-pass scheme, bone-biomaterials systems were associated to median random errors of the strain components of 194 (ε_{zz}) – 483 (ε_{yz}) με, and 161 (ε_{xz}) - 544 (ε_{yz}) με for raw and masked images, respectively. The use of a multi-pass scheme reduced the random errors to 171 (ε_{zz}) – 304 (ε_{yz}) με, and 112 (ε_{xz}) – 338 ($\varepsilon\varepsilon_{yz}$) με for raw and masked images, respectively. Similarly, for the trabecular bone specimens the random errors were found to be between 485 (ε_{zz}) – 731 (ε_{yy}) με for the raw images, and 562 (ε_{xz}) – 839 (ε_{yy}) με for the masked images when using a single-pass scheme and between 261 (ε_{zz}) – 436 (ε_{xx}) με for raw images, and 205 (ε_{xz}) – 426 (ε_{yy}) με for masked images in the multi-pass scheme.

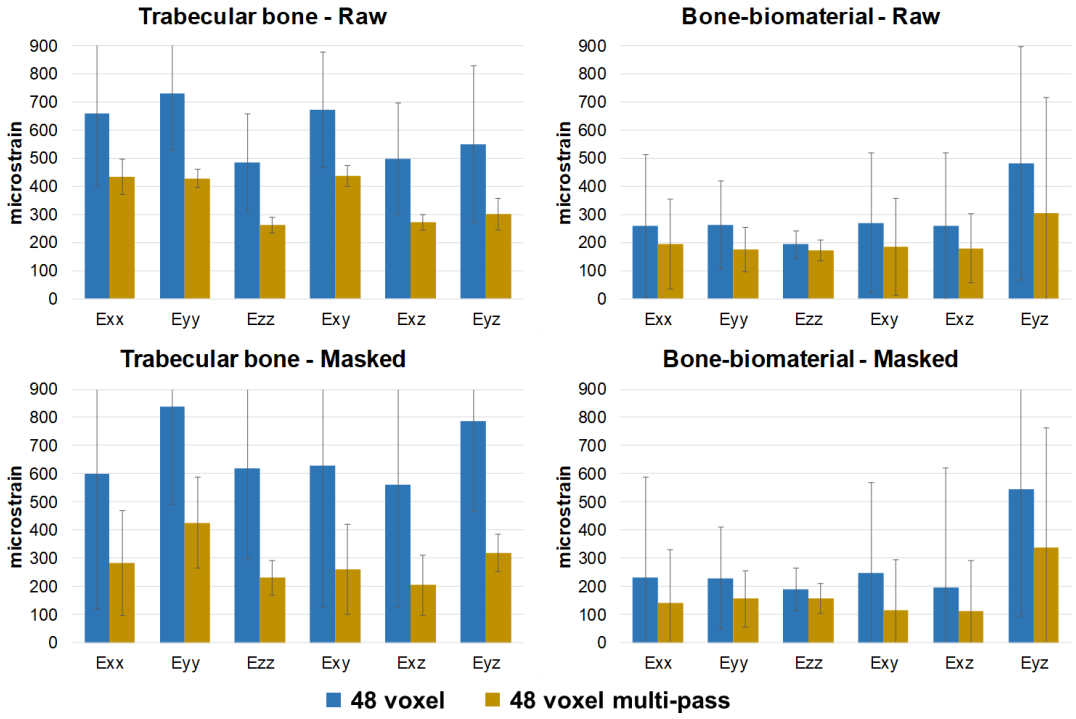

Figure 6. Random errors of each strain component for trabecular bone (left) and bone-biomaterial systems (right), computed using raw (top) and masked (bottom) images for a final sub-volume size of 48 voxels using a single-pass (blue) and a multi-pass (yellow) scheme. Bars represent the median value, while error bars represent the standard deviation accounting for the total number of specimens of each type.

3.1.3.7. Spatial distribution of the errors

Generally, larger errors were found for the trabecular bone compared to the bone-biomaterial specimens. In particular, the distribution of the apparent normal strain in the z-direction (chosen as a representative strain component for the obtained results) seemed to be more homogeneous in the bone-biomaterial systems when compared to the trabecular bone (Figure 7). As the DVC analysis is based on 'zero-strain' repeated scans, the strain distribution in Figure 7 depicted the error distribution for the ε_{zz} strain component. In areas

presenting bone-biomaterial, a reasonably uniform distribution of the strain was obtained. Conversely, for the trabecular bone sample and areas of trabecular bone in the bone-biomaterial, larger strain errors and a more heterogeneous strain distribution was observed.

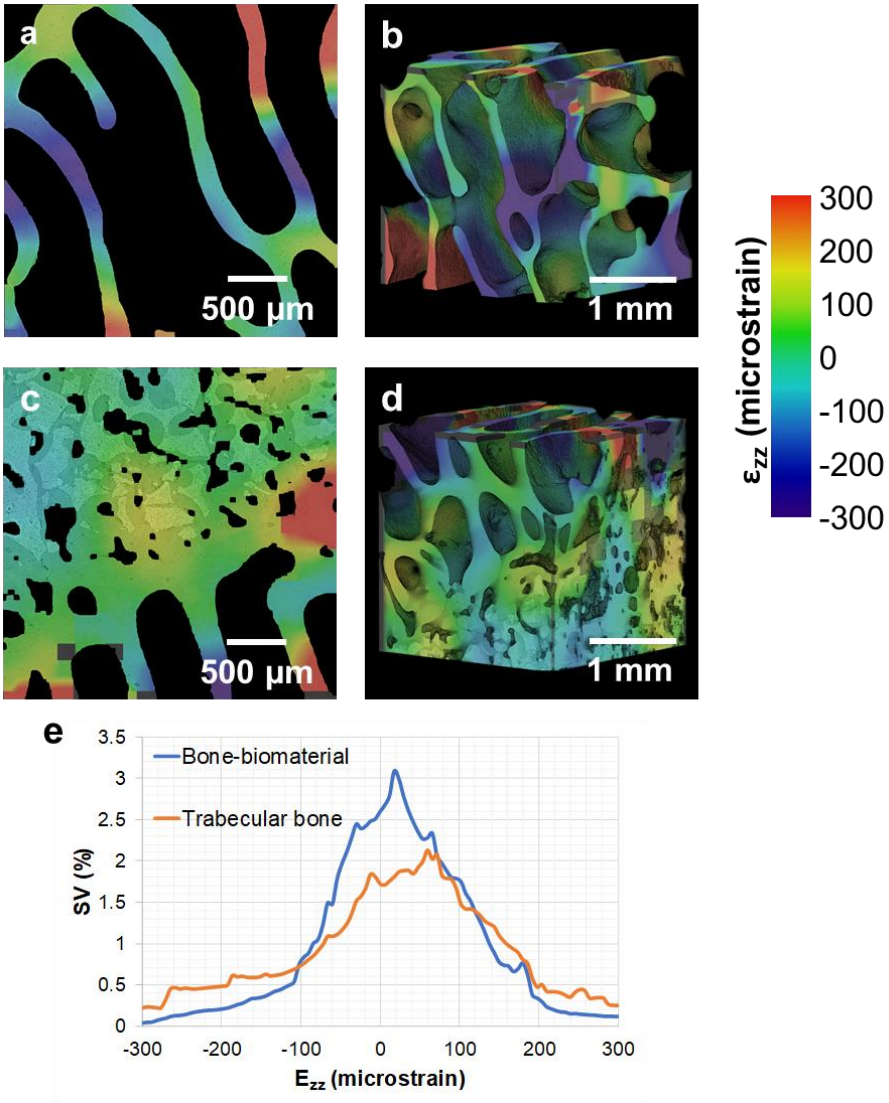

Figure 7. Distribution of the z-direction strain (ε_{zz}) component for a cross-section of a trabecular bone (a) and a bone-biomaterial specimen(c) and for their VOIs (trabecular bone (b) and bone-biomaterial (d)), computed using a multi-pass scheme (48 voxel final sub-volume size) on the masked images. As the DVC was applied to 'zero-strain' repeated scans, the reported strains represent the measured DVC uncertainties. Histograms of εzz strain distribution (e) showed lower strain values in the bone-biomaterial compared to trabecular bone.

3.1.4. Discussion

The goal of this study was to evaluate the influence of imaging post-processing and DVC settings on the displacement and strain error distribution within trabecular bone and bone-biomaterial systems, using a SR-microCT based local DVC approach. More specifically, this work aimed at optimising those settings in order to provide accurate 3D strain measurements, at tissue level for further micromechanical characterisation under applied load. A detailed analysis of the distinct settings was covered, providing guidelines to DVC

users when performing experiments on similar materials (i.e. cellular/porous structures) with images acquired at comparable resolution and SNR (signal-to-noise ratio) in any SR beamline and/or lab-based system.

The application of DVC based on high-resolution SR-microCT images of bone remains partially unexplored. In fact, to the author's knowledge only three publications reported the used of DVC based on SR-microCT images for 3D strain measurement on bone at tissue level. Christen et al. [19] focused on crack propagation in murine femora, but the uncertainties of the computed strain were only assessed in virtually displaced images and not in repeated scans. Therefore, the real error induced by image noise was not taken into account, possibly leading to an underestimation of the errors [23]. More recently, Palanca at al. [26] showed that reliable strain measurements could be obtained at tissue-level using a global DVC approach for trabecular bone, cortical bone and murine tibia, but the performance of a local DVC approach and the study of bone-biomaterial interfaces was not explored. A comparison of two DVC algorithms (global and local approaches) in different bone typologies at different dimensional scales based on laboratory microCT and SR-microCT was conducted by Dall'Ara et al. [22], including the precision of a local approach of bone-biomaterial systems also investigated in this study. However, only the precision of the DVC algorithm in terms of strain (SDER) and displacements (displacement random errors) was reported for the mask images, but the accuracy (MAER) and the random errors of each strain component were not evaluated. Furthermore, the uncertainties were evaluated on the entire 3D images, producing higher errors when compared to an evaluation exclusively within the hard phase (i.e. bone/biomaterial). In fact, the present study showed (Figure 5) that when computing the strain values only in the hard phase, the SDER for bone-biomaterial systems was found to be in the region of 100 με, whereas Dall'Ara et al. [22] reported values in the order of 150 με, for the same multi-pass scheme with a final sub-volume of 48 voxels, thus resulting in a 33% decrease in the SDER after the optimisation herein presented. Moreover, a comparison of the influence of different imaging post-processes and DVC settings on the resulting measurement uncertainties was not detailed.

Despite the potential of using high-quality tomograms acquired with SR-microCT on DVC applications of bone and bone-materials, concerns are still raising on the damage induced by SR X-ray radiation [49]. In fact, when prolonged exposures times to SR X-ray radiation are required, the microstructural integrity of the bone tissue is compromised (Figure 1), and microcracks appear clearly visible in the tissue after continuous irradiation. Therefore, this study used low exposures times (~2 min scanning time) and kept the specimens immersed in saline solution during image acquisition, in order to preserve the mechanical integrity of the analysed specimens [31]. These two factors negatively contributed to the quality of the acquired tomograms (Figure 2), and further optimisation on the imaging and DVC settings was needed.

In order to understand the effect of filtering the images prior to DVC computation, two different filters were applied and compared to the DVC results obtained with the raw noisy tomograms (Table 1). For instance, this is the first time that the performance of DVC is compared for the same images with different denoised methods, even though the use of filters is common practice in image post-processing prior to DVC computation [26]. It was shown that the use of advanced filters (i.e. NLM filter), not only improved the correlation coefficient but also reduced the uncertainties for both displacements and strains in both types of specimens, suggesting that image denoising should be carefully considered and evaluated when low-quality tomograms are acquired. Furthermore, the use of robust filters is an essential step before image segmentation (Figure 3) prior to masking.

In this study an iterative approach for image segmentation was adopted, allowing the discrimination of mineralised tissue and biomaterial from soft/watery material. Despite segmenting images of bone acquired via microCT is commonly performed using global thresholds set manually, those introduce inter-observer variation [50]. Local adaptive algorithms [51] can successfully segment images with strong edges (high contrast) and relatively uniform signal intensity. However, low-quality tomograms like those in the current study required a different segmentation approach. The iterative approach used in this study showed good visual agreement to the grey-scale image (Figure 3). However, the quality of the segmentation was only checked visually, resulting on an operator-dependent approach; thus, introducing inter-observer variation. Although stronger iterative thresholding algorithms [52] have proven to provide accurate results in terms of bone volume fraction, specific surface, and surface curvature [53], it was not within the scope of this paper to evaluate the morphology of the analysed specimen, but only the performance of DVC when artifacts presented in the non-bone may be included. Therefore, a validation of the segmentation procedure herein applied was not conducted, and stronger methods were not tested.

The effect of the masking operation on the trabecular bone and bone-biomaterial composites was evaluated for the first time on a local DVC approach. Previously results on a global DVC approach based on masked images showed lower error compared to the ones obtained by raw images [26], in agreement with the results of this study (Table 2). The exclusion of soft phases, for which noise and artifacts (i.e. bubbles in saline solution) were probably dominant, was beneficial for DVC registration when the ‘background’ was treated as ‘zero’ intensity, enhancing the correlation coefficient and lowering the errors. However, the use of a threshold-based algorithmic mask (DaVis-masked), in which the ‘background’ region is excluded from DVC computation, provided higher errors and lower correlation values. That approach to masking may work for masking away regions outside the analysed specimen (i.e. to mask away regions of tooth structure in bone-periodontal ligament and tooth fibrous joint [54]). However, when the masking is performed at tissue level in trabecular structure, DVC algorithm is not able to provide a good correlation if the edges between trabeculae and marrow (high intensity gradient) are excluded from the computation and only gradients within

the trabecula are considered. In this sense, even a variation on the mfvp (Table 2) was not able to substantially improve the results, as those parameters affect only to the number of voxels to be contained within a sub-volume for being included in the computation (Figure 4). Despite that, the computed SDER using DaVis-masked was found to be approximately 400 με for the bone-biomaterial systems and 650 με for trabecular bone using a multi-pass approach with a final sub-volume of 48 voxels. Those values are still tolerable for investigating the deformation of both types of specimens at tissue level. In fact, yielding of trabecular bone occurs at 10000 με in compression [55], one order of magnitude higher than the computed uncertainties. Considering that the use of DaVis-masked images is the only way that allows displacement/strain field measurement only in the tissue using DaVis software, further development should be conducted to improve its performance. In fact, the application of DaVis-masked to high resolution images of trabecular bone at higher SNR may improve the performance of the algorithm, as more features would be seen within the trabeculae.

In line with previous studies [22,26], the larger the sub-volume size, the lower the measurement uncertainties for both trabecular bone and bone-biomaterials (Figure 5). Furthermore, it was confirmed [11] that the multi-pass approach available in DaVis provided lower errors when compared to the same final sub-volume using a single-pass (Figure 6), due to the optimised correlation ability implemented in DaVis. For a sub-volume size of 48 voxels or larger, equivalent to approximately 125 μm, the SDER was found close to 100 με for both trabecular bone and bone-biomaterial composites, whereas random error for each strain component was close to or below 300 με for the bone-biomaterial systems and close to or below 400 με for trabecular bone. These values represent 20% of the physiological strain range (1000-2000 με [56]) at tissue level [57], and 4% of the yielding strain value (10000 με [55]); thus, suggesting that depending on the deformation mechanism object of this study, a different compromise between spatial resolution and strain uncertainties may be accepted. Palanca et al. [26] reported a SDER of 120 με for a similar sub-volume size (120 μm) in masked trabecular bone images; however, the random errors for the strain components were below 350 με. The differences between both studies probably lie on the different effective pixel size (larger in this study) and the SNR, lower in this work due to the low exposure times used to minimise the irradiation-induced damage in the tissue. Furthermore, the difference in DVC approach (local vs global) may influence the measurement uncertainties based on the same datasets. In this sense, a comparison between global and local DVC approaches based on high-resolution SR-microCT images still remains unexplored. However, the measurement uncertainties were lower compared to local DVC approach based on laboratory microCT systems [22]. Better results were found for the bone-biomaterial systems compared to the trabecular bone, likely due to the much higher number of features present in such composites. Similar results were found in Tozzi et al. [24], in which the presence of bone cement in vertebral bodies strongly modified the material texture, and therefore, positively influence the DVC analysis. In fact, the analysis of the

spatial distribution of the errors (Figure 7) confirmed that hypothesis: the areas with higher errors in the bone-biomaterial were correlated to native trabecular bone regions.

The current study has some limitations. Firstly, only two trabecular bone controls and four bone-biomaterial systems were analysed; thus, minimal statistical information can be extracted. The size of the bone defects and the short time allocated in the beamline made not possible to enlarge the sample size. Additionally, the strain errors were only calculated in a 'zero-strain' condition for repeated scans. Even though this approach allows to account for the intrinsic image noise, this analysis should be expanded in order to evaluate the error within strained specimens. Particularly, Dall'Ara et al. [22] suggested to overcome this limitation by evaluating the precision of the DVC approach on repeated scans of the structure under load. Eventually, they found that the precision was similar for both loaded and unloaded structures, but the accuracy could not be evaluated as the displacement field is unknown. In addition, Palanca et al. [26] proposed to perform the analysis in synthetically deformed images after imposing an affine transformation on the unloaded repeated scans; thus, not accounting for a realistic heterogeneous strain field. Future work must be done to account for more realistic loading scenarios.

3.1.5. Conclusion

This study demonstrated the suitability of a local DVC approach based on SR-microCT images to investigate the micromechanics of trabecular bone and bone-biomaterial systems at tissue level. This was achieved after an optimisation of image post-processing and DVC settings. Image quality had to be reduced by decreasing the exposure time to SR X-ray radiation to minimise irradiation-induce tissue damage. The use of advanced 3D filters on the acquired dataset enhanced DVC computation and provided a better segmentation of bone and biomaterial. The computation of displacement and strain values only in the mineralised tissue and biomaterial allowed for the exclusion of artifacts, resulting in lower errors. This approach has proven to be valid to evaluate full-field strain in bone and bone-biomaterial composites under load at the tissue level (in the region of 150 µm spatial resolution), with a standard deviation of the errors of approximately 100 µε.

Author contributions

Marta Peña Fernández: Study design, data curation, formal analysis, data interpretation; Asa H. Barber: Supervision; Gordon W. Blunn: Supervision; Gianluca Tozzi: Study design, data interpretation, supervision.

Acknowledgments

The authors would like to thank Diamond Light Source for time at the Diamond-Manchester Imaging Branchline I13-2 and I13 Data Beamline [58] (proposal number MT14080), and the Zeiss Global Centre (University of Portsmouth) for image post-processing. We further acknowledge Dr. David Hollis, Dr. Dirk Michaelis and Dr. Manuel Grewer (LaVision Ltd) for

assistance with DaVis software and Dr. Andrew Bodey, Dr. Krazimir Wanelik and Rachna Parwani for help with the acquisition of the images at Diamond Light Source. The project was partially funded by Innovate UK Innovation Vouchers and LaVision Ltd UK.

References

[1] W. Wang, K.W.K. Yeung, Bone grafts and biomaterials substitutes for bone defect repair: A review, Bioact. Mater. 2 (2017) 224–247. doi:https://doi.org/10.1016/j.bioactmat.2017.05.007.

[2] G. Tozzi, A. De Mori, A. Oliveira, M. Roldo, Composite hydrogels for bone regeneration, Materials (Basel). 9 (2016) 1–24. doi:10.3390/ma9040267.

[3] M.M. Stevens, Biomaterials for bone tissue engineering, Mater. Today. 11 (2008) 18–25. doi:https://doi.org/10.1016/S1369-7021(08)70086-5.

[4] D. Sriranganathan, N. Kanwal, K.A. Hing, R.G. Hill, Strontium substituted bioactive glasses for tissue engineered scaffolds : the importance of octacalcium phosphate, J. Mater. Sci. Mater. Med. 27 (2016) 1–10. doi:10.1007/s10856-015-5653-6.

[5] S. V Dorozhkin, Calcium Orthophosphate-Based Bioceramics, Materials (Basel). 6 (2013) 3840–3942. doi:10.3390/ma6093840.

[6] E. Garcia-Gareta, M.J. Coathup, G.W. Blunn, E. García-Gareta, M.J. Coathup, G.W. Blunn, Osteoinduction of bone grafting materials for bone repair and regeneration, Bone. 81 (2015) 112–121. doi:10.1016/j.bone.2015.07.007.

[7] G. Tozzi, Q.H. Zhang, J. Tong, 3D real-time micromechanical compressive behaviour of bone-cement interface: Experimental and finite element studies, J. Biomech. 45 (2012) 356–363. doi:10.1016/j.jbiomech.2011.10.011.

[8] G. Tozzi, Q.H. Zhang, J. Tong, Microdamage assessment of bone-cement interfaces under monotonic and cyclic compression, J. Biomech. 47 (2014) 3466–3474. doi:10.1016/j.jbiomech.2014.09.012.

[9] V. Danesi, G. Tozzi, L. Cristofolini, Application of digital volume correlation to study the efficacy of prophylactic vertebral augmentation, Clin. Biomech. 39 (2016) 14–24. doi:10.1016/j.clinbiomech.2016.07.010.

[10] G. Tozzi, V. Danesi, M. Palanca, L. Cristofolini, Elastic Full-Field Strain Analysis and Microdamage Progression in the Vertebral Body from Digital Volume Correlation, Strain. 52 (2016) 446–455. doi:10.1111/str.12202.

[11] M. Palanca, G. Tozzi, L. Cristofolini, M. Viceconti, E. Dall'Ara, 3D Local Measurements of Bone Strain and Displacement: Comparison of Three Digital Volume Correlation Approaches., J. Biomech. Eng. 137 (2015) 1–14. doi:10.1115/1.4030174.

[12] L. Grassi, H. Isaksson, Extracting accurate strain measurements in bone mechanics: A critical review of current methods, J. Mech. Behav. Biomed. Mater. 50 (2015) 43–54. doi:10.1016/j.jmbbm.2015.06.006.

[13] J.Y. Buffiere, E. Maire, J. Adrien, J.P. Masse, E. Boller, *In situ* experiments with X ray tomography: An attractive tool for experimental mechanics, Proc. Soc. Exp. Mech. Inc. 67 (2010) 289–305. doi:10.1007/s11340-010-9333-7.

[14] A. Nazarian, R. Müller, Time-lapsed microstructural imaging of bone failure behavior, J. Biomech. 37 (2004) 55–65. doi:10.1016/S0021-9290(03)00254-9.

[15] B.K. Bay, T.S. Smith, D.P. Fyhrie, M. Saad, Digital volume correlation: Three-dimensional strain mapping using X-ray tomography, Exp. Mech. 39 (1999) 217–226. doi:10.1007/BF02323555.

[16] B.C. Roberts, E. Perilli, K.J. Reynolds, Application of the digital volume correlation technique for the measurement of displacement and strain fields in bone: A literature review, J. Biomech. 47 (2014) 923–934. doi:10.1016/j.jbiomech.2014.01.001.

[17] L. Liu, E.F. Morgan, Accuracy and precision of digital volume correlation in quantifying displacements and strains in trabecular bone, J. Biomech. 40 (2007) 3516–3520. doi:10.1016/j.jbiomech.2007.04.019.

[18] F. Gillard, R. Boardman, M. Mavrogordato, D. Hollis, I. Sinclair, F. Pierron, M. Browne, The application of digital volume correlation (DVC) to study the microstructural behaviour of trabecular bone during compression, J. Mech. Behav. Biomed. Mater. 29 (2014) 480–499. doi:10.1016/j.jmbbm.2013.09.014.

[19] D. Christen, A. Levchuk, S. Schori, P. Schneider, S.K. Boyd, R. Müller, Deformable image registration and 3D strain mapping for the quantitative assessment of cortical bone microdamage, J. Mech. Behav. Biomed. Mater. 8 (2012) 184–193. doi:10.1016/j.jmbbm.2011.12.009.

[20] A.I. Hussein, P.E. Barbone, E.F. Morgan, Digital volume correlation for study of the mechanics of whole bones, Procedia IUTAM. 4 (2012) 116–125. doi:10.1016/j.piutam.2012.05.013.

[21] K. Madi, G. Tozzi, Q.H. Zhang, J. Tong, A. Cossey, A. Au, D. Hollis, F. Hild, Computation of full-field displacements in a scaffold implant using digital volume correlation and finite element analysis, Med. Eng. Phys. 35 (2013) 1298–1312. doi:10.1016/j.medengphy.2013.02.001.

[22] E. Dall'Ara, M. Peña-Fernández, M. Palanca, M. Giorgi, L. Cristofolini, G. Tozzi, Precision of DVC approaches for strain analysis in bone imaged with μCT at different dimensional levels, Front. Mater. 4:31 (2017). doi:10.3389/fmats.2017.00031.

[23] E. Dall'Ara, D. Barber, M. Viceconti, About the inevitable compromise between spatial resolution and accuracy of strain measurement for bone tissue: A 3D zero-strain study, J. Biomech. 47 (2014) 2956–2963. doi:10.1016/j.jbiomech.2014.07.019.

[24] G. Tozzi, E. Dall, M. Palanca, M. Curto, F. Innocente, L. Cristofolini, Strain uncertainties from two digital volume correlation approaches in prophylactically augmented vertebrae : Local analysis on bone and cement- bone microstructures, J. Mech. Behav. Biomed. Mater. 67 (2017) 117–126. doi:10.1016/j.jmbbm.2016.12.006.

[25] M. Palanca, L. Cristofolini, E. Dall'Ara, M. Curto, F. Innocente, V. Danesi, G. Tozzi, Digital volume correlation can be used to estimate local strains in natural and augmented vertebrae: an organ-level study, J. Biomech. 49 (2016) 3882–3890. doi:10.1016/j.jbiomech.2016.10.018.

[26] M. Palanca, A.J. Bodey, M. Giorgi, M. Viceconti, D. Lacroix, L. Cristofolini, E. Dall'Ara, Local displacement and strain uncertainties in different bone types by digital volume correlation of synchrotron microtomograms, J. Biomech. c (2017). doi:10.1016/j.jbiomech.2017.04.007.

[27] M.J. Coathup, T.C. Edwards, S. Samizadeh, W.J. Lo, G.W. Blunn, The effect of an alginate carrier on bone formation in a hydroxyapatite scaffold, J. Biomed. Mater. Res. - Part B Appl. Biomater. 104 (2016) 1328–1335. doi:10.1002/jbm.b.33395.

[28] T.M. Keaveny, R.E. Borchers, L.J. Gibson, W.C. Hayes, Theoretical analysis of the experimental artifact in trabecular bone compressive modulus, J. Biomech. 25 (1993) 599–607.

[29] H. Toda, E. Maire, S. Yamauchi, H. Tsuruta, T. Hiramatsu, M. Kobayashi, *In situ* observation of ductile fracture using X-ray tomography technique, Acta Mater. 59 (2011) 1995–2008. doi:10.1016/j.actamat.2010.11.065.

[30] R.C. Atwood, A.J. Bodey, S.W.T. Price, M. Basham, M. Drakopoulos, A high-throughput system for high-quality tomographic reconstruction of large datasets at Diamond Light Source, Philos. Trans. R. Soc. A Math. Phys. Eng. Sci. 373 (2015). doi:10.1098/rsta.2014.0398.

[31] M. Peña Fernández, S. Cipiccia, A.J. Bodey, R. Parwani, E. Dall'Ara, G. Blunn, M. Pani, A.H. Barber, G. Tozzi, Effect of SR-microCT exposure time on the mechanical integrity of trabecular bone using *in situ* mechanical testing and digital volume correlation, J. Mech. Behav. Biomed. Mater. 88 (2018) 109–119. doi:https://doi.org/10.1016/j.jmbbm.2018.08.012.

[32] M. Basham, J. Filik, M.T. Wharmby, P.C.Y. Chang, B. El Kassaby, M. Gerring, J. Aishima, K. Levik, B.C.A. Pulford, I. Sikharulidze, D. Sneddon, M. Webber, S.S. Dhesi, F. Maccherozzi, O. Svensson, S. Brockhauser, G. Náray, A.W. Ashton, Data Analysis WorkbeNch (DAWN), J. Synchrotron Radiat. 22 (2015) 853–858. doi:10.1107/S1600577515002283.

[33] V. Titarenko;, R. Bradley;, C. Martin;, P.J. Withers;, S. Titarenko;, Regularization methods for inverse problems in x-ray tomography, Proc. SPIE 7804. (2010). doi:doi: 10.1117/12.860260.

[34] J. Schindelin, I. Arganda-Carreras, E. Frise, V. Kaynig, M. Longair, T. Pietzsch, S. Preibisch, C. Rueden, S. Saalfeld, B. Schmid, J.-Y. Tinevez, D.J. White, V. Hartenstein, K. Eliceiri, P. Tomancak, A. Cardona, Fiji: an open-source platform for biological-image analysis, Nat Meth. 9 (2012) 676–682. doi:10.1038/nmeth.2019.

[35] B. Schmid, Computational tools for the segmentation and registration of confocal brain images of Drosophila melanogaster, 2010. http://opus.bibliothek.uni-wuerzburg.de/frontdoor.php?source_opus=5149&la=de.

[36] E.H.W. Meijering, W.J. Niessen, M.A. Viergever, Quantitative Evaluation of Convolution-Based Methods for Medical Image Interpolation, Med. Image Anal. 5 (2001) 111–126. doi:doi.org/10.1016/S1361-8415(00)00040-2.

[37] A. Buades, B. Coll, J.-M. Morel, Non-Local Means Denoising, Image Process. Line. 1 (2011) 490–530. doi:10.5201/ipol.2011.bcm_nlm.

[38] J. Darbon, A. Cunha, T.F. Chan, S. Osher, G.J. Jensen, Fast nonlocal filtering applied to electron cryomicroscopy, 2008 5th IEEE Int. Symp. Biomed. Imaging from Nano to Macro, Proceedings, ISBI. IEEE. (2008) 1331–1334. doi:10.1109/ISBI.2008.4541250.

[39] J. Immerkær, Fast noise variance estimation, Comput. Vis. Image Underst. 64 (1996) 300–302. doi:10.1006/cviu.1996.0060.

[40] A. Buades, B. Coll, J. Morel, J.M. A, A review of image denoising algorithms , with a new one To cite this version :, 4 (2010) 490–530.

[41] L.-K. Huang, M.-J.J. Wang, Image thresholding by minimizing the measures of fuzziness, Pattern Recognit. 28 (1955) 41–51.

[42] M. Doube, M.M. Klosowski, I. Arganda-Carreras, F.P. Cordelières, R.P. Dougherty, J.S. Jackson, B. Schmid, J.R. Hutchinson, S.J. Shefelbine, BoneJ: Free and extensible bone image analysis in ImageJ, Bone. 47 (2010) 1076–1079. doi:10.1016/j.bone.2010.08.023.

[43] A. Odgaard, H.J.G. Gundersen, Quantification of connectivity in cancellous bone, with special emphasis on 3-D reconstructions, Bone. 14 (1993) 173–182. doi:https://doi.org/10.1016/8756-3282(93)90245-6.

[44] A. Cheminet, B. Leclaire, F. Champagnat, A. Plyer, R. Yegavian, G. Le Besnerais, Accuracy assessment of a Lucas-Kanade based correlation method for 3D PIV, 17th Int. Symp. Appl. Laser Tech. to Fluid Mech. (2014) 7–10.

[45] F.F.J. Schrijer, F. Scarano, Effect of predictor-corrector filtering on the stability and spatial resolution of iterative PIV interrogation, Exp. Fluids. 45 (2008) 927–941. doi:10.1007/s00348-008-0511-7.

[46] F. Scarano, Tomographic PIV: Principles and practice, Meas. Sci. Technol. 24 (2013). doi:10.1088/0957-0233/24/1/012001.

[47] A. Germaneau, P. Doumalin, J.C. Dupré, 3D strain field measurement by correlation of volume images using scattered light: Recording of images and choice of marks, Strain. 43 (2007) 207–218. doi:10.1111/j.1475-1305.2007.00340.x.

[48] A. Germaneau, P. Doumalin, J.C. Dupré, Full 3D Measurement of Strain Field by Scattered Light for Analysis of Structures, Exp. Mech. 47 (2007) 523–532. doi:10.1007/s11340-006-9029-1.

[49] H.D. Barth, M.E. Launey, A.A. MacDowell, J.W. Ager, R.O. Ritchie, On the effect of X-ray irradiation on the deformation and fracture behavior of human cortical bone, Bone. 46 (2010) 1475–1485. doi:10.1016/j.bone.2010.02.025.

[50] J.H. Waarsing, J.S. Day, H. Weinans, An improved segmentation method for *in vivo* µCT imaging, J. Bone Miner. Res. 19 (2004) 1640–1650. doi:10.1359/JBMR.040705.

[51] J. Kaipala, M. Bordallo, S. Saarakkala, Automatic Segmentation of Bone Tissue from Computed Tomography Using a Volumetric Local Binary Patterns Based Method, Scand. Conf. Image Anal. (2017) 221–232. doi:10.1007/978-3-319-59129-2.

[52] H.S. Wu, J. Barba, J. Gil, Iterative thresholding for segmentation of cells from noisy images, J. Microsc. 197 (2000) 296–304. doi:10.1046/j.1365-2818.2000.00653.x.

[53] C.R. Slyfield, K.E. Niemeyer, E.V. Tkachenko, R.E. Tomlinson, G.G. Steyer, C.G. Patthanacharoenphon, G.J. Kazakia, D.L. Wilson, C.J. Hernandez, Three-Dimensional Surface Texture Visualization of Bone Tissue Through Epifluorescence-Based Serial Block Face Imaging, J. Microsc. 236 (2009) 52–59. doi:10.1037/a0015862.Trajectories.

[54] A. Jang, R. Prevost, S.P. Ho, Strain mapping and correlative microscopy of the alveolar bone in a bone-periodontal ligament-tooth fibrous joint, Proc. Inst. Mech. Eng. Part H J. Eng. Med. 230 (2016) 847–857. doi:10.1177/0954411916655183.

[55] H.H. Bayraktar, E.F. Morgan, G.L. Niebur, G.E. Morris, E.K. Wong, T.M. Keaveny, Comparison of the elastic and yield properties of human femoral trabecular and cortical bone tissue, J. Biomech. 37 (2004) 27–35. doi:10.1016/S0021-9290(03)00257-4.

[56] P.F. Yang, G.P. Brüggemann, J. Rittweger, What do we currently know from *in vivo* bone strain measurements in humans?, J. Musculoskelet. Neuronal Interact. 11 (2011) 8–20.

[57] P. Fratzl, H.S. Gupta, E.P. Paschalis, P. Roschger, Structure and mechanical quality of the collagen–mineral nano-composite in bone, J. Mater. Chem. 14 (2004) 2115–2123. doi:10.1039/B402005G.

[58] A.J. Bodey, C. Rau, Launch of the I13-2 data beamline at the Diamond Light Source synchrotron, J. Phys. Conf. Ser. 849 (2017). doi:10.1088/1742-6596/849/1/012038.

Chapter 4. Bone preservation strategies in SR-microCT experiments

4.1. Effect of SR-microCT radiation on the mechanical integrity of trabecular bone

Marta Peña Fernández[1], Silvia Cipiccia[2], Enrico Dall'Ara[3], Andrew J Bodey[2], Rachna Parwani[1], Martino Pani[1], Gordon W Blunn[4], Asa H Barber[1,5], Gianluca Tozzi[1]

[1] *Zeiss Global Centre, School of Engineering, University of Portsmouth, Portsmouth, UK.*

[2] *Diamond Light Source, Oxfordshire, OX11 0QX, UK.*

[3] *Department of Oncology and Metabolism and INSIGNEO institute for in silico medicine, University of Sheffield, Sheffield, UK.*

[4] *School of Pharmacy and Biomedical Sciences, University of Portsmouth, Portsmouth, UK.*

[5] *School of Engineering, London South Bank University, London, UK.*

Published in:

Journal of Mechanical Behavior of Biomedical Materials, 2018, 88, 109-119.

doi: 10.1016/j.jmbbm.2018.08.012

as *"Effect of SR-microCT radiation on the mechanical integrity of trabecular bone using in situ mechanical testing and digital volume correlation".*

Abstract

The use of synchrotron radiation micro-computed tomography (SR-microCT) is becoming increasingly popular for studying the relationship between microstructure and bone mechanics subjected to *in situ* mechanical testing. However, it is well known that the effect of SR X-ray radiation can considerably alter the mechanical properties of bone tissue. Digital volume correlation (DVC) has been extensively used to compute full-field strain distributions in bone specimens subjected to step-wise mechanical loading, but tissue damage from sequential SR-microCT scans has not been previously addressed. Therefore, the aim of this study is to examine the influence of SR irradiation-induced microdamage on the apparent elastic properties of trabecular bone using DVC applied to *in situ* SR-microCT tomograms obtained with different exposure times. Results showed how DVC was able to identify high local strain levels (>10,000 με) corresponding to visible microcracks at high irradiation doses (~230 kGy), despite the apparent elastic properties remained unaltered. Microcracks were not detected and bone plasticity was preserved for low irradiation doses (~33 kGy), although image quality and consequently, DVC performance were reduced. DVC results suggested some local deterioration of tissue that might have resulted from mechanical strain concentration further enhanced by some level of local irradiation even for low accumulated dose.

Keywords: Bone; X-ray radiation; dose; tissue damage; SR-microCT; digital volume correlation; *in situ* testing.

4.1.1. Introduction

A deep understanding of bone mechanics at different dimensional scales is of fundamental importance since musculoskeletal pathologies such as osteoporosis or bone metastasis are associated with alterations in the bone structure [1]. Thus, advances in mechanical characterisation of bone at the micro- and nanoscale [2–4] would ultimately improve the assessment of the effect of treatments and interventions in pathological conditions [5,6].

Several studies have investigated the relationship between microstructure and bone tissue mechanics using a combination of mechanical testing and X-ray micro-computed tomography (microCT), known as *in situ* (or 4D) microCT [7–10]. However, *in situ* experiments performed in laboratory microCT systems require long times to acquire high quality tomograms (high signal to noise ratio (SNR)) and reducing the scanning time is therefore an essential requirement. In this perspective, high-energy synchrotron radiation micro-computed tomography (SR-microCT) has become a very powerful technique able to combine fast acquisition of three-dimensional (3D) microstructures with high spatial resolution (~1 µm voxel size) [11,12]. Over the past decade, SR-microCT was employed for studying the microarchitecture and deformation field of bone under *in situ* mechanical testing [13–15], notably enhancing the understanding of bone failure mechanisms. Unfortunately, the cumulative effect of sequential step-wise SR-microCT irradiation on the mechanical properties of bone tissue was never addressed.

Important guidelines to date on the effect of X-ray irradiation on bone mechanics were described in Barth et al. [16,17] who reported how high exposures to SR X-ray radiation lead to a deterioration of the mechanical properties of bone resulting in reduced strength, ductility and toughness as a consequence of collagen matrix degradation. Particularly, in [16, 17] deformation and fracture of human cortical bone were evaluated following irradiations up to 630 kGrays (kGy) to simulate typical scan time for a tomographic data set. It was shown how plastic deformation was suppressed after 70 kGy of radiation, due to the reduction of strain carried by the collagen fibrils from ~80% (unirradiated) to ~40% of the applied tissue strain, and apparent strain decreased by a factor of five after tripling the radiation dose; ultimately, suggesting that *in situ* SR-microCT testing, typically requiring multiple sequential tomograms of the same sample over time, may result in accumulation of significantly large radiation doses that affect mechanical properties [6]. However, despite an ideal safety value in the region of 35 kGy (and below) was suggested, corresponding to the typical dose used to sterilize bone allografts [18], uncertainties still remain on what is the effect of X-ray SR radiation on the genesis and development of bone microdamage with different accumulated dose. Particularly, the impact of the total radiation dose, close to the proposed limit of 35 kGy, on bone elastic properties. In addition, dose calculation on bone in Barth et al. [16, 17] was carried out on mathematical terms taking into account only bone mass and assuming a reasonably uniform distribution for the absorption of X-rays within the sample. This may be working well in some experiments but not in others where multiple materials are on the

beam-path (i.e. *in situ* loading devices containing the bone in saline solution) and certainly can only provide an average evaluation, where local dose on the tissue cannot be estimated.

With the recent and rapid advances of high-resolution microCT in conjunction with *in situ* mechanical testing [19,20], digital volume correlation (DVC) [21] has gained increasing popularity as the only image-based experimental technique capable of investigating 3D full-field displacement and strain in trabecular bone [22–25], cortical bone [25,26], wholes bones [27–30], biomaterials [31] and bone-biomaterial systems [32] under different loading conditions. Very recently, DVC applied to SR-microCT of bone has been used to characterise the level of uncertainties in displacement and strain measurements for different bone types, including bovine trabecular, bovine cortical and murine tibiae [33]. However, to the authors knowledge, there is only one study using DVC for actual *in situ* SR-microCT testing of cortical bone [26], but none reporting SR-microCT-based DVC for trabecular bone. In addition, Christen et al. [26] proposed a DVC analysis, assuming that the obtained displacements and strains were only related to the bone mechanics and virtually 'unaffected' by the SR radiation and total accumulated radiation dose during sequential tomography. Therefore, it is critical to evaluate how bone mechanics, particularly in the elastic regime, is influenced by SR-microCT exposure during *in situ* experiments on bone, confirming that the irradiation does not induce important damage to the tissue. This is also a mandatory pre-requisite to fully enable the application of DVC computed on bone undergoing *in situ* SR-microCT mechanical testing, particularly for tomograms with resulting quality that may be limited by safe X-ray dose. On the other hand, the unique ability of DVC to detect local levels of strains in bone structures with the consequent possibility of predicting failure location [30] when values in the range of 8,000-10,000 με (deemed sufficient to produce bone tissue yielding [34,35]) are computed can provide precious indications on the local degree of tissue deterioration due to cumulative SR X-ray exposure.

The aim of this study was therefore to use DVC applied to *in situ* SR-microCT images of trabecular bone in order to investigate, for the first time, the influence of SR irradiation-induced tissue damage on the apparent elastic properties at variable radiation doses. In addition, the dose distribution delivered to bone specimens was simulated to gain a better understanding on the combination of local irradiation and mechanical strain concentration on tissue damage. Doses ranging from 4.7 to 32.9 kGy per tomogram were investigated, achieved by varying the exposure time to SR X-ray radiation (from 64 to 512 ms per projection). The findings of this paper will improve knowledge on bone degradation during SR X-ray exposure and provide important indications on procedures to be used for *in situ* mechanics and DVC evaluation.

4.1.2. Methods

4.1.2.1. Specimen preparation

Ovine trabecular bone from fresh frozen femoral condyles was used in this study, following Ethics approval granted by the Royal Veterinary College and in compliance with the United Kingdom Home Office regulations (Animal Scientific Procedures Act [1986]). Four cylindrical cores, 18 mm in height, 4 mm in diameter were extracted from the femoral lateral condyles in proximal-distal direction by drilling with a coring tool and the ends of the cores were trimmed plane and parallel. End-constraint was achieved by embedding the ends of the samples in poly-methyl-methacrylate (PMMA) endcaps. Approximately, 5 mm of bone was embedded into each endcap to achieve a 2:1 aspect ratio and reduce experimental artifacts [36]. Samples were kept frozen at –20° and thawed for approximately 2h in saline solution at room temperature before testing.

4.1.2.2. SR-microCT imaging and *in situ* mechanics

SR-microCT was performed at the Diamond-Manchester Imaging Branchline I13-2 [37] of Diamond Light Source (DLS), UK. A filtered (1.3 mm pyrolytic graphite, 3.2 mm aluminium and 60 µm steel) polychromatic 'pink' beam (5-35 keV) was used with an undulator gap of 5 mm for data collection and, to limit sample damage, 11 mm for low-dose alignment. The propagation (sample-to-scintillator) distance was approximately 50 mm. Images were recorded by a pco.edge 5.5 (PCO AG, Germany) detector which was coupled to a 500 µm-thick CdWO4 scintillator and a visual light microscope (Figure 1-I). The effective voxel size was 2.6 µm, with a field of view of 6.7 x 5.6 mm. Different X-ray radiation doses were obtained for each specimen by using variable exposure times per projection: 512, 256, 128 and 64 ms, with 11 ms overhead per exposure. For each dataset, 1801 projection images were collected over 180 degrees of continuous rotation ('fly scan'). The final image was not used for reconstruction but was compared to the first image to check for experimental problems including sample deformation and bulk movements [38]. The projection images were flat and dark corrected prior to reconstruction. For each dataset, 40 flat and dark images were collected. Reconstruction was performed at DLS using the in-house software, DAWN [38,39], incorporating ring artefact suppression.

In situ uniaxial compression testing was performed via a micro-mechanical loading stage (CT5000, Deben Ltd, UK). Specimens were immersed in saline solution throughout the test to simulate physiological conditions. All tests were carried out under displacement control at a constant cross-head speed of 0.1 mm/min. A small preload (5 N) was first applied to ensure good end contact prior to testing, followed by 10 cycles of preconditioning. Each bone specimen was then subjected to seven loading cycles in the apparent elastic range [39] (0.5% global strain) and full tomographic datasets were acquired under compression at the end of each cycle (Figure 2), after allowing the samples to settle for 10 minutes to reduce stress relaxation during imaging. Specimens that did not show any visible microdamage (i.e.

microcracks) after visual inspection of the reconstructed images at the end of the loading cycles were loaded up to failure to investigate the presence of apparent plasticity in the bone.

For each specimen, seven datasets were obtained corresponding to the different loading cycles. The 3D images (Figure 1-II, III) were filtered (Figure 1-IV) and masked (Figure 1-V) prior to DVC analysis (Supplementary material S1). Additionally, the bone volume (BV) was obtained using BoneJ [40] plugin for Fiji to assess possible correlations with DVC measurements.

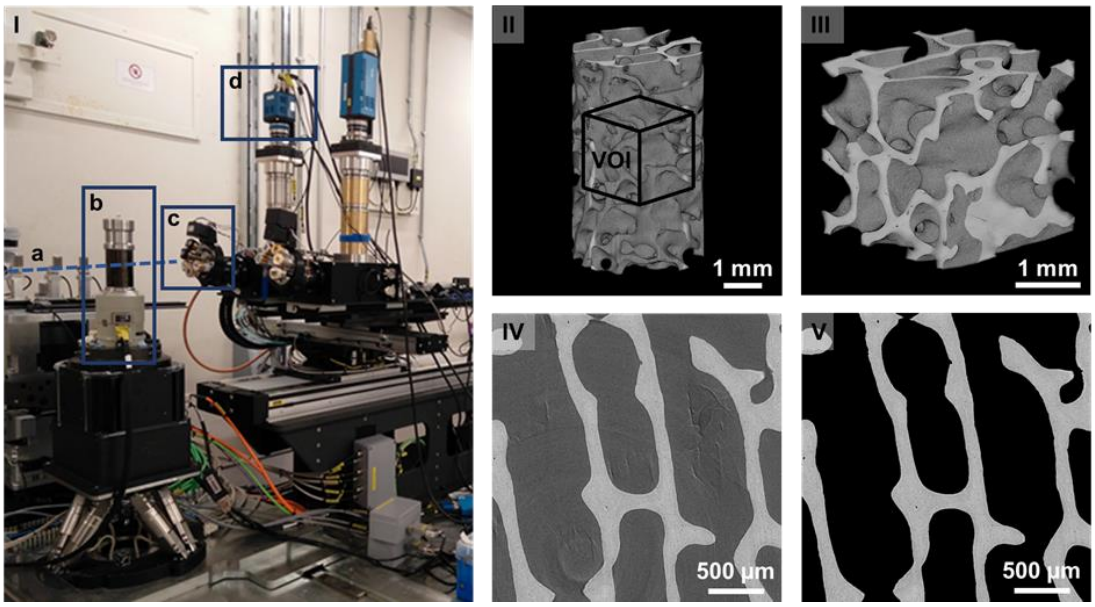

Figure 1. (I) Experimental setup at I13-2 beamline. The direction of the beam is indicated by the dashed line (a). Samples were scanned within the loading stage (b) using a pco.edge 5.5 detector (c) and a 1.25X objective (2.5X total magnification) (d). SR-microCT reconstruction of trabecular bone (II): each cylindrical specimen was imaged with an effective voxel size of 2.6 µm using different exposure times: 512, 256, 128 and 64 ms. A cubic (1000*1000*1000 voxels) volume of interest (VOI) was obtained at the centre of each specimen (III). 2-dimensional (2D) slice through the middle of the VOI before (IV) and after (V) mineralised tissue was masked from the marrow.

4.1.2.3. Dose calculation

The average photon energy and photon flux during the synchrotron experiment was estimated using SPECTRA code [41], to be 28.93 keV and 4.9 x 10^{13} photons/s respectively (23 keV and 3 x 10^{10} photons/s during alignment), using a 2 x 2 mm aperture 220 m after the X-ray source. These values took in consideration the transmission of the filters and the reflectivity of the platinum mirror used during the experiment. The delivered dose rate was simulated using FLUKA Monte Carlo code [42], for the fixed set of parameters used in the Beamline. The geometry simulated in FLUKA consisted on a trabecular bone specimen within the loading device (Supplementary material S2). The bone specimen was assumed as a cylinder (4 mm diameter, 10 mm length, density of 0.5 g/cm^3 [43]) placed in the centre of the environmental chamber (40 mm inner diameter, 3 mm thickness) made of glassy-carbon

(density of 1.5 g/cm^3) and filled with saline solution (density of 1 g/cm^3). The chamber was located inside the loading stage glassy-carbon tube (56 mm inner diameter, 4.5 mm thickness). The implemented stoichiometry was the following: Ca-22.5, P-10.3, C-15.5, N-4.2, O-43.5, S-0.3, Mg-0.2. The simulation results have an error below 15%. Further details on the dose simulation can be found on the Supplementary material S2. The nominal radiation dose absorbed by each sample during sequential tomography was computed multiplying the dose rate by the scanning time (Table 1).

4.1.2.4. Digital volume correlation

DaVis-DC software (v8.3, LaVision, Goettingen, Germany) was used to couple SR irradiation-induced damage and mechanical bone yielding with the differences in full-field strains developed in the tissue after each loading cycle for the highly- and lowly-irradiated specimens (32.9 and 4.7 kGy/tomogram). The software is based on a local approach of DVC computation, which has been deemed sufficiently precise to be used in bone mechanics [24,32,44–47]. Details on the computation algorithm used in DaVis-DC are reported elsewhere [31,44]. The evaluation of the level of uncertainties or 'baseline strains' was performed in the first two consecutive datasets for both specimens, obtained under the same constant nominal strain, where the irradiation-induced damage was deemed as minimal (Supplementary material S1). DVC was applied to the masked images (where the non-bone was treated as a black 'zero count' region), to avoid large strain artefacts in regions with no pattern (i.e. saline solution, marrow). The presented DVC computation relied on a multi-pass scheme with a final sub-volume of 64 voxels, producing the best compromise between precision and spatial resolution (precision errors below 2 µm for displacements and lower than 510 µε. This was then used to register the reference image (first loading cycle) with each of the remaining images after each loading cycle and computing the corresponding differential strain field (Figure 2).

To allow comparisons with previous studies, two different scalar indicators were computed for each registration: mean absolute differential strain value and standard deviation of the differential strain value, defined as the mean and standard deviation, respectively, of the average of the absolute values of the six components of strain for each sub-volume (similar to MAER and SDER [33,48]). The correlated volume (CV) was assessed as the volume where correlation was achieved. The correlated bone volume (CV/BV) was then computed dividing the CV by the BV. Data were screened for outliers applying the criterion of Peirce [49] to the CV/BV. In order to evaluate the full-field differential strain distribution in the VOIs over time in relation to the deformation induced by the SR irradiation damage, maximum and minimum principal differential strains were computed for the samples exposed to higher and lower radiation. Additionally, the damaged bone volume (BVy) was computed as the tissue voxels exceeding ±10,000 µε.

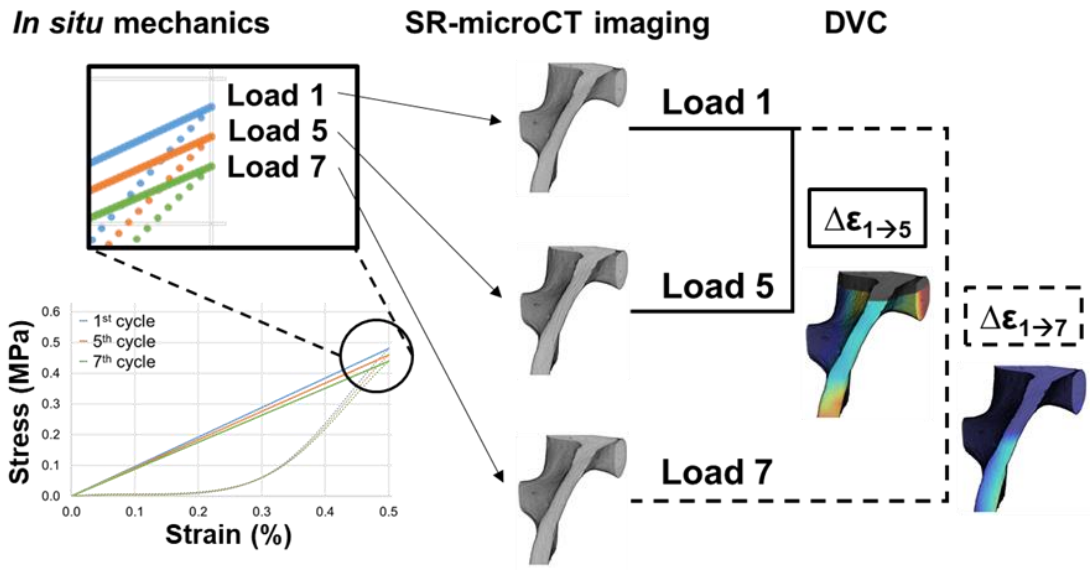

Figure 2. Workflow used to combine *in situ* SR-microCT and DVC. Specimens were cyclically loaded in the apparent elastic regime (up to 0.5% nominal strain) seven times and SR-microCT images were acquired under maximum load. DVC was performed using the first 3D image as a reference state and computing the differential strain field between the reference and the remaining consecutive tomograms.

4.1.3. Results

A qualitative inspection of the SR-microCT images showed the development of multiple microcracks (Figure 3-I, 3-II) in the samples exposed to high radiation doses (32.9 and 16.8 kGy/tomogram) that started to be visible after the fifth (164.7 kGy accumulated dose) and sixth cycles (100.9 kGy accumulated dose), respectively. Microdamage in the second one (16.8 kGy/tomogram) degenerated into a trabecular collapse. Samples imaged at lower radiation doses (8.8 and 4.7 kGy/tomogram) did not present any visible microcracks. Detailed images of a single trabecula (Figure 3-III) allow a better comparison of the image quality, dependent on the exposure time. Bone lacunae can be identified only for the highest exposures (32.9, 16.8 kGy/tomogram). Additionally, important ring artifacts are visible in the 8.8 kGy specimen.

The stress-strain curves (Figure 4) presented a different behaviour for each of the specimens studied. The apparent mechanics of the 32.9 kGy/tomogram sample (Figure 4-I) remained within the elastic range even after the microcracks started to develop (after the fifth cycle). A maximum global stress of 0.4 MPa was reached at 0.5% nominal strain in the first cycle, and a progressive reduction of the stiffness was observed. The 16.8 kGy/tomogram sample reached the same maximum global stress (0.4 MPa) at 0.5% strain, however, the reduction of the stiffness after 5 cycles was considerably higher. A less pronounced reduction of stiffness was found for the 8.8 kGy/tomogram specimen (Figure 4-III)., whereas the sample imaged at lower radiation dose did not show any notable changes in the apparent elastic properties during the seven loading cycles (Figure 4-IV). At a nominal applied strain of 0.5%, maximum global stress of 0.48 and 0.60 MPa were obtained for the

8.8 and 4.7 kGy/tomogram specimens, respectively. Samples imaged at the highest radiation doses failed within the estimated elastic range from the previous cycles (Figure 4-V). For the 16.8 kGy/tomogram sample, a fragile failure was reached after the sixth loading cycle, when the microcracks started to be visible, under an applied load within the previously estimated elastic range. Conversely, the less irradiated samples did not reach the failure within the seven applied loading cycles, in agreement with the visual inspection of SR-microCT images. The 8.8 kGy/tomogram specimen did not present any plasticity before failing, which was then reached at ~1.7% global strain with an applied stress of 1.4 MPa. The stress-strain curve of the 4.7 kGy/tomogram specimen instead presented the typical behaviour of ductile cellular materials, such as trabecular bone. The yield was observed at 0.9% strain, resulting in a 0.99 MPa yield stress. Failure was experienced at 0.97 MPa stress and 3.9% strain.

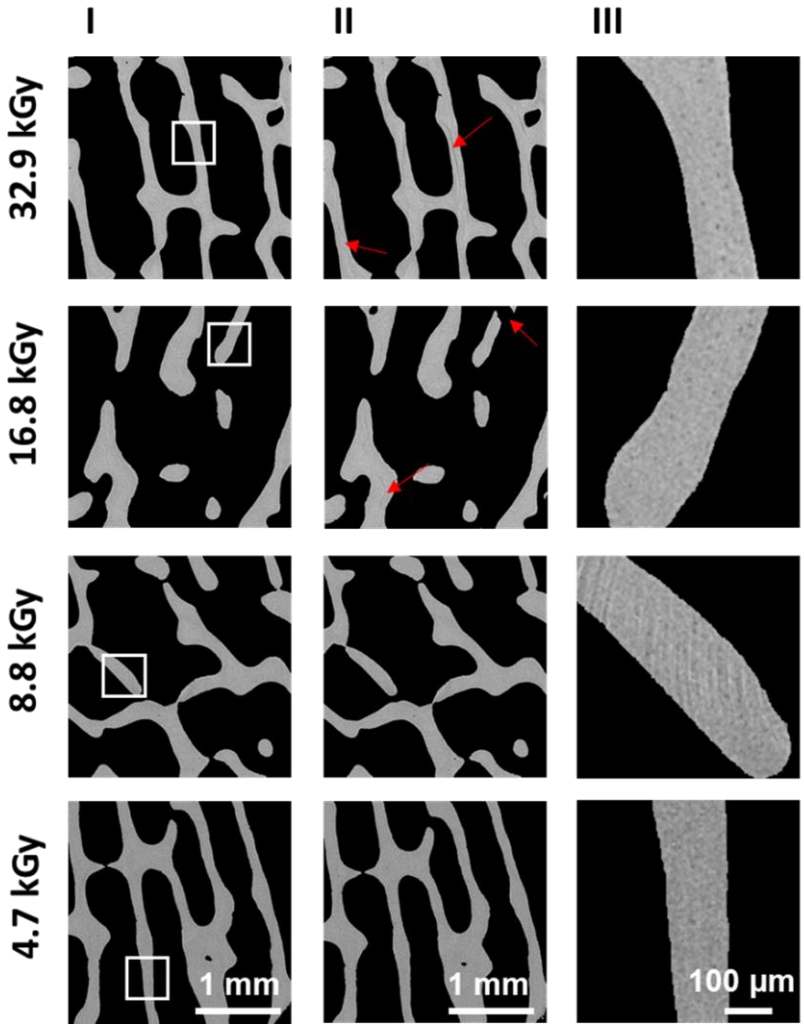

Figure 3. SR-microCT 2D slices acquired under load in the trabecular elastic range (0.5% apparent strain) at different radiation doses (rows for 32.9, 16.8, 8.8 and 4.7 kGy/tomogram) after the 1st (column I) and 7th (column II) loading cycles. White squares indicate regions augmented to show a single trabecula (column III). Red arrows indicate damage location in the tissue (i.e. microcrack, fracture). Bone lacunae remain visible within the trabeculae (column III) only for the highest exposures (32.9, 16.8 kGy), whereas no features could be identified for the lowest exposures (8.8, 4.7 kGy). Scale bars are valid for same columns.

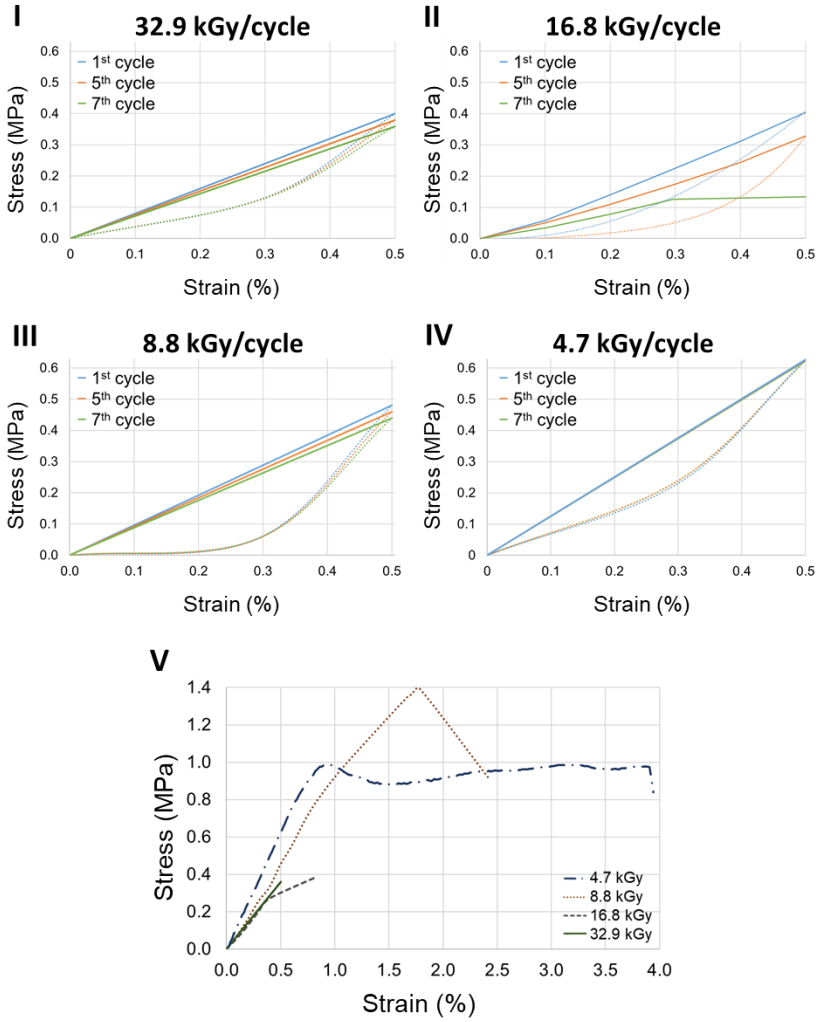

Figure 4. Stress-strain curves for the tested specimens. (I-IV) are showing the 1st (blue), 4th (orange) and 7th (green) loading-unloading cycles (solid-dotted curve, respectively). Reduction in the stiffness after each cycle is observed in I-III. Samples exposed to lowest doses (8.8 and 4.7 kGy/tomogram) were loaded up to failure after the seven loading cycles (V), whereas the ones at higher doses (16.8 and 32.9 kGy/tomogram) were damaged or failed within the previous seven elastic cycles.

The dose rate distribution simulated in the bone cylinder is shown in Figure 5. Maximum dose (58 Gy/s) is accumulated in the centre of the specimen (Figure 5-II, III) where the X-ray beam impinges on and decreases through the sample (Figure 5-I), with minimum dose (2.7Gy/s) towards the base of the cylinder. The average dose rate within the simulated cylinder was computed as 35 Gy/s (6.4 Gy/s standard deviation) during image acquisition (0.2 Gy/s during alignment). The accumulated dose for each specimen during the sequential tomograms is reported in Table 1, together with the total scan time computed as a function of the exposure time per projection.

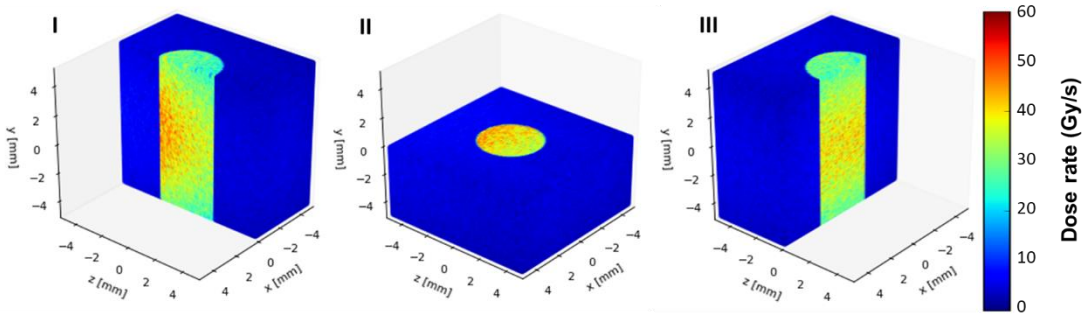

Figure 5. Dose rate distribution within a cylindrical trabecular bone specimen simulated in FLUKA. 3D sections in x (I), y (II) and z (III) directions of the simulated bone specimen within the saline solution are shown. The X-ray beam comes along the z direction from negative to positive direction.

Table 1. Total scan time and nominal radiation dose absorbed by each sample per cyclic loading, calculated by varying the exposure time. Values were truncated to one decimal place.

Exposure time	**512 ms/projection**						
Load cycles	1	2	3	4	5	6	7
Scan time (min)	15.7	31.4	47.1	62.8	78.5	94.1	109.8
Dose accumulated (kGy)	32.9	65.9	98.8	131.8	164.7	197.7	230.6
Exposure time	**256 ms/projection**						
Load cycles	1	2	3	4	5	6	7
Scan time (min)	8.0	16.0	24.0	32.0	40.1	48.1	56.1
Dose accumulated (kGy)	16.8	33.6	50.5	67.3	84.1	100.9	117.7
Exposure time	**128 ms/projection**						
Load cycles	1	2	3	4	5	6	7
Scan time (min)	4.2	8.3	12.5	16.7	20.9	25.0	29.2
Dose accumulated (kGy)	8.8	17.5	26.3	35.0	43.8	52.5	61.3
Exposure time	**64 ms/projection**						
Load cycles	1	2	3	4	5	6	7
Scan time (min)	2.3	4.5	6.8	9.0	11.3	13.5	15.8
Dose accumulated (kGy)	4.7	9.5	14.2	18.9	23.6	28.4	33.1

Values of the correlated bone volume, damaged bone volume and (mean and standard deviation) differential strain values from DVC are summarized in Table 2. The more irradiated specimen (32.9 kGy/tomogram) presented a decrease in the CV/BV as the number of load cycles increased (from 93.6% to 66.3%), consistent with the development of microcracks in the tissue. Conversely, the less irradiated specimen (4.7 kGy/tomogram) showed a more stable CV/BV for all the analysed images. The application of Peirce's criterion concluded that the CV/BV after 4 and 6 cycles (lowest CV/BV) were outliers and strain results were therefore not computed. Mean and standard deviation of the differential strain values after the second loading cycle (first two consecutive tomograms) can be

interpreted as indicators of the baseline strain uncertainties; these increase for lower exposure due to the decrease of image quality, with a precision value below 150 με for the highly-irradiated specimen and slightly above 500 με for the lowly-irradiated specimen. Both bone volume damage and differential strain value progressively increase with the applied loading cycles and consecutive scans. This increment was more dramatic in the 32.9 kGy specimen, with more than half its volume exceeding the considered threshold in the yield strain (± 10,000 με).

Table 2. Correlated bone volume (CV/BV), damaged bone volume (BV_y) and mean ± standard deviation of the differential strains (Δε) for each loading cycle in the specimens subjected to highest (32.9 kGy/tomogram) and lowest (4.7 kGy/tomogram) radiation doses, as computed using DVC.

Dose/cycle	**32.9 kGy**					
Load cycles	2	3	4	5	6	7
CV/BV (%)	93.6	90.6	85.6	74.2	73.4	66.3
BV_y (%)	0	0	0.24	30.1	61.2	57.1
Δε (με)	405 ± 142	828 ± 320	1546 ± 582	3632 ± 1660	5546 ± 2078	6752 ± 2830
Dose/cycle	**4.7 kGy**					
Load cycles	2	3	4	5	6	7
CB/BV (%)	94.3	88.5	72.7	88.4	73.7	88.3
BV_y (%)	0	0	NC[1]	7.0	NC[1]	13.9
Δε (με)	928 ± 504	868 ± 502	NC[1]	1369 ± 1155	NC[1]	1563 ± 3142

[1] Not computed data. Data identified as outlier after applying the criterion of Peirce.

The internal differential strain distributions (first and third principal strain components) for the highly irradiated sample imaged are reported in Figure 6. The distribution of both components well described the damage events. After the first two loading cycles, the differential strain distribution was homogeneous throughout the entire volume (Figure 6-I). As the loading cycles increased, the strain values increased, and the strain field became more heterogeneous (Figure 6-II, III), in agreement with the random distribution of microcracks within the entire volume. The histograms for both differential principal strains (Figure 6-IV) captured the strain evolution within the studied VOI. After two loading cycles, the number of sub-volumes exceeding ±1,000 με was considerably low, however, increasing the loading cycles and therefore the total exposure to radiation, the number of sub-volumes exceeding those values increased significantly, reaching maximum amplitude values exceeding ± 10,000 με at the end of the test. In addition, a single trabecula was tracked during the different cycles to visualize the progression of strain coupled with the microdamage in the tissue (Figure 7). It can be seen how maximum differential strains were reached in regions of microcracks development (red arrows). Microcracks location corresponded to strain values above 8,000 με in tension and 6,000 με in compression after 5 loading steps and exceeded ± 10,000 με at the end of the test. Despite the development of multiple microcracks, the overall look of the tracked trabecula did not present any noticeable change in the deformed

configuration. Additionally, before damage became identifiable (5th cycle), the strain distribution seemed to predict the location of damage initiation. In an analogous manner, the differential strain distribution was plotted for the sample imaged at low radiation dose (4.7 kGy/tomogram). Both first and third differential principal strains are shown in Figure 8. Although slightly higher strain values were found after loading the sample for seven cycles, the differences in the 3D full-field differential strains at the end of each step were minimal. The histograms (Figure 8-IV) showed maximum amplitudes below 1,000 με in tension and compression after the 5th loading cycle and close to 3,000 με after the last loading step.

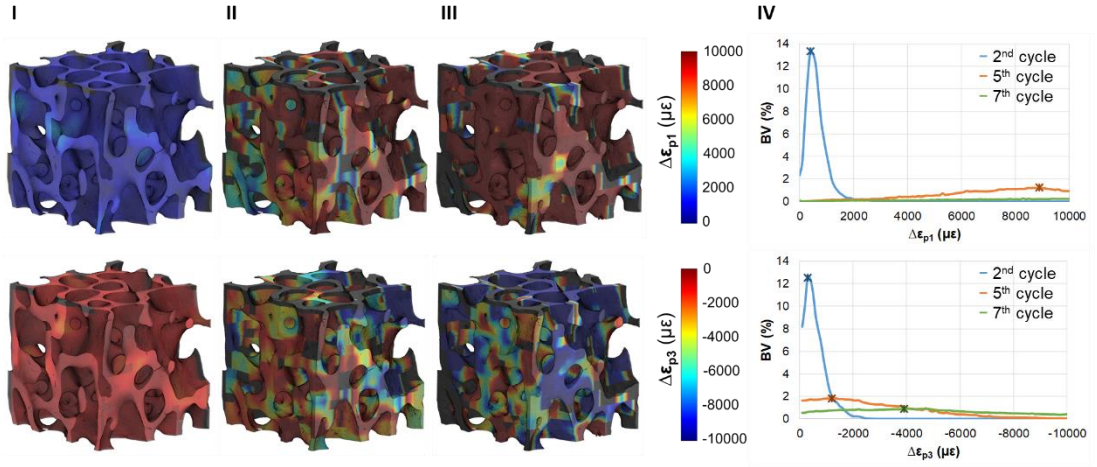

Figure 6. 3D differential strain distribution in trabecular bone tissue for the highly-irradiated sample (32.9 kGy/tomogram). First ($\Delta\varepsilon_{p1}$) and third ($\Delta\varepsilon_{p3}$) differential principal strains are represented after two (I), five (II) and seven (III) loading cycles. Histograms of the differential strain distribution in the tissue voxels (IV) after the same loading cycles are shown with the correspondent maximum strain amplitudes. High exposures produced an important damage in the bone during sequential tomograms and the differential first ($\Delta\varepsilon_{p1}$) and third ($\Delta\varepsilon_{p3}$) principal strains were largely above 10,000 με after the 7th cycle.

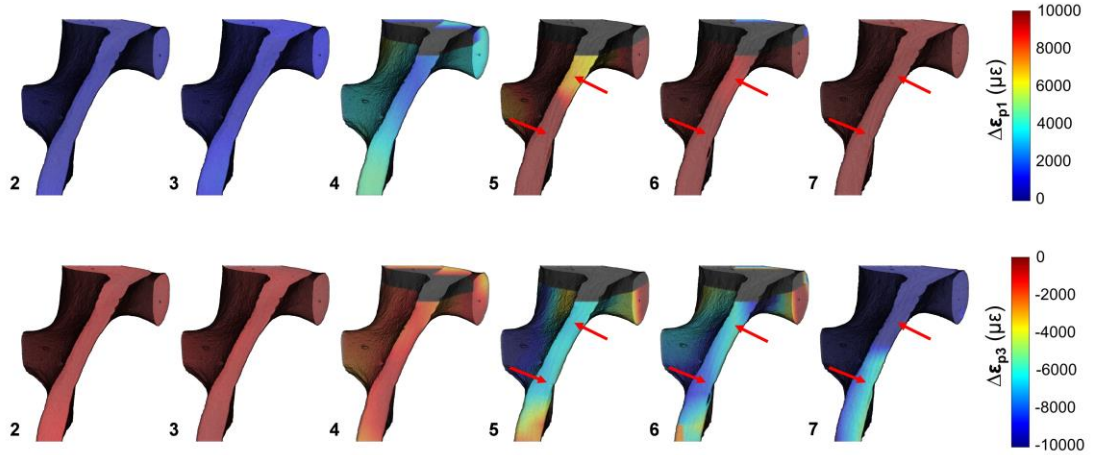

Figure 7. 3D distribution of first ($\Delta\varepsilon_{p1}$) and third ($\Delta\varepsilon_{p3}$) principal differential strains on a single trabecula tracked during the different loading cycles (cycle number indicated for each DVC computation) for the highly irradiated sample (32.9 kGy/tomogram). Arrows indicate microcracks visible in the tissue.

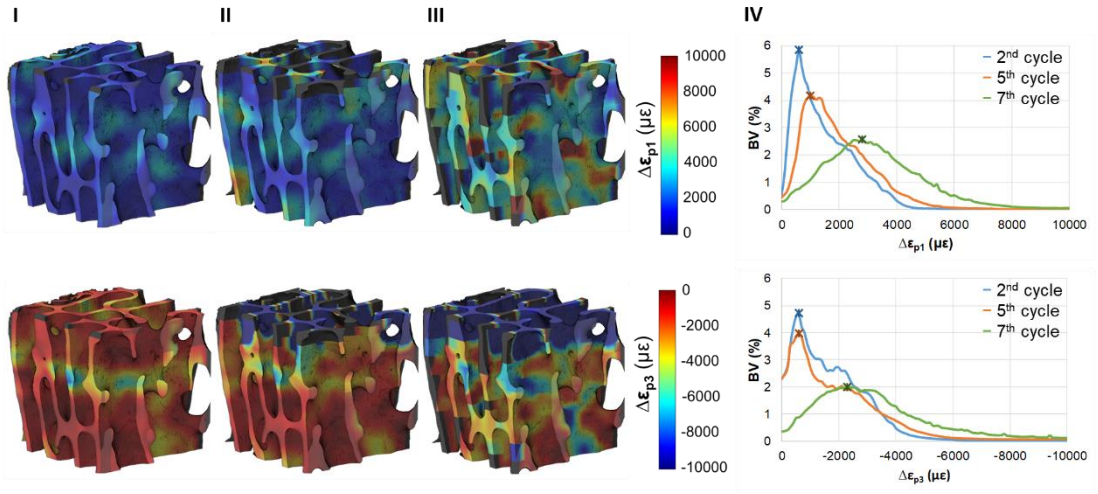

Figure 8. 3D differential strain distribution in trabecular bone tissue for the low-irradiated sample (4.7 kGy/tomogram). First ($\Delta\varepsilon_{p1}$) and third ($\Delta\varepsilon_{p3}$) differential principal strains are represented after two (I), five (II) and seven (III) loading cycles. Histograms of the differential strain distribution in the tissue voxels (IV) after the same loading cycles are shown with the correspondent maximum strain amplitudes. The reduction in exposure time considerably reduced the damage induced in the bone during sequential tomograms, although some areas of strain concentration could be identified.

4.1.4. Discussion

The main aim of this paper was to investigate and quantify, for the first time, the influence of the irradiation-induced trabecular bone damage on its apparent elastic properties and local deformation using DVC applied to *in situ* SR-microCT images. Structurally, the irradiation affects the collagen environment (increasing the degree of cross-linking), resulting in a progressive loss in the post-yield deformation leading to a decline in strength, toughness and ductility of bone [16]; thus, special attention is needed for *in situ* mechanical studies involving high flux X-ray radiation. A deeper understanding of the full-field differential strain accumulated in the tissue due to the X-ray synchrotron radiation was achieved. In fact, despite that a number of studies used SR-microCT in conjunction with *in situ* mechanical testing to characterize bone microstructure and mechanics [13–15], the potential of DVC to high resolution SR-microCT remains partially unexplored [26,33].

The results reported in this paper clearly show the progressive strain accumulation in the tissue when increasing the total exposure time to SR X-ray radiation (Figs. 6, 7), and consequently the accumulated radiation dose. Furthermore, DVC successfully correlated the presence of microcracks in the highly-irradiated sample to large levels of tensile and compressive strains, above or close to the typical values of trabecular bone yielding (i.e. 6,200 με in tension and 10,400 με in compression [34] for human trabecular tissue and 7,800 με in tension and 10,900 με in compression [35] for bovine trabecular tissue). In fact, the main potential of DVC is in its ability to predict damage location before gross failure occurs, when high-strain concentrations typical of tissue yielding are building up [29,30]. In this sense, the results herein obtained clearly show how local strain concentration progressed

from the 4th loading cycle and resulted in microcracks detection in the next cycle (Figure 7). It could be argued that the applied repetitive loading during the experiment, much like a low cycle fatigue, may influence the full-field strain measured in the tissue. In fact, it is not easy to decouple both phenomena. Singhal et al. [50] distinguished between the damage due to mechanical loading and irradiation by using control samples subjected only to load or irradiation and found that although the apparent modulus remained unaffected by both events, the residual strains were largely altered primarily due to the irradiation, and, to a lower extent, by mechanical loading. However, this type of analysis is not possible when using DVC applied to SR-microCT *in situ* tested samples, as image acquisition is needed, and this necessarily involves exposure to irradiation. Furthermore, for the less irradiated specimen (4.7 kGy/tomogram) some areas of strain concentration were identified using DVC from the second load cycle (Figure 8) even though the apparent mechanical behaviour of such specimen was normal (Figure 4-IV). This localised strain concentration was further recognised, and its evolution was tracked during the remaining loading steps. Despite the fact that all the specimens were loaded in the apparent elastic regime (0.5% global strain) and that the stress-strain curve for the 4.7 kGy specimen presented a linear elastic behaviour beyond 0.5% strain, some microstructural damage can still appear. In fact, as reported by Moore et al. [39] while an applied compressive strain of 0.4% resulted in no microdamage to the specimens, an increment of the strain from 0.4% to 0.8% showed an increase in the number of damaged trabeculae. Additionally, the top face of the specimen experienced important levels of compressive strain, more likely due to the applied load than to the radiation exposure. Also, as only a small VOI at the centre of the specimens was analysed it is then possible that strain concentration out of that region was not assessed using DVC, what may affect the computation on the edges of the VOI. However, the aim of this study was to quantify the effect of the irradiation on the bone tissue and it has been shown (Figure 5) that maximum doses are accumulated in the centre of the specimen where the X-ray beam impinges.

In order to define a safe exposure that would not compromise the mechanical stability of the tissues, different exposure times to SR irradiation were evaluated, leading to a wide range of radiation doses. The total radiation dose absorbed by the specimens depends on multiple factors (i.e. beam size, flux, energy, filters). However, the delivered dose rate is based on the specifications of the tomography beamlines (i.e. flux, energy) and it is more complex for users to control. Therefore, varying the total exposure time (number of projections and/or exposure per projection) results on a straightforward approach to achieve different radiation doses. In addition, being the current study based on DVC performance itself, it was decided to control exposure as for image quality. It has been shown (Figure 3) that reducing the accumulated dose to 33 kGy facilitated tissue preservation, but at the same time the image quality was significantly reduced, as the exposure time was set to 64 ms/projection. This was perceived by DVC as important levels of strain uncertainties up to ~500 με, although still acceptable to discriminate tissue yielding. Furthermore, the reduction of image quality may

also be responsible for the low CV/BV found for the 4th and 6th loading cycles, identified as outliers. In any case, DVC indicated that the microdamage induced by irradiation was by far more important that the uncertainties (Figs. 6, 7). Two recent studies [33,47] measuring strain uncertainties on high-quality images obtained by SR-microCT reported SDER values below 150 με for an equivalent sub-volume size, close to the values obtained in this study for the highly irradiated specimen, where image quality is comparable. It is worth to recall that the strain uncertainties computed in this study were not based on a zero-strain test that is typically performed in DVC studies [33,44,46], as all the images were acquired under applied load and this can potentially alter the significance of uncertainty measurement due to the random presence of mechanically accumulated strains. For this reason, all the registrations performed using DVC were considered as differential or residual strains, where the strain produced in the compression stage up to 0.5% could not be computed. In fact, since the aim of this work was to assess the effect of X-ray radiation on the apparent mechanics of the tissue, introducing two more scans before loading the specimens would have produced an additional dose accumulation on the specimens prior to the mechanical testing; hence, potentially altering the tissue properties. The reliability of DVC in terms of strain uncertainties on tissue measurements is limited in most microCT systems [44,51] that typically have low spatial resolution and SNR. By contrast, SR-microCT enables micro-resolution at high SNR, providing more features to improve DVC computation, and therefore the characterization in a 3D manner of bone microdamage. However, this study illustrates that when prolonged exposure times are required, the microstructural integrity of bone tissue is compromised. Consequently, one could question the results of any mechanical studies involving high irradiation levels. Hence, it is surprising that bone tissue behaviour has been previously studied using time-lapsed SR-microCT [14,26] and, although concerns about the effect of the irradiation were discussed, the possible microcracks formation and/or progression due to irradiation damage was never addressed.

The accumulated dose distribution delivered to each bone specimen was simulated using FLUKA Monte Carlo code, which has been extensively used for dose calculations in the medical field [52–54]. The simulation considered not only the trabecular bone specimen but also its environment, which seemed to considerably reduce the average dose rate compared to that of the bone in dry air (decrease on the average dose rate from 90 Gy/s in dry conditions (air) to 35 Gy/s in saline solution within the loading device). Bone specimens were simulated as homogeneous cylinders with an apparent density of 0.5 g/cm^3 (see supplementary material S2). The chosen density value is well aligned with the bone mineral density of ovine femoral condyles [55] and the average volume fraction (0.33 ± 0.04) of the four specimens, and in agreement with previous literature [43] on ovine trabecular bone. Despite a simulation based on the real trabecular geometry would be beneficial for a more accurate computation of the local dose accumulation in the tissue, it was not within the scope of this study to perform sample-specific dose simulations, but to have a close estimation on the absorbed dose. However, a correlation between tissue strain developed

due to SR radiation and related local dose would be an attractive topic for further studies in the field.

The average dose computed in this study with FLUKA is well in agreement to that obtained using mathematical formulation previously proposed [16] (see supplementary material S2). Barth et al. [16] defined a “safe” irradiation level of 35 kGy and since then, this has been considered as a reference in several studies using SR radiation for imaging bone tissue [56,57]. That dose value corresponds to the maximum standard dose typically used in tissue banks in order to sterilize bone allografts for bone replacement [18]. In a follow-up study [17], it was suggested that no notable difference in the mechanical integrity of the bone could be detected for irradiation doses below 35 kGy. In agreement with that statement, the present study showed that for the less irradiated specimen (dose of ~33 kGy) the stress-strain curve presented a normal behaviour, although DVC identified higher strain values at the end of the loading cycles. High strains may as well be caused by localised tissue irradiation, other than local mechanical strain concentration, which could not be visually detected in the reconstructed images due to the low SNR. In fact, the simulated dose rate can locally reach values of 60 Gy/s (Figure 5), which results in a radiation dose of ~50 kGy for the less irradiated specimen after seven tomograms, and this may induce some tissue microdamage accumulated over sequential acquisition. This is an important aspect as some local microdamage could still be produced by SR radiation even when apparent average dose is contained within safe values. Additionally, it could be seen that for a total dose ~60 kGy, a loss of plasticity was observed for the 8.8 kGy/tomogram specimen (Figure 4-V), in a comparable way as found by Barth et al. [16] for irradiation doses as low as 70 kGy. Most importantly, this study illustrates that the presence of microcracks is not always correlated with an alteration on the apparent mechanical properties of the bone (Figure 3-I). In fact, despite the accumulated dose was above 230 kGy, the elastic apparent properties remained unaltered. This finding is particularly interesting and suggests how only apparent mechanical behaviour of bone is not necessarily indicative of structural integrity and preserved properties, when specimen is exposed to high-flux synchrotron radiation.

To date, different studies have investigated how SR radiation affects the deformation and fracture properties of human cortical bone [16,17] and bovine cortical bone [50], nevertheless this work presented the first quantification of the irradiation-induce damage at tissue level. At the apparent level, this study reported insignificant effect on the elastic behaviour; conversely, the plastic deformation was largely affected, in accordance to previous literature [16,17,50]. Strain evaluation on the irradiated specimens was carried out by Barth et al. [17] and Singhal et al. [50] using *in situ* Small- and Wide-Angle X-ray Scattering (SAXS and WAXS). A partition of strain between the collagen fibrils and mineral crystal is possible using both techniques; however, *in situ* SR-microCT overcome the limitations of two-dimensional information in SAXS and WAXS experiments, providing three-dimensional structural information. A correlation of different imaging techniques at various

dimensional scales would allow a better understanding of the main mechanism causing the damage accumulation in the bone tissue. While SAXS and WAXS could provide information on the changes in the toughening at the level of the mineralized collagen fibrils and the mineral particles, *in situ* SR-microCT would allow visualization and quantification of the induced damage, as well as a full-field strain computation using DVC.

In situ SR-microCT mechanical testing and DVC require the acquisition of several tomograms to study deformation mechanisms. This process inevitably exposes the samples to higher SR radiation, sensitive in the case of biological tissues, and can vary depending on the proposed experimental design (i.e. number of *in situ* steps p/experiment). Synchrotron users could interact with beamline scientists ahead of the beamtime to evaluate the expected irradiation dose levels in advance and consequently plan the experiment based on the total amount of time that samples can be exposed.

However, further investigation should be performed to evaluate the optimal imaging setting preserving bone tissue integrity while maximizing imaging quality, and clearly establishing the damage induced on the tissue. In this way, DVC measured strain uncertainties could be minimised and successfully applied to SR-microCT *in situ* mechanically tested bone samples.

4.1.5. Conclusion

The internal full-field strain from DVC applied to SR-microCT images under a constant applied load at different cycling steps was measured in trabecular bone samples for different exposures to X-ray SR radiation. Local and average dose on the bone were simulated taking into account all the materials in the beam-path. Average maximum dose values ranged between ~33 and ~ 230 kGy for exposures of 64 and 512 ms per frame, respectively. Irradiation-induced microcracks developed in the tissue were successfully matched with important level of strain when a higher dose of 32.9 kGy/tomogram was used. Reduced exposure (64 ms/projection), leading to a considered safe average dose of 35 kGy, was able to control the microdamage and preserve the mechanical performance of the tissue, but notably decreased the quality of the images and consequently the DVC performance. Image settings and number of scans performed should be carefully chosen prior to any *in situ* SR-microCT experiment in order to maintain the radiation dose below the suggested safe threshold (35 kGy), without compromising the mechanical properties of the tissue. Future work is mandatory to clearly establish the damage induced on the tissue in SR-microCT for *in situ* mechanics, as well as consequent DVC performance.

Author contributions

Marta Peña Fernandez: Study design, data curation, formal analysis, data interpretation; Enrico Dall'Ara: Study design, supervision; Silvia Cipiccia: Data curation (dose simulation); Andrew J. Bodey: Data curation; Rachna Parwani: Data curation; Asa H. Barber: Data

curation; Gordon W. Blunn: Supervision; Gianluca Tozzi: Data curation, data interpretation, supervision.

Acknowledgments

The authors would like to thank Diamond Light Source for time at the Diamond-Manchester Imaging Branchline I13-2 and the I13 Data Beamline [58] (proposal number MT14080), and the Zeiss Global Centre (University of Portsmouth) for post-processing. We further acknowledge Dr Dave Hollis (LaVision Ltd) for assistance with DaVis software and Dr Kazimir Wanelik for help during the experiment at Diamond Light Source.

Supplementary material S1

Image post-processing

For each specimen, seven datasets were obtained corresponding to the different loading cycles. These 3D images (Figure 1-II) were registered with Fiji software [59] using the first acquired dataset as a reference to align them rigidly. Registration was performed minimizing the Euclidean difference between the reference and the target image, followed by a resampling using a cubic spline interpolation [60]. After registration, a volume of interest (VOI) was cropped for each 3D image, consisting of a parallelepiped with side lengths of 1000 voxels (2.6 mm^3) in the centre of the scanned volume (Figure 1-II, III). Noise in the images was reduced by applying a 3D median filter (radius = 2 pixels) (Figure 1-IV). Additionally, the original SR-microCT images were also masked (Figure 1-V) by setting to zero the voxels in the background (i.e. bone marrow). A binary image (value one for bone voxel and zero elsewhere) was first created from the filtered images using Otsu's threshold algorithm [61] followed by two cycles of closing (erosion followed by dilation), opening (dilation followed by erosion) and purifying (location of all particles in 3D and removal of all but the largest foreground and background particles [62]). These three operations removed isolated pixels and filled in small holes. The quality of the binary images was checked by visual inspection. Masked images, with the original greyscale value in the bony voxels, and zero elsewhere, were obtained multiplying the filtered to the binary images.

Evaluation of 'baseline' strains

The evaluation of the level of uncertainties or 'baseline' stains was performed in the first two consecutive datasets for the highly- and lowly-irradiated specimens, obtained under the same constant nominal strain (0.5%), where both irradiation-induced and mechanical damage were deemed as minimal. As the images were acquired in the same deformed state, same displacement and strain fields are expected. Therefore, any non-zero values of the measured differential displacement and derived differential strain using DVC were considered as error. Six sub-volume sizes (from 16 to 112, in steps of 16 voxels), and a multi-pass scheme with a final sub-volume of 64 voxels were investigated. For each sub-volume, three different parameters were computed.

- Random errors for the differential displacement: standard deviation of each displacement component, as in [44].
- Mean absolute differential strain value: average of the average of the absolute values of the six components of the differential strain, similar to MAER or “accuracy”, as in [22,33]
- Standard deviation of the differential strain value: standard deviation of the average of the absolute values of the six components of the differential strain, similar to SDER or “precision”, as in [22,33].

The random errors of each differential component of the displacement never exceeded 0.34 voxels (0.89 µm) for the 512 ms specimen and 0.81 voxels (2.10 µm) for the 64 ms specimen (Table S1). The errors obtained for the displacements in the 512 ms were lower than those for the 64 ms, due to the decreased of image quality. A trend could be observed for both specimens, the higher the sub-volume size, the lower the random errors. Furthermore, the multi-pass approach reduced the random errors compared to a single-pass using the same sub-volume size.

Table S1. Random errors for the three displacement components for the highly- and lowly-irradiated specimens (512 ms and 64 ms).

Sub-volume (voxel)	**Differential displacement random errors (µm)**					
	512 ms			**64 ms**		
	X	Y	Z	X	Y	Z
16	0.78	0.75	0.84	2.11	2.08	0.86
32	0.74	0.81	0.89	1.99	1.92	0.56
48	0.69	0.66	0.79	1.99	1.86	0.41
64	0.65	0.52	0.74	1.97	1.77	0.31
80	0.60	0.41	0.69	1.90	1.59	0.23
96	0.58	0.33	0.65	1.90	1.54	0.20
112	0.62	0.33	0.65	1.93	1.57	0.20
Multipass (64)	0.62	0.38	0.60	1.96	1.68	0.24

As expected from previous studies on bone [33,47], the strain uncertainties of the DVC had decreasing trends with respect to the sub-volume size, and the values of the mean value of the differential strain were larger than the standard deviation (Figure S1). The mean differential strain value ranged between 3856 µε and 329 µε for the 512 ms samples and between 6200 µε and 731 µε for the 64 ms sample, in sub-volumes of 16 to 112 voxels (41.6 to 291.2 µm). The standard deviation of the differential strain value ranged between 2192 µε and 119 µε for the 512 ms samples and between 3721 µε and 269 µε for the 64 ms sample, in the same sub-volumes. The multi-pass approach provided a lower level of uncertainties compared to the same sub-volume using a single-pass.

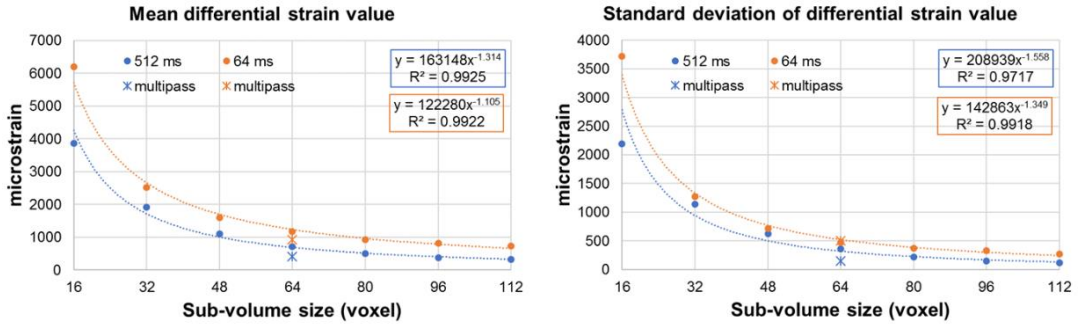

Figure S1. Relationship between the mean differential strain value (right) and standard deviation of the differential strain value (left) with the sub-volume size for both specimens and corresponding power laws. Power laws and coefficients of determination (R2) are also reported.

Supplementary material S2: Estimation of radiation exposures

Introduction

Trabecular bone specimens in this study underwent several consecutive tomograms using high-energy synchrotron radiation, which resulted in a progressive radiation dose accumulation within the bone tissue. To the author's knowledge only two studies [16,63] addressed a similar procedure for estimating the radiation dose absorbed by bone samples subjected to SR-microCT. However, the proposed formulation considered a uniform distribution for the absorption of X-rays within the samples. Therefore, the manuscript used a simulation using FLUKA Monte Carlo code [42] of the delivered dose during the acquisition of one tomography scan, providing not only the average dose absorbed by the specimen, but also the local distribution. Nevertheless, an estimation of the delivered dose was also carried out and presented in this text following the proposed formulation in previous studies and compared to average simulated dose.

Simulated geometry (FLUKA Monte Carlo)

The geometry simulated in FLUKA consisted on a trabecular bone sample within the loading device as described in the manuscript. A scheme of the simulated geometry is shown in Figure S1-I, in which a different colour is assigned to each material. The bone specimen was assumed as a cylinder (orange, 4 mm diameter, 10 mm length, density of 0.5 g/cm^3 [43]) placed in the centre of the environmental chamber (40 mm inner diameter, 3 mm thickness) made of glassy-carbon (grey, density of 1.5 g/cm^3) and filled with saline solution (blue, density of 1 g/cm^3). The absorption profile (Fig S2-II) was obtained from the simulation and the transmitted (I) and incident (I0) X-ray intensities where calculated as the intensities after and before the bone, respectively, where the bone sample (4 mm in diameter, 10 mm in length) was positioned in the centre of the geometry.

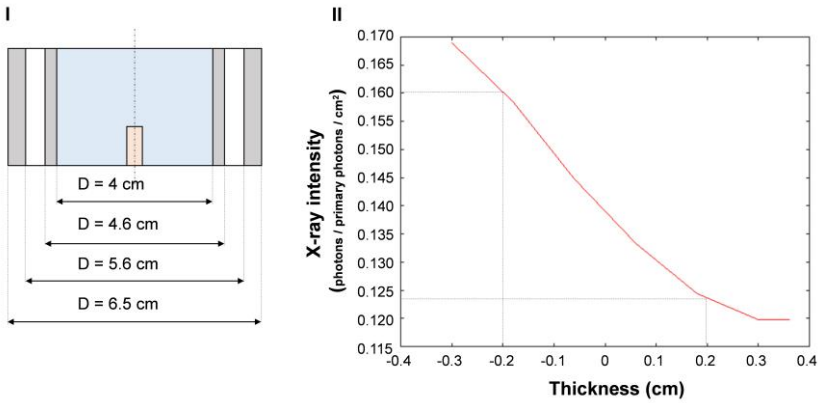

Beam parameters

The average photon energy and photon flux during the experiment was estimated using SPECTRA code [41] as described in the manuscript, using a 2 x 2 mm aperture 220 m after the X-ray source. Filters (1.3 mm pyrolytic graphite, 3.2 mm aluminium and 60 µm steel) and reflectivity of the platinum mirror used during the experiment were considered. An average beam energy, $E = 28.93\ keV$ and photon flux, $\Phi = 4.9 \times 10^{13}\ photons/s$ was calculated.

Average simulated dose (FLUKA Monte Carlo)

The delivered dose was simulated for the previously described geometry. The simulation results have an error below 15%, such an error is associated to the standard deviation of the energy deposition of the simulated X-ray when interacts with an object. In fact, it is the statistical error associated to the probability of absorption in matter. From the simulation, the absorption profile (Figure S2-II) and the energy deposition (Figure 5) is calculated. The average dose rate in the target volume was obtained as an output of the simulation $\dot{d}_{average,simulated} = 35\ Gy\ s^{-1}$ ($6.4\ Gy\ s^{-1}$ standard deviation).

Estimated dose (previous formulation)

1. Estimation of mass attenuation coefficient, α

The mass attenuation coefficient was calculated using the Beer-Lambert Law [64]:

$$T = \frac{I}{I_0} = e^{-\alpha\rho l}$$

Where *T* is the transmission of X-rays through a material, of thickness *l*, α is the mass attenuation coefficient ($cm^2\ g^{-1}$) and *ρ* is the density ($g\ cm^{-3}$).

2. Estimation of the flux density, ψ

Due to the cylindrical geometry of the bone specimen, the X-ray path through it is not constant. Therefore, a numerical integration is performed splitting half of the cylinder (considering symmetry) in 90 steps of 1 degree. For each angle, the surface seen by the incident X-rays can be calculated as:

$$S_i = \sin \Delta\theta_i \times r \times h$$

Where S_i is the surface seen by the X-rays at each angle θ_i, r is the radius of the specimen and h is its height.

The flux at the surface, ψ_{surf} is then calculated from the value of the photon flux, Φ(photons s^{-1}), simulated using SPECTRA code [41]:

$$\psi_{surf,i} = S_i \times I_o \times \Phi$$

The thickness of the sample, l, varies as a function of the angle θ.

$$l_i = \cos\vartheta_i \times r \times 2$$

The transmission, T, of X-rays through the cylinder is expressed using the Beer-Lambert Law:

$$T_i = e^{-\alpha\rho l_i}$$

The fraction of X-rays absorbed, A, by the samples is given as (1-T). The flux absorbed $\psi_{a,i}$ (photons s^{-1}) is then calculated as:

$$\psi_{a,i} = A \times \psi_{surf,i}$$

Doing a numerical integration of the flux absorbed at each angular step, the total absorbed flux, ψ (photons s^{-1}) is obtained:

$$\psi_T = 2 \times \sum_{i=1}^{90} \psi_{a,i}$$

And the flux density, ψ (photons/s/cm^3), is obtained dividing the total flux divided by the volume of the specimen, V:

$$\psi = {\psi_T}/{V}$$

3. Estimation of the radiation dose

To estimate the radiation dose absorbed by the sample, which is measured is grays (1 Gy ≡ 1 J kg^{-1}), the radiation flux density is converted into an energy density, E_p (J s^{-3} cm-^{3}).

$$E_p = \psi \times 1.6 \times \dot{10}^{-19} {J}/{eV} \times E$$

Where E is the energy of the beam in eV and the dose rate, $\dot{d}$ (Gy s^{-1}), can be obtained as:

$$\dot{d} = \frac{E_p}{\rho} = 43.7\ Gy\ s^{-1}$$

Comparison

The total irradiation dose, d, received during each exposure can be then found from the dose rate and the total exposure time during image acquisition.

$$d = \dot{d} \times t$$

A comparison between the accumulated dose for each specimen during the seven sequential tomographies is reported in Table S2, computed varying the exposure time.

Table S2. Nominal radiation absorbed by each specimen after each loading cycle, calculated by varying the exposure time. Values were truncated to one decimal place.

Exposure time	**512 ms**						
Load cycles	1	2	3	4	5	6	7
Average accumulated dose simulated (kGy)	32.9	65.9	98.8	131.8	164.7	197.7	230.6
Estimated accumulated dose (kGy)	41.1	82.3	123.4	164.6	205.7	246.8	288.0
Exposure time	**256 ms**						
Load cycles	1	2	3	4	5	6	7
Average accumulated dose simulated (kGy)	16.8	33.6	50.5	67.3	84.1	100.9	117.7
Estimated accumulated dose (kGy)	21.0	42.0	63.0	84.0	105.0	126.0	147.0
Exposure time	**128 ms**						
Load cycles	1	2	3	4	5	6	7
Average accumulated dose simulated (kGy)	8.8	17.5	26.3	35.0	43.8	52.5	61.3
Estimated accumulated dose (kGy)	10.9	21.9	32.8	43.7	54.7	65.6	76.5
Exposure time	**64 ms**						
Load cycles	1	2	3	4	5	6	7
Average accumulated dose simulated (kGy)	4.7	9.5	14.2	18.9	23.6	28.4	33.1
Estimated accumulated dose (kGy)	5.9	11.8	17.7	23.6	29.5	35.4	41.3

Discussion

The average dose simulated in this study is in well agreement to the estimated dose using mathematical formulation previously proposed [16,63]. The estimation presented herein assumed that the X-rays pierce a constant thickness of bone material (a constant value is used in the Beer-Lambert Law), corresponding to the sample diameter. However, due to the cylindrical geometry of the specimen, X-rays go through a different thickness at the centre of the specimen while off centre. Therefore, the extra thickness assumed in this estimation overestimate the dose absorbed by the specimen compared to the simulation using FLUKA Monte Carlo.

References

[1] C.M.J. de Bakker, W.-J. Tseng, Y. Li, H. Zhao, X.S. Liu, Clinical Evaluation of Bone Strength and Fracture Risk, Curr. Osteoporos. Rep. 15 (2017) 32–42. doi:10.1007/s11914-017-0346-3.

[2] M.A. Hammond, M.A. Gallant, D.B. Burr, J.M. Wallace, Nanoscale changes in collagen are reflected in physical and mechanical properties of bone at the microscale in diabetic rats, Bone. 60 (2014) 26–32. doi:10.1016/j.bone.2013.11.015.

[3] A. Karunaratne, C.R. Esapa, J. Hiller, A. Boyde, R. Head, J.H.D. Bassett, N.J. Terrill, G.R. Williams, M.A. Brown, P.I. Croucher, S.D.M. Brown, R.D. Cox, A.H. Barber, R. V.

Thakker, H.S. Gupta, Significant deterioration in nanomechanical quality occurs through incomplete extrafibrillar mineralization in rachitic bone: Evidence from in-situ synchrotron X-ray scattering and backscattered electron imaging, J. Bone Miner. Res. 27 (2012) 876–890. doi:10.1002/jbmr.1495.

[4] M.L. Bouxsein, Bone quality: where do we go from here?, Osteoporos. Int. 14 (2003) 118–127. doi:10.1007/s00198-003-1489-x.

[5] J.Y. Rho, L. Kuhn-Spearing, P. Zioupos, Mechanical properties and the hierarchical structure of bone, Med. Eng. Phys. 20 (1998) 92–102. doi:10.1016/S1350-4533(98)00007-1.

[6] S. Ma, O. Boughton, A. Karunaratne, A. Jin, J. Cobb, U. Hansen, R. Abel, Synchrotron Imaging Assessment of Bone Quality, Clin. Rev. Bone Miner. Metab. 14 (2016) 150–160. doi:10.1007/s12018-016-9223-3.

[7] S. Li, E. Demirci, V. V. Silberschmidt, Variability and anisotropy of mechanical behavior of cortical bone in tension and compression, J. Mech. Behav. Biomed. Mater. 21 (2013) 109–120. doi:10.1016/j.jmbbm.2013.02.021.

[8] J.S. Nyman, H. Leng, X. Neil Dong, X. Wang, Differences in the mechanical behavior of cortical bone between compression and tension when subjected to progressive loading, J. Mech. Behav. Biomed. Mater. 2 (2009) 613–619. doi:10.1016/j.jmbbm.2008.11.008.

[9] C. Öhman, M. Baleani, E. Perilli, E. Dall'Ara, S. Tassani, F. Baruffaldi, M. Viceconti, Mechanical testing of cancellous bone from the femoral head: Experimental errors due to off-axis measurements, J. Biomech. 40 (2007) 2426–2433. doi:10.1016/j.jbiomech.2006.11.020.

[10] U. Wolfram, H.J. Wilke, P.K. Zysset, Damage accumulation in vertebral trabecular bone depends on loading mode and direction, J. Biomech. 44 (2011) 1164–1169. doi:10.1016/j.jbiomech.2011.01.018.

[11] L. Babout, W. Ludwig, E. Maire, J.Y. Buffiere, J.Y. Buffi, Damage assessment in metallic structural materials using high resolution synchrotron X-ray tomography, Nucl. Instruments Methods Phys. Res. Sect. B Beam Interact. with Mater. Atoms. 200 (2003) 303–307. doi:10.1016/S0168-583X(02)01692-0.

[12] J.A. Elliott, A.H. Windle, J.R. Hobdell, G. Eeckhaut, R.J. Oldman, W. Ludwig, E. Boller, P. Cloetens, J. Baruchel, In-situ deformation of an open-cell flexible polyurethane foam characterised by 3D computed microtomography, J. Mater. Sci. 37 (2002) 1547–1555. doi:10.1023/A:1014920902712.

[13] R. Voide, P. Schneider, M. Stauber, P. Wyss, M. Stampanoni, U. Sennhauser, G.H. van Lenthe, R. Müller, Time-lapsed assessment of microcrack initiation and propagation in murine cortical bone at submicrometer resolution, Bone. 45 (2009) 164–173. doi:10.1016/j.bone.2009.04.248.

[14] P.J. Thurner, P. Wyss, R. Voide, M. Stauber, M. Stampanoni, U. Sennhauser, R. Müller, Time-lapsed investigation of three-dimensional failure and damage

accumulation in trabecular bone using synchrotron light, Bone. 39 (2006) 289–299. doi:10.1016/j.bone.2006.01.147.

[15] A. Larrue, A. Rattner, N. Laroche, L. Vico, F. Peyrin, Feasibility of micro-crack detection in human trabecular bone images from 3D synchrotron microtomography, Annu. Int. Conf. IEEE Eng. Med. Biol. - Proc. (2007) 3918–3921. doi:10.1109/IEMBS.2007.4353190.

[16] H.D. Barth, M.E. Launey, A.A. MacDowell, J.W. Ager, R.O. Ritchie, On the effect of X-ray irradiation on the deformation and fracture behavior of human cortical bone, Bone. 46 (2010) 1475–1485. doi:10.1016/j.bone.2010.02.025.

[17] H.D. Barth, E.A. Zimmermann, E. Schaible, S.Y. Tang, T. Alliston, R.O. Ritchie, Characterization of the effects of x-ray irradiation on the hierarchical structure and mechanical properties of human cortical bone, Biomaterials. 32 (2011) 8892–8904. doi:10.1016/j.biomaterials.2011.08.013.

[18] H. Nguyen, D.A.F. Morgan, M.R. Forwood, Sterilization of allograft bone: Effects of gamma irradiation on allograft biology and biomechanics, Cell Tissue Bank. 8 (2007) 93–105. doi:10.1007/s10561-006-9020-1.

[19] J.Y. Buffiere, E. Maire, J. Adrien, J.P. Masse, E. Boller, *In situ* experiments with X ray tomography: An attractive tool for experimental mechanics, Proc. Soc. Exp. Mech. Inc. 67 (2010) 289–305. doi:10.1007/s11340-010-9333-7.

[20] A. Nazarian, R. Müller, Time-lapsed microstructural imaging of bone failure behavior, J. Biomech. 37 (2004) 55–65. doi:10.1016/S0021-9290(03)00254-9.

[21] B.K. Bay, T.S. Smith, D.P. Fyhrie, M. Saad, Digital volume correlation: Three-dimensional strain mapping using X-ray tomography, Exp. Mech. 39 (1999) 217–226. doi:10.1007/BF02323555.

[22] L. Liu, E.F. Morgan, Accuracy and precision of digital volume correlation in quantifying displacements and strains in trabecular bone, J. Biomech. 40 (2007) 3516–3520. doi:10.1016/j.jbiomech.2007.04.019.

[23] B.C. Roberts, E. Perilli, K.J. Reynolds, Application of the digital volume correlation technique for the measurement of displacement and strain fields in bone: A literature review, J. Biomech. 47 (2014) 923–934. doi:10.1016/j.jbiomech.2014.01.001.

[24] F. Gillard, R. Boardman, M. Mavrogordato, D. Hollis, I. Sinclair, F. Pierron, M. Browne, The application of digital volume correlation (DVC) to study the microstructural behaviour of trabecular bone during compression, J. Mech. Behav. Biomed. Mater. 29 (2014) 480–499. doi:10.1016/j.jmbbm.2013.09.014.

[25] E. Dall'Ara, D. Barber, M. Viceconti, About the inevitable compromise between spatial resolution and accuracy of strain measurement for bone tissue: A 3D zero-strain study, J. Biomech. 47 (2014) 2956–2963. doi:10.1016/j.jbiomech.2014.07.019.

[26] D. Christen, A. Levchuk, S. Schori, P. Schneider, S.K. Boyd, R. Müller, Deformable image registration and 3D strain mapping for the quantitative assessment of cortical

bone microdamage, J. Mech. Behav. Biomed. Mater. 8 (2012) 184–193. doi:10.1016/j.jmbbm.2011.12.009.

[27] A.I. Hussein, Z.D. Mason, E.F. Morgan, Presence of intervertebral discs alters observed stiffness and failure mechanisms in the vertebra, J. Biomech. 46 (2013) 1683–1688. doi:10.1016/j.jbiomech.2013.04.004.

[28] A.I. Hussein, P.E. Barbone, E.F. Morgan, Digital volume correlation for study of the mechanics of whole bones, Procedia IUTAM. 4 (2012) 116–125. doi:10.1016/j.piutam.2012.05.013.

[29] V. Danesi, G. Tozzi, L. Cristofolini, Application of digital volume correlation to study the efficacy of prophylactic vertebral augmentation, Clin. Biomech. 39 (2016) 14–24. doi:10.1016/j.clinbiomech.2016.07.010.

[30] G. Tozzi, V. Danesi, M. Palanca, L. Cristofolini, Elastic Full-Field Strain Analysis and Microdamage Progression in the Vertebral Body from Digital Volume Correlation, Strain. 52 (2016) 446–455. doi:10.1111/str.12202.

[31] K. Madi, G. Tozzi, Q.H. Zhang, J. Tong, A. Cossey, A. Au, D. Hollis, F. Hild, Computation of full-field displacements in a scaffold implant using digital volume correlation and finite element analysis, Med. Eng. Phys. 35 (2013) 1298–1312. doi:10.1016/j.medengphy.2013.02.001.

[32] G. Tozzi, Q.H. Zhang, J. Tong, Microdamage assessment of bone-cement interfaces under monotonic and cyclic compression, J. Biomech. 47 (2014) 3466–3474. doi:10.1016/j.jbiomech.2014.09.012.

[33] M. Palanca, A.J. Bodey, M. Giorgi, M. Viceconti, D. Lacroix, L. Cristofolini, E. Dall'Ara, Local displacement and strain uncertainties in different bone types by digital volume correlation of synchrotron microtomograms, J. Biomech. c (2017). doi:10.1016/j.jbiomech.2017.04.007.

[34] H.H. Bayraktar, E.F. Morgan, G.L. Niebur, G.E. Morris, E.K. Wong, T.M. Keaveny, Comparison of the elastic and yield properties of human femoral trabecular and cortical bone tissue, J. Biomech. 37 (2004) 27–35. doi:10.1016/S0021-9290(03)00257-4.

[35] G.L. Niebur, M.J. Feldstein, J.C. Yuen, T.J. Chen, T.M. Keaveny, High-resolution finite element models with tissue strength asymmetry accurately predict failure of trabecular bone, J. Biomech. 33 (2000) 1575–1583. doi:10.1016/S0021-9290(00)00149-4.

[36] T.M. Keaveny, R.E. Borchers, L.J. Gibson, W.C. Hayes, Theoretical analysis of the experimental artifact in trabecular bone compressive modulus, J. Biomech. 25 (1993) 599–607.

[37] C. Rau, U. Wagner, Z. Pešić, A. De Fanis, Coherent imaging at the Diamond beamline I13, Phys. Status Solidi Appl. Mater. Sci. 208 (2011) 2522–2525. doi:10.1002/pssa.201184272.

[38] R.C. Atwood, A.J. Bodey, S.W.T. Price, M. Basham, M. Drakopoulos, A high-throughput system for high-quality tomographic reconstruction of large datasets at

Diamond Light Source, Philos. Trans. R. Soc. A Math. Phys. Eng. Sci. 373 (2015). doi:10.1098/rsta.2014.0398.

[39] T.L.A. Moore, L.J. Gibson, Microdamage Accumulation in Bovine Trabecular Bone in Uniaxial Compression, J. Biomech. Eng. 124 (2002) 63. doi:10.1115/1.1428745.

[40] M. Doube, M.M. Klosowski, I. Arganda-Carreras, F.P. Cordelières, R.P. Dougherty, J.S. Jackson, B. Schmid, J.R. Hutchinson, S.J. Shefelbine, BoneJ: Free and extensible bone image analysis in ImageJ, Bone. 47 (2010) 1076–1079. doi:10.1016/j.bone.2010.08.023.

[41] T. Tanaka, H. Kitamura, SPECTRA: A synchrotron radiation calculation code, J. Synchrotron Radiat. 8 (2001) 1221–1228. doi:10.1107/S090904950101425X.

[42] G. Battistoni, F. Cerutti, A. Fassò, A. Ferrari, S. Muraro, J. Ranft, S. Roesler, P.R. Sala, The FLUKA code: Description and benchmarking, AIP Conf. Proc. 896 (2007) 31–49. doi:10.1063/1.2720455.

[43] A. Nafei, C.C. Danielsen, A. Odgaard, F. Linde, I. Hvid, Properties of growing trabecular ovine bone. Part I: mechanical and physical properties., J. Bone Joint Surg. Br. 82 (2000) 910–920.

[44] M. Palanca, G. Tozzi, L. Cristofolini, M. Viceconti, E. Dall'Ara, 3D Local Measurements of Bone Strain and Displacement: Comparison of Three Digital Volume Correlation Approaches., J. Biomech. Eng. 137 (2015) 1–14. doi:10.1115/1.4030174.

[45] G. Tozzi, Q.H. Zhang, J. Tong, 3D real-time micromechanical compressive behaviour of bone-cement interface: Experimental and finite element studies, J. Biomech. 45 (2012) 356–363. doi:10.1016/j.jbiomech.2011.10.011.

[46] G. Tozzi, E. Dall, M. Palanca, M. Curto, F. Innocente, L. Cristofolini, Strain uncertainties from two digital volume correlation approaches in prophylactically augmented vertebrae : Local analysis on bone and cement- bone microstructures, J. Mech. Behav. Biomed. Mater. 67 (2017) 117–126. doi:10.1016/j.jmbbm.2016.12.006.

[47] E. Dall'Ara, M. Peña-Fernández, M. Palanca, M. Giorgi, L. Cristofolini, G. Tozzi, Precision of DVC approaches for strain analysis in bone imaged with μCT at different dimensional levels, Front. Mater. 4:31 (2017). doi:10.3389/fmats.2017.00031.

[48] M. Palanca, L. Cristofolini, E. Dall'Ara, M. Curto, F. Innocente, V. Danesi, G. Tozzi, Digital volume correlation can be used to estimate local strains in natural and augmented vertebrae: an organ-level study, J. Biomech. 49 (2016) 3882–3890. doi:10.1016/j.jbiomech.2016.10.018.

[49] S.M. Ross, Peirce's criterion for the elimination of suspect experimental data, J. Eng. Technol. 20 (2003) 1–12. http://classes.engineering.wustl.edu/2009/fall/che473/handouts/OutlierRejection.pdf.

[50] A. Singhal, A.C. Deymier-Black, J.D. Almer, D.C. Dunand, Effect of high-energy X-ray doses on bone elastic properties and residual strains, J. Mech. Behav. Biomed. Mater. 4 (2011) 1774–1786. doi:10.1016/j.jmbbm.2011.05.035.

[51] L. Grassi, H. Isaksson, Extracting accurate strain measurements in bone mechanics: A critical review of current methods, J. Mech. Behav. Biomed. Mater. 50 (2015) 43–54. doi:10.1016/j.jmbbm.2015.06.006.

[52] T.T. Böhlen, F. Cerutti, M.P.W. Chin, A. Fassò, A. Ferrari, P.G. Ortega, A. Mairani, P.R. Sala, G. Smirnov, V. Vlachoudis, The FLUKA Code: Developments and challenges for high energy and medical applications, Nucl. Data Sheets. 120 (2014) 211–214. doi:10.1016/j.nds.2014.07.049.

[53] F. Botta, A. Mairani, R.F. Hobbs, A. Vergara Gil, M. Pacilio, K. Parodi, M. Cremonesi, M.A. Coca Pérez, A. Di Dia, M. Ferrari, F. Guerriero, G. Battistoni, G. Pedroli, G. Paganelli, L.A. Torres Aroche, G. Sgouros, Use of the FLUKA Monte Carlo code for 3D patient-specific dosimetry on PET-CT and SPECT-CT images., Phys. Med. Biol. 58 (2013) 8099–120. doi:10.1088/0031-9155/58/22/8099.

[54] K. Parodi, A. Ferrari, F. Sommerer, H. Paganetti, Clinical CT-based calculations of dose and positron emitter distributions in proton therapy using the FLUKA Monte Carlo code, Phys. Med. Biol. 52 (2007) 3369–3387. doi:10.1088/0031-9155/52/12/004.

[55] Z. Wu, W. Lei, Y. Hu, H. Wang, S. Wan, Z. Ma, H. Sang, S. Fu, Y. Han, Effect of ovariectomy on BMD, micro-architecture and biomechanics of cortical and cancellous bones in a sheep model, Med. Eng. Phys. 30 (2008) 1112–1118. doi:10.1016/j.medengphy.2008.01.007.

[56] A. Karunaratne, L. Xi, L. Bentley, D. Sykes, A. Boyde, C.T. Esapa, N.J. Terrill, S.D.M. Brown, R.D. Cox, R. V. Thakker, H.S. Gupta, Multiscale alterations in bone matrix quality increased fragility in steroid induced osteoporosis, Bone. 84 (2016) 15–24. doi:10.1016/j.bone.2015.11.019.

[57] S. Ma, E.L. Goh, A. Jin, R. Bhattacharya, O.R. Boughton, B. Patel, A. Karunaratne, N.T. Vo, R. Atwood, J.P. Cobb, U. Hansen, R.L. Abel, Long-term effects of bisphosphonate therapy : perforations , microcracks and mechanical properties, Nat. Publ. Gr. (2017) 1–10. doi:10.1038/srep43399.

[58] A.J. Bodey, C. Rau, Launch of the I13-2 data beamline at the Diamond Light Source synchrotron, J. Phys. Conf. Ser. 849 (2017). doi:10.1088/1742-6596/849/1/012038.

[59] J. Schindelin, I. Arganda-Carreras, E. Frise, V. Kaynig, M. Longair, T. Pietzsch, S. Preibisch, C. Rueden, S. Saalfeld, B. Schmid, J.-Y. Tinevez, D.J. White, V. Hartenstein, K. Eliceiri, P. Tomancak, A. Cardona, Fiji: an open-source platform for biological-image analysis, Nat Meth. 9 (2012) 676–682. doi:10.1038/nmeth.2019.

[60] E.H.W. Meijering, W.J. Niessen, M.A. Viergever, Quantitative Evaluation of Convolution-Based Methods for Medical Image Interpolation, Med. Image Anal. 5 (2001) 111–126. doi:doi.org/10.1016/S1361-8415(00)00040-2.

[61] N. Otsu, A threshold selection method from gray-level histograms, IEEE Trans. Syst. Man. Cybern. 9 (1979) 62–66. doi:10.1109/TSMC.1979.4310076.

[62] A. Odgaard, H.J.G. Gundersen, Quantification of connectivity in cancellous bone, with special emphasis on 3-D reconstructions, Bone. 14 (1993) 173–182. doi:https://doi.org/10.1016/8756-3282(93)90245-6.

[63] A. Pacureanu, M. Langer, E. Boller, P. Tafforeau, F. Peyrin, Nanoscale imaging of the bone cell network with synchrotron X-ray tomography: optimization of acquisition setup., Med. Phys. 39 (2012) 2229–38. doi:10.1118/1.3697525.

[64] F. Swinehart, The Beer-Lambert, J. Chem. Educ. 39 (1962) 333–335. doi:10.1021/ed039p333.

4.2. Preservation of bone tissue integrity with temperature control

Marta Peña Fernández[1], Enrico Dall'Ara[2], Alexander P Kao[1], Andrew J Bodey[3], Aikaterina Karali[1], Gordon W Blunn[4], Asa H Barber[1,5], Gianluca Tozzi[1]

[1] *Zeiss Global Centre, School of Engineering, University of Portsmouth, Portsmouth, UK.*
[2] *Department of Oncology and Metabolism and INSIGNEO institute for in silico medicine, University of Sheffield, Sheffield, UK.*
[3] *Diamond Light Source, Oxfordshire, OX11 0QX, UK.*
[4] *School of Pharmacy and Biomedical Sciences, University of Portsmouth, Portsmouth, UK.*
[5] *School of Engineering, London South Bank University, London, UK.*

Published in:
Materials, 2018, 11, 2155
doi: 10.3390/ma11112155
as *"Preservation of bone tissue integrity with temperature control for in situ SR-microCT experiments".*

Abstract

Digital volume correlation (DVC), combined with *in situ* synchrotron micro-computed tomography (SR-microCT) mechanics, allows for 3D full-field strain measurement in bone at the tissue level. However, long exposures to SR radiation are known to induce bone damage and reliable experimental protocols able to preserve tissue properties are still lacking. This study aimed to propose a proof-of-concept methodology to retain bone tissue integrity, based on residual strain determination using DVC, by decreasing the environmental temperature during *in situ* SR-microCT testing. Compact and trabecular bone specimens underwent five consecutive full tomographic data collections either at room temperature or 0°C. Lowering the temperature seemed to reduce microdamage in trabecular bone but had minimal effect on compact bone. A consistent temperature gradient was measured at each exposure period, and its prolonged effect in time may induce localised collagen denaturation and subsequent damage. DVC provided useful information on irradiation-induced microcrack initiation and propagation. Future work is necessary to apply these findings to *in situ* SR-microCT mechanical tests, and to establish protocols aiming to minimise the SR irradiation-induced damage of bone.

Keywords: Bone; X-ray radiation; tissue damage; SR-microCT; digital volume correlation; temperature control.

4.2.1. Introduction

Bone is a highly heterogenous, anisotropic and hierarchical material that is organised at various levels to optimise its mechanical competence [1]. Thus, it is essential to understand the mechanics of its different components and the structural relationships between them at the different dimensional scales [2–4]. This is of fundamental importance since many musculoskeletal pathologies, such as osteoporosis, are associated with alterations in bone quality at the micro- and nanoscale [5]. Therefore, novel techniques aim at characterising the deformation mechanisms of bone in a three-dimensional (3D) manner, from apparent to tissue level, and establishing their links with bone structure [6–8].

To date, the only experimental method that allows for 3D strain measurements within the bone structure is digital volume correlation (DVC) in combination with *in situ* microcomputed tomography (microCT) testing [9–11]. DVC has been widely used in bone mechanics to investigate full-field displacement and strain in cortical [12] and trabecular [13,14] bone at different dimensional scales and loading conditions, providing a unique insight to the 3D deformation of such complex material. Nevertheless, in order to characterise bone failure mechanisms at the tissue level, high-resolution microCT is needed [11,15,16]. High-energy synchrotron radiation (SR) microCT has proven to provide fast high-quality image acquisition of bone microstructure with high spatial resolution (~1 μm), and together with *in situ* mechanical studies, it has allowed for a detailed coupling between 3D bone microstructure and deformation [6,17,18]. Furthermore, recent studies have combined *in situ* SR-microCT mechanics with DVC to investigate the internal strain and microdamage evaluation of cortical bone [12], trabecular bone [14] and bone-biomaterial systems [19], enhancing the understanding of bone failure at the microscale.

However, it is known that high exposures to SR X-ray radiation lead to a deterioration in the mechanical properties of bone as a consequence of collagen matrix degradation [20,21]. Similarly, ionising radiation, such as gamma rays, commonly used to sterilise bone allografts [22], and X-rays, negatively affects the mechanical and biological properties of the tissue by the degradation of the collagen present in the bone matrix [20,23–27]. Specifically, radiation produces reactive free radicals by the radiolysis of water molecules, which splits the polypeptides chains of the collagen and induces cross-linking reactions, causing collagen denaturation [28–30]. In clinical practice, the adverse effects of gamma radiation during sterilization have been successfully reduced by irradiating the bone while frozen [31,32]. Lowering the temperature is beneficial, as it reduces the mobility of free radicals and, therefore, their ability to interact with collagen molecules [33,34]. Particularly, Hamer et al. [31] observed that cortical bone irradiated at low temperatures (−78 °C) was less brittle and had less collagen damage when compared to the bone irradiated at room temperature. Additionally, Cornu et al. [32] showed that ultimate strength, stiffness and work to failure were not reduced significantly on trabecular bone irradiated under dry ice. In the field of high-resolution X-ray imaging of biological samples, protection against radiation damage is also

essential to preserve their integrity. Cryofixation methods have been demonstrated to protect biological samples from visible structural damage and have enabled cryo-soft X-ray tomography (cryo-SXT) to become the only imaging modality able to provide nanoscale 3D information of whole cells in a near-native state [35–37]. However, soft X-rays (~0.1–1 keV) are not able to penetrate bone tissue, nor can they be accommodated for *in situ* mechanics protocols. Furthermore, cryotechniques involve freeze-drying of the specimens at −150 °C and have been shown to induce microdamage and significantly reduce torsional strength, compressive yield stress and compressive modulus of cortical bone [32,38–40]. Hence, low temperatures positively influence bone preservation during irradiation. However, mechanical testing of bone in such conditions, below the freezing temperature of water, cannot be conducted, as the mechanical properties of bone would be affected. In fact, due to the large water content of bone, ice crystals may cause structural damage to the tissue [23].

Therefore, it is essential to define some guidelines in order to preserve bone tissue integrity and mechanics during *in situ* SR-microCT experiments. Very recently, DVC applied to SR-microCT images of trabecular bone was used to investigate the influence of SR irradiation-induced microdamage on the bone's apparent mechanics [14]. Microcracks were detected in the bone tissue after long exposures to SR radiation, despite the apparent elastic properties remaining unaltered. Also, high local strain levels were observed that corresponded to the microdamaged areas. However, reducing the total exposure to SR X-ray radiation was able to preserve bone integrity and plasticity. The results of that study [14] provided important information on bone degradation and residual strain accumulation resulting from SR X-ray exposure, but the study had some limitations. Firstly, bone specimens were subjected to cyclic mechanical loading during SR-microCT imaging; thus, the full-field strain measurements were not entirely due to SR irradiation but also to the mechanics. In fact, DVC results showed that even at reduced exposures to SR radiation, there were some regions of high strain concentration, which may have been induced by the mechanical load and further enhanced by the irradiation. Secondly, reducing the total exposure by decreasing the exposure time per projection during SR-microCT acquisition notably decreased image quality and, consequently, DVC performance. Hence, further evaluation and optimisation of the imaging setup is needed in order to preserve bone integrity while maximising image quality for reliable DVC-computed full-field measurement within the bone tissue.

In this context, there is a clear need to define experimental protocols for *in situ* SR-microCT mechanics able to preserve bone tissue integrity against SR X-ray radiation-induced damage, exploiting the research conducted in different fields. The aim of this study is, therefore, to propose a novel proof-of-concept methodology to retain bone tissue integrity, based on residual strain determination via DVC, by decreasing the environmental temperature during SR-microCT testing.

4.2.2. Materials and methods

4.2.2.1. Specimen preparation

Samples were obtained from a fresh bovine femur. A section (20 mm in thickness) was cut with a hacksaw from the proximal diaphysis of the femur and a diamond-coated core drill was used to extract 4 mm cylindrical compact (n = 2) and 6 mm trabecular (n = 2) bone specimens under constant water irrigation. The ends of the cores were trimmed to achieve a 12 mm length for the compact and a 16 mm length for the trabecular bone specimens. Brass endcaps were used to embed the ends of the specimens (~2 mm), ensuring perpendicularity between the bone cores and the endcap bases. Samples were kept frozen at −20 °C and thawed for approximately 2 h in saline solution at room temperature before imaging.

4.2.2.2. SR-microCT imaging

SR-microCT was performed at the Diamond-Manchester Imaging Branchline I13-2 (Figure 1a) of Diamond Light Source (DLS), Oxfordshire, UK. A partially coherent polychromatic 'pink' beam (5–35 keV) of parallel geometry was generated by an undulator from an electron storage ring of 3.0 GeV. The undulator gap was set to 5 mm for data collection and, to limit bone damage, 11 mm for low-dose alignment. The beam was reflected from the platinum stripe of a grazing-incidence focusing mirror and high-pass filtered with 1.4 mm pyrolytic graphite, 3.2 mm aluminium and 50 µm steel. The propagation (sample-to-scintillator) distance was approximately 40 mm. Images were recorded by a sCMOS (2560 × 2160 pixels) pco.edge 5.5 (PCO AG, Kelheim, Germany) detector which was coupled to a 500 µm-thick $CdWO_4$ scintillator and a visual light microscope with a 4× objective lens, providing a total magnification of 8×. This resulted in an effective voxel size of 0.81 µm and a field of view of 2.1 × 1.8 mm^2. A total of 1801 projection images were collected over 180° of continuous rotation ('fly-scan'), with an exposure time of 512 ms per projection (11 ms overhead per exposure), adopting the imaging conditions reported in [14]. The total scanning time was approximately 15 min. The projection images were flat-field- and dark-field-corrected prior to image reconstruction using SAVU [41], which incorporated ring artefact suppression and optical distortion correction [42]. Each specimen underwent five full consecutive tomographic data collections.

4.2.2.3. *In situ* testing and temperature control

Specimens were placed within an *in situ* testing device (CT5000-TEC, Deben, Bury Saint Edmunds, UK) and kept in saline solution during image acquisition (Figure 1a). The device is equipped with a 5 kN load cell, Peltier heated and cooled jaws with a temperature range from −20 °C to +160 °C and an environmental chamber. A small preload (2–5 N) was first applied to ensure good end-contact and avoid motion artefacts during tomographic acquisition, after which the actuator was stopped, and the jaws' positions held throughout the test. Bone specimens (N = 1 compact and N = 1 trabecular) were imaged at room temperature (Troom ≈ 23 °C) and at ~0 °C (N = 1 compact and N = 1 trabecular) by cooling

and keeping the Peltier jaws at the target temperature. A thermocouple (Type K, RS Pro, RS Components, UK) was also attached to the surface of the bone samples and was used during the *in situ* test to monitor the temperature directly at the tissue during image acquisition and between tomographies. Temperature measurements and recordings were processed with a thermocouple data logger (USB TC-08, Pico Technology, UK). For reliable temperature measurements, the thermocouple was calibrated prior to the experiment.

4.2.2.4. Image post-processing

Five datasets were obtained for each specimen and further processed using Fiji platform [43]. After image reconstruction, each 3D dataset consisted of 2000 images (2400 × 2400 pixels) with 32-bit grey-levels. Images were converted to 8-bit greyscale and cropped to parallelepipeds (volume of interest (VOI)) with a cross-section of 1400 × 1400 pixels (1.134 × 1.134 mm2) and a height equal to 1800 pixels (1.46 mm) in the centre of the scanned volume (Figure 1b,c). Noise in the images was reduced by applying a nonlocal means filter [44], where the variance of the noise was automatically estimated for each dataset [45]. The five consecutive scans per specimen were first rigidly registered using the first acquired dataset as a reference. The 3D rigid registration was based on sum of squares differences as a similarity measurement between the reference and each target image. Finally, the filtered VOIs were masked by setting to zero-intensity the non-bony voxels (i.e., Haversian and Volkmann's canals in compact bone and bone marrow space in trabecular bone). A binary image (value of one for bone voxel and zero elsewhere) was first created using Otsu's threshold algorithm followed by a despeckling filter to remove 3D regions less than three voxels in volume both in white and black areas, which are mainly related to nonfiltered noise. Additionally, isolated pixels were removed, and small holes were filled by using a series of morphological operations as described in [16]. The quality of the binary images was checked by visual inspection. Masked images, with the original greyscale value in the bony voxels and zero elsewhere, were obtained by multiplying the filtered image with the final binary image (Figure 1d,e).

4.2.2.5. Digital volume correlation

Digital volume correlation (DaVis v10.0, LaVision, Göttingen, Germany) was carried out to evaluate the residual strain in the bone tissue due to progressive damage induced by X-ray exposure to SR radiation during SR-microCT at different temperatures. DaVis software is based on a local approach of correlation, which has been widely used in bone mechanics [13,14,46]. Details on the operating principles of the software are reported elsewhere [16,47]. DVC was applied to the masked images to avoid large strain artefacts in regions with insufficient greyscale pattern (i.e. bone marrow) [16]. A different multi-pass scheme was used for the DVC computation on compact and trabecular specimens after an evaluation of the baseline strains in the first two consecutive tomograms for the four specimens, obtained in a nominal 'zero-strain' state, where the irradiation-induced damage was considered minimal (Supporting Information S1). A final subvolume of 32 voxels, reached via

successive(predictor) passes using subvolumes of 112, 56, 48 and 40 voxels, was used for the compact bone, whereas, for the trabecular bone, a final subvolume of 64 voxels, reached via successive passes of 112, 88, 80 and 72 voxels, was adopted. Given the voxel size of the SR-microCT images, the final DVC measurement spatial resolution was 25.9 µm for compact and 51.8 µm for trabecular bones. Additionally, in both cases, subvolumes with a correlation coefficient below 0.6 were removed from the resultant displacement vectors to avoid artefacts due to poor correlation. The different processing schemes for both bone typologies mainly depended on the higher number of features (i.e. osteocyte lacunae) available in the compact bone specimens compared to the trabecular ones, which allowed a smaller subvolume size to be used for the former [11].

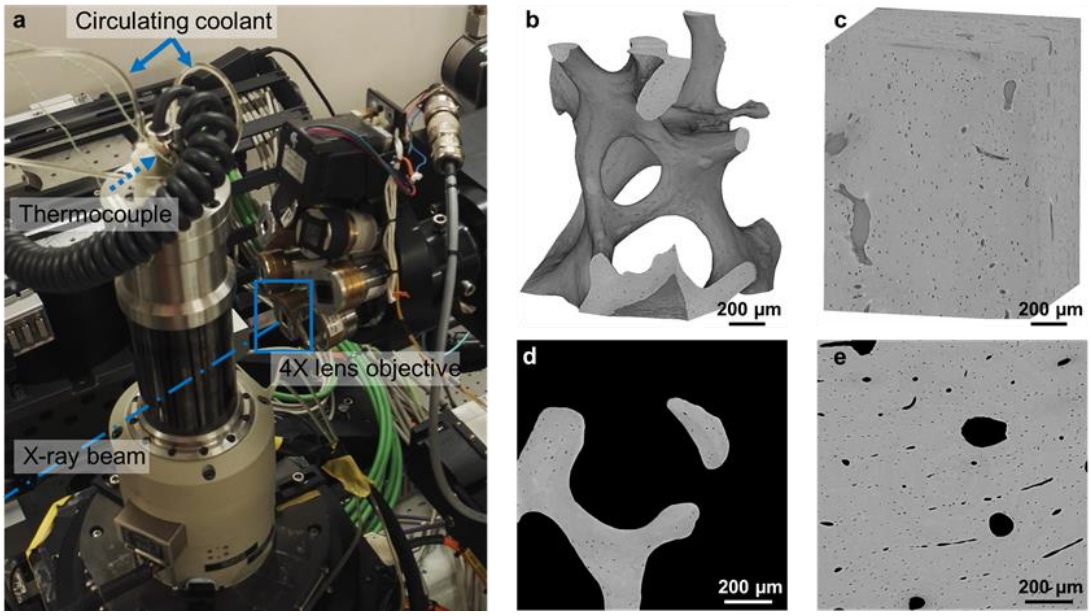

Figure 1. (a) Experimental setup at I13-2 beamline. The direction of the beam is indicated by the dashed-dotted line. Specimens were scanned within a loading device using a 4X lens objective. The temperature in the device was controlled with a circulating coolant and monitored on the tissue via an additional thermocouple attached to the surface of the specimens. SR-microCT reconstructed volume of interest (VOI) (1.13 x 1.13 x 1.46 mm^3) analysed for (b) trabecular and (c) compact bones with an effective voxel size of 0.81 µm. 2D cross-section through the middle of the VOI after masking the bone marrow (d) from the trabecular bone and the Haversian and Volkmann's canals (e) from the compact bone.

To evaluate the 3D full-field residual strain distribution in the bone tissue over time in relation to the damage induced by continuous X-ray exposure to SR radiation, DVC was performed by registering the reference image (first acquired tomogram) with each of the remaining tomograms. First (ε_{p1}) and third (ε_{p3}) principal strains and maximum shear (γ_{max}) strain were computed within the bone volume after a bicubic interpolation of the measured strain. Furthermore, in order to couple the initiation and propagation of microcracks in the tissue with the displacement and first principal strain directions, dedicated MATLAB (v2018a, MathWorks, Natick, Massachusetts, USA) scripts were developed. The MATLAB scripts allow for the representation of any set of orthogonal slices within the volume and for the

computation of the displacement and first principal strain values and their corresponding direction for each subvolume.

4.2.3. Results

4.2.3.1. *In situ* testing and temperature control

Temperature readings from the thermocouple attached to the surface of the bone specimens suggested a consistent temperature gradient (ΔT = 0.4 °C) at each exposure period (Figure 2a) corresponding to the opening (rise in temperature) and closing (drop in temperature) of the X-ray shutter. Small fluctuations in the temperature were recorded once the X-ray shutter was open, as they are more evident during tomographic acquisition compared to the steady position. However, those fluctuations were far less important than the temperate gradients recorded between consecutive tomographies. The stress-relaxation curves recorded during *in situ* testing showed that the X-ray beam significantly influenced the relaxation behaviour of the trabecular bone specimen at room temperature (Figure 2b). A consistent increase in the force was recorded after the start of each tomographic acquisition. This trend was not observed for the compact bone specimen.

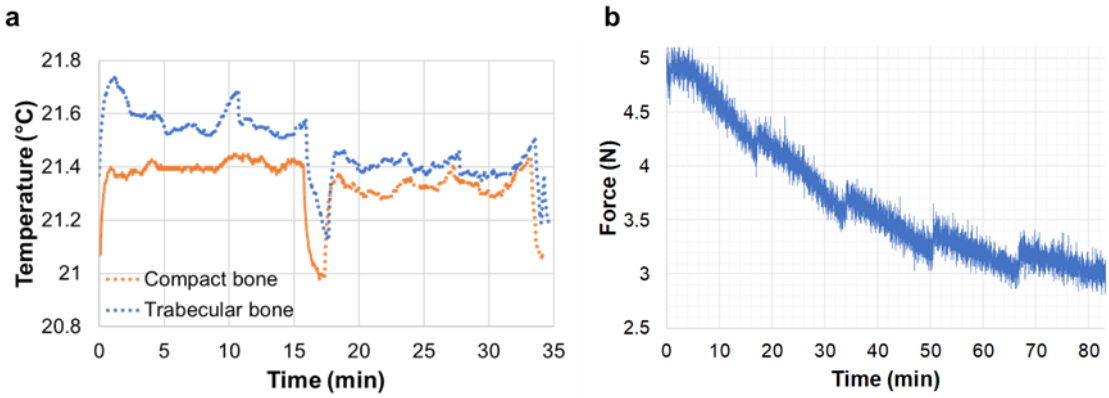

Figure 2. (a) Temperature readings measured using a thermocouple attached to the compact and trabecular bone surface at room temperature. The solid line corresponds to thermocouple readings during ~15 min with the X-ray shutter opened and the thermocouple in the beam path. Dotted lines represent thermocouple readings during tomographic acquisition. The sudden drop and consequent rise in temperature coincide with the closing and opening of the X-ray shutter. (b) Force readings in trabecular bone specimen at room temperature during five consecutive tomograms. An increase in the force was observed and corresponded with the opening of the X-ray shutter.

4.2.3.2. Compact bone

No damage was visually detected in the compact bone specimens after five tomograms, either at room temperature or 0°C. The residual ε_{p1} distribution (Figure 3) did not show any notable changes in the tissue after the acquisition of two (Figure 3a) and five (Figure 3b) tomograms, with some localised areas of higher residual strain in the specimen imaged at room temperature. The strain histograms (Figure 3c) showed peak values below 1000 με for both specimens, and no clear trends were observed between exposure to SR radiation and peak strain values. However, histograms showed tails with higher strains after five tomograms at room temperature compared to 0°C. Similar findings were observed for the

residual ε_{p3} and γ_{max} (Supporting Information, Figure S2), suggesting a strain redistribution between consecutive tomographies, which did not cause important damage overall. Highly strained regions of the specimen tested at room temperature were localised around the Haversian and Volkmann's canals (Figure 4). Residual strain in a region of approximately 20 µm surrounding the canals was compared to the strain in the internal bone matrix volume. Particularly, the cumulative histograms of γ_{max} (Figure 4e) after two and five acquired tomograms showed slightly higher strains around the canals for the same bone volume percentage.

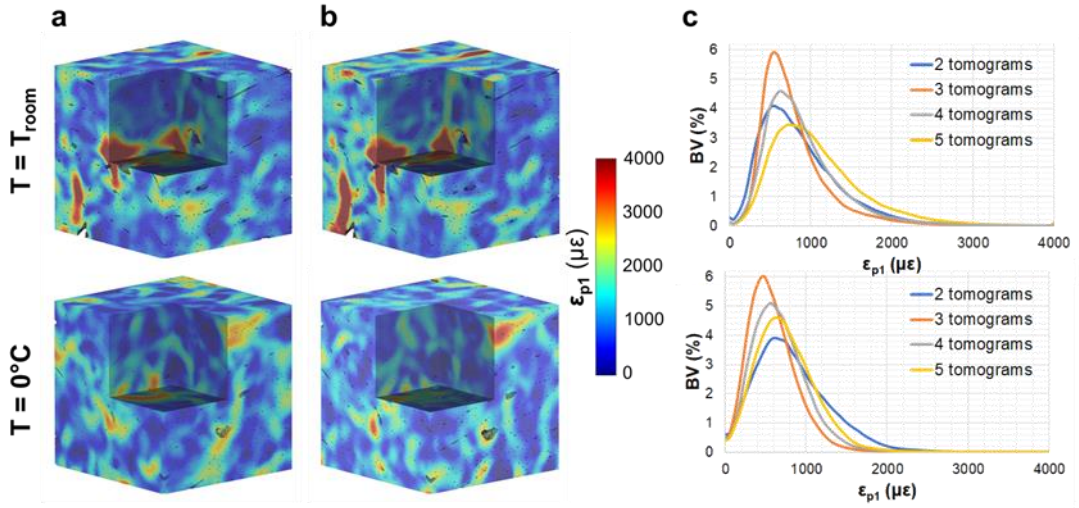

Figure 3. Three-dimensional first principal strain (ε_{p1}) distribution in compact bone tissue imaged at room temperature (top) and 0 °C (bottom) after two (a) and five (b) acquired tomograms. A representative cube (~1 mm^3) in the centre of the analysed VOI is represented. Histograms of the residual strain distribution (c) in the tissue are shown for all the acquired tomograms.

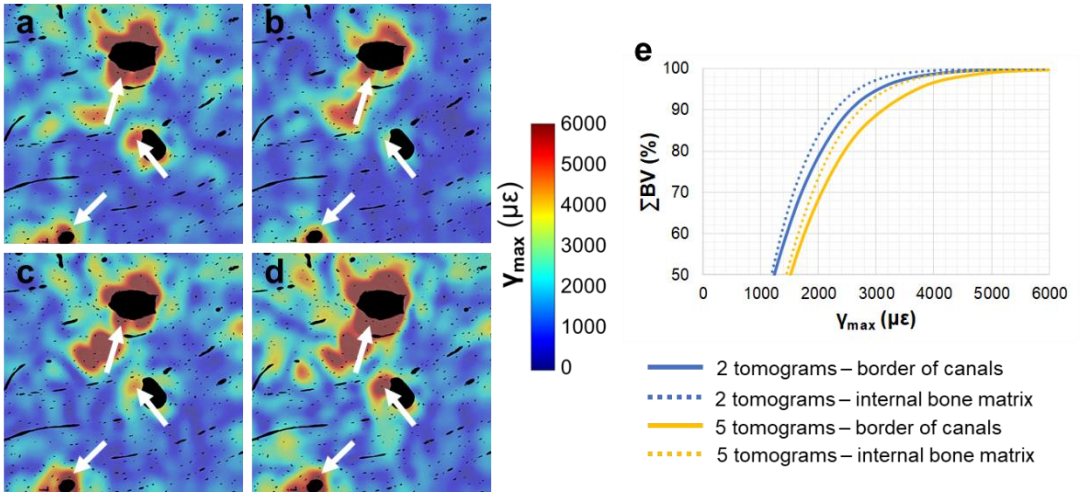

Figure 4. Maximum shear strain (γ_{max}) distribution in compact bone tissue imaged at room temperature. Cross-sections in 2D are shown after (a) two, (b) three, (c) four and (d) five acquired tomograms. Arrows indicate highly strained regions. A cumulative histogram of the residual strain (e) in the tissue voxels around the canals (solid lines) and the remaining bone matrix (dotted lines) is shown for after two and five tomograms.

4.2.3.3. Trabecular bone

A visual inspection of the reconstructed images showed the presence of several microcracks after five tomograms, corresponding to ~80 min of total exposure to SR X-ray radiation, in the trabecular bone specimen at room temperature. However, decreasing the temperature to 0 °C facilitated tissue preservation, as microdamage was not observed. Furthermore, the high levels of residual strain measured with DVC correlated well with the microdamage visible from the images. The histograms of residual strain distributions (Figure 5) after each tomogram highlighted the differences between the two trabecular bone specimens. On one hand, the specimen imaged at room temperature showed a consistent increase in residual strain when increasing the exposure to X-ray radiation (Figure 5a–c). This trend was clearly observed in ε_{p1} (Figure 5a), for which strain peak values increased from ~1500 to ~3000 με after two and five consecutive scans, respectively. ε_{p3} (Figure 5b) peak values were found to be below −1500 με, whereas peak γmax (Figure 5c) ranged from ~2000 με to ~3500 με after two and five tomograms, respectively. The residual strain accumulation was less evident for the trabecular bone specimen maintained at 0°C (Figure 5d–f). In fact, peak strain values remained below ±1000 με for ε_{p1} (Figure 5d) and ε_{p3} (Figure 5 e), respectively, and below 2000 με for γ_{max} (Figure 5f) after five tomograms. The 3D full-field strain distribution in the trabecular bone (Figure 6) was accumulated in the tissue after each tomogram. In particular, for the specimen at room temperature (Figure 6, top), it could be seen that ε_{p1} was increasing after each tomography, and regions of high residual strains after two full tomographies (Figure 6a, top) were progressively enlarged, reaching strain values of over 4000 με after five tomograms (Figure 6d, top). This strain accumulation was less pronounced in the specimen at 0 °C (Figure 6, bottom), although some areas of high strain concentration were observed after each tomogram. Furthermore, some strain redistributions could be seen after three (Figure 6b, bottom) and four (Figure 6c, bottom) full tomographies.

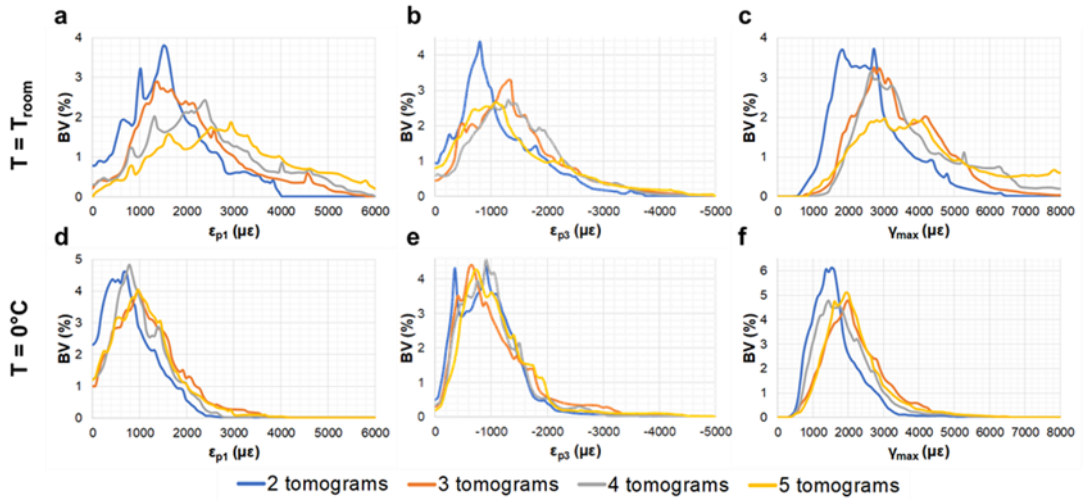

Figure 5. Histograms of the residual strain distribution in trabecular bone tissue imaged at room temperature (top) and 0°C (bottom). (a, d) First principal strains (ε_{p1}), (b, e) third principal strains (ε_{p3}), and (c, f) maximum shear strains (γ_{max}) after each acquired tomogram are shown.

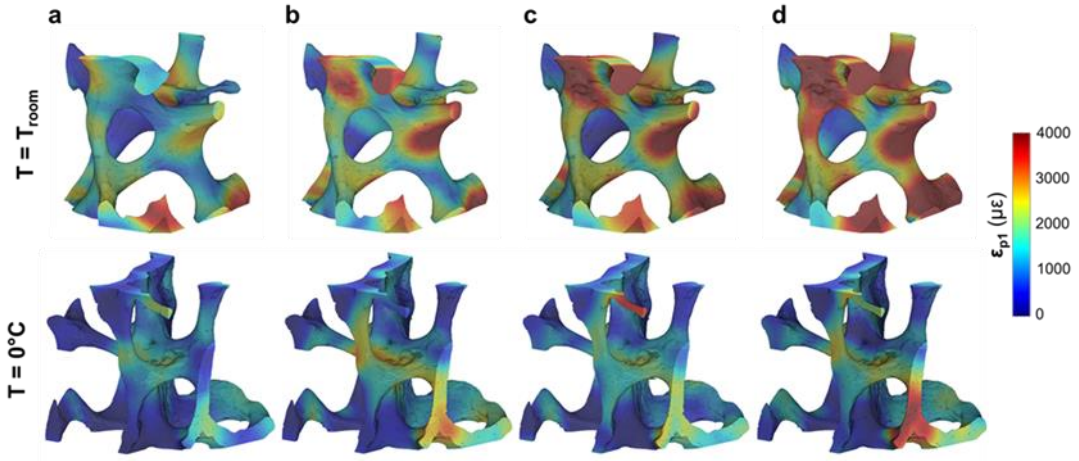

Figure 6. Three-dimensional full-field first principal strain (ε_{p1}) distribution in trabecular bone tissue imaged at room temperature (top) and 0 °C (bottom) after the acquisition of (a) two, (b) three, (c) four, and (d) five consecutive tomograms. A representative cube (~1 mm^3) in the centre of the analysed VOI is represented. Animations of strain distribution over time available online (see available electronic data AVI_4.2.6 in thesis annexes).

4.2.3.4. Tracking of crack formation

Microcracks were clearly visible in the trabecular bone specimen imaged at room temperature after five tomograms (Figure 7a,b). A region inside a trabecula (Figure 7b) was tracked during the *in situ* test to couple the residual strain accumulation with the crack formation. The displacement field around the damaged region (Figure 7c–f) suggested a relative motion between regions at both sides of the cracks since the earliest stages, before cracking was visible (Figure 7c–e). In fact, low displacements were found on one side, and those were mainly directed toward the positive z-direction, whereas, in the neighbouring side, displacements were progressively increased and reoriented toward the negative z-direction. After cracking (Figure 7f), displacements further increased around the crack, and a pronounced reorientation of their direction was observed. A deeper look at the displacement in the orthogonal planes (Figure 8), before and after crack formation, evidenced the discontinuities in the displacement field in proximity to the crack. Particularly, before crack formation (Figure 8a), displacement showed a high misorientation in the XY and XZ planes. After cracking (Figure 8b), the displacement field at one end of the crack was found perpendicular to the crack direction (XY plane), whereas it seemed aligned with the crack on the other end, which may indicate the further propagation direction. Both ε_{p1} and γ_{max} showed a progressive increase in the microcracked region, reaching values above 4000 με for ε_{p1} (Figure 9b) and approximately 5000 με for γ_{max} (Figure 10b) in the damaged area. In general, tensile strains were the most correlated to microdamage detection. In fact, the directions of ε_{p1} (Figure 9) suggested a combination of tensile and shear modes of crack formation. In addition, the principal directions before cracking seemed to be highly disordered throughout the analysed volume. In particular, the highlighted vectors before cracking (Figure 9a) exhibited a very abrupt change in orientation, whereas the same areas after cracking (Figure 9b) were considerably aligned with the microcrack. γ_{max} (Figure 10) increased after crack

formation, and discontinuities at both sides of the crack were observed (Figure 10b). Moreover, higher shear strain levels were found at one side of the crack (XY plane), which also corresponded to principal strains and displacements perpendicular to the crack, thus possibly suggesting the direction of crack propagation.

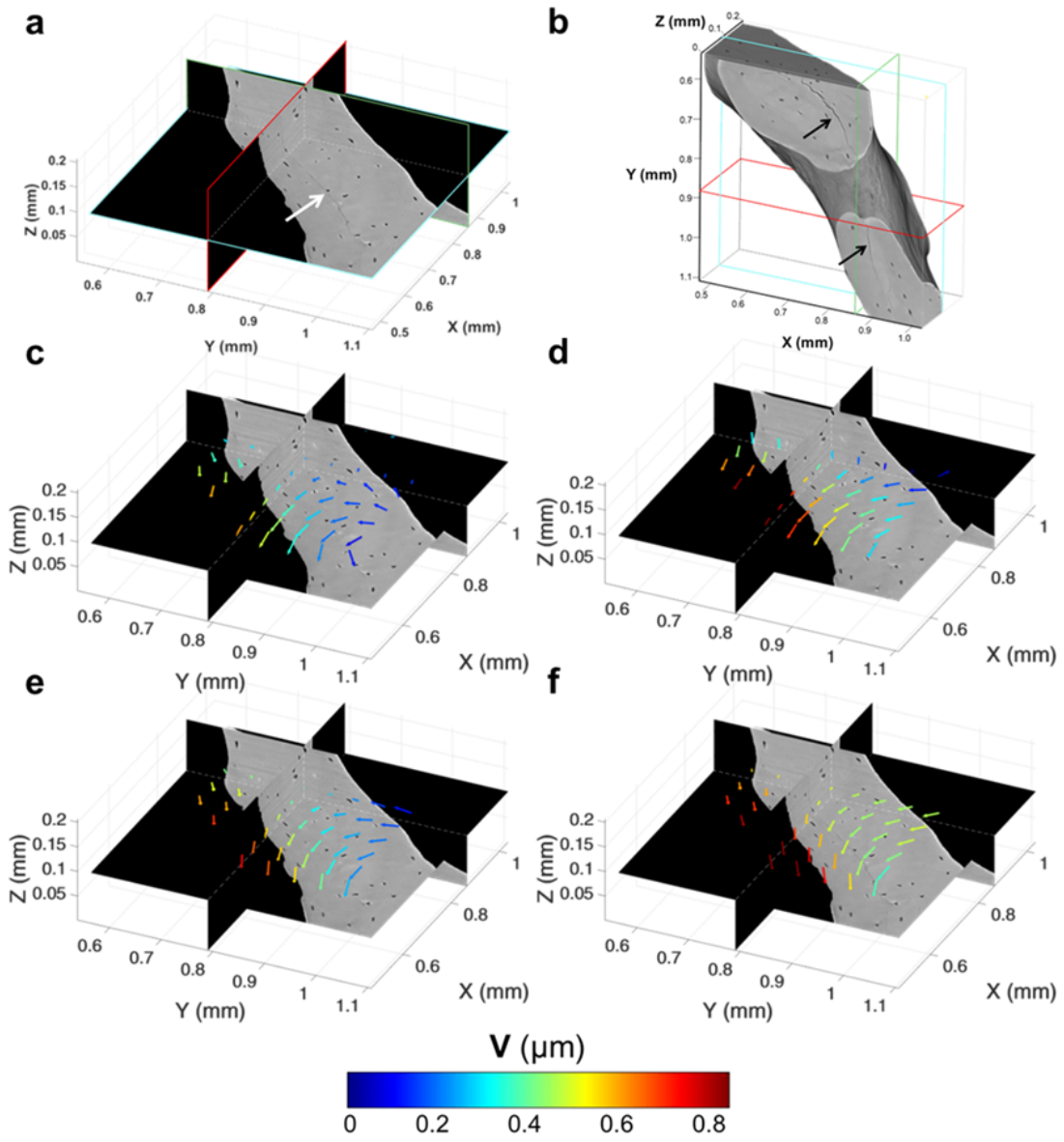

Figure 7. Microcrack tracking in trabecular bone tissue imaged at room temperature. (a) Representative orthoslices and (b) 3D representation of the trabecular bone region tracked over time. Arrows indicate the microcracks visible in the tissue. (c-f) DVC-computed displacement field (V) in each sub-volume on the analysed region of interest around a microcrack at different time points corresponding to the acquisition of (c) two, (d) three, (e) four and (f) five tomograms. Vector lengths are identical, and the color code refers to the V magnitude in micrometres. Animations of 3D displacement field available online (see available electronic data AVI_4.2.7 in thesis annexes).

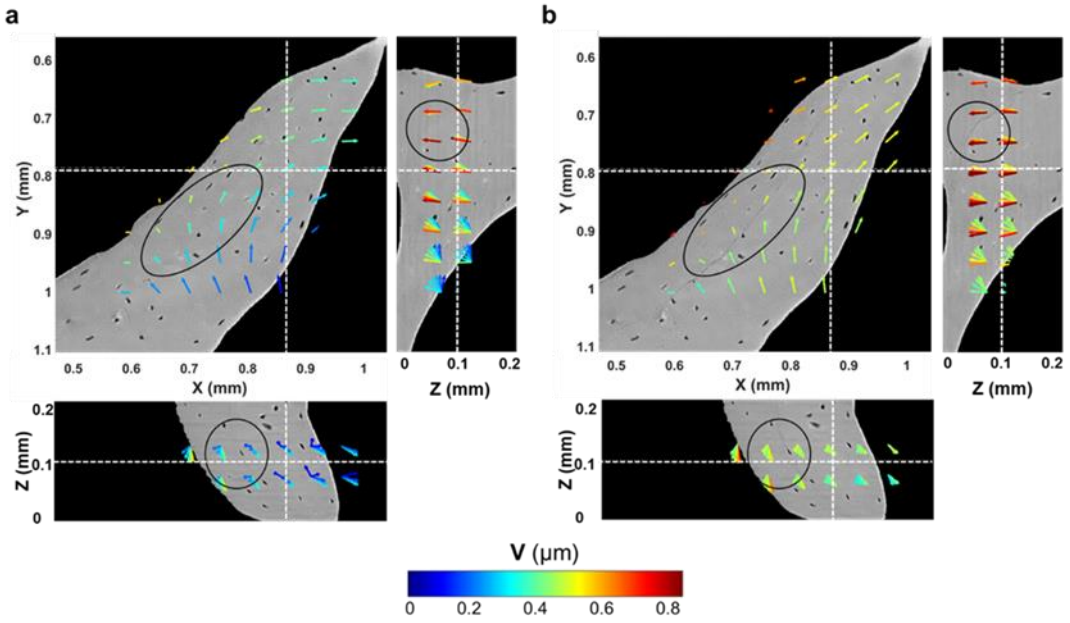

Figure 8. DVC-computed displacement field through the region of interest analysed around the microcracked area (a) before (fourth tomogram) and (b) after cracking was visible (fifth tomogram). Oval regions highlight damaged areas of bone tissue. Vector lengths are identical, and the color code refer to the displacement vector length (V) in micrometres.

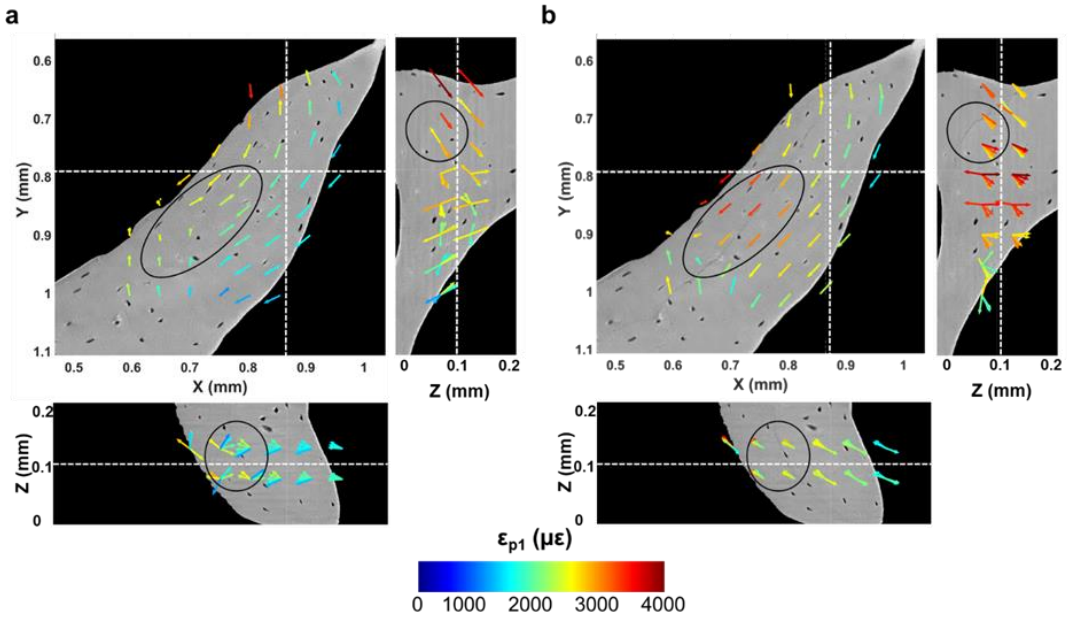

Figure 9. DVC-computed first principal strain (ε_{p1}) through the region of interest analysed around microcracked area (a) before (fourth tomogram) and (b) after cracking was visible (fifth tomogram). Vectors indicate first principal strain directions in each sub-volume. Oval regions highlight damaged areas of bone tissue, which correspond to high orientation changes in the principal strain direction before and after cracking. Vector lengths are identical, and the color code refer to the ε_{p1} magnitude.

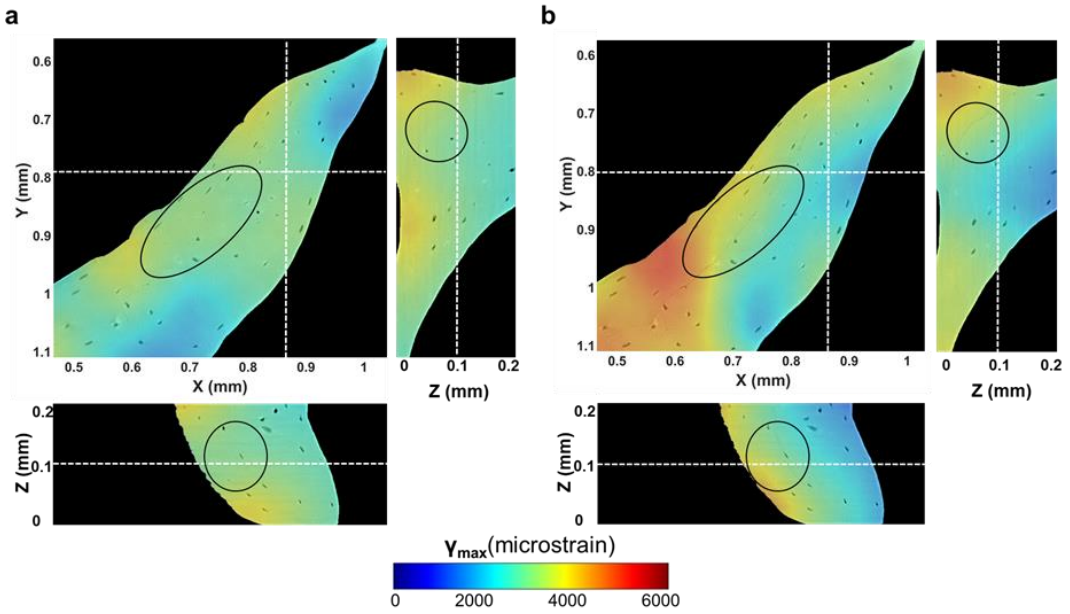

Figure 10. DVC-computed maximum shear strain (γ_{max}) through the region of interest analysed around microcracked area (a) before (fourth tomogram) and (b) after cracking was visible (fifth tomogram). Oval regions highlight damaged areas of bone tissue, which correspond to an increase of shear strain values before and after cracking. High discontinuities in shear strains were identified in the damage region (b), which may suggest the direction of crack propagation.

4.2.4. Discussion

The proof-of-concept experiment reported herein enabled important understanding of the SR X-ray radiation-induced damage to the integrity of bone tissue. The residual strain accumulation caused by SR X-ray radiation was quantified for the first time using DVC applied to *in situ* SR-microCT images, and the effect of the environmental temperature on the SR irradiation-induced damage in bone tissue was addressed. It is known that irradiation has a deleterious effect on the structural and mechanical properties of bone as a result of collagen matrix degradation due to the formation of collagen cross-links and eventual rupture of the collagen fibres [20,27]. Several studies have addressed the effect of high-energy SR X-ray radiation on the mechanical properties of bone [20,21,26,48], and safe dose values (35 kGrays) were defined to preserve bone mechanics [20]. However, during *in situ* SR-microCT studies, a reduction of the dose is related to a reduction in the total exposure to SR radiation and, therefore, the signal-to-noise ratio of the acquired tomograms, with a consequent reduction in image quality and increased DVC errors [14]. Therefore, new protocols need to be defined in order to preserve bone tissue while maintaining good image quality. Furthermore, whether bone integrity can be preserved by controlling the temperature during *in situ* SR experiments still remains unexplored.

The overall change in temperature during image acquisition was minimal (ΔT = 0.4 °C) (Figure 2a) and in line with previous reports on SR beam heating [49,50]. Wallander and Wallentin [51] showed that X-ray-induced heating can lead to significant temperature increase (e.g. nanowire at 8 °C above room temperature) at typical synchrotron beamline

fluxes. As a strategy for reducing the X-ray-induced heating, it was suggested to improve the heat transfer of the target material to the surroundings, for example, by immersing the samples in liquid [51]. However, it still remains unclear whether that thermal gradient in a very short period of time (opening/closing of the beam shutter) may induce collagen degradation. As specimens were held between the loading stage platens during the *in situ* test, the effect of the X-ray beam on the stress-relaxation behaviour of the specimens could be observed (Figure 2b), similar to the data reported in [52]. With only a fixed preload applied, an increase in the load was identified for the trabecular bone specimen at each cyclic period that corresponded with the opening of the X-ray shutter. Both trabecular and compact bone exhibit a highly viscoelastic behaviour; however, this is more evident for trabecular bone due to the large content of bone marrow in its cavities. Thus, the loadcell of the loading stage was not accurate enough to capture any changes in the stress-relaxation behaviour for the compact bone specimen. Heat causes a transformation of the collagen molecule, known as the collagen shrinkage phenomenon [53], whereby the collagen molecule develops a contractile force that is held constant [54,55] at a given temperature (shrinkage temperature). This shrinkage behaviour is related to the cross-links in the collagen and its stability [53]. Even though the specimens in the current study were kept at a constant temperature (~23 °C), the beam-induced temperature rise of 0.4 °C may contribute to the activation of a similar contractile force, which is a clear indicator of the harmful effects of the SR irradiation on bone tissue.

The results obtained from the current study have shown that reducing the temperature to 0°C notably reduced the irradiation-induced microdamage and residual strain in trabecular bone specimens (Figure 6). However, minimal effect was observed for compact bone (Figure 3). Nguyen et al. [30] reported that the mechanical properties of compact bone were decreased by a lower dose than that affecting trabecular bone. However, it has been shown here (Figure 3) that the structural integrity of compact bone tissue was not compromised, as microcracks were not detected as in the trabecular bone tissue. In any case, specimens were not mechanically tested; thus, whether the regions of high strain concentration found in compact bone (Figure 3) influence the mechanical properties is still unknown. Furthermore, Peña Fernández et al. [14] showed that the presence of microcracks was not always related to changes in the apparent elastic properties of the irradiated bone.

Although the overall residual strain in compact bone imaged at room temperature was low, with peak strain values below 1000 με for ε_{p1} (Figure 3), some highly strained regions were identified in close proximity to Haversian and Volkmann's canals (Figure 4). Canals and osteocyte lacunae are known to act as stress concentrating features in specimens subjected to mechanical load [6,12]; however, the effect of irradiation on these specific sites has never been considered. Haversian canals contain unbound water [56], and as ionising radiation produces the release of free radicals via radiolysis of water molecules [29], it is expected that

a larger number of free radicals, which could interact with the collagen and induce cross-linking reactions, are found in proximity to the canals due to the higher water content.

Lowering the environmental temperature to 0 °C had a positive effect on the DVC-measured residual strain in trabecular bone, which showed a peak principal strain value below 1000 με (Figure 5); furthermore, no microdamage was visually detected on the reconstructed tomograms. These results are consistent with medical studies on the effect of gamma irradiation, where it was shown that irradiating bone specimens while frozen did not affect the mechanical properties of bone [31,34]. In fact, decreasing the temperature reduces the mobility of the water, and, therefore, decreases the mobility of highly reactive oxygen free radicals produced by high-energy X-ray radiation. Impairing that mobility protects the collagen by reducing cross-linking reactions within its molecules [57,58]. The effect of freezing on the mechanical properties of bone has been previously studied [59–62] and no statistical differences were found after freezing, nor after several freeze-thaw cycles [63,64]. It should be noted that, during the proposed experiment, specimens were immersed in saline solution at 0 °C, and ice crystals, which may cause structural damage to the tissue [63], were not observed at any stage of the experiment.

The irradiation-induced damage in the trabecular bone imaged at room temperature resulted in microcracks that were visible in the tissue even if the specimen was not subjected to any mechanical load. At the nanoscale, SR irradiation-induced free radical attack of the collagen network results in a cross-linking reaction that degrades the structural integrity of the collagen fibres [20,29,30]. Previous studies using atomic force microscopy have shown that crack formation and bone fracture occur between the mineralised collagen fibrils. Fantner et al. [65] proposed that the mineralised collagen fibres are held together by a nonfibrillar organic matrix that acts as a glue. The glue resists the separation of the mineralised collagen fibrils, avoiding the formation of cracks, when a load is applied to the bone. During the formation of microcracks, work that stretches the glue molecules would be required to separate the mineralised collagen fibrils. Irradiation may affect that mechanism by damaging the sacrificial bonds, resulting in the shrinkage behaviour observed with SR X-ray radiation, which could lead to the rupture of those bonds after prolonged exposure to irradiation and consequent microcrack formation. At the macroscale, DVC-computed displacements (Figure 7) suggest a vortex motion around the microcracked region, which results in a shrinkage process of the material and the formation of a microcrack that follows an unusual pattern in fracture mechanics. The denaturation of the collagen may not be homogeneous throughout the bone tissue; therefore, crack propagation would follow the degeneration process of the collagen.

DVC was successfully used to understand crack formation and propagation in bone. Christen et al. [12] investigated the initiation and propagation of microcracks in cortical bone using DVC; however, full-field displacements and strains were only evaluated in terms of magnitude, but the directions were not explored. Additionally, specimens were pre-cracked

before mechanical testing; thus, crack initiation and propagation was expected around the notch region. In this study, microcracks were not induced by mechanical loading, but by SR irradiation instead. Discontinuities in the displacement field (Figure 8a) corresponded to high-orientation changes in the strain field (Figure 9a) that could indicate crack formation. Furthermore, perpendicularity of displacement (Figure 8b) and principal strains (Figure 9b) to the crack might be related to a crack propagation front. Similar crack formation mechanisms were observed in clay deformation using digital image correlation (DIC) following desiccation [66,67]. Like the results herein reported, in opening mode, the direction of the crack was perpendicular to that of ε_{p1}, whereas, for cracks in mixed opening-sliding mode, ε_{p1} was found parallel to the direction of the crack (Figure 9b). Those studies [66,67] concluded that cracks formed a network which is found after thermal shocks, and the authors emphasized the need to develop a multiscale approach to better understand crack formation and propagation. Similar to those findings, irradiation-induced microcracks need to be further investigated at different dimensional levels to properly understand the formation mechanisms.

This study has some limitations. First, only one specimen per bone type was tested at each temperature, and the mechanical properties of the bone specimens were not evaluated after irradiation. Residual strain maps suggested that a decrease in the temperature had a beneficial effect on preserving bone integrity and mechanics, but specimens were maintained far below physiological conditions (~37 °C); thus, it could be argued that the mechanical properties of bone tissue could have been altered. Further analyses are needed to properly assess the effect of the environmental temperature during *in situ* SR-microCT experiments, translating the findings of the proposed methodology to *in situ* SR-microCT bone mechanics. Moreover, a combination of techniques at different dimensional scales would enhance the knowledge of the irradiation-induced damage in bone tissue.

4.2.5. Conclusions

The 3D full-field residual strain distribution of compact and trabecular bone subjected to high-energy SR irradiation was computed using DVC applied to SR-microCT images acquired at different temperatures. Lowering the temperature during irradiation to only 0 °C had a positive effect on trabecular bone tissue, which — unlike such bone imaged at room temperature—did not present visible microcracks, and residual strain values were not increased with further radiation. However, a minimal effect was observed in compact bone. A shrinkage behaviour induced by both the beam-induced temperature and high-energy irradiation may well be the source of the irradiation-induced damage and microcracks in bone tissue. DVC applied to high-resolution SR-microCT images has proven to be a useful tool for understanding crack formation and propagation in bone tissue. Further work is needed to clearly establish protocols for the application of SR-microCT to the *in situ* mechanics of bone and potentially extend the knowledge to other biological tissues in order to minimise SR irradiation-induced damage.

Author contributions

Marta Peña Fernández: Study design, data curation, formal analysis, data interpretation; Enrico Dall'Ara: Study design, data interpretation, supervision; Alexander P. Kao: Data curation data interpretation; Andrew J. Bodey: Data curation; Aikaterina Karali: Data curation; Gianluca Tozzi: Study design, data interpretation, supervision.

Acknowledgments

The authors would like to thank Diamond Light Source (UK) for time at the Diamond-Manchester Imaging Branchline I13-2 and its associated Data Beamline [67] under proposal MT16497, and the Zeiss Global Centre (University of Portsmouth) for post-processing. We further acknowledge Dr Dave Hollis (LaVision Ltd) for assistance with DaVis software, Dr Kazimir Wanelik for help during the experiment and image reconstruction at Diamond Light Source, and Dr Kamel Madi for fruitful discussions during the experiment.

Supplementary material S1

Methods

The evaluation of the baseline strains was performed in the first two consecutive datasets for the four specimens, where irradiation-induced damage was deemed as minimal. As the images were acquired in the same deformed state (i.e. 'zero-strain' repeated scans), null displacement and strain fields are expected. Therefore, any non-zero values of the measured displacement and derived strains using DVC were considered as error. Ten multi-pass schemes [16] with final sub-volume sizes ranging from 8 to 80, in steps of 8 voxels were investigated. For each sub-volume, three different parameters were computed.

- Random errors of the displacements: standard deviation of each displacement component, as in [47].
- Mean absolute strain value: average of the average of the absolute values of the six components of the differential strain, similar to MAER or "accuracy", as in [15]
- Standard deviation of the strain value: standard deviation of the average of the absolute values of the six components of the differential strain, similar to SDER or "precision", as in [15,68].

Results

The random errors of each component of the displacement never exceeded 0.30 µm for the compact bone specimens and 0.33 µm for the trabecular bone specimens (Table S1). The errors obtained for the displacements in the compact bone were higher than those for the trabecular bone in x and y directions, but lower in z direction. A trend could be observed for both bone type specimens where the higher the sub-volume size, the lower the random errors.

Table 1. Random errors for the three displacement components for compact and trabecular bone specimens. Median values of the two specimens per group are shown.

Multi-pass scheme sub-volume sizes (voxels)	Displacement random errors (µm)					
	Compact bone			Trabecular bone		
	X	Y	Z	X	Y	Z
64-32-24-16-8	0.30	0.27	0.12	0.32	0.33	0.26
80-40-32-24-16	0.25	0.24	0.08	0.25	0.26	0.19
96-48-40-32-24	0.23	0.23	0.07	0.23	0.24	0.18
112-56-48-40-32	0.23	0.23	0.07	0.20	0.21	0.17
128-64-56-48-40	0.22	0.22	0.07	0.17	0.18	0.17
144-72-64-56-48	0.22	0.22	0.06	0.16	0.16	0.17
160-80-72-64-56	0.21	0.22	0.06	0.13	0.16	0.15
178-88-80-72-64	0.21	0.22	0.06	0.13	0.16	0.15
192-96-88-80-72	0.20	0.21	0.06	0.13	0.15	0.14
192-112-96-88-80	0.20	0.21	0.06	0.12	0.15	0.14

As expected from previous studies on bone [11,15], the strain uncertainties of the DVC had decreasing trends with respect to the sub-volume size, and the values of the mean value of the strain (MAER) were larger than the standard deviation (SDER) (Figure SI1). The MAER ranged between 3000 µε and 100 µε for the compact bone samples and between 5500 µε and 300 µε for the trabecular bone samples, in sub-volumes of 8 to 80 voxels (6.5 to 65 µm). The SDER ranged between 1250 µε and 30 µε for the compact bone and between 5000 µε and 140 µε for the trabecular bone, in the same sub-volumes.

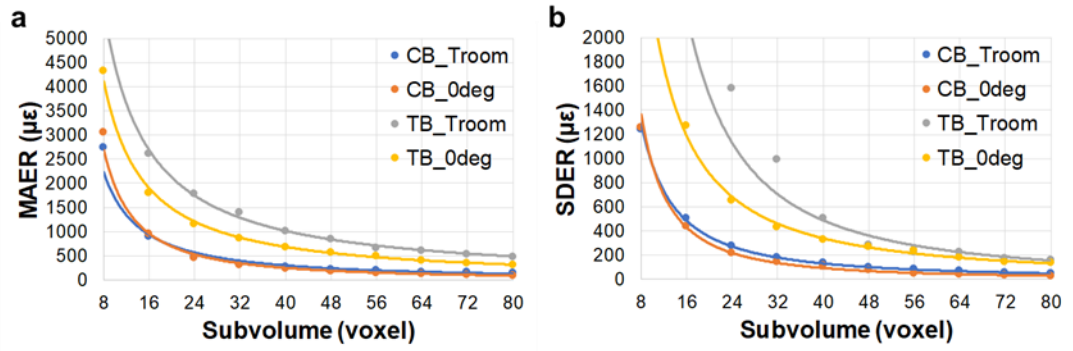

Figure SI1. Relationship between (a) MAER and (b) SDER with the sub-volume size for the four bone specimens.

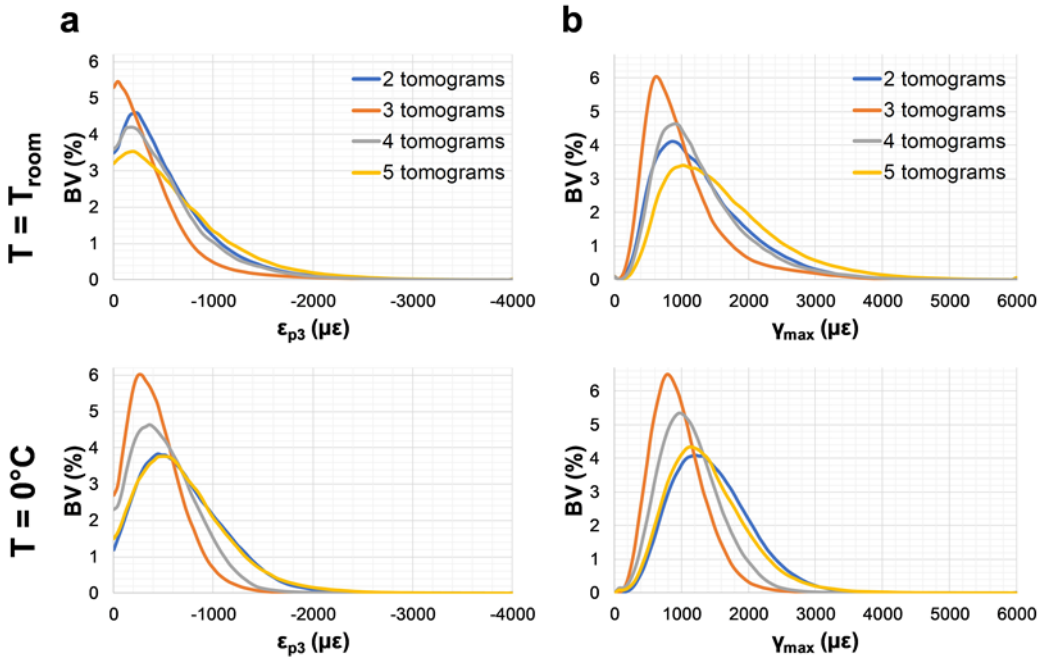

Figure SI2. Histograms of the (a) third principal (ε_{p3}) and maximum shear (γ_{max}) residual strain distribution in the cortical bone tissue for all the acquired tomograms at room temperature (top) and 0°C (bottom)

References

[1] J.Y. Rho, L. Kuhn-Spearing, P. Zioupos, Mechanical properties and the hierarchical structure of bone, Med. Eng. Phys. 20 (1998) 92–102. doi:10.1016/S1350-4533(98)00007-1.

[2] P. Fratzl, H.S. Gupta, E.P. Paschalis, P. Roschger, Structure and mechanical quality of the collagen–mineral nano-composite in bone, J. Mater. Chem. 14 (2004) 2115–2123. doi:10.1039/B402005G.

[3] J.D. Currey, How well are bones designed to resist fracture?, J. Bone Miner. Res. 18 (2003) 591–598. doi:10.1359/jbmr.2003.18.4.591.

[4] S. Weiner, W. Traub, H.D. Wagner, Lamellar bone: structure– function relations., J. Struct. Biol. 126 (1999) 241–255.

[5] C.M.J. de Bakker, W.-J. Tseng, Y. Li, H. Zhao, X.S. Liu, Clinical Evaluation of Bone Strength and Fracture Risk, Curr. Osteoporos. Rep. 15 (2017) 32–42. doi:10.1007/s11914-017-0346-3.

[6] R. Voide, P. Schneider, M. Stauber, P. Wyss, M. Stampanoni, U. Sennhauser, G.H. van Lenthe, R. Müller, Time-lapsed assessment of microcrack initiation and propagation in murine cortical bone at submicrometer resolution, Bone. 45 (2009) 164–173. doi:10.1016/j.bone.2009.04.248.

[7] U. Wolfram, H.J. Wilke, P.K. Zysset, Damage accumulation in vertebral trabecular bone depends on loading mode and direction, J. Biomech. 44 (2011) 1164–1169. doi:10.1016/j.jbiomech.2011.01.018.

[8] S. Li, E. Demirci, V. V. Silberschmidt, Variability and anisotropy of mechanical behavior of cortical bone in tension and compression, J. Mech. Behav. Biomed. Mater. 21 (2013) 109–120. doi:10.1016/j.jmbbm.2013.02.021.

[9] B.K. Bay, T.S. Smith, D.P. Fyhrie, M. Saad, Digital volume correlation: Three-dimensional strain mapping using X-ray tomography, Exp. Mech. 39 (1999) 217–226. doi:10.1007/BF02323555.

[10] L. Grassi, H. Isaksson, Extracting accurate strain measurements in bone mechanics: A critical review of current methods, J. Mech. Behav. Biomed. Mater. 50 (2015) 43–54. doi:10.1016/j.jmbbm.2015.06.006.

[11] E. Dall'Ara, M. Peña-Fernández, M. Palanca, M. Giorgi, L. Cristofolini, G. Tozzi, Precision of DVC approaches for strain analysis in bone imaged with μCT at different dimensional levels, Front. Mater. 4:31 (2017). doi:10.3389/fmats.2017.00031.

[12] D. Christen, A. Levchuk, S. Schori, P. Schneider, S.K. Boyd, R. Müller, Deformable image registration and 3D strain mapping for the quantitative assessment of cortical bone microdamage, J. Mech. Behav. Biomed. Mater. 8 (2012) 184–193. doi:10.1016/j.jmbbm.2011.12.009.

[13] F. Gillard, R. Boardman, M. Mavrogordato, D. Hollis, I. Sinclair, F. Pierron, M. Browne, The application of digital volume correlation (DVC) to study the microstructural behaviour of trabecular bone during compression, J. Mech. Behav. Biomed. Mater. 29 (2014) 480–499. doi:10.1016/j.jmbbm.2013.09.014.

[14] M. Peña Fernández, S. Cipiccia, A.J. Bodey, R. Parwani, E. Dall'Ara, G. Blunn, M. Pani, A.H. Barber, G. Tozzi, Effect of SR-microCT exposure time on the mechanical integrity of trabecular bone using *in situ* mechanical testing and digital volume correlation, J. Mech. Behav. Biomed. Mater. 88 (2018) 109–119. doi:https://doi.org/10.1016/j.jmbbm.2018.08.012.

[15] M. Palanca, A.J. Bodey, M. Giorgi, M. Viceconti, D. Lacroix, L. Cristofolini, E. Dall'Ara, Local displacement and strain uncertainties in different bone types by digital volume correlation of synchrotron microtomograms, J. Biomech. c (2017). doi:10.1016/j.jbiomech.2017.04.007.

[16] M. Peña Fernández, A.H. Barber, G.W. Blunn, G. Tozzi, Optimisation of digital volume correlation computation in SR-microCT images of trabecular bone and bone-biomaterial systems, J. Microsc. 00 (2018) 1–16. doi:doi: 10.1111/jmi.12745.

[17] P.J. Thurner, P. Wyss, R. Voide, M. Stauber, M. Stampanoni, U. Sennhauser, R. Müller, Time-lapsed investigation of three-dimensional failure and damage accumulation in trabecular bone using synchrotron light, Bone. 39 (2006) 289–299. doi:10.1016/j.bone.2006.01.147.

[18] A. Larrue, A. Rattner, N. Laroche, L. Vico, F. Peyrin, Feasibility of micro-crack detection in human trabecular bone images from 3D synchrotron microtomography, Annu. Int. Conf. IEEE Eng. Med. Biol. - Proc. (2007) 3918–3921. doi:10.1109/IEMBS.2007.4353190.

[19] M. Peña Fernández, E. Dall'Ara, A.J. Bodey, R. Parwani, A.H. Barber, G.W. Blunn, G. Tozzi, Full-field strain analysis of bone-biomaterial systems produced by the implantation of osteoregenerative biomaterials in an ovine model, ACS Biomater. Sci. Eng. (2018). doi:Under review.

[20] H.D. Barth, M.E. Launey, A.A. MacDowell, J.W. Ager, R.O. Ritchie, On the effect of X-ray irradiation on the deformation and fracture behavior of human cortical bone, Bone. 46 (2010) 1475–1485. doi:10.1016/j.bone.2010.02.025.

[21] H.D. Barth, E.A. Zimmermann, E. Schaible, S.Y. Tang, T. Alliston, R.O. Ritchie, Characterization of the effects of x-ray irradiation on the hierarchical structure and mechanical properties of human cortical bone, Biomaterials. 32 (2011) 8892–8904. doi:10.1016/j.biomaterials.2011.08.013.

[22] R. Singh, D. Singh, A. Singh, Radiation sterilization of tissue allografts: A review, World J. Radiol. 8 (2016) 355. doi:10.4329/wjr.v8.i4.355.

[23] A.J. Hamer, J.R. Strachan, M.M. Black, C.J. Ibbotson, I. Stockley, R.A. Elson, Biomechanical Properties of Cortical Allograft Bone Using a New Method of Bone Strength Measurement: a Comparison of Fresh, Fresh-Frozen and Irradiated Bone, J Bone Jt. Surg Br. 78–B (1996) 363–368. doi:10.1302/0301-620X.78B3.0780363.

[24] J.D. Currey, J. Foreman, I. Laketić, J. Mitchell, D.E. Pegg, G.C. Reilly, Effects of ionizing radiation on the mechanical properties of human bone, J. Orthop. Res. 15 (1997) 111–117. doi:10.1002/jor.1100150116.

[25] L. Vastel, A. Meunier, H. Siney, L. Sedel, J.P. Courpied, Effect of different sterilization processing methods on the mechanical properties of human cancellous bone allografts, Biomaterials. 25 (2004) 2105–2110. doi:10.1016/j.biomaterials.2003.08.067.

[26] A. Singhal, A.C. Deymier-Black, J.D. Almer, D.C. Dunand, Effect of high-energy X-ray doses on bone elastic properties and residual strains, J. Mech. Behav. Biomed. Mater. 4 (2011) 1774–1786. doi:10.1016/j.jmbbm.2011.05.035.

[27] C.D. Flanagan, M. Unal, O. Akkus, C.M. Rimnac, Raman spectral markers of collagen denaturation and hydration in human cortical bone tissue are affected by radiation sterilization and high cycle fatigue damage, J. Mech. Behav. Biomed. Mater. 75 (2017) 314–321. doi:10.1016/j.jmbbm.2017.07.016.

[28] S.-S. Gouk, N.M. Kocherginsky, Y.Y. Kostetski, M.O. Moser, P. Yang, T.-M. Lim, W.Q. Sun, H.O. Moser, P. Yang, T.-M. Lim, W.Q. Sun, Synchrotron radiation-induced formation and reaction of free radicals in the human acellular dermal matrix, Radiat. Res. 163 (2005) 535–543. http://www.ncbi.nlm.nih.gov/pubmed/15850415.

[29] O. Akkus, R.M. Belaney, P. Das, Free radical scavenging alleviates the biomechanical impairment of gamma radiation sterilized bone tissue, J. Orthop. Res. 23 (2005) 838–845. doi:10.1016/j.orthres.2005.01.007.

[30] H. Nguyen, D.A.F. Morgan, M.R. Forwood, Sterilization of allograft bone: Effects of gamma irradiation on allograft biology and biomechanics, Cell Tissue Bank. 8 (2007) 93–105. doi:10.1007/s10561-006-9020-1.

[31] A.J. Hamer, I. Stockley, R.A. Elson, Changes in allograft bone irradiated at different temperatures, J Bone Jt. Surg. 81 (1999) 342–4. doi:10.1302/0301-620X.81B2.9083.

[32] O. Cornu, J. Boquet, O. Nonclercq, P.L. Docquier, J. Van Tomme, C. Delloye, X. Banse, Synergetic effect of freeze-drying and gamma irradiation on the mechanical properties of human cancellous bone, Cell Tissue Bank. 12 (2011) 281–288. doi:10.1007/s10561-010-9209-1.

[33] H. Hiemstra, M. Tersmette, A.H. V Vos, J. Over, M.P. Berkel, H. Bree, Inactivation of human immunodeficiency virus by gamma radiation and its effect on plasma and coagulation factors, Transfusion. 31 (1991) 32–39. doi:10.1046/j.1537-2995.1991.31191096182.x.

[34] T.A. Grieb, R.Y. Forng, R.E. Stafford, J. Lin, J. Almeida, S. Bogdansky, C. Ronholdt, W.N. Drohan, W.H. Burgess, Effective use of optimized, high-dose (50 kGy) gamma irradiation for pathogen inactivation of human bone allografts, Biomaterials. 26 (2005) 2033–2042. doi:10.1016/j.biomaterials.2004.06.028.

[35] R. Carzaniga, M.C. Domart, L.M. Collinson, E. Duke, Cryo-soft X-ray tomography: A journey into the world of the native-state cell, Protoplasma. 251 (2014) 449–458. doi:10.1007/s00709-013-0583-y.

[36] E. Duke, K. Dent, M. Razi, L.M. Collinson, Biological applications of cryo-soft X-ray tomography, J. Microsc. 255 (2014) 65–70. doi:10.1111/jmi.12139.

[37] R. Carzaniga, M.-C. Domart, E. Duke, L.M. Collinson, Correlative Cryo-Fluorescence and Cryo-Soft X-Ray Tomography of Adherent Cells at European Synchrotrons, Methods Cell Biol. 124 (2014) 151–178. doi:https://doi.org/10.1016/B978-0-12-801075-4.00008-2.

[38] G. Voggenreiter, R. Ascherl, G. Blumel, K.P. Schmit-Neuerburg, Effects of preservation and sterilization on cortical bone grafts, Arch. Orthop. Trauma Surg. 113 (1994) 294–296. doi:10.1007/BF00443821.

[39] O. Cornu, X. Banse, P.L. Docquier, S. Luyckx, C. Delloye, Effect of freeze-drying and gamma irradiation on the mechanical properties of human cancellous bone, J. Orthop. Res. 18 (2005) 426–431. doi:10.1002/jor.1100180314.

[40] L. Yin, S. Venkatesan, D. Webb, S. Kalyanasundaram, Q.H. Qin, Effect of cryo-induced microcracks on microindentation of hydrated cortical bone tissue, Mater. Charact. 60 (2009) 783–791. doi:10.1016/j.matchar.2009.01.004.

[41] R.C. Atwood, A.J. Bodey, S.W.T. Price, M. Basham, M. Drakopoulos, A high-throughput system for high-quality tomographic reconstruction of large datasets at Diamond Light Source, Philos. Trans. R. Soc. A Math. Phys. Eng. Sci. 373 (2015). doi:10.1098/rsta.2014.0398.

[42] N.T. Vo, R.C. Atwood, M. Drakopoulos, Radial lens distortion correction with sub-pixel accuracy for X-ray micro-tomography, Opt. Express. 23 (2015) 32859–32868. doi:10.1364/OE.23.032859.

[43] J. Schindelin, I. Arganda-Carreras, E. Frise, V. Kaynig, M. Longair, T. Pietzsch, S. Preibisch, C. Rueden, S. Saalfeld, B. Schmid, J.-Y. Tinevez, D.J. White, V. Hartenstein, K. Eliceiri, P. Tomancak, A. Cardona, Fiji: an open-source platform for biological-image analysis, Nat Meth. 9 (2012) 676–682. doi:10.1038/nmeth.2019.

[44] A. Buades, B. Coll, J.-M. Morel, Non-Local Means Denoising, Image Process. Line. 1 (2011) 490–530. doi:10.5201/ipol.2011.bcm_nlm.

[45] J. Immerkær, Fast noise variance estimation, Comput. Vis. Image Underst. 64 (1996) 300–302. doi:10.1006/cviu.1996.0060.

[46] G. Tozzi, V. Danesi, M. Palanca, L. Cristofolini, Elastic Full-Field Strain Analysis and Microdamage Progression in the Vertebral Body from Digital Volume Correlation, Strain. 52 (2016) 446–455. doi:10.1111/str.12202.

[47] M. Palanca, G. Tozzi, L. Cristofolini, M. Viceconti, E. Dall'Ara, 3D Local Measurements of Bone Strain and Displacement: Comparison of Three Digital Volume Correlation Approaches., J. Biomech. Eng. 137 (2015) 1–14. doi:10.1115/1.4030174.

[48] A.C. Deymier-Black, A. Singhal, J.D. Almer, D.C. Dunand, Effect of X-ray irradiation on the elastic strain evolution in the mineral phase of bovine bone under creep and load-free conditions, Acta Biomater. 9 (2013) 5305–5312. doi:10.1016/j.actbio.2012.07.046.

[49] M. Witala, J. Han, A. Menzel, K. Nygård, *In situ* small-angle X-ray scattering characterization of X-ray-induced local heating, J. Appl. Crystallogr. 47 (2014) 2078–2080. doi:10.1107/S1600576714020159.

[50] W. Bras, H. Stanley, Unexpected effects in non crystalline materials exposed to X-ray radiation, J. Non. Cryst. Solids. 451 (2016) 153–160. doi:10.1016/j.jnoncrysol.2016.06.020.

[51] H. Wallander, J. Wallentin, Simulated sample heating from a nanofocused X-ray beam, J. Synchrotron Radiat. 24 (2017) 925-933.

[52] U. Wolfram, J. Schwiedrzik, A. Bürki, A. Rack, C. Olivier, F. Peyrin, J. Best, J. Michler, P.K. Zysset, Microcrack evolution in microindentation of ovine cortical bone investigated with lapsed SRmicroCT, 23rd Congr. Eur. Soc. Biomech. (2017) 2017.

[53] P. Zioupos, J.D. Currey, A.J. Hamer, The role of collagen in the declining mechanical properties of aging human cortical bone, J. Biomed. Mater. Res. 45 (1999). doi:10.1002/(SICI)1097-4636(199905)45:2<108::AID-JBM5>3.0.CO;2-A.

[54] T.W. Mitchell, B.J. Rigby, *In vivo* and *in vitro* aging of collagen examined using an isometric melting technique., Biochim. Biophys. Acta. 393 (1975) 531–541.

[55] J.M. Lee, C.A. Pereira, D. Abdulla, W.A. Naimark, I. Crawford, A multi-sample denaturation temperature tester for collagenous biomaterials, Med. Eng. Phys. 17 (1995) 115–121. doi:10.1016/1350-4533(95)91882-H.

[56] M. Unal, A. Creecy, J.S. Nyman, The Role of Matrix Composition in the Mechanical Behavior of Bone, Curr. Osteoporos. Rep. 16 (2018) 205–215. doi:10.1007/s11914-018-0433-0.

[57] W. Ginoza, Radiosensitive Molecular Weight of Single-Stranded Virus Nucleic Acids, Nature. 199 (1963) 453. http://dx.doi.org/10.1038/199453a0.

[58] E.S. Kempner, H.T. Haigler, The influence of low temperature on the radiation sensitivity of enzymes., J. Biol. Chem. 257 (1982) 13297–13299.

[59] M.M. Panjabi, M. Krag, D. Summers, T. Videman, Biomechanical time-tolerance of fresh cadaveric human spine specimens, J. Orthop. Res. 3 (1985) 292–300. doi:10.1002/jor.1100030305.

[60] F. Linde, H.C.F. Sørensen, The effect of different storage methods on the mechanical properties of trabecular bone, J. Biomech. 26 (1993) 1249–1252. doi:https://doi.org/10.1016/0021-9290(93)90072-M.

[61] Q. Kang, Y.H. An, R.J. Friedman, Effects of multiple freezing-thawing cycles on ultimate indentation load and stiffness of bovine cancellous bone, Am. J. Vet. Res. 58 (1997) 1171—1173. http://europepmc.org/abstract/MED/9328673.

[62] R.E. Borchers, L.J. Gibson, H. Burchardt, W.C. Hayes, Effects of selected thermal variables on the mechanical properties of trabecular bone, Biomaterials. 16 (1995) 545–551. doi:10.1016/0142-9612(95)91128-L.

[63] W. Lee, I. Jasiuk, Effects of freeze-thaw and micro-computed tomography irradiation on structure-property relations of porcine trabecular bone, J. Biomech. 47 (2014) 1495–1498. doi:10.1016/j.jbiomech.2014.02.022.

[64] A. Mazurkiewicz, The effect of trabecular bone storage method on its elastic properties, Acta Bioeng. Biomech. 20 (2018) 21–27. doi:10.5277/ABB-00967-2017-03.

[65] G.E. Fantner, T. Hassenkam, J.H. Kindt, J.C. Weaver, H. Birkedal, L. Pechenik, J.A. Cutroni, G.A.G. Cidade, G.D. Stucky, D.E. Morse, P.K. Hansma, Sacrificial bonds and hidden length dissipate energy as mineralized fibrils separate during bone fracture, Nat. Mater. 4 (2005) 612–616. doi:10.1038/nmat1428.

[66] S. Hedan, A.L. Fauchille, V. Valle, J. Cabrera, P. Cosenza, One-year monitoring of desiccation cracks in Tournemire argillite using digital image correlation, Int. J. Rock Mech. Min. Sci. 68 (2014) 22–35. doi:10.1016/j.ijrmms.2014.02.006.

[67] X. Wei, M. Hattab, P. Bompard, J.-M. Fleureau, Highlighting some mechanisms of crack formation and propagation in clays on drying path, Géotechnique. 66 (2016) 287–300. doi:10.1680/jgeot.14.P.227.

[68] A.J. Bodey, C. Rau, Launch of the I13-2 data beamline at the Diamond Light Source synchrotron, J. Phys. Conf. Ser. 849 (2017). doi:10.1088/1742-6596/849/1/012038.

Chapter 5. Full-field strain analysis of bone regeneration

5.1. Full-field strain analysis of bone-biomaterial systems produced by the implantation of osteoconductive biomaterials

Marta Peña Fernández[1], Enrico Dall'Ara[3], Andrew J Bodey[2], Rachna Parwani[1], Asa H Barber[1,4], Gordon W Blunn[5], Gianluca Tozzi[1]

[1] *Zeiss Global Centre, School of Engineering, University of Portsmouth, Portsmouth, UK.*

[2] *Department of Oncology and Metabolism and INSIGNEO institute for in silico medicine, University of Sheffield, Sheffield, UK.*

[3] *Diamond Light Source, Oxfordshire, OX11 0QX, UK.*

[4] *S chool of Engineering, London South Bank University, London, UK.*

[5] *School of Pharmacy and Biomedical Sciences, University of Portsmouth, Portsmouth, UK.*

Under review as

"Full-field strain analysis of bone-biomaterial systems produced by the implantation of osteoregenerative biomaterials in an ovine model".

Reprinted with permission from all authors.

Abstract

Osteoregenerative biomaterials for the treatment of bone defects are under much development, with the aim of favouring osteointegration up to complete bone regeneration. A detailed investigation of bone-biomaterial integration is vital to understanding and predicting the ability of such materials to promote bone formation, preventing further bone damage and supporting load-bearing regions. This study aims to characterise the *ex vivo* micromechanics and microdamage evolution of bone-biomaterial systems at the tissue level, combining high resolution synchrotron micro-computed tomography, *in situ* mechanics and digital volume correlation. Results showed that the main microfailure events were localised close to or within the newly formed bone tissue, in proximity to the bone-biomaterial interface. The apparent nominal compressive load applied to the composite structures resulted in a complex loading scenario, mainly due to the higher heterogeneity but also to the different biomaterial degradation mechanisms. The full-field strain distribution allowed characterisation of microdamage initiation and progression. The findings reported in this study provide a deeper insight into bone-biomaterial integration and micromechanics in relation to the osteoregeneration achieved *in vivo*, for a variety of biomaterials. This could ultimately be used to improve bone tissue regeneration strategies.

Keywords: Osteoregenerative biomaterials, bone-biomaterial interface, SR-microCT, *in situ* mechanics, digital volume correlation.

5.1.1. Introduction

Bone is constantly undergoing remodelling during life due to the necessity of adapting to loading conditions and to remove old damaged bone, replacing it with new, mechanical stronger tissue; thus preserving bone strength [1]. As a dynamically adaptable material, bone displays excellent regenerative properties [2]; however, non-union fractures, tumour resections and some musculoskeletal diseases can lead to critical size bone defects [3], which cannot heal spontaneously and require additional treatments before they can regenerate [4]. Bone is the second most frequent transplanted tissue, right after blood transfusion [5]. It is estimated that over two million bone grafting procedures are performed annually worldwide [6] aiming at augmenting bone formation. Current strategies for bone grafts include the use of autografts, allografts and synthetic grafts. Although autografting is still considered as the gold standard [7–9] for stimulating bone repair and regeneration, it is accompanied with risks of donor site morbidity and limited availability [10,11]. Despite the use of allografts, taken from cadavers or donors, circumvent some of the shortcomings of autografts, the procedure is limited by risk of transmission of disease and a high non-union rate with the host tissue [12,13]. The development of synthetic bone substitutes during the past decades has provided a valuable alternative, addressing the limitations of autologous and allogeneic bone grafts and improving bone regeneration by incorporating osteoconductive properties [7,14–16]. Among those synthetic materials, calcium phosphate ceramics and bioactive glasses are widely used in reconstruction of large bone defects [7,17,18].

Calcium phosphates ceramics (CPCs) are constituted by calcium hydroxyapatites (HA), which is similar in chemical composition to the mineral phase of bone [19]. The composition of the final product can be controlled by adjusting the calcium/phosphate ratio (Ca/P). Among CPCs, HA-based ceramics show excellent osteoconductive and osteointegrative properties [17,19]. Therefore, they have gained great attention in clinical studies [20–24]. However, their relative high Ca/P ratio and crystallinity delay the resorption rate of HA, which typically exhibit a slow resorption at the early stages (weeks 1 to 6) and require long times (months to years) for a complete integration *in vivo* and subsequent replacement by newly formed bone [17]. Conversely, bioactive glass refers to a group of synthetic silicate-based ceramics, characterized mainly by their osteoconductive properties, but they also present some osteoinductivity [25–27]. Bioactive glasses are composed of silicate, sodium oxide, calcium oxide, and phosphorous pentoxide; the key component, silicate, constitutes 45-52% of its weight. This optimised constitution lead to a strong and rapid bonding to bone tissue [28,29]. Additionally, they show a fast resorption rate in the first weeks of implantation and can be completely resorbed within six months [18]. Bioactive glass materials are widely used clinically to repair bone defects in maxillofacial and orthopaedic interventions [27,30].

Bone defect animal models remain essential tools for preclinical research of novel biomaterials [31,32], overcoming limitations of *in vitro* studies due to the reduced complexity

of the environment. Appropriate *in vivo* bone healing models allow to assess bone substitutes materials under different loading conditions; for extended duration, in different tissue qualities and age [32,33]. Therefore, the establishment of a suitable animal model is essential prior to the evaluation of novel biomaterials. The use of ovine models to test new bone grafts has increased over time because of their similarities with humans in weight, bone structure and bone regeneration [34–37]. Typically, defects are created in a weight-bearing region of the sheep bone, which provides similarities in bone composition, defect size and healing rate compared to humans [36,38]. Critical defects models generally evaluate the *in vivo* performance of biomaterials in terms of bone regeneration, remodelling, biomaterial resorption and biological effects [35,39,40]. However, their biomechanical competence after implantation is poorly understood [41]. A micromechanical characterisation of the bone-biomaterial systems produced *in vivo* after different bone grafting procedures is essential to demonstrate their ability to produce bone that is comparable with the native tissue they are meant to replace, and therefore, support load-bearing regions. More specifically, an understanding of the internal microdamage progression at the bone-biomaterial interface, which could promote the failure of the entire bone structure, is needed to further characterise the mechanical performance and overall structural response of such composites.

A combination of time-lapsed micro-computed tomography (microCT) with *in situ* mechanics allows the evaluation of the internal microdamage progression in bone and biomaterials [42,43]. Furthermore, a quantification of full-field strain field can be achieved using digital volume correlation (DVC). In fact, during the past decade DVC has become a powerful and unique tool to examine the three-dimensional (3D) internal deformations in bone [44–46] and bone-biomaterial composites [47,48]. Particularly, Tozzi et al. [47] assessed the microdamage of bone-cement interfaces under monotonic and cyclic compression, and more recently, Danesi el al. [48] applied DVC to study failure mechanisms of cement-augmented vertebral bodies. Despite both studies successfully showed the internal strain distribution in bone-biomaterial composites under different loading scenarios, some questions remain. Firstly, bone-cement composites were produced *in vitro*, restricting the real integration of both materials, and therefore the *in vivo* competence. In addition, strain measurements were computed at apparent level, enabling the classification of high- or lowly localised strains in relatively large regions (above 0.6 mm); thus, unable to provide information of the strain distribution at the interface and in the tissue. Actually, deformation mechanisms at the bone-biomaterial interfaces are still missing due to the intrinsic limitation of laboratory-based microCT systems, unable to offer sufficient spatial resolution and signal to noise ratio (SNR) to properly resolve features at the boundary without the requirement of long acquisitions times. This problem can be overcome using synchrotron radiation (SR) based microCT, able to combine fast imaging with high spatial resolution and SNR [49–51]. Additionally, DVC based on SR-microCT images has recently proven to provide reliable strain measurements

at tissue level [52–54], suggesting that an accurate 3D full-field strain evaluation can be obtained at the bone-biomaterial interfaces [55].

The main purpose of this study was to investigate, for the first time, the 3D full-field strain distribution at the bone-biomaterial interface, in relation to the newly regenerated bone produced *in vivo* after the implantation of osteoregenerative commercial grafts in an ovine model. DVC in conjunction with *in situ* SR-microCT mechanics was performed to evaluate the internal strain and microdamage evolution of bone-biomaterial systems under compression. The finding of this paper will improve the understanding of the micromechanical behaviour of bone-biomaterial structures formed *in vivo* due to bone regeneration process associated with bone grafting procedures.

5.1.2. Methods

5.1.2.1. Biomaterials

Cylindrical bone defects (8 mm diameter by 14 mm depth) were surgically created [56] in the femoral condyles of a female adult sheep (80 Kg). Four different synthetic bone graft materials were then implanted in the defects under Ethics approval granted by the Royal Veterinary College and in compliance with the United Kingdom Home Office regulations (Animal Scientific Procedure Act [1986]).

The selected bone graft materials are commercially available biomaterials: Actifuse; ApaPore (ApaTech Ltd, UK); StronBone and StronBone-P (RepRegen Ltd, UK). Actifuse and ApaPore are HA-based bioceramics. Whereas ApaPore presents a pure HA phase, Actifuse is a silicon-substituted HA (Si-HA), containing 0.8% silicon by weight [57]. Both materials have an interconnected macro and microporous structure, which favours the scaffold osteoconduction. Additionally, the incorporation of silicon to the bone graft promotes rapid bone formation [58]. StronBone and StronBone-P are silicate-based bioactive glasses containing strontium, which has shown a positive effect on bone metabolism [27]. StronBone-P is a more porous version of StronBone and has been proven to promote a more rapid bone growth and higher remodelling rate [59]. The choice of four different biomaterials was intended at exploring microdamage mechanisms at the bone-biomaterial interface, in relation to their different osteointegration and osteoconduction performance on the same animal model following *in vivo* service.

5.1.2.2. microCT scanning and sample preparation

Six weeks after implantation, both left and right condyles were harvested. X-ray micro-computed tomography (microCT) was conducted (Zeiss Xradia Versa 520) using a flat panel detector to identify areas of bone and biomaterial, as shown in Figure 1. Condyles were kept immersed in saline solution throughout image acquisition. The instrument was set to a voltage of 110 kV and a current of 91 µA. With an isotropic effective voxel size of 56 µm, 2001 projections were acquired over 360^0 with an exposure time of 0.36 s per projection.

After inspection of the reconstructed microCT images, the desired sample locations were identified (Figure 1) and a trephine blur drill was manually positioned following the condyle and defect geometry. Cylindrical samples (4 mm in diameter and 18 mm in length) were then cored from the thawed condyles in the proximal-distal direction (Figure 1).The ends of the cores were trimmed plane and parallel, and end-constraint was achieved by embedding the samples in poly-methyl-methacrylate (PMMA) endcaps. Approximately 5 mm of the core was embedded into each endcap to achieve a 2:1 aspect ratio, reducing experimental artifacts [60]. In total, four bone-biomaterial systems from the bone defect areas and one control sample (trabecular bone) were analysed (Figure 2b, c). Samples were kept frozen at -20° and thawed for around 2 h in saline solution at room temperature before image acquisition.

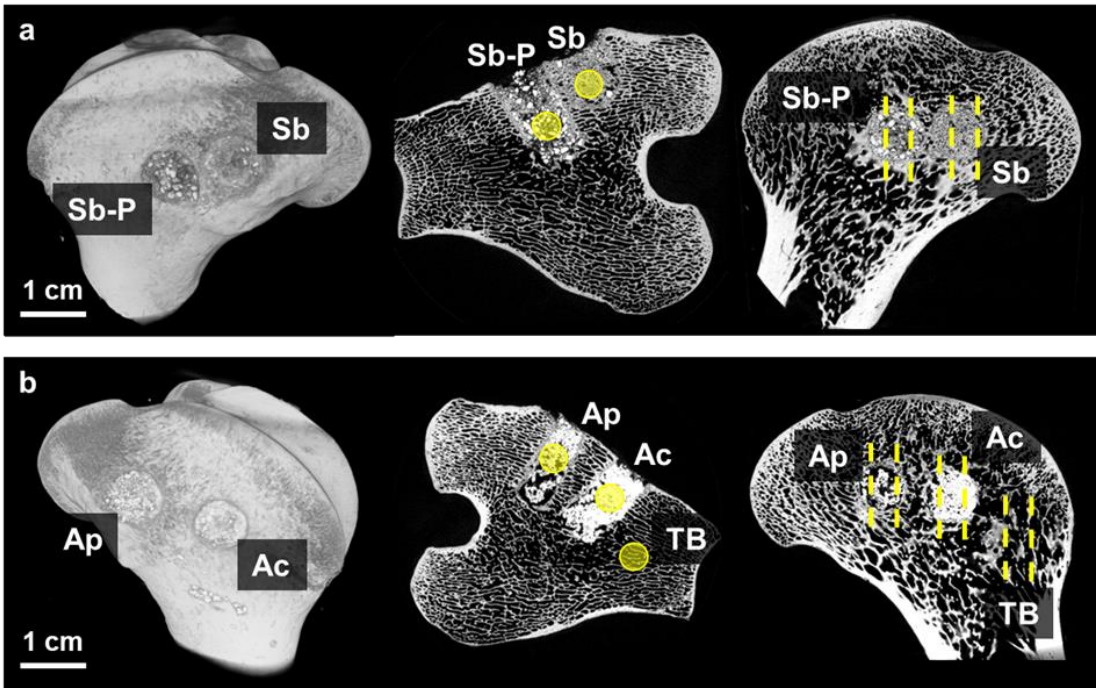

Figure 1. 3D volume reconstruction (left) and representative microCT slices of the four bone defects in the left (a) and right (b) femoral condyles, showing osteointegration of the bone grafts. (Ac: Actifuse; Ap: ApaPore; Sb: StronBone, Sb-P: StronBone-P, TB: Trabecular bone control). Sites of sample extraction are marked with yellow circles (middle figures), whilst direction of extraction is marked with dashed lines (right figures).

5.1.2.3. SR-microCT and *in situ* mechanics

SR-microCT imaging (Figure 2a) was performed at the Diamond-Manchester Imaging Branchline I13-2 (Diamond Light Source, UK), using a filtered (1.3 mm pyrolytic graphite, 3.2 mm aluminium and 60µm steel), partially-coherent, polychromatic 'pink' beam (5-35 keV) of near-parallel geometry with an undulator gap of 5 mm. Samples were aligned for imaging under low-dose conditions (~10 minutes per sample) by temporarily setting the undulator gap to 10 mm [61]. Projections were recorded by a sCMOS (2560 x 2160 pixels) pco.edge 5.5 (PCO AG, Germany) detector, which was coupled to a visual light microscope. A 1.25X objective lens (with 500 µm-thick CdWO4 scintillator) was used to achieve a total

magnification of 2.5X, resulting in an effective voxel size of 2.6 µm and a field of view of 6.7 x 5.6 mm. For each dataset, 1801 projection images were collected over 180 degrees of continuous rotation ('fly scan'). The exposure time was set to 64 ms per projection in order to minimise irradiation-induced damage during image acquisition [62]. The propagation distance (sample to detector) was set to 150 mm to provide sufficient in-line phase contrast and better visualise the microstructure [55]. The projection images were flat-field and dark-field corrected prior to reconstruction. For each dataset, 40 flat and dark images were collected. Reconstruction was performed at Diamond using the in-house software, DAWN [63,64], incorporating ring artefact suppression.

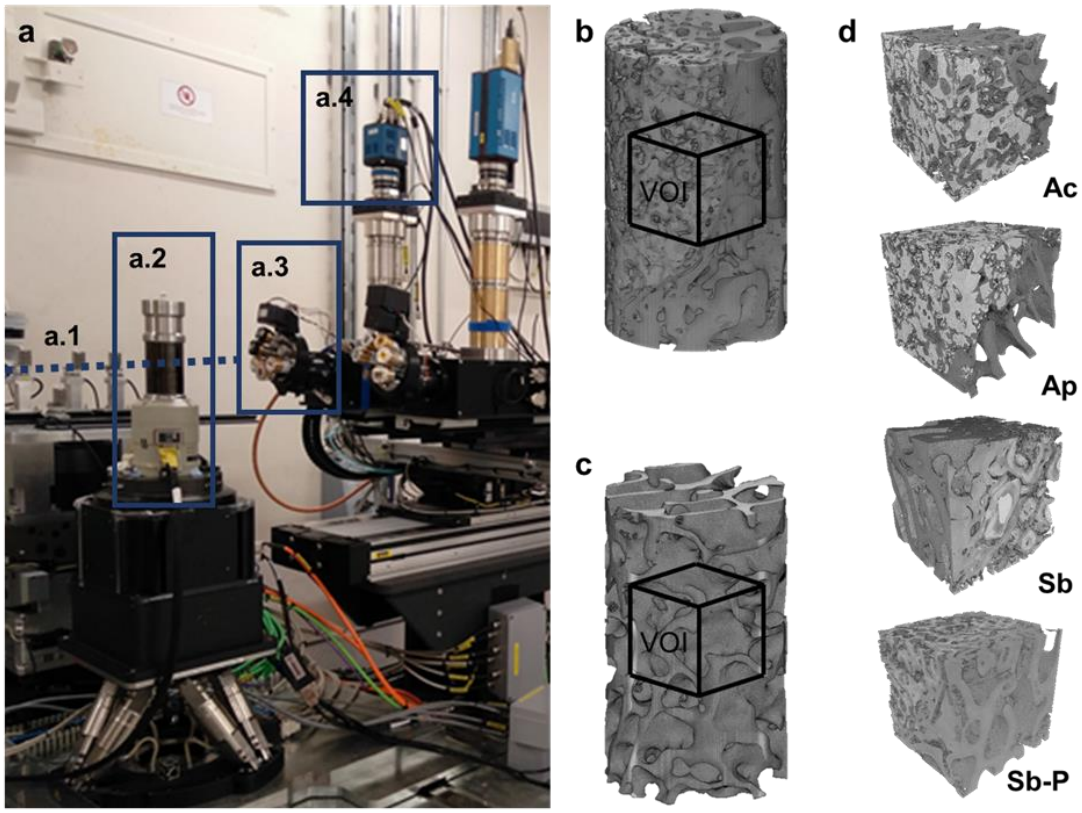

Figure 2. (a) Experimental setup at the I13-2 beamline. The direction of the beam is indicated by the dashed line (a.1). Specimens were scanned with a loading stage (a.2) using a pco.edge 5.5 detector (a.4) and a 1.25X objective (a.3). SR-microCT reconstruction of one representative bone-biomaterial (b) and trabecular bone control (c) showing the volume of interest (VOI) used for DVC analysis. VOIs for the bone-biomaterial systems (d) were selected to include the interface between the different grafts (Ac: Actifuse; Ap: ApaPore; Sb: StronBone, Sb-P: StronBone-P) and the bone tissue.

In situ uniaxial compression testing was performed using a micro-mechanical loading stage equipped with a 5kN load cell and environmental chamber (CT5000, Deben Ltd, UK). Specimens were immersed in saline solution throughout the duration of the test to simulate physiological conditions. A small preload (~5N) was first applied to ensure good end contact prior to testing. Each specimen was subjected to four compression steps under displacement control at a constant cross-head speed of 0.1 mm/min. The first three compression steps were set to 0.1, 0.25 and 0.5 mm of displacement, whereas for the last step the actuator was

stopped after failure detection from the load-displacement curve. Specimens were allowed to settle for 10 minutes after each compression step before image acquisition to reduce stress relaxation during imaging. Full tomographic datasets were acquired at each loading step, under the applied displacement, after two repeated scans (preload state) prior to loading for DVC error analysis [52].

5.1.2.4. Image post-processing

After image acquisition, the 3D datasets were rigidly registered using the unloaded image as a reference [55]. Then, a volume of interest (VOI) was cropped from each tomogram, consisting of a parallelepiped with side lengths of 1000 voxels (2.6 mm^3). The VOI was set in the centre of the volume for the control trabecular bone specimen, and manually selected for the bone-biomaterial specimens in order to include the interface (Figure 2d). Images were denoised by applying a non-local means filter [65,66]. The original SR-microCT images were masked by setting to zero the grayscale intensity of non-bone/biomaterial voxels [55]. Briefly, binary images (value one for bone-biomaterial voxels and zero elsewhere) were created using a global thresholding segmentation followed by an iterative approach that filled small holes and removed isolated pixels. Masked images were obtained by multiplying the filtered and binary 3D images. The same approach was used to segment the remaining bone graft from the bone tissue in bone-Actifuse, bone-ApaPore and bone-StronBone-P specimens. This procedure could not be applied to the bone-StronBone as the biomaterial was considerably more resorbed and the difference in the grey-level intensity between bone and biomaterial was minimal (Figure 2).

5.1.2.5. Digital volume correlation

DVC (DaVis v8.4, LaVision, Goettingen, Germany) was used to compute full-field strains throughout the bone-biomaterial composites and the control trabecular bone specimens after each compression step. DaVis is a cross-correlation method operating on the intensity values (grey-level) of 3D images. The operating principles have been extensively reported elsewhere [55,67]. The DVC parameters used in this study relied on a previous methodological work based on repeated SR-microCT scans of the specimens in a ‘zero-strain’ condition for the error assessment as a function of sub-volume size and imaging post-processing [55].

Thus, DVC computation was conducted using a multi-pass scheme [67] with a final sub-volume of 48 voxels, reached via successive (predictor) passes using sub-volumes of 112, 96, 80 and 64 voxels, with 0% overlap between the sub-volumes. DVC was applied to the masked images, treating the non-hard phase as a black ‘zero-count’ region to avoid large strain artifacts in regions without a clear pattern distribution (i.e. saline, bone marrow). Additionally, sub-volumes with a correlation coefficient below 0.6 were removed from the resultant vector, to avoid artifacts due to poor correlation. Errors on the DVC-computed displacements using the described settings did not exceed 0.22 μm, whereas the mean

absolute error (MAER) and the standard deviation of the error (SDER) of the strain components were found to be ~200 με and ~100 με, respectively. Given the voxel size of the SR-microCT images, the final DVC computed spatial resolution corresponded to ~125 μm; thus, providing full-field strain at tissue level, within the bone tissue and/or biomaterial [52,55].

In order to evaluate the 3D full-field strain distribution in the selected specimens over time in relation to the deformation induced by the compressive applied load, first (ε_{p1}) and third (ε_{p3}) principal strains and maximum shear strain (γ_{max}) were computed within the bone-biomaterial volume after a bi-cubic interpolation of the measured strain to allow a strain value per voxel. Histograms of the strain distribution were calculated as the number of voxels for bone/biomaterial with strains corresponding to a specific bin, divided by the total number of mineralised voxels. 1000 bins were used to cover a range from 0 με to ±10000 με for the first and third principal strains, and 0 με to 15000 με for the shear strain. Additionally, the damaged solid volume (SV_y) was computed as the mineralised voxels exceeding +/-10000 με in tension/compression, or above 15000 μεin shear [68,69].

5.1.2.6. Multi-scale microCT

Following the *in situ* mechanical test, multi-scale microCT was performed in the bone-biomaterial systems to acquire high-resolution images in regions of newly formed bone. MicroCT was performed (Zeiss Xradia Versa 510, CA) at three different resolutions (4 μm, 1.5 μm and 0.5 μm voxel size) using the 'scout-and-zoom' workflow available in the system and different optical magnification. Firstly, medium-resolution (4 μm voxels) was set using 60 kV at 0.4X optical magnification with an exposure time of 5 seconds per projection in order to have the entire specimen diameter in the field of view (~ 4 mm). Then, a VOI (1.5 mm^3) at the bone-biomaterial interface was identified and a high-resolution (1.5 μm voxels) acquisition was performed using 60kV energy at 4X optical magnification with an exposure time of 6 seconds. Finally, the 'zoom-in' process converged on a smaller VOI (0.5 mm^3) from the second reconstructed volume to include some remaining bone graft material and most of the newly formed bone. The highest-resolution (0.5 μm voxels) imaging was conducted at 80kV and a 20X optical magnification with an exposure time of 30 seconds per projection. 2001 projections were acquired for the three tomograms at a rotational step of 0.18°, resulting in a total scanning time of 23 hours per specimen approximately.

5.1.3. Results

5.1.3.1. *In situ* SR-microCT mechanics

The force-displacement curves (Figure 3) showed an initial toe region, followed by a monotonic trend that was linear during the first two steps up to 0.25 mm of compression. Stress relaxation was also visible at the end of each compression step, when the actuator was stopped to allow SR-microCT scanning. Failure was considered at the point where force

reached a plateau or eventually dropped. This occurred either during the third step (bone-StronBone), or during the fourth step (all others). The bone-StronBone specimen presented a more ductile behaviour with respect to the others, and failure was only reached after 1 mm of compression. On the other hand, the bone-Actifuse seemed to be much stiffer, and failure was reached for an applied load an order of magnitude higher than the other specimens (160 N for bone-Actifuse compared to ~60N for bone-ApaPore). Bone-ApaPore and bone-StronBone-P specimens showed behaviour more similar to the trabecular bone control, with elastic regions fairly parallel. Furthermore, failure for bone-StronBone-P and control specimens was experienced at a similar point (~ 50 N force and ~ 0.8 mm compression).

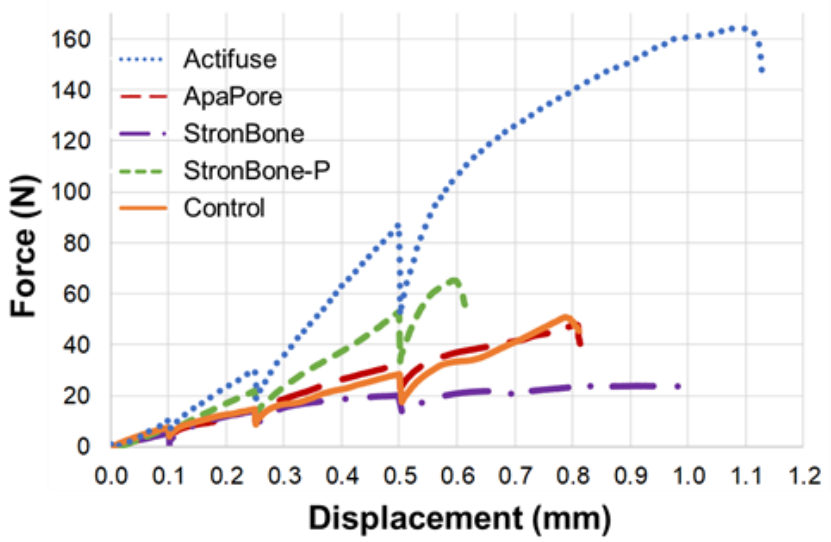

Figure 3. Load-displacement curves for the tested specimens. The force shows a drop at the end of each compression step, corresponding to the stress relaxation while the specimen was allowed to settle (10 min) before image acquisition (~2 min).

A qualitative inspection of the SR-microCT images of the four bone-biomaterial systems before and after failure (Figure 4) showed the different integration of the bone graft materials within the bone matrix. SR-microCT evaluation allowed to clearly distinguish the three distinct materials that were present: bone marrow (dark grey), bone tissue gradients (medium greys), and remaining bone graft (light grey). In addition, the newly formed bone is easily recognisable in proximity of the remaining biomaterial and differs from the more remodeled trabecular bone, present in bone-ApaPore and bone-Actifuse specimens, in the more amorphous organisation (i.e. woven type). A comparison of the SR-microCT images before and after failure revealed how microdamage accumulated during *in situ* compression mainly developed in proximity (Actifuse- ApaPore-bone) or within (StronBone- StronBone-P-bone) the new regenerated tissue. Failure in bone-Actifuse and bone-ApaPore specimens degenerated in trabecular fracture, whereas microcracks were clearly visible in the newly formed bone at the interface for the bone-StronBone-P. Microdamage in bone-StronBone was not possible to detect by visual inspection, in accordance to the fact that overall failure was not identified (Figure 3).

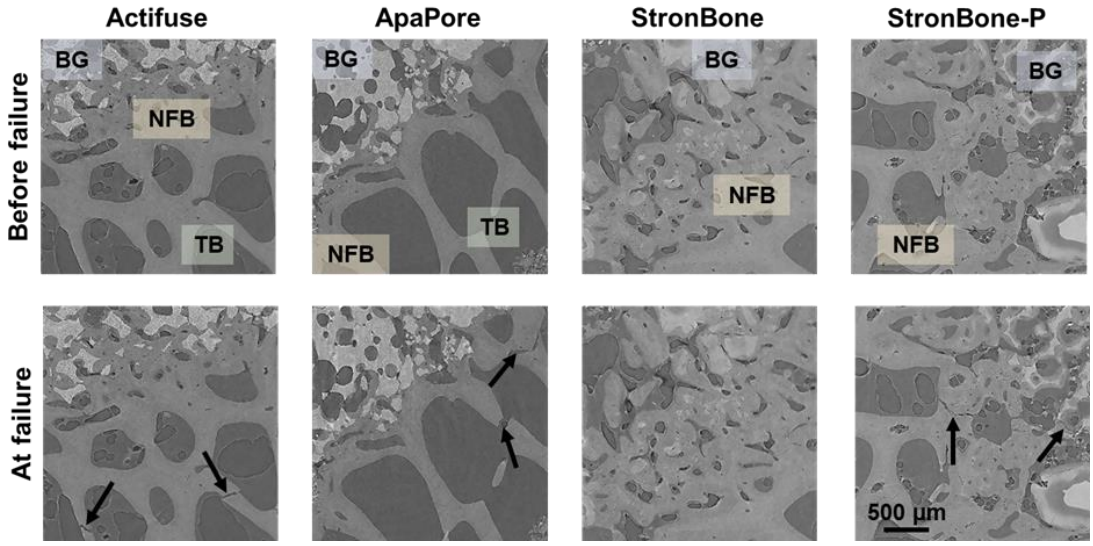

Figure 4. SR-microCT cross-sections through the VOI of each bone-biomaterial system before (top) and after (bottom) failure. Areas corresponding to trabecular bone (TB), newly formed bone (NFB) and bone graft material (BG) are indicated in the top row before failure. Arrows in the bottom row of images indicate visible microcracks developed either in the pre-existing bone for bone-Actifuse and bone-ApaPore or in the newly formed bone for bone-StronBone and bone-StronBone-P after mechanical loading. Scale bar is valid for all images.

5.1.3.2. Digital volume correlation

The third principal strain distributions (ε_{p3}) for the four compression steps are reported in Figure 5 for a representative VOI including the bone-biomaterial interface. A strain accumulation in regions of trabecular bone was observed for the bone-Actifuse and bone-ApaPore specimens (Figure 5, first and second row), where failure was located at the end of the test. After the second compression step (Δl = 0.25 mm), a strain redistribution appeared in bone-Actifuse specimen; however, a further increase in the applied load (third step, Δl = 0.5 mm) led to higher compressive strains in the original (Δl = 0.1 mm) more strained areas, which further developed in trabecular fracture. Additionally, after fracture, the structure lacked support for load transfer; thus, high differences of residual strain were observed between the fractured regions (trabecular bone) and the undamaged one (bone graft). The compressive strain distribution of bone-StronBone and bone-StronBone-P presented an opposite behaviour, as the graft integration within the newly formed bone was different (Figure 4). Bone-StronBone system (Figure 5, third row) showed strain accumulation mainly in areas of newly formed bone, whereas areas in which bone graft remained unabsorbed presented low strain levels. Conversely, higher compressive strains were found in the bone graft regions for the bone-StronBone-P system (Figure 5, fourth row) and low strain values in the newly formed tissue.

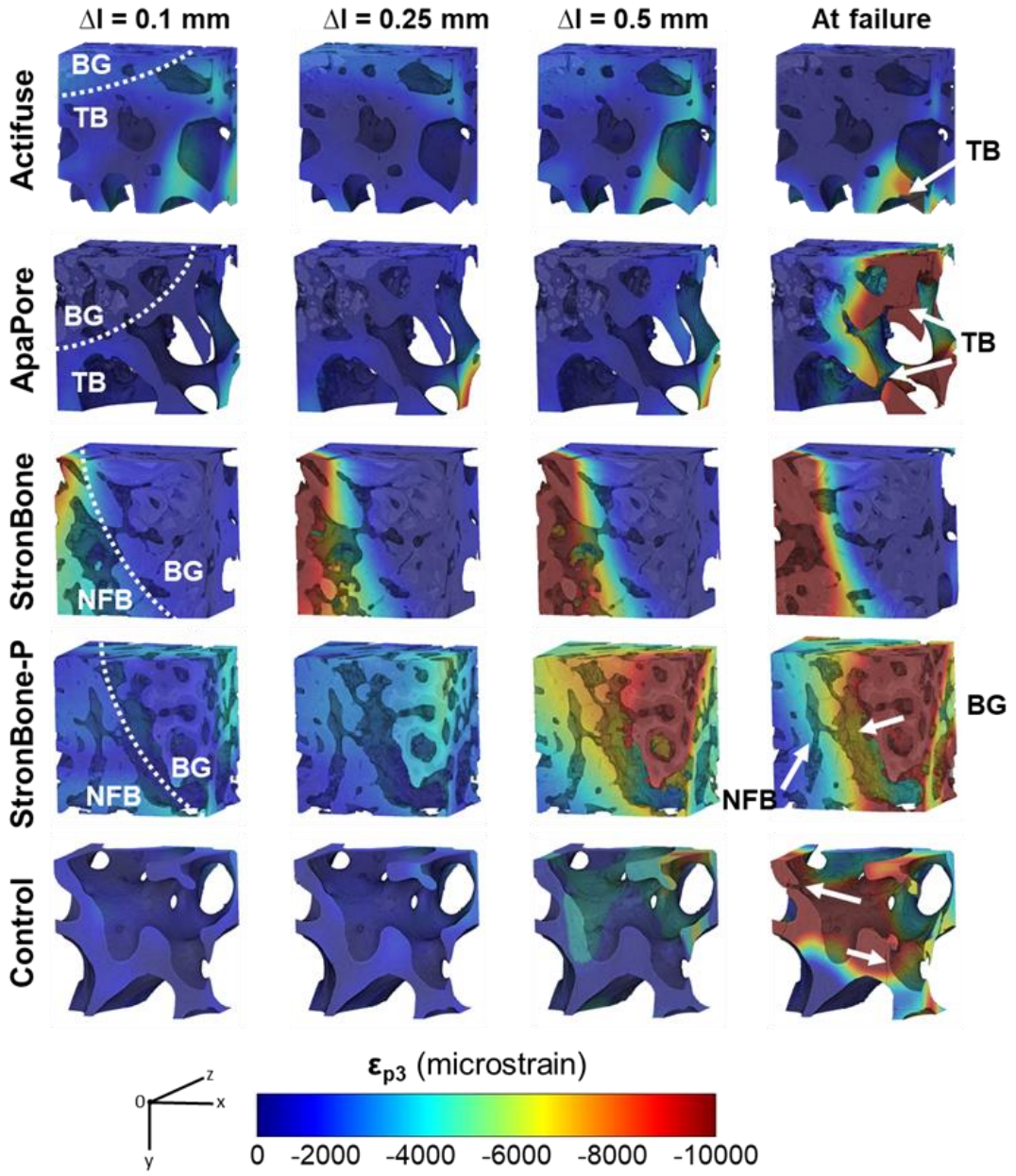

Figure 5. 3D full-field third principal strain distribution (ε_{p3}) at each compression step for the bone-biomaterial systems and the trabecular bone control. A representative VOI (1.6 x 1.6 x 1.0 mm^3) at the bone-biomaterial interface was analysed. Bone-biomaterial interface is indicated by a dotted line in the first column. Microcracks after failure are indicated with arrows as well as material in which failure was observed. Samples were compressed in the z direction. TB: Trabecular bone; NFB: newly formed bone; BG: bone graft material. Animations of strain distribution over time available online (see available electronic data AVI_5.1.5 in thesis annexes).

Full-field first principal strain (ε_{p1}) and shear strain (γ_{max}) distributions are reported in Figure 6 and 7, respectively, for all the specimens. A similar progressive strain accumulation as for the compressive strain (ε_{p3}) was observed for the bone-Actifuse and bone-ApaPore specimens, where the strain development seemed to predict the failure in the trabecular bone regions. Tensile strains in bone-StronBone (Figure 6, third row) were considerably

lower than compressive strains, whereas an important difference in the shear and compressive strain between areas of remaining bone graft and newly formed bone was observed (Figure 7, third row) in the same specimen. On the other hand, the distribution of tensile and shear strains in the bone-StronBone-P (Figure 6 and 7, fourth row) at failure were different to the compressive strain, where high strain magnitudes were identified along the microcracks developed through the bone-biomaterial interface.

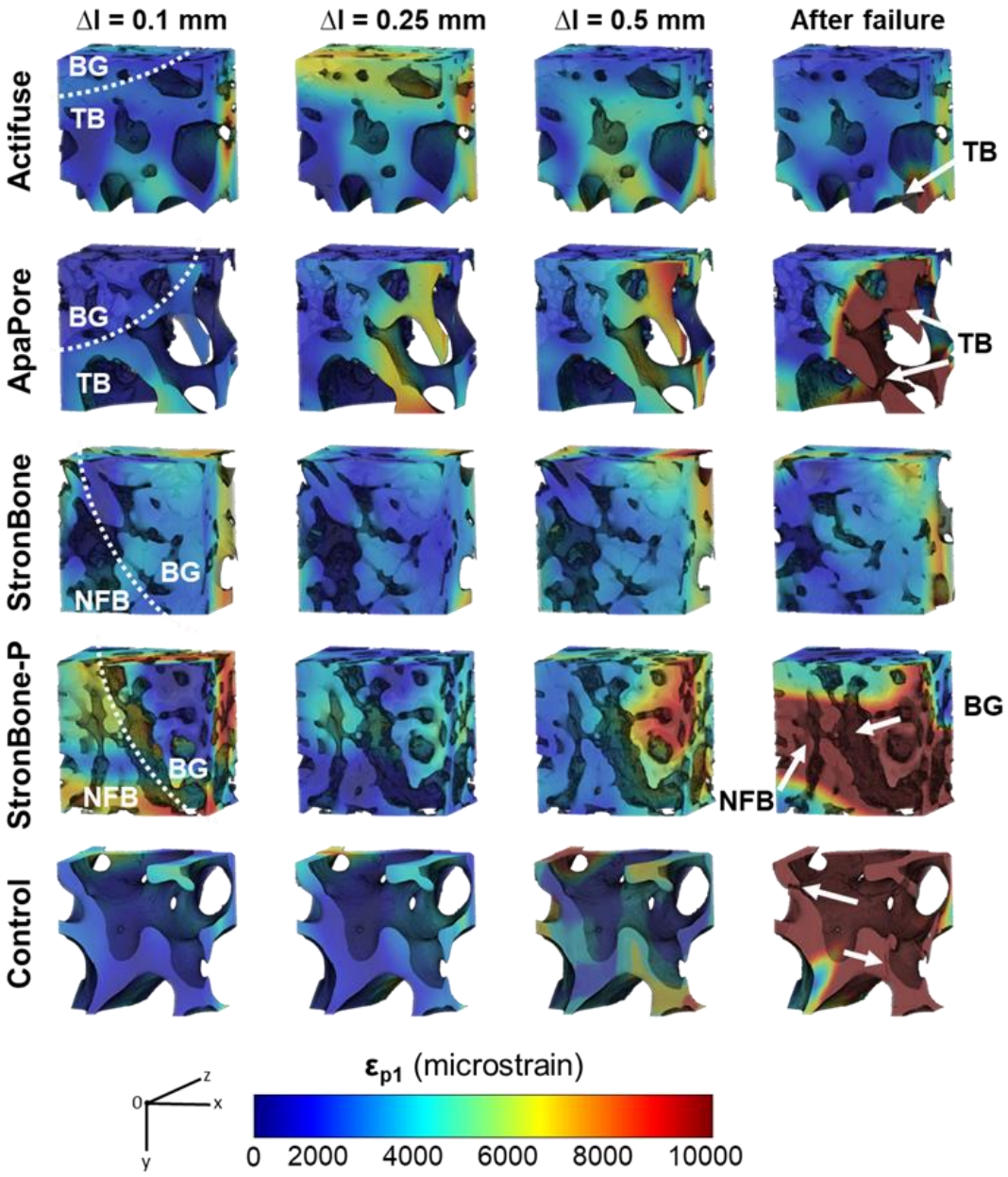

Figure 6. 3D full-field first principal strain distribution (ε_{p1}) at each compression step for the bone-biomaterial systems and the trabecular bone control. A representative VOI (1.6 x 1.6 x 1.0 mm^3) at the bone-biomaterial interface was analysed. Bone-biomaterial interface is indicated by a dotted line in the first column. Microcracks after failure are indicated with arrows as well as material in which failure was observed. Samples were compressed in the z direction. TB: Trabecular bone; NFB: newly formed bone; BG: bone graft material. Animations of strain

distribution over time available online (see available electronic data AVI_5.1.6 in thesis annexes).

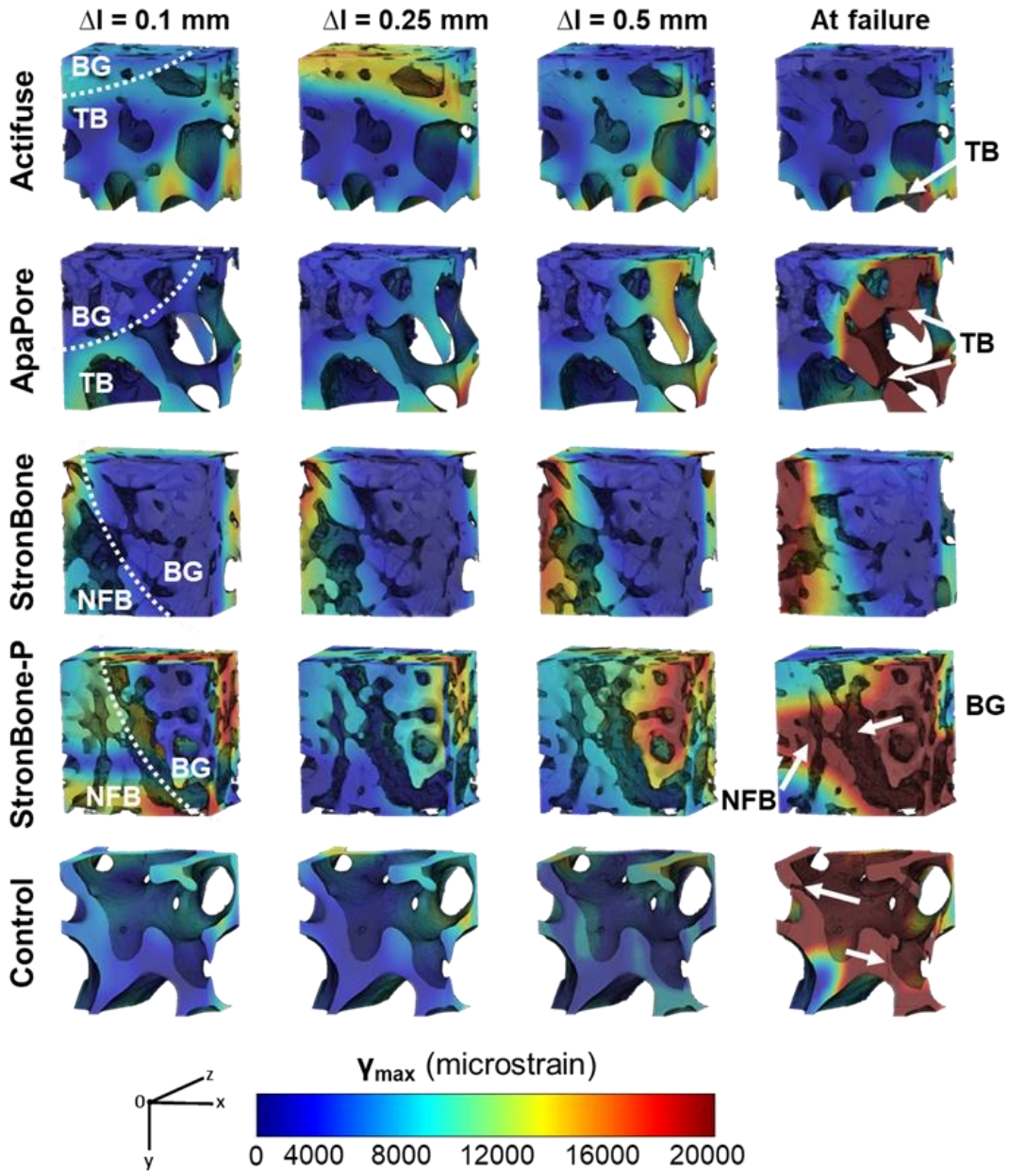

Figure 7. 3D full-field maximum shear strain distribution (γ_{max}) at each compression step for the bone-biomaterial systems and the trabecular bone control. A representative VOI (1.6 x 1.6 x 1.0 mm^3) at the bone-biomaterial interface was analysed. Bone-biomaterial interface is indicated by a dotted line in the first column. Microcracks after failure are indicated with arrows as well as material in which failure was observed. Samples were compressed in the z direction. TB: Trabecular bone; NFB: newly formed bone; BG: bone graft material. Animations of strain distribution over time available online (see available electronic data AVI_5.1.7 in thesis annexes).

The yielded solid volume (Table 1) after failure emphasised the different behaviour for the bone-Actifuse and bone-ApaPore compared to bone-StronBone and bone-StronBone-P specimens. The first two presented a small percentage of damaged volume, which was more important in the bone tissue than in the remaining bone graft, and a higher yielded volume

was reached in a combination of tensile and shear states. Conversely, a yielded solid fraction started to accumulate in the bone-StronBone right after the first compression step, resulting in over 25% of damaged volume after the third step, and 40% after failure in both compression and shear. The yielded volume after failure for the bone-StronBone-P was also over 40% in tensile and shear, and it was more important in the biomaterial region than in the bone tissue areas. Tensile and shear strains were also more negative in the trabecular bone control specimen, with 30% of its volume yielded after failure.

Table 1. Damaged solid volume in tension (SV_y,ε_{p1}), compression (SV_y,ε_{p3}) and shear (SV_y,γ_{max}) after failure in the four bone-biomaterial and the control specimens, as computed using DVC. SVy was computed as the hard phase voxels exceeding +/- 10000 με in tension/compression, or above 15000 με in shear.

		SV_y,ε_{p1} (%)	SV_y,ε_{p3} (%)	SV_y,γ_{max}(%)
Actifuse				
	Bone	0.79	0.23	0.83
	Biomaterial	0	0	0
ApaPore				
	Bone	10.89	5.37	8.99
	Biomaterial	0.02	0.02	0.02
StronBone				
	Bone	25.63	42.43	42.49
	Biomaterial	--	--	--
StronBone-P				
	Bone	45.53	17.43	43.99
	Biomaterial	50.21	38.08	57.03
Control				
	Bone	30.54	13.52	29.85
	Biomaterial	--	--	--

The histograms of shear strain (Figure 8) for the first and last compression steps well described the strain evolution in the bone and biomaterial areas of the analysed specimens. As expected, maximum amplitudes were reached for lower strain values after the first compression step compared to the last (failure). Additionally, peak values corresponded to lower strains in the biomaterial areas in bone-Actifuse and bone-ApaPore, but to higher strain levels in the StronBone-P.

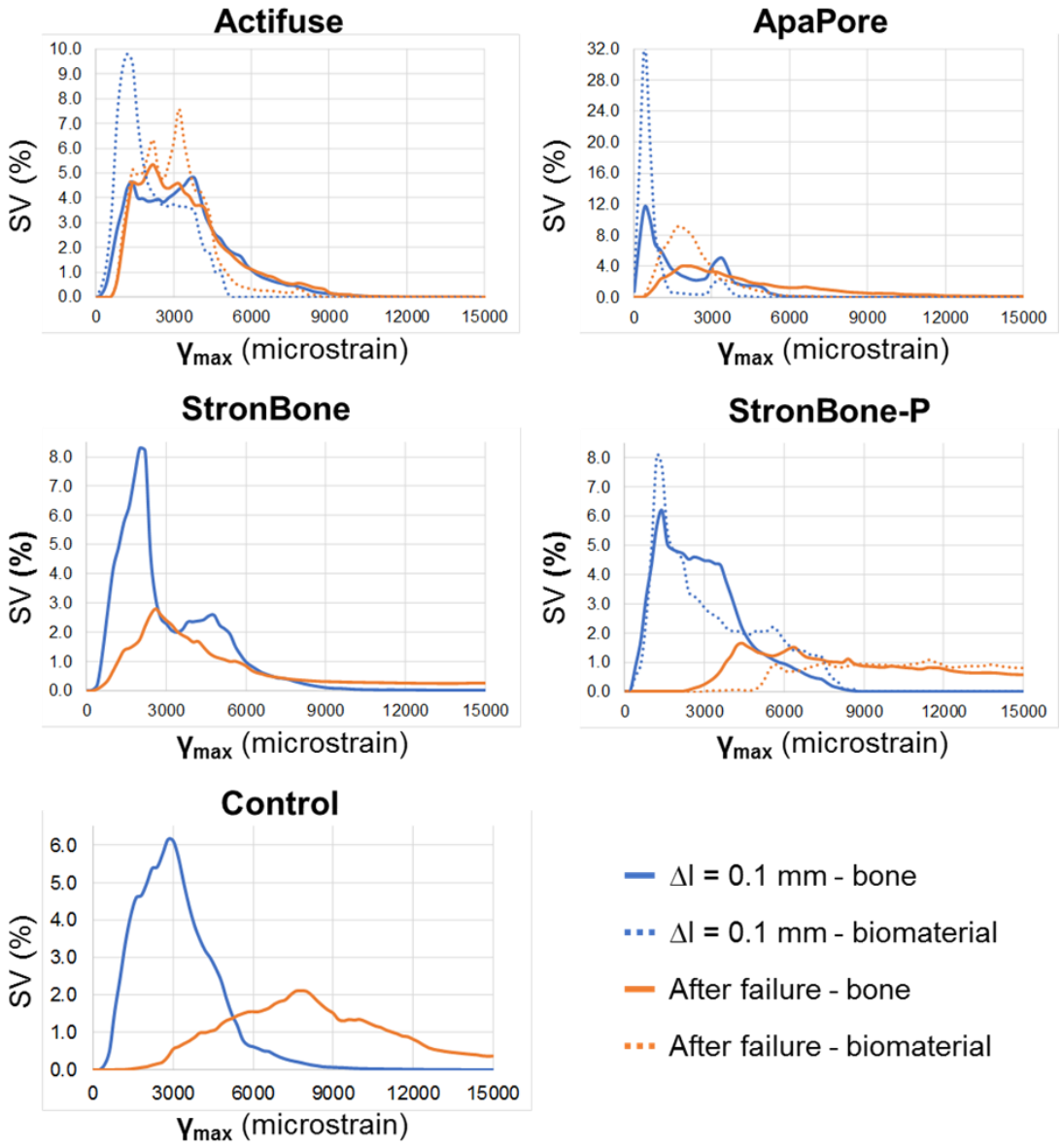

Figure 8. Histograms of the maximum shear strain distribution (γ_{max}) in the hard phase (bone-biomaterial) of the VOI as computed using DVC for the first compression step (blue) and after failure (orange). Values exceeding 15000 με are reported in Table 1. A partition of the strain in the bone (trabecular and newly formed, solid line) and biomaterial (bone graft, dotted line) is shown for the bone-Actifuse, bone-ApaPore and bone-StronBone-P specimens. Bone-StronBone specimen did not show enough contrast (Figure 4) to segment the graft material from the bone tissue.

5.1.3.3. Multi-scale microCT

High resolution microCT images (Figure 9) provided morphological and degree of mineralisation information that allowed for differentiation of trabecular bone, newly formed bone and remaining bone graft, as well as the osteoconduction around the graft material. Bone-Actifuse and bone-ApaPore showed minimal dissolution of the biomaterials, with large areas of remnants with no signs of resorption. Bone formation was identified within the graft

granules and in their proximity. More newly formed bone tissue, characterised for highly disorganised structure (callus bone) compared to the native trabecular structure, was observed in the bone-Actifuse, further remodeled into trabecular bone. However, bone-ApaPore presented a more organised bone formation directly from the graft material. Bone-StronBone and bone-StronBone-P specimens also showed some remnants of biomaterial in the bone defect areas; however, resorption was observed within the newly formed bone regions, characterised for a higher mineral density (lighter grey-level). The interface between the biomaterial and bone was almost completely assimilated (Figure 9-I) but some gaps were visible at higher magnification (Figure 9-II, III, green arrows) in bone-Actifuse, bone-ApaPore and bone-StronBone-P. For all bone-biomaterial systems bone was identified not only in contact with the outer surface of the graft but also within its pores (Figure 9, blue arrows). The higher-resolution scans enabled to identify osteocyte lacunae within the newly formed bone (Figure9-III, yellow arrows). Furthermore, the larger pores found in the newly formed bone may probably correspond to blood vessel formation (Figure 9-III, white arrows). Additionally, cracks in the ApaPore and StronBone-P, more probably associated with the bone impaction grafting procedure, could be identified at the highest resolution (Figure 9-II, III, red arrows).

5.1.4. Discussion

The aim of this study was to investigate and quantify, for the first time, the full-field strain distribution of bone-biomaterial systems produced *in vivo* by osteoregenerative bone graft materials in an ovine model combining *in situ* SR-microCT mechanical testing and DVC. More specifically, this work aimed at evaluating the internal strain and microdamage progression of such composites, and the specific strain distribution in bone graft remnants, newly formed bone and trabecular bone. A deeper characterisation of the micromechanical behaviour of bone-biomaterial constructs was achieved. In fact, despite synthetic bone grafts have shown excellent performance in terms of bone regeneration [17], their mechanical competence remained partially unexplored [47,48].

At an apparent level similar forces were observed in the first two compressive steps within the elastic range for the bone-biomaterial systems and the control trabecular bone sample. However, a further increase of the load evidenced the dissimilarities between the analysed specimens. A comparison of the apparent behaviour of the studied composites is challenging, as it depends not only on the distinct implanted bone graft material, but also on their integration through the regeneration process and their volume fraction. However, it can be seen that bone-Actifuse and bone-StronBone-P systems showed a stiffer behaviour (Figure 3), which may be related to the higher solid volume fraction (66% and 65%, respectively) compared to bone-ApaPore (53%) or the control specimen (24%). It is also interesting to note the ductile apparent behaviour (Figure 3) of the bone-StronBone system that may be due to the dense regions of newly formed bone (Figure 9) with different mineralisation levels.

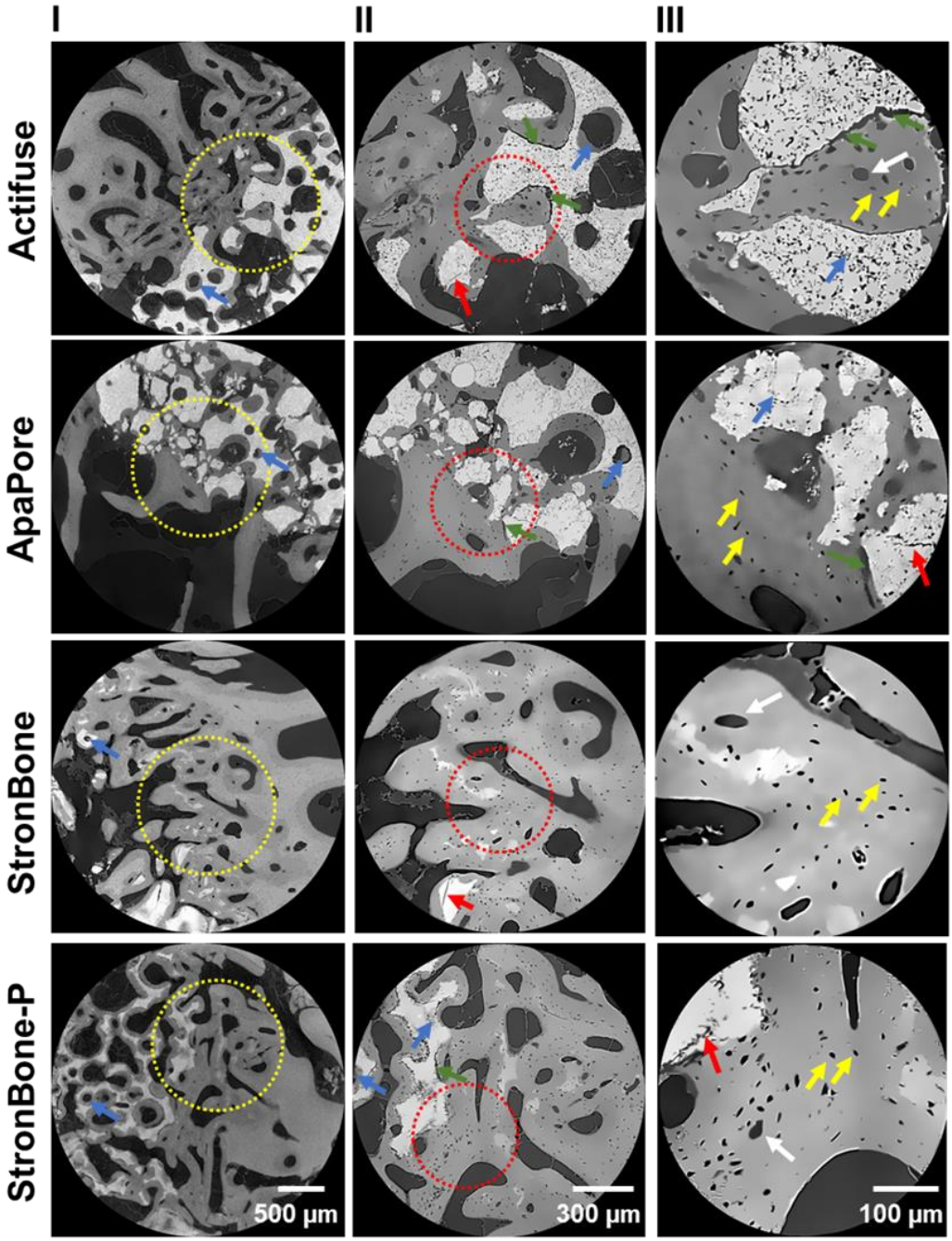

Figure 9. Multi-scale microCT images of the bone-biomaterial systems obtained by increasing the spatial resolution. Images were first acquired at a medium resolution (4 μm^3 voxel size, I). A VOI (yellow circle) was selected and a higher resolution acquisition was performed (1.5 μm^3 voxel size, II). A second VOI (red circle) was then chosen to achieve the highest resolution (0.5 μm^3 voxel size, III). Bone formation was observed within pores (blue arrows), and some gaps were visible at the bone-biomaterial interface (green arrows). Bone graft material presented some cracks (red arrows). Osteocyte lacunae (yellow arrows), and blood vessels (white arrows) were identified at the highest resolution. Scale bars are valid for all images in the same column.

A better characterisation of the mechanical properties of the newly bone formed could be achieved using different mechanical tests. Particularly, Gauthier at al., [41] measured the compressive strength of the newly regenerated tissue after implantation of an injectable bone substitute using micro-indentation. It was shown that the implanted biomaterial could

support the formation of new bone with compressive strength higher than in the native trabecular tissue. Similar findings have been shown in bone-StronBone (Figure 5, third row). Despite high levels of compressive strain were identified in the newly formed bone damage was not visible.

The results herein reported clearly showed that the main microfailure events seemed to be localised close to or within the newly formed bone (Figure 4), at the bone-biomaterial interface. The higher stiffness and strength of the bone graft compared to the more remodelled trabecular tissue induced a critical region at the boundary of the bone-biomaterial, where the initiation of the failure was identified, consistently with previous work on bone-cements composites [43,47,48]. Furthermore, the high-resolution SR-microCT images used in this study allowed for the detection of microdamage (i.e. microcracks) in the tissue (Figure 4), thus providing a deeper insight of the deformation mechanisms at the bone-biomaterial interface. Danesi el al. [48] and Tozzi et al. [43,47] characterised the damage progression in bone-cements composites using microCT images obtained in a lab-based system at 39 µm and 20 µm, respectively. Despite a qualitative inspection and quantitative information of the microdamage was obtained at apparent level, the image spatial resolution was not enough to characterise the deformation at a lower dimensional scale. In fact, this is the first time that a characterisation of the microdamage evolution of bone-biomaterial composites at tissue level has been performed, allowing not only the visual identification of the internal microdamage at the boundary of the bone and biomaterial, but also the quantification of the localised strain in both materials. The potential of DVC based on SR-microCT images to characterised bone deformation at tissue level remains partially unexplored [51,62], and questions still arise on the effect of high-flux SR X-ray radiation on the mechanical properties of the tissue [70]. However, this study limited the total radiation dose absorbed by the tissue (~30 kGy) following previous methodologies [62] in order to minimise the effect of the X-ray radiation in the mechanical integrity of the specimens.

DVC successfully showed how local strains built up from the elastic regime highlighting internal weaker areas that could further result in microdamage initiation and progression up to failure (Figure 5, 6, 7). A complex load transfer was developed in the highly heterogeneous composite structures during compression; however, the DVC-computed 3D full-field strain allowed a description of the microdamage progression. Particularly, high levels of compressive strain, above the typical values of trabecular bone yielding [71,72] were found in areas of trabecular bone fracture (Figure 5) in bone-Actifuse, bone-ApaPore and control specimens. Interestingly, localised strain concentration was observed in bone-Actifuse system (Figure 5, top row) from the first compressive step, resulting in fractured regions at the final compression step. Although bone-StronBone presented high compressive strains since early stages of compression in areas of newly formed bone (Figure 5, third row), microdamage was not visible, remarking the important ability of bone to accumulate microdamage at tissue level prior to the initiation of microcracks [51,73]. Despite

the specimens were subjected to compressive loading, initiation and propagation of microcracks in bone-StronBone-P system were not related to compressive strains but shear strains (Figure 7, fourth row). Christen et al. [51] showed similar finding during microcrack propagation in cortical bone. While compressive (Figure 5) and tensile (Figure 6) strain magnitudes were comparable, a stronger tensile strains accumulation was found around microcracks and trabecular bone fracture regions. As suggested by Christen et al. [51], tensile strains could be used to detect microcracks in the first place. In fact, the tensile strain evolution in bone-Actifuse, bone-ApaPore, bone-StronBone-P and control specimens (Figure 6) seemed to predict the initiation of internal microdamage before it was visible.

The strain partition between bone and biomaterial in bone-Actifuse, bone-ApaPore and bone-StronBone-P systems indicated how the different reabsorption mechanism of the distinct graft materials affected the load transfer and therefore, the microdamage progression. In particular, the slower resorption of Actifuse and ApaPore (Figure 4) with higher stiffness of the biomaterial compared to the bone tissue induced an insufficient load transfer from the trabecular bone tissue towards the bone graft regions; therefore, producing higher strains in bone areas (Figure 8), which ultimately induced microdamage in the trabeculae (Table 1). Conversely, the faster resorption of StronBone-P and better integration within the newly formed bone (Figure 4) produced a more effective load transfer through the specimen, leading to a more equal strain distribution (Figure 8), resulting in microdamage at the interface (Figure 4). Similar findings were reported by Tozzi el al. [47] and Goodheart et al. [74] for bone-cement composites. It was shown that the accumulated strain in the biomaterial region and the bone-cement interface was much lower compared to the trabecular bone when the two phases were clearly distinct, but a better load transfer through the interface was found in the more integrated composites. Despite Li et al. [36] recently suggest that the presence of grafts remnants in the defect area may provide adequate mechanical support during healing, the results herein presented have shown that when the biomaterial is less reabsorbed (bone-Actifuse and bone-ApaPore) load cannot be transferred in an efficient way, leading to a highly heterogenous strain distribution with large localised peaks in the pre-existing bone tissue, which may cause bone fracture in the event of an overload postoperatively. However, the more immature tissue filling the defect after faster degradation of StronBone and StronBone-P was able to carry the load in a more satisfactory way and the structure did not collapse at the end of the compression test. Additionally, microdamage was not observed in bone-StronBone system suggesting that although the newly formed bone was still very immature and little remodelled, it was able to fulfil and exceed the mechanical performance of the native tissue it was meant to restore. These results indicate that a faster resorption rate and higher osteoinduction of synthetic bone grafts for bone replacement may be more beneficial for efficient micromechanics *in vivo* in a postoperative overloading scenario.

The multi-scale microCT results provided a three-dimensional characterisation of bone regeneration induced by the action of osteoconductive biomaterials. The analysis of *in vivo* bone repair for the evaluation of bone graft substitutes has traditionally been assessed using scanning electron microscopy (SEM) combined with histological analysis [35,36,39,40,75,76]. Despite those methods produce highly valuable data on bone-biomaterial interactions relating the morphology, amount and functional properties of the newly formed bone, they are restricted to sample sectioning and only surface analysis can be conducted. Therefore, microCT shows a clear advantage to describe bone-biomaterial interfaces *ex vivo*. Similar to previous findings using SEM [75,77], bone ingrowth was observed within both the larger macropores (Figure 9-I, II, blue arrows) and within strut pores (Figure 9-II, III, blue arrows). When compared to published histological analysis [36,76], osteocyte lacunae (Figure9-III, yellow arrows) were found in the new bone and the gaps between the bone and biomaterial (Figure 9-II, III, green arrows) suggest the presence of loose connective tissue. In addition, the multi-scale microCT approach herein presented could be combined with *in situ* mechanics and DVC to obtain not only the three-dimensional characterisation of bone-biomaterial composites, but also to provide the deformation mechanisms at different scales, from apparent to tissue level. Through the correlation of DVC-measured strains at multiple resolutions to complementary data such as histology or local material properties, a deeper understanding of the *in vivo* bone repair through the action of biomaterials could be achieved.

The results of this study revealed important details on the bone-biomaterial interactions and micromechanics in a clinically relevant bone defect model using synthetic bone graft substitutes. The findings have the potential to better inform numerical models of bone tissue and bioresorbable material adaptation to enable predictions of the long-term *in vivo* behaviour of such materials in the repair of critical size bone defects. Moreover, the strain analysis of bone-biomaterial composites after *in vivo* service in the animal model was performed for the first time; thus, providing clinical relevant biomaterial-tissue integration compared to previous experiments carried out *in vitro* [43,47,48]. The current study is limited considering that only one time point (6 weeks after implantation) was evaluated. However, the outcomes herein presented can be considered as a representative case for the event of an overload during *in vivo* service in a postoperative period. The inability of bone graft materials to restore bone mechanical functions could jeopardise the surgical intervention, with consequent clinical and economic impact. Furthermore, due to the limited sample size (one specimen per group), the generalisation of the results will need further analyses. Additional insights may be gained in future studies by increasing the sample size and comparing the bone repair processes and full-field strain at the bone-biomaterial interface among different bone graft substitutes, as well as over different implantation times.

5.1.5. Conclusion

The combination of high-resolution SR-microCT images and DVC has allowed characterisation, for the first time, of the full-field strain in bone-biomaterial systems produced *in vivo* in an ovine critical size bone defects model. It has been shown that complex strain patterns developed through the highly heterogeneous composites during compression, promoting primary microdamage either in the pre-existing trabecular bone or in the newly formed bone at the bone-biomaterial interface. DVC allowed for a detailed analysis of the internal strain distribution and its association with the microdamage initiation and progression in proximity to the bone-biomaterial interface. These findings highlight the importance of understanding the interaction and micromechanics of bone graft materials and bone tissue. This should facilitate biomaterial development and predictions of long-term bone healing following biomaterial implantation.

Author contribution

Marta Peña Fernández: Study design, data curation, formal analysis, data interpretation. Enrico Dall'Ara: Supervision; Andrew J. Bodey: Data curation; Rachna Parwani: Data curation; Asa H. Barber: Data curation; Gordon W. Blunn: Supervision; Gianluca Tozzi: Data curation, data interpretation, supervision.

Acknowledgements

The authors gratefully acknowledge Diamond Light Source for beamtime at the Diamond-Manchester Imaging Branchline I13-2 and its associated Data Beamline [78] (proposal number MT14080), and the Zeiss Global Centre (University of Portsmouth) for image processing. We further acknowledge Dr. Dave Hollis (LaVision Ltd) for assistance with Davis software, Dr. Kazimir Wanelik for help during the experiment at Diamond Light Source, Dr. Alexander Kao for support during multi-scale microCT imaging and Dr. Robin Rumney for the fruitful discussions.

References

[1] N.A. Sims, J.H. Gooi, Bone remodeling: Multiple cellular interactions required for coupling of bone formation and resorption., Semin. Cell Dev. Biol. 19 (2008) 444–451. doi:10.1016/j.semcdb.2008.07.016.

[2] A. Oryan, S. Monazzah, A. Bigham-Sadegh, Bone injury and fracture healing biology., Biomed. Environ. Sci. 28 (2015) 57–71. doi:10.3967/bes2015.006.

[3] T. Schubert, S. Lafont, G. Beaurin, G. Grisay, C. Behets, P. Gianello, D. Dufrane, Critical size bone defect reconstruction by an autologous 3D osteogenic-like tissue derived from differentiated adipose MSCs., Biomaterials. 34 (2013) 4428–4438. doi:10.1016/j.biomaterials.2013.02.053.

[4] P. V. Giannoudis, T.A. Einhorn, D. Marsh, Fracture healing: The diamond concept, Injury. 38 (2007) 3–6. doi:10.1016/S0020-1383(08)70003-2.

[5] O. Faour, R. Dimitriou, C.A. Cousins, P. V. Giannoudis, The use of bone graft substitutes in large cancellous voids: Any specific needs?, Injury. 42 (2011) S87–S90. doi:10.1016/j.injury.2011.06.020.

[6] V. Campana, G. Milano, E. Pagano, M. Barba, C. Cicione, G. Salonna, W. Lattanzi, G. Logroscino, Bone substitutes in orthopaedic surgery: from basic science to clinical practice, J. Mater. Sci. Mater. Med. 25 (2014) 2445–2461. doi:10.1007/s10856-014-5240-2.

[7] J.E. Schroeder, R. Mosheiff, Tissue engineering approaches for bone repair: Concepts and evidence, Injury. 42 (2011) 609–613. doi:10.1016/j.injury.2011.03.029.

[8] F.W. Bloemers, T.J. Blokhuis, P. Patka, F.C. Bakker, B.W. Wippermann, H.J.T.M. Haarman, Autologous bone versus calcium-phosphate ceramics in treatment of experimental bone defects., J. Biomed. Mater. Res. B. Appl. Biomater. 66 (2003) 526–531. doi:10.1002/jbm.b.10045.

[9] M.K. Sen, T. Miclau, Autologous iliac crest bone graft: Should it still be the gold standard for treating nonunions?, Injury. 38 (2007) 2–7. doi:10.1016/j.injury.2007.02.012.

[10] R. Dimitriou, G.I. Mataliotakis, A.G. Angoules, N.K. Kanakaris, P. V. Giannoudis, Complications following autologous bone graft harvesting from the iliac crest and using the RIA: A systematic review, Injury. 42 (2011) S3–S15. doi:10.1016/j.injury.2011.06.015.

[11] J.C. Banwart, M.A. Asher, R.S. Hassanein, Iliac Crest Bone Graft Harvest Donor Site Morbidity: A Statistical Evaluation, Spine (Phila. Pa. 1976). 20 (1995). https://journals.lww.com/spinejournal/Fulltext/1995/05000/Iliac_Crest_Bone_Graft_Harvest_Donor_Site.12.aspx.

[12] D.L. Wheeler, W.F. Enneking, Allograft bone decreases in strength *in vivo* over time., Clin. Orthop. Relat. Res. (2005) 36–42.

[13] H.J. Mankin, F.J. Hornicek, K.A. Raskin, Infection in Massive Bone Allografts., Clin. Orthop. Relat. Res. 432 (2005). https://journals.lww.com/corr/Fulltext/2005/03000/Infection_in_Massive_Bone_Allografts_.28.aspx.

[14] Y. Fillingham, J. Jacobs, Bone grafts and their substitutess, Bone Jt. J. 98–B (2016) 6–9. doi:10.1302/0301-620X.98B1.36350.

[15] T.T. Roberts, A.J. Rosenbaum, Bone grafts , bone substitutes and orthobiologics Bone grafts , bone substitutes and orthobiologics The bridge between basic science and clinical advancements in fracture healing, 6278 (2016) 114–124. doi:10.4161/org.23306.

[16] P. V. Giannoudis, H. Dinopoulos, E. Tsiridis, Bone substitutes: An update, Injury. 36 (2005) S20–S27. doi:10.1016/j.injury.2005.07.029.

[17] W. Wang, K.W.K. Yeung, Bone grafts and biomaterials substitutes for bone defect repair: A review, Bioact. Mater. 2 (2017) 224–247. doi:10.1016/j.bioactmat.2017.05.007.

[18] T. Kurien, R.G. Pearson, B.E. Scammell, Bone graft substitutes currently available in orthopaedic practice: The evidence for their use, Bone Jt. J. 95 B (2013) 583–597. doi:10.1302/0301-620X.95B5.30286.

[19] S. Zwingenberger, C. Nich, R.D. Valladares, Z. Yao, M. Stiehler, S.B. Goodman, Recommendations and considerations for the use of biologics in orthopedic surgery, BioDrugs. 26 (2012) 245–256. doi:10.2165/11631680-000000000-00000.

[20] J.H. Scheer, L.E. Adolfsson, Tricalcium phosphate bone substitute in corrective osteotomy of the distal radius, Injury. 40 (2009) 262–267. doi:10.1016/j.injury.2008.08.013.

[21] C. Nich, L. Sedel, Bone substitution in revision hip replacement, Int. Orthop. 30 (2006) 525–531. doi:10.1007/s00264-006-0135-6.

[22] R.D.A. Gaasbeek, H.G. Toonen, R.J. Van Heerwaarden, P. Buma, Mechanism of bone incorporation of β-TCP bone substitute in open wedge tibial osteotomy in patients, Biomaterials. 26 (2005) 6713–6719. doi:10.1016/j.biomaterials.2005.04.056.

[23] C. Schwartz, R. Bordei, Biphasic phospho-calcium ceramics used as bone substitutes are efficient in the management of severe acetabular bone loss in revision total hip arthroplasties, Eur. J. Orthop. Surg. Traumatol. 15 (2005) 191–196. doi:10.1007/s00590-005-0244-8.

[24] H. Oonishi, Y. Iwaki, N. Kin, S. Kushitani, N. Murata, S. Wakitani, K. Imoto, Hydroxyapatite In Revision Of Total Hip Replacements With Massive Acetabular Defects: 4- To 10-year Clinical Results, J. Bone Jt. Surg. 79 (1997) 87–92. doi:10.1302/0301-620X.79B1.1290.

[25] S. Kargozar, F. Baino, S. Hamzehlou, R.G. Hill, M. Mozafari, Bioactive Glasses : Sprouting Angiogenesis in Tissue Engineering, Trends Biotechnol. xx (2017) 1–15. doi:10.1016/j.tibtech.2017.12.003.

[26] L.L. Hench, N. Roki, M.B. Fenn, Bioactive glasses: Importance of structure and properties in bone regeneration, J. Mol. Struct. 1073 (2014) 24–30. doi:10.1016/j.molstruc.2014.03.066.

[27] J.R. Jones, Review of bioactive glass: From Hench to hybrids, Acta Biomater. 9 (2013) 4457–4486. doi:10.1016/j.actbio.2015.07.019.

[28] L.L. Hench, The story of Bioglass®, J. Mater. Sci. Mater. Med. 17 (2006) 967–978. doi:10.1007/s10856-006-0432-z.

[29] L.L. Hench, H.A. Paschall, Direct chemical bond of bioactive glass-ceramic materials to bone and muscle, J. Biomed. Mater. Res. 7 (1973) 25–42. doi:10.1002/jbm.820070304.

[30] L.L. Hench, Bioactive Materials for Gene Control, in: New Mater. Technol. Healthc., IMPERIAL COLLEGE PRESS, 2011: pp. 25–48. doi:10.1142/9781848165595_0003.

[31] Y. Li, S. Chen, L. Li, L. Qin, Bone defect animal models for testing efficacy of bone substitute biomaterials, (2015). doi:10.1016/j.jot.2015.05.002.

[32] A.A. El-Rashidy, J.A. Roether, L. Harhaus, U. Kneser, A.R. Boccaccini, Regenerating bone with bioactive glass scaffolds: A review of *in vivo* studies in bone defect models, Acta Biomater. 62 (2017) 1–28. doi:10.1016/j.actbio.2017.08.030.

[33] A.I. Pearce, R.G. Richards, S. Milz, E. Schneider, S.G. Pearce, Animal models for implant biomaterial research in bone: A review, Eur. Cells Mater. 13 (2007) 1–10. doi:10.22203/eCM.v013a01.

[34] P. Augat, K. Margevicius, J. Simon, S. Wolf, G. Suger, L. Claes, Local tissue properties in bone healing: Influence of size and stability of the osteotomy gap, J. Orthop. Res. 16 (2005) 475–481. doi:10.1002/jor.1100160413.

[35] C.P.G. Machado, S.C. Sartoretto, A.T.N.N. Alves, I.B.C. Lima, A.M. Rossi, J.M. Granjeiro, M.D. Calasans-Maia, Histomorphometric evaluation of strontium-containing nanostructured hydroxyapatite as bone substitute in sheep, Braz. Oral Res. 30 (2016) 1–11. doi:10.1590/1807-3107BOR-2016.vol30.0045.

[36] J.J. Li, A. Akey, C.R. Dunstan, M. Vielreicher, O. Friedrich, D. Bell, H. Zreiqat, Effects of material-tissue interactions on bone regeneration outcomes using baghdadite implants in a large animal model, Adv. Healthc. Mater. 1800218 (2018) 1–9. doi:10.1002/adhm.201800218.

[37] A.M. Pobloth, K.A. Johnson, H. Schell, N. Kolarczik, D. Wulsten, G.N. Duda, K. Schmidt-Bleek, Establishment of a preclinical ovine screening model for the investigation of bone tissue engineering strategies in cancellous and cortical bone defects, BMC Musculoskelet. Disord. 17 (2016) 1–12. doi:10.1186/s12891-016-0964-4.

[38] G.F. Muschler, V.P. Raut, T.E. Patterson, J.C. Wenke, J.O. Hollinger, The design and use of animal models for translational research in bone tissue engineering and regenerative medicine., Tissue Eng. Part B. Rev. 16 (2010) 123–145. doi:10.1089/ten.TEB.2009.0658.

[39] W.R. Walsh, R.A. Oliver, C. Christou, V. Lovric, E.R. Walsh, G.R. Prado, T. Haider, Critical size bone defect healing using collagen-calcium phosphate bone graft materials, PLoS One. 12 (2017) 1–21. doi:10.1371/journal.pone.0168883.

[40] Z. Sheikh, M.N. Abdallah, A.A. Hanafi, S. Misbahuddin, H. Rashid, M. Glogauer, Mechanisms of *in vivo* degradation and resorption of calcium phosphate based biomaterials, Materials (Basel). 8 (2015) 7913–7925. doi:10.3390/ma8115430.

[41] O. Gauthier, R. Müller, D. Von Stechow, B. Lamy, P. Weiss, J.M. Bouler, E. Aguado, G. Daculsi, *In vivo* bone regeneration with injectable calcium phosphate biomaterial: A three-dimensional micro-computed tomographic, biomechanical and SEM study, Biomaterials. 26 (2005) 5444–5453. doi:10.1016/j.biomaterials.2005.01.072.

[42] A. Nazarian, R. Müller, Time-lapsed microstructural imaging of bone failure behavior, J. Biomech. 37 (2004) 55–65. doi:10.1016/S0021-9290(03)00254-9.

[43] G. Tozzi, Q.H. Zhang, J. Tong, 3D real-time micromechanical compressive behaviour of bone-cement interface: Experimental and finite element studies, J. Biomech. 45 (2012) 356–363. doi:10.1016/j.jbiomech.2011.10.011.

[44] G. Tozzi, V. Danesi, M. Palanca, L. Cristofolini, Elastic Full-Field Strain Analysis and Microdamage Progression in the Vertebral Body from Digital Volume Correlation, Strain. 52 (2016) 446–455. doi:10.1111/str.12202.

[45] F. Gillard, R. Boardman, M. Mavrogordato, D. Hollis, I. Sinclair, F. Pierron, M. Browne, The application of digital volume correlation (DVC) to study the microstructural behaviour of trabecular bone during compression, J. Mech. Behav. Biomed. Mater. 29 (2014) 480–499. doi:10.1016/j.jmbbm.2013.09.014.

[46] L. Liu, E.F. Morgan, Accuracy and precision of digital volume correlation in quantifying displacements and strains in trabecular bone, J. Biomech. 40 (2007) 3516–3520. doi:10.1016/j.jbiomech.2007.04.019.

[47] G. Tozzi, Q.H. Zhang, J. Tong, Microdamage assessment of bone-cement interfaces under monotonic and cyclic compression, J. Biomech. 47 (2014) 3466–3474. doi:10.1016/j.jbiomech.2014.09.012.

[48] V. Danesi, G. Tozzi, L. Cristofolini, Application of digital volume correlation to study the efficacy of prophylactic vertebral augmentation, Clin. Biomech. 39 (2016) 14–24. doi:10.1016/j.clinbiomech.2016.07.010.

[49] R. Voide, P. Schneider, M. Stauber, P. Wyss, M. Stampanoni, U. Sennhauser, G.H. van Lenthe, R. Müller, Time-lapsed assessment of microcrack initiation and propagation in murine cortical bone at submicrometer resolution, Bone. 45 (2009) 164–173. doi:10.1016/j.bone.2009.04.248.

[50] P.J. Thurner, P. Wyss, R. Voide, M. Stauber, M. Stampanoni, U. Sennhauser, R. Müller, Time-lapsed investigation of three-dimensional failure and damage accumulation in trabecular bone using synchrotron light, Bone. 39 (2006) 289–299. doi:10.1016/j.bone.2006.01.147.

[51] D. Christen, A. Levchuk, S. Schori, P. Schneider, S.K. Boyd, R. Müller, Deformable image registration and 3D strain mapping for the quantitative assessment of cortical bone microdamage, J. Mech. Behav. Biomed. Mater. 8 (2012) 184–193. doi:10.1016/j.jmbbm.2011.12.009.

[52] E. Dall'Ara, M. Peña-Fernández, M. Palanca, M. Giorgi, L. Cristofolini, G. Tozzi, Precision of DVC approaches for strain analysis in bone imaged with μCT at different dimensional levels, Front. Mater. 4:31 (2017). doi:10.3389/fmats.2017.00031.

[53] M. Palanca, A.J. Bodey, M. Giorgi, M. Viceconti, D. Lacroix, L. Cristofolini, E. Dall'Ara, Local displacement and strain uncertainties in different bone types by digital volume correlation of synchrotron microtomograms, J. Biomech. c (2017). doi:10.1016/j.jbiomech.2017.04.007.

[54] F. Comini, M. Palanca, L. Cristofolini, E. Dall'Ara, Uncertainties of Synchrotron microCT-based DVC bone strain measurements under simulated deformation, J. Biomech. (2018).

[55] M. Peña Fernández, A.H. Barber, G.W. Blunn, G. Tozzi, Optimisation of digital volume correlation computation in SR-microCT images of trabecular bone and bone-biomaterial systems, J. Microsc. 00 (2018) 1–16. doi:doi: 10.1111/jmi.12745.

[56] M.J. Coathup, T.C. Edwards, S. Samizadeh, W.J. Lo, G.W. Blunn, The effect of an alginate carrier on bone formation in a hydroxyapatite scaffold, J. Biomed. Mater. Res. - Part B Appl. Biomater. 104 (2016) 1328–1335. doi:10.1002/jbm.b.33395.

[57] M. Vallet-Regi, Bio-Ceramics with Clinical Applications, 1st ed., John Wiley & Sons, Incorporated, 2014.

[58] D.L. Wheeler, L.G. Jenis, M.E. Kovach, J. Marini, A.S. Turner, Efficacy of silicated calcium phosphate graft in posterolateral lumbar fusion in sheep, Spine J. 7 (2007) 308–317. doi:10.1016/j.spinee.2006.01.005.

[59] D. Sriranganathan, N. Kanwal, K.A. Hing, R.G. Hill, Strontium substituted bioactive glasses for tissue engineered scaffolds : the importance of octacalcium phosphate, J. Mater. Sci. Mater. Med. 27 (2016) 1–10. doi:10.1007/s10856-015-5653-6.

[60] T.M. Keaveny, R.E. Borchers, L.J. Gibson, W.C. Hayes, Trabecular bone modulus and strenght can depend on specimen geometry, J. Biomech. 26 (1993) 991–1000.

[61] R.C. Atwood, A.J. Bodey, S.W.T. Price, M. Basham, M. Drakopoulos, A high-throughput system for high-quality tomographic reconstruction of large datasets at Diamond Light Source, Philos. Trans. R. Soc. A Math. Phys. Eng. Sci. 373 (2015). doi:10.1098/rsta.2014.0398.

[62] M. Peña Fernández, S. Cipiccia, A.J. Bodey, R. Parwani, E. Dall'Ara, G. Blunn, M. Pani, A.H. Barber, G. Tozzi, Effect of SR-microCT exposure time on the mechanical integrity of trabecular bone using *in situ* mechanical testing and digital volume correlation, J. Mech. Behav. Biomed. Mater. 88 (2018) 109–119. doi:https://doi.org/10.1016/j.jmbbm.2018.08.012.

[63] M. Basham, J. Filik, M.T. Wharmby, P.C.Y. Chang, B. El Kassaby, M. Gerring, J. Aishima, K. Levik, B.C.A. Pulford, I. Sikharulidze, D. Sneddon, M. Webber, S.S. Dhesi, F. Maccherozzi, O. Svensson, S. Brockhauser, G. Náray, A.W. Ashton, Data Analysis WorkbeNch (DAWN), J. Synchrotron Radiat. 22 (2015) 853–858. doi:10.1107/S1600577515002283.

[64] V. Titarenko;, R. Bradley;, C. Martin;, P.J. Withers;, S. Titarenko;, Regularization methods for inverse problems in x-ray tomography, Proc. SPIE 7804. (2010). doi:doi: 10.1117/12.860260.

[65] A. Buades, B. Coll, J.-M. Morel, Non-Local Means Denoising, Image Process. Line. 1 (2011) 490–530. doi:10.5201/ipol.2011.bcm_nlm.

[66] J. Darbon, A. Cunha, T.F. Chan, S. Osher, G.J. Jensen, Fast nonlocal filtering applied to electron cryomicroscopy, 2008 5th IEEE Int. Symp. Biomed. Imaging from Nano to Macro, Proceedings, ISBI. IEEE. (2008) 1331–1334. doi:10.1109/ISBI.2008.4541250.

[67] M. Palanca, G. Tozzi, L. Cristofolini, M. Viceconti, E. Dall'Ara, 3D Local Measurements of Bone Strain and Displacement: Comparison of Three Digital Volume Correlation Approaches., J. Biomech. Eng. 137 (2015) 1–14. doi:10.1115/1.4030174.

[68] C.M. Ford, T.M. Keaveny, The dependence of shear failure properties of trabecular bone on apparent density and trabecular orientation, J. Biomech. 29 (1996) 1309–1317. http://www.sciencedirect.com/science/article/pii/0021929096000620.

[69] G.L. Niebur, M.J. Feldstein, J.C. Yuen, T.J. Chen, T.M. Keaveny, High-resolution finite element models with tissue strength asymmetry accurately predict failure of trabecular bone, J. Biomech. 33 (2000) 1575–1583. doi:10.1016/S0021-9290(00)00149-4.

[70] H.D. Barth, M.E. Launey, A.A. MacDowell, J.W. Ager, R.O. Ritchie, On the effect of X-ray irradiation on the deformation and fracture behavior of human cortical bone, Bone. 46 (2010) 1475–1485. doi:10.1016/j.bone.2010.02.025.

[71] H.H. Bayraktar, E.F. Morgan, G.L. Niebur, G.E. Morris, E.K. Wong, T.M. Keaveny, Comparison of the elastic and yield properties of human femoral trabecular and cortical bone tissue, J. Biomech. 37 (2004) 27–35. doi:10.1016/S0021-9290(03)00257-4.

[72] L. Cristofolini, *In vitro* evidence of the structural optimization of the human skeletal bones, J. Biomech. 48 (2015) 787–796. doi:10.1016/j.jbiomech.2014.12.010.

[73] R. Jungmann, M.E. Szabo, G. Schitter, R. Yue-Sing Tang, D. Vashishth, P.K. Hansma, P.J. Thurner, Local strain and damage mapping in single trabeculae during three-point bending tests, J. Mech. Behav. Biomed. Mater. 4 (2011) 523–534. doi:10.1016/j.jmbbm.2010.12.009.

[74] J.R. Goodheart, M.A. Miller, K.A. Mann, *In vivo* loss of cement-bone interlock reduces fixation strength in total knee arthroplasties, J. Orthop. Res. 32 (2014) 1052–1060. doi:10.1002/jor.22634.

[75] M. Coathup, N. Smith, C. Kingsley, T. Buckland, R. Dattani, G.P. Ascroft, G. Blunn, Impaction grafting with a bone-graft substitute in a sheep model of revision hip replacement, J. Bone Jt. Surg. - Br. Vol. 90–B (2008) 246–253. doi:10.1302/0301-620X.90B2.19675.

[76] P. Wang, L. Zhao, J. Liu, M.D. Weir, X. Zhou, H.H.K. Xu, Bone tissue engineering via nanostructured calcium phosphate biomaterials and stem cells, Bone Res. 2 (2015). doi:10.1038/boneres.2014.17.

[77] M.J. Coathup, K.A. Hing, S. Samizadeh, O. Chan, Y.S. Fang, C. Campion, T. Buckland, G.W. Blunn, Effect of increased strut porosity of calcium phosphate bone graft substitute biomaterials on osteoinduction, J. Biomed. Mater. Res. - Part A. 100 A (2012) 1550–1555. doi:10.1002/jbm.a.34094.

[78] A.J. Bodey, C. Rau, Launch of the I13-2 data beamline at the Diamond Light Source synchrotron, J. Phys. Conf. Ser. 849 (2017). doi:10.1088/1742-6596/849/1/012038.

5.2. Full-field strain analysis and bone regeneration following the implantation of osteoinductive biomaterials

Marta Peña Fernández[1], Cameron Black[2], Jon Dawson[2], David Gibbs[2], Janos Kanczler[2], Richard OC Oreffo[2], Gianluca Tozzi[1]

[1] *Zeiss Global Centre, School of Engineering, University of Portsmouth, Portsmouth, UK.*

[2] *Bone & Joint Research Group, Centre for Human Development Stem Cells and Regeneration, University of Southampton, UK.*

Under review as

"Full-field strain analysis and bone regeneration following the implantation of osteoinductive biomaterials in critical-sized defects".

Reprinted with permission from all authors.

Abstract

Biomaterials for bone regeneration are constantly under development and their application in critical sized defects represents a promising alternative to bone grafting techniques. However, the ability of these therapies to produce bone mechanically comparable with the native tissue remains unclear. This study examines the morphometry, mineralisation and load-bearing capacity of newly formed bone produced *in vivo* by two different biomaterial-mediated delivery systems for BMP-2 release combining *in situ* high-resolution X-ray micro-computed tomography (microCT) and digital volume correlation (DVC). In addition, a comparison with the current gold standard biomaterial (autograft) for bone critical defects healing was performed. Results indicated a more efficient load-transfer ability and bone remodelling in autograft-treated defects compared to BMP-2-treated defects, which showed less remodelled trabeculae and larger highly-strained regions. Additionally, DVC-computed full-field strains suggested a mechanical adaptation of bone structure present from the early stages of bone healing. The findings and analysis reported herein, using microCT and DVC, provide a deeper understanding of the micromechanics of newly formed bone produced *in vivo* following different tissue engineering strategies in relation to its microstructure and tissue mineral density. This could ultimately be used to improve and enhance novel bone regeneration approaches.

Keywords: Bone regeneration, BMP-2 delivery systems, *in situ* mechanics, microCT, digital volume correlation.

5.2.1. Introduction

Bone tissue possesses excellent healing capacity as a result of the regenerative growth and remodelling process [1,2]. However, many clinical situations, including fracture non-union, tumour resection and musculoskeletal diseases, impair the natural bone-healing process, due to the critical size of the defects to bridge [3–5]. Common treatments for critical size bone defects include bone autografts and allografts [6]. Although autografts are considered the gold standard for promoting bone repair [7–9], autografts present several limitations including risks of donor site injury, morbidity and limited availability [10,11]. There is thus a clear need to define novel strategies to improve and facilitate bone regeneration, which has led to the development of bone tissue engineering approaches [12–17].

Novel tissue engineering techniques seek to further enhance bone regeneration. A promising approach relies on the local delivery of growth factors [16,18,19], such as bone morphogenetic proteins (BMPs). In particular, BMP-2 has been shown to play a critical role in bone formation and bone healing given the capacity of BMP-2 to induce osteoblast differentiation [20–22]. BMP-2 is a highly osteoinductive growth factor, generally delivered onto an osteoconductive carrier, such as collagen, which provides the structural matrix for bone regeneration [23,24]. However, BMPs are soluble proteins and typically dissipate from their intended location, leading to several complications [6]. Therefore, the development of optimal delivery systems of BMPs is an area of intense research with the aim to provide spatiotemporal control of BMPs release *in vivo* [16,19]

In order to validate and improve bone tissue engineering strategies, it is essential to evaluate the *in vivo* competence of the newly formed bone induced following applied treatment [25,26]. Critical bone defect animal models provide a robust evaluation of the *in vivo* response (i.e. new bone formation, remodelling, implant resorption) of the biomaterial-mediated delivery of growth factors; thus, defect models have been widely used to investigate bone regeneration ability [23,27–29]. However, a biomechanical evaluation of the newly regenerated bone during the healing process is still lacking. This evaluation is of fundamental importance to demonstrate the ability of different treatments to restore new bone with biological and biomechanical properties that are comparable with native bone. Specifically, understanding the load-bearing capacity and load-transfer mechanisms is essential to fully characterise the mechanical competence of the newly formed bone structures.

High-resolution X-ray imaging (i.e. microCT) has been extensively used to investigate, in a three-dimensional (3D) approach, the *ex vivo* implantation site in a non-destructive way [23,25,30]. MicroCT imaging allows for a morphological analysis of the regenerated bone tissue [31], as well as the distribution and degree of tissue mineralisation, when appropriate densiometric calibration is carried out [32]. Furthermore, when combined with *in situ* mechanical testing [33] and digital volume correlation (DVC) [34,35], microCT provides a

unique tool to investigate the 3D internal deformation of bone at the microscale and correlation to the bone microstructure. To date, *in situ* microCT mechanics in conjunction with DVC have been used to examine 3D full-field displacement and strain in trabecular bone samples [36,37], cortical bone samples [38], entire bones [39] and bone-biomaterial systems [40,41]. However, to the author's knowledge, *in situ* microCT mechanics in conjunction with DVC has never been applied to newly regenerated bone tissue entirely produced *in vivo* following the delivery of growth factors in critical size bone defects.

The BMP-2 delivery system employed, is known to influence the bone healing process [16,23,24], and therefore, the morphometry, mineralisation and load-transfer ability of the newly formed bone. This study aims to investigate 3D full-field strain distribution throughout the apparent elastic regime in newly regenerated bone tissue produced *in vivo* following the delivery of BMP-2 from two different biomaterials in a critical size bone defect model, with autografts used as a positive control. Bone mineral distribution, morphometry, and load transfer response were evaluated combining high-resolution microCT, *in situ* mechanical testing and DVC. The findings of this paper provide important insights on the relationships between deformation, microstructure and mineralisation of newly formed bone. Hence, improving the description and understanding of bone regeneration process as a result of different tissue engineering strategies..

5.2.2. Materials and methods

5.2.2.1. Specimen preparation

Bone defects (9 mm diameter by 10 mm depth) were performed bilaterally in the medial femoral condyles of aged (>5 years) Welsh Upland Ewes (60-75 kg) (n = 4) under Home Office license PPL30/2880. Three different treatments were applied: Autograft, InductOs® [42] and Laponite [43,44]. Autografts were prepared from the extracted bone cores following defect creation; InductOs and Laponite consist of a collagen sponge incorporating BMP-2 (100 µg) in a formulation buffer or in a Laponite clay gel, respectively. 10 weeks post implantation condyles were harvested and fixed in 4% paraformaldehyde solution in a phosphate buffered solution (PBS) for one week and stored in PBS at 4°C. Cylindrical bone specimens (n = 6, ~5 mm in diameter and ~11 mm in length) were obtained from the bone defect areas by drilling with a coring tool under constant water irrigation. The ends of the cores were trimmed plane and parallel. Samples were kept in PBS at 4°C prior to *in situ* microCT mechanical testing. Pre-testing, brass endcaps were used to embed the ends of the specimens (~ 2 mm each side) to ensure perpendicularity between the bone cores and the endcaps base. In total, six specimens were prepared (n = 2 /treatment).

5.2.2.2. *In situ* mechanics and microCT imaging

Specimens were placed within an environmental chamber in a loading device (CT500, Deben Ltd, UK) that was positioned in the chamber of a high-resolution 3D X-ray microscope (Versa 510, Zeiss, USA) (Figure 1a). First, a small preload (~2N) was applied to ensure

good end contact prior to testing, followed by *in situ* uniaxial step-wise compression at three different levels of compression (1%, 2% and 3%). The force-displacement recordings from the loading device were used to calculate the stiffness of the specimens. A linear regression equation (coefficient of determination R^2 > 0.997) was used to fit the experimental data between 0.8 - 1% and 1.8 - 2% compression, and the stiffness was determined from the slope of that line. MicroCT images were acquired (60 keV, 5 W, 5 µm voxel size, 10 s exposure time, 1800 projections) at each compression step after two repeated scans in the preload configuration for DVC error analysis (Appendix A). Image reconstruction was performed via the manufacturer's software (TXM Reconstructor, Zeiss, USA). In total five tomographic datasets were acquired for each specimen.

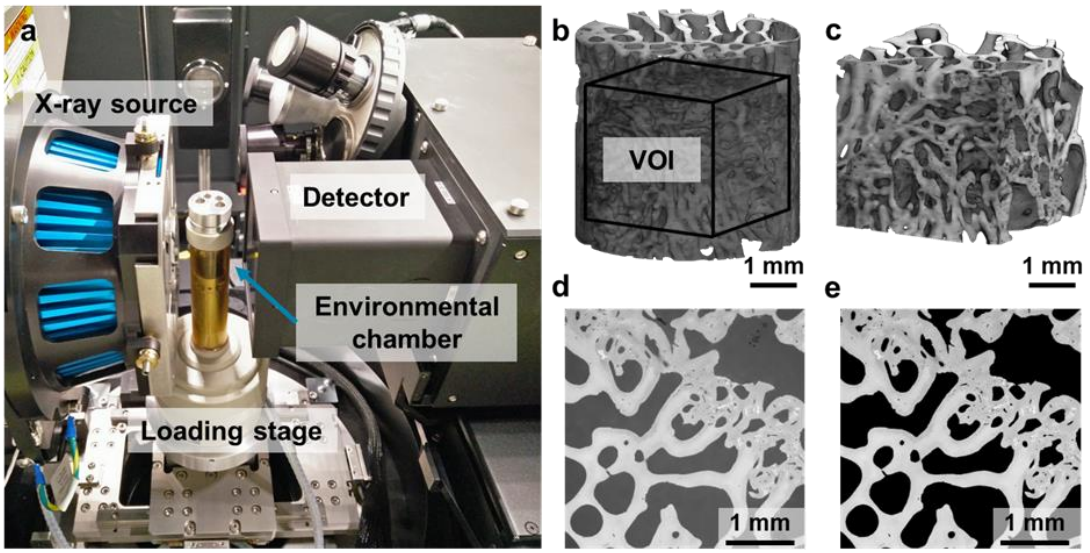

Figure 1. (a) Experimental setup for *in situ* microCT experiment in the Zeiss Versa 510. Specimens were imaged within an environmental chamber inside the loading stage. Uniaxial step-wise compression was carried out in displacement control at a constant cross-head speed of 0.2 mm/min. (b) 3D volume reconstruction of a cylindrical specimen and (c) a corresponding cubic (3.5 x 3.5 x 3.5 mm) volume of interest (VOI) that was cropped at the centre of each specimen. Representative cross-section through the VOI (d) before and (e) after masking out the soft material (i.e. bone marrow) from the mineralised tissue.

5.2.2.3. Mineral density distribution

A densiometric calibration phantom (microCT-HA, QRM, Germany) containing five insertions with hydroxyapatite (HA) concentrations (1200, 800, 200, 50, 0 mg HA / cm^3) was imaged under identical experimental conditions and used to calibrate the microCT grey-scale values of the first acquired tomogram for each specimen into tissue mineral density (TMD). A cubic volume of interest (VOI) with side lengths of 700 voxels (3.5 mm^3) was cropped from the centre of the scaled images (Figure 1b, c) and the average and peak TMD (Avg-TMD and Peak-TMD) were calculated from the calibrated histograms of each specimen.

5.2.2.4. Image post-processing

Following image reconstruction, the microCT datasets were rigidly aligned using as reference the first acquired tomogram. The rigid registration was based on the sum of squares differences as a similarity measurement. The images were then denoised by applying a non-local means filter (σ = 10) (Figure 1c) and masked by setting to zero the grey-scale values corresponding to the non-mineralised tissue voxels (i.e. bone marrow) (Figure 1d). A binary image was first created by applying a global thresholding based on Otsu's algorithm [45], followed by a 'purify' analysis in BoneJ [46] plugin for Fiji [47], which locates all particles in 3D and removes all but the largest foreground (bone tissue) and background (bone marrow) particles. Masked images (Figure 1d) were obtained by multiplying the filtered image to the binary image.

5.2.2.5. Morphometric analysis

Morphometric analysis was performed using BoneJ [46] plugin. The same cubic VOI, as for the mineral density distribution (Figure 1c), was cropped from the binary images and bone volume fraction (BV/TV) was computed. Due to the irregular bone microarchitecture induced by the different treatments, trabecular thickness (Tb.Th) and trabecular spacing (Tb.Sp) were computed in smaller sub-VOIs (1.75 mm^3). Data were subsequently screened using Peirce's criterion [48] to identify outliers and to remove large voids or callus bone regions from the computation. Following removal of outliers, mean Tb.Th and Tb.Sp were calculated for each specimen.

5.2.2.6. Digital volume correlation

DVC (DaVis v8.4, LaVision, Germany) was carried out to evaluate the 3D full-field strain distribution in the newly regenerated bone tissue throughout the apparent elastic regime. DaVis software is based on a local approach [49] of deformable registration, which has been extensively used in bone mechanics [36,37,39]. The operating principles of the algorithm are detailed elsewhere [50]. DVC was applied to the masked images (entire cylinders) to avoid possible artefacts in regions with insufficient grey-scale pattern (i.e. bone marrow). A multi-pass scheme with a final sub-volume of 40 voxels (200 μm), reached via predictor passes using sub-volumes of 56, 48 and 44 voxels was used. Furthermore, sub-volumes with a correlation coefficient below 0.6 were removed from the resultant vectors. Errors on the DVC-computed displacement (zero-strain test) did not exceed 2 μm, whereas the mean absolute error (MAER) and the standard deviation of the error (SDER) of the strain components [51] were found to be ~530 με and 160 με, respectively (Appendix A). The third principal strain (ε_{p3}) for each loading step was computed within the bone volume in the VOI (Figure 1b) previously described, after a bi-cubic interpolation.

5.2.3. Results

The *in situ* mechanical tests (Figure 2a) demonstrated the distinct response of each specimen under the same applied compression, with stiffness ranging from 131.9 N/mm for Laponite # 1 to 547.6 N/mm for InductOS #2 (Table 1). Force-compression curves exhibited a monotonic profile that was observed to be, in essence, linear during the three loading steps. The TMD distribution (Figure 2b) in the VOI of the specimens showed little difference, with mean Avg-TMD of 1168.5 mgHA/cm^3 (± 50.4 mgHA/cm^3) and mean Peak-TMD of 1236.4 mgHA/cm^3 (± 47.4 mgHA/cm^3) (Table 1).

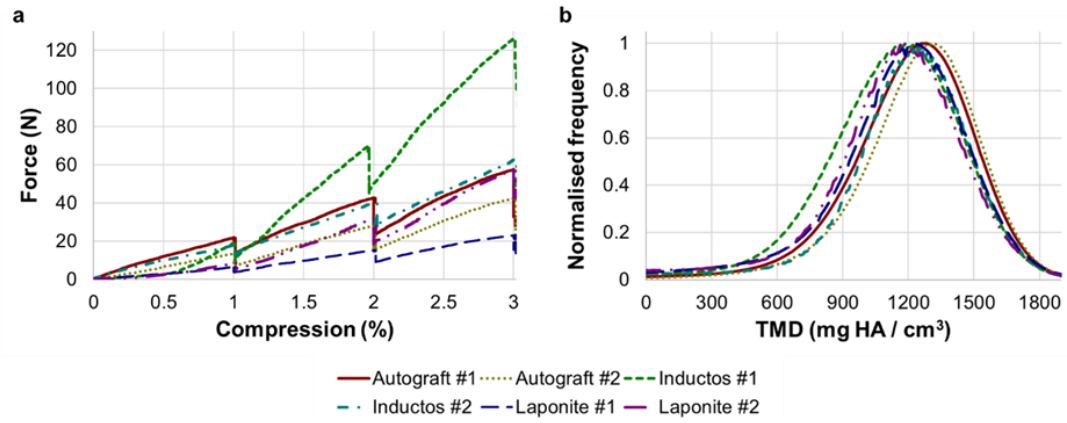

Figure 2. (a) Force-compression curves for the six specimens. The force shows a drop at the end of each step of compression, which corresponds to the time while the specimen was allowed to settle (~30 min) prior to image acquisition (~5 h). An initial toe region was observed in Inductos #1 and Laponite #2, mainly dependant on the initial lack of co-planarity between the ends of the specimens. (b) Normalised tissue mineral density histograms for the six analysed specimens showed minimal differences in peak values and distribution.

Table 1. Overview of the mechanical, mineral and morphological parameters of the analysed specimens. For each specimen, stiffness, average tissue mineral density (Avg-TMD), peak tissue mineral density (Peak-TMD), bone volume fraction (BV/TV), trabecular thickness (Tb.Th) and trabecular spacing (Tb.Sp) are detailed.

	Stiffness (N / mm)	**Avg-TMD (mgHA/cm^3)**	**Peak-TMD (mgHA/cm^3)**	**BV/TV (%)**	**Tb.Th (µm)**	**Tb.Sp (µm)**
Autograft #1	249.3	1207.8	1279.5	46.1	222±71	484±168
Autograft #2	212.1	1247.9	1314.8	33.9	267 ± 72	736±246
InductOs #1	547.6	1107.2	1185.4	52.2	233 ± 68	477±183
InductOs #2	322.6	1183.1	1232.5	54.6	147±41	338±198
Laponite #1	131.9	1152.3	1220.7	22.4	107±47	466±282
Laponite #2	363.0	1112.5	1185.4	45.4	141±35	339±189

High-resolution microCT images (Figure 3) allows visualisation of the characteristic microstructure and mineral distribution in the newly formed bone induced by the different treatments. Greater remodelled bone trabeculae were observed in Autograft specimens in comparison to other groups with the presence of highly mineralised regions (lightest grey) within the newly formed bone. InductOs specimens presented the highest BV/TV, above 50% (Table 1) with dense areas of woven bone observed. InductOs #1 was able to regenerate trabeculae with comparable thickness to Autograft specimens (~250 µm), whereas thinner trabeculae (~150 µm) were observed in InductOs #2 (Table 1). The thinnest trabeculae (below 150 µm) were identified in Laponite specimens, where larger voids were found in Laponite #1 that was unable to entirely bridge the defect site, compared to Laponite #2.

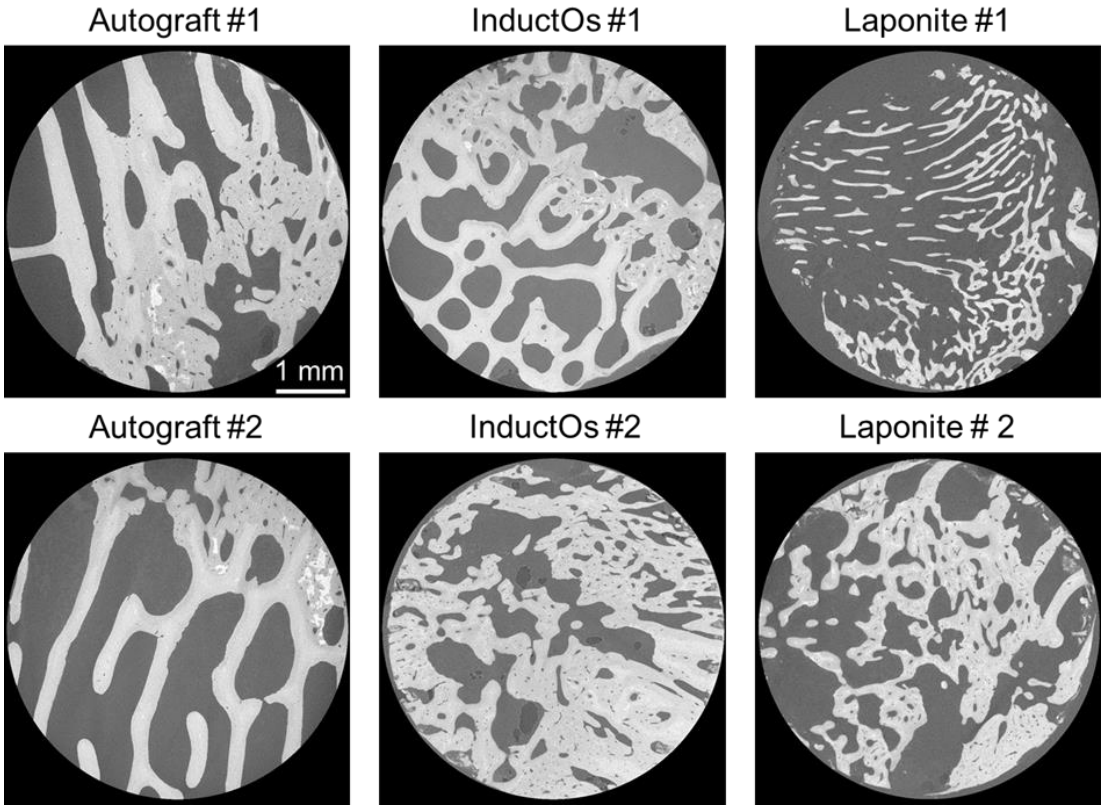

Figure 3. MicroCT cross-sections through the six analysed specimens showing differences in microstructure and mineralisation. Large agglomerates of mineral (white) were identified in Autografts specimens. Laponite #1 showed considerably thinner trabeculae. Large areas of woven bone were present in InductOs and Laponite #2 specimens. Scale bar is valid for all images.

The distributions of ε_{p3} (Figure 4) correlated with the strain accumulation at each compression step. Autograft specimens showed small differences between mean and median values, whose magnitudes ranged between 1000 µε at 1% compression and 2500 µε at 3% compression with highly homogeneous distributions and thin tails. Higher strain accumulation was observed for InductOs and Laponite specimens, which showed a broader distribution. This was more evident at 3% compression, where mean and median values

differed considerably, and large inter-quartile ranges were found. The highest compressive strains were observed in Laponite #1, with mean strain magnitudes varying from 2000 με at 1% compression to 8000 με at 3%, whereas mean strain magnitudes never exceeded 3500 με for the other specimens.

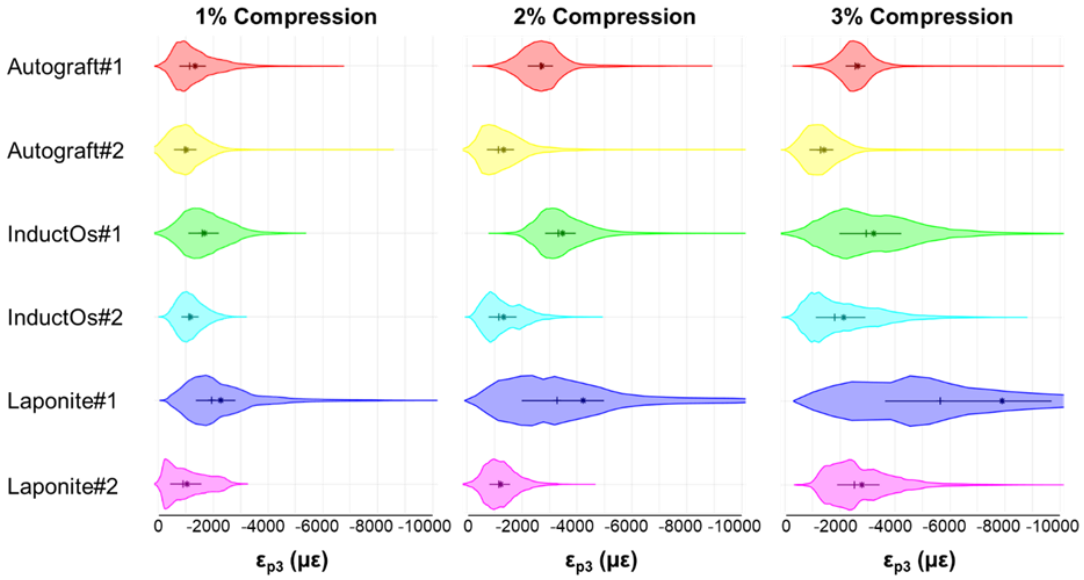

Figure 4. Violin plots showing the third principal strain distribution (ε_{p3}) in the VOI of the six specimens at each compression step smoothed by a kernel density function. Median (+) and mean (*) values are indicated in each plot. Horizontal lines show the inter-quartile range (IQR, between 25th and 75th percentile of the data).

3D full-field ε_{p3} in Autograft specimens (Figure 5a) revealed small strain accumulation with increasing compression levels. Areas of high strain concentration (Figure 5b) were predominantly within the more remodelled trabeculae from the first compressive step, with strain magnitudes exceeding -8000 με in some regions at 3% compression. Newly formed bone regions showed less mineralisation (Figure 5c) compared to the greater remodelled trabecular bone, however this was not related to higher deformation. Strain accumulation within the InductOs specimens (Figure 6a) was observed to be more progressive than for Autograft specimens, showing higher differences at each compressive level. Highly strained areas were typically observed in the newly formed bone (woven) for InductOs #1 and in the newly formed trabeculae in InductOs #2 (Figure 6b), experiencing lower levels of strain. Interestingly, less mineralisation (Figure 6c) was detected in the high strain regions. InductOs #2 specimen included large mineralised areas within the woven bone (Figure 6c.2). Laponite #1 specimen (Figure 7a.1) displayed a marked and abrupt strain accumulation compared to Laponite #2 (Figure 7a.2), with areas with strain magnitude exceeding 10000 με from the first compression step (Figure 7b.2). Full-field εp3 in Laponite #2 was largely homogeneous after 1% and 2% of applied compression; however, larger strain values were found at 3% compression. Both specimens experienced higher strains in the newly formed

thin trabeculae (Figure 7b), which also matched the lower mineralised regions (Figure 7c). TMD was found to be higher in callus new bone.

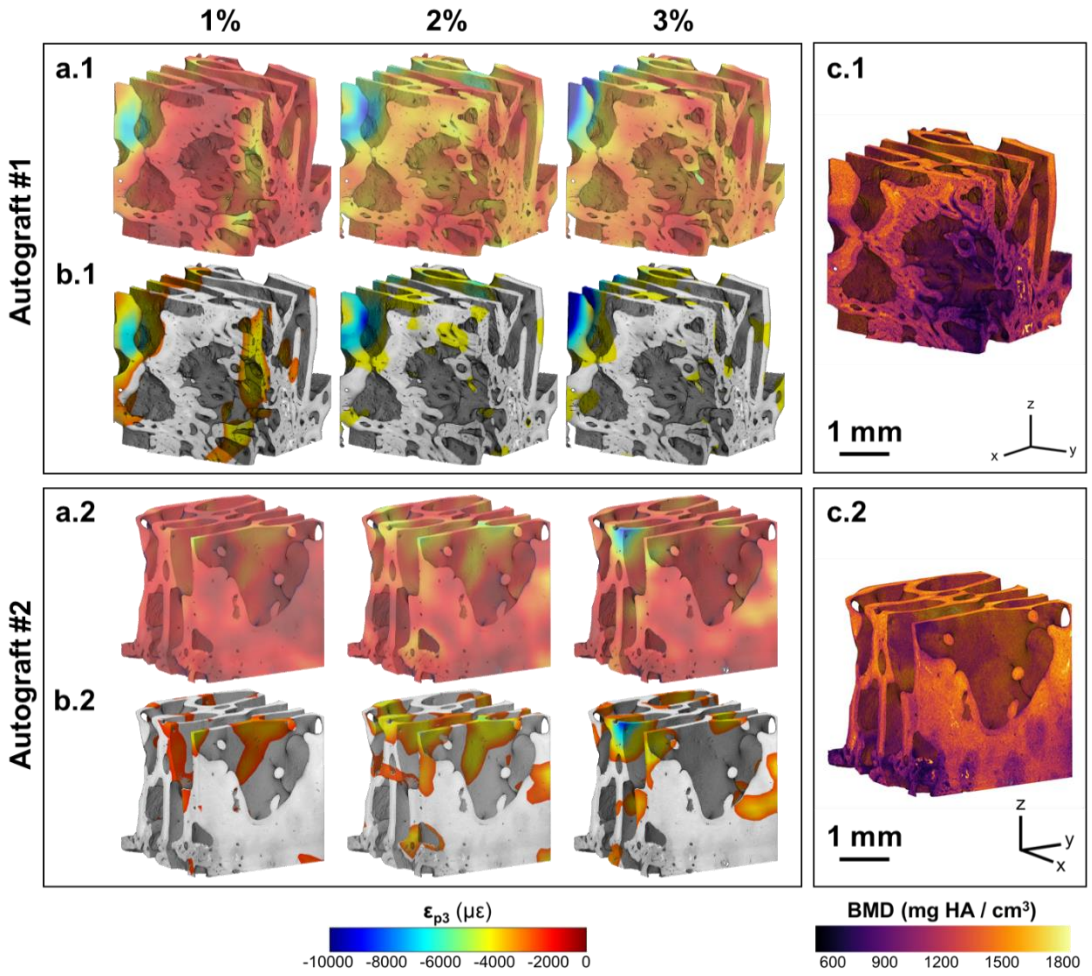

Figure 5. (a) 3D full-field third principal strain distribution (ε_{p3}) at each compression step for the VOI of Autograft specimens and (b) corresponding 20% of bone volume fraction (BV/TV) highly strained. An increase and redistribution in the accumulated strain is observed after consecutive compression steps. (c) Tissue mineral density distribution in the VOI of each specimen. The more remodelled trabeculae showed higher mineralisation compared to newly formed bone tissue in both specimens. Animations of strain distribution over time available online (see available electronic data AVI_5.2.5 in thesis annexes).

5.2.4. Discussion

The main aim of this study was to provide a detailed 3D characterisation of the microarchitecture, tissue mineral density and full-field strain in newly formed bone induced *in vivo* in a large animal critical bone defect following three distinct reparative strategies. High-resolution X-ray imaging in combination with *in situ* mechanical testing and DVC was used to generate insights into differenced in the morphometry, mineralisation and load transfer capacity of the regenerated bone.

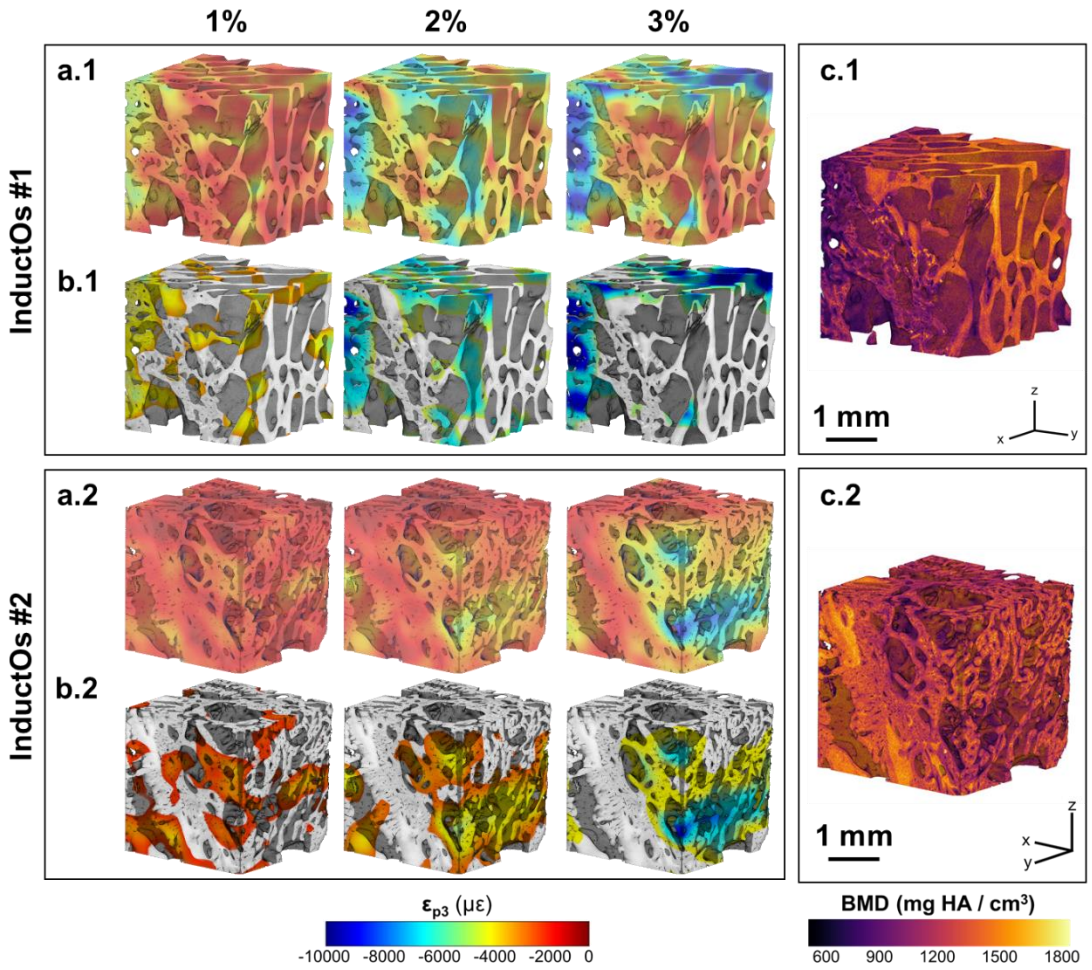

Figure 6. (a) 3D full-field third principal strain distribution (ε_{p3}) at each compression step for the VOI of InductOs specimens and (b) corresponding 20% of bone volume fraction (BV/TV) highly strained. An increase and redistribution in the accumulated strain is observed after consecutive compression step. (c) Tissue mineral density (TMD) distribution in the VOI of each specimen. The more remodelled trabeculae showed higher mineralisation compared to newly formed bone tissue in InductOs #1. Highly mineralised areas were identified in woven bone in InductOs #2. Animations of strain distribution over time available online (see available electronic data AVI_5.2.6 in thesis annexes).

The distinct treatments applied to the bone defect produced a clear influence on the microstructure of the newly regenerated tissue (Figure 3). Ten weeks post-implantation was observed to be insufficient time to completely remodel bone within the defect; thus, woven bone was observed in all specimens. Even though, Autograft induced better bone formation, evidenced by the greater remodelled trabeculae observed, compared to the BMP-2 treated defects. Both InductOs and Laponite specimens showed a considerably more irregular microarchitecture, and the presence of large voids within the structure. *In vivo*, collagen degrades rapidly, resulting in the development of voids within the new bone matrix. This is mainly due to the inability of collagen to provide structural support for cell migration in

adequate time [18,52]. InductOS specimens induced the greatest bone formation (Table 1), although large regions of woven bone were observed. Conversely, Laponite induced the thinnest trabeculae, but less woven bone. Trabecular thickness and spacing of all the specimens were measured in smaller sub-VOIs and examined for possible outliers [48] to avoid misleading data as a consequence of compact woven regions and empty voids. As a result, outliers were removed from the data and presented values (Table 1) are representative of the trabecular-like structure of each specimen.

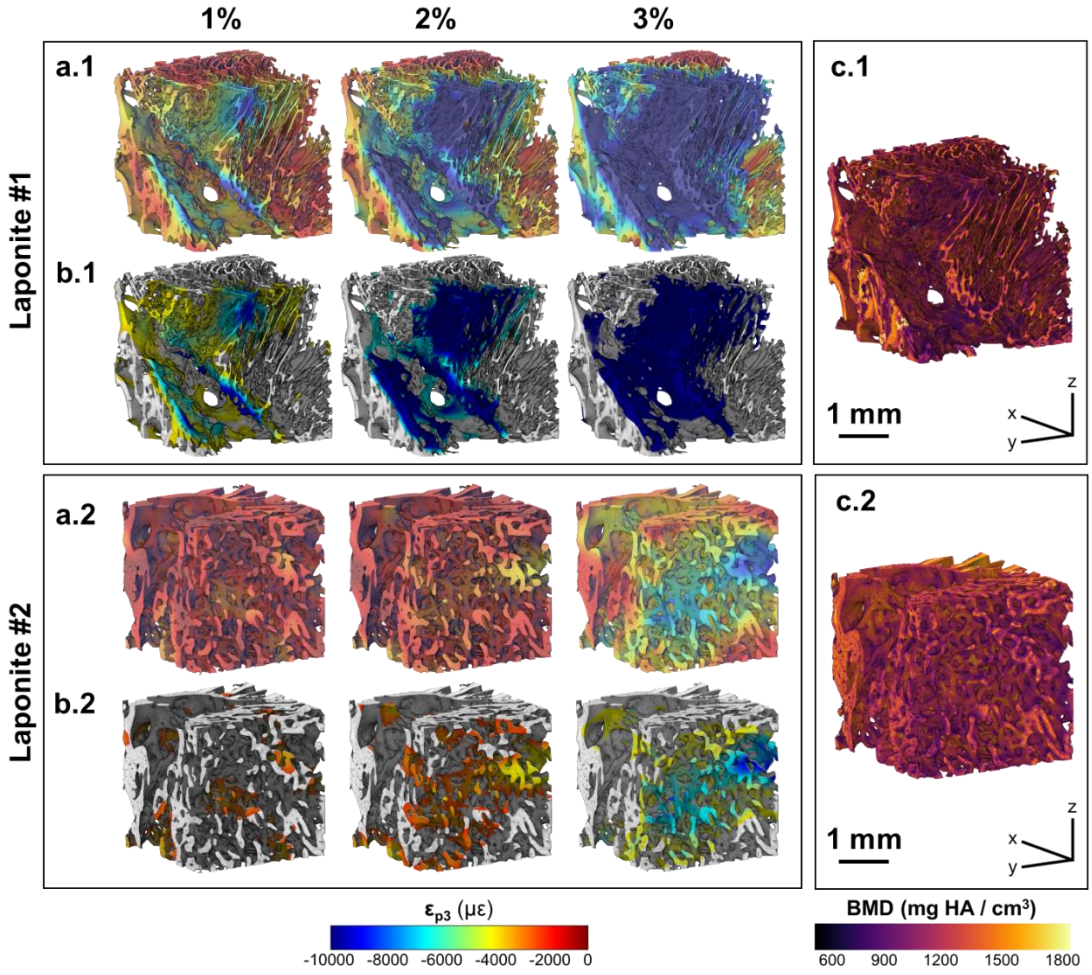

Figure 7. (a) 3D full-field third principal strain distribution (ε_{p3}) at each compression step for the VOI of Laponite specimens and (b) corresponding 20% of bone volume fraction (BV/TV) highly strained. An increase and redistribution in the accumulated strain is observed after consecutive compression step. (c) Tissue mineral density distribution in the VOI of each specimen. Highly mineralised regions were found in within the woven bone, whereas the newly formed thin trabecula showed lower mineralisation. Animations of strain distribution over time available online (see available electronic data AVI_5.2.7 in thesis annexes).

The different microarchitecture induced *in vivo* in the bone defects clearly influence their apparent mechanics (Figure 2a). It is known that the elastic behaviour of trabecular bone depends on the loading direction [53–56], anatomical site [57–59] and size of the sample [60–62]. This study showed a low correlation ($R^2 < 0.6$) between the measured stiffness and any morphometric parameter. However, it must be noted that specimens tested were not

fully remodelled into trabecular bone at the time of extraction. Furthermore, the specimens were not cored and tested along the principal direction, mainly due to the experimental difficulties related to the bone defect size and location of the newly formed bone within specimens. Although the microstructure and stiffness of the analysed specimens clearly differed, negligible changes were observed in their TMD distribution (Figure 2b). Higher mineralisation was found in the greater remodelled trabeculae of the Autograft (Figure 5c) and InductOs #1 (Figure 6c.1) specimens compared to the less remodelled and thinner trabeculae in InductOs #2 (Figure 6c.2) and Laponite (Figure 7c) specimens.

The DVC-computed full-field strain in the specimens allowed for characterisation of the load transfer ability of the newly regenerated bone tissue. Despite the fact that applied loads at each compression step do not correspond to any physiological load *in vivo*, specimens were predominantly tested in their apparent elastic regime. This provided enhanced insight on the load-bearing capacity of such bone structures away from failure. A more homogeneous strain distribution was observed for Autograft specimens (Figure 5a) during the three compression steps, where the bone tissue experienced strains mainly within physiological strain values (magnitude below 3200 με [63]). Similar behaviour was observed for InductOs #2 (Figure 6a.1) and Laponite #2 (Figure 7a.1). In fact, during the first two compression steps, strains were typically below 3000 με in magnitude, and only higher strain concentrations were observed after 3% compression in the newly formed trabeculae, with strain values approaching the yielding (10000 με in compression [64]). In contrast, full-field strain distribution in InductOs #1 and Laponite #1 showed the inefficiency of both structures to transfer the applied load. As a result, highly strained regions (above yielding) were observed and further increased since the early stages of compression, 1% for Laponite #1 (Figure 7a.2) and 2% for InductOs #1 (Figure 6a.2).

Identification of highly strained regions further improved understanding as to where failure may develop in such structures and how the regeneration process, with changes in bone microarchitecture and mineralisation, is optimised to bear externally applied loads. Interestingly, highly strained regions were predominantly localised in the newly regenerated trabeculae in all the specimens, independent of mineralisation. This suggests that from the earliest stages of bone formation, the bone structure is adapted to withstand external loads [65], regardless of the specific treatment applied to the bone defect. Furthermore, enhanced mineralised regions of the BMP-2 treated specimens (Figure 6 and 7) appeared to act as a shielding mechanism, driving the load towards the trabecular-like structure, which is adapted to the external mechanical demands *in vivo*. It is well known that the mechanical environment highly influences the pathways through which bone healing occurs [66,67]. However, determining the precise strains that tissues are experiencing *in vivo* remains a significant challenge [68], and most research, to date, has focused on in silico studies [69]. Despite the *ex vivo* nature and the non-relevant physiological load applied to the specimens, the findings of this study provide insight into how the bone repair process in a large animal

critical defect is highly influenced by the mechanical stimulus. Critically, higher strains were measured within the newly formed trabeculae, which in an *in vivo* scenario (i.e. cyclic load during walking) could result in a mechanical stimulation [70] to the adjacent woven bone to further enhance and continue the remodelling process.

Nevertheless, a number of caveats must be considered within this study. The limited quantity of newly formed bone within the defects resulted in a limited sample size (two specimens per treatment) and the inability to extract the specimens in the principal direction of the newly formed trabeculae. In addition, a single time point was evaluated; given these were large animal ovine studies, therefore, generalisation and extrapolation of the current results warrants further analysis. However, the results herein presented have the potential to better inform *in silico* models of bone remodelling to enable long-term predictions of bone adaptation under different loading conditions. While it could be argued that the mechanics of bone tissue may be altered due to the fixation process, it should be noted that the specimens were left in fixative for only one week and testing was undertaken in the apparent elastic regime. It has been shown that fixation for up to 4 weeks does not alter the compressive properties of bone [71] and appears not to influence the elastic properties of bone [72]. Furthermore, the aim of this study was not to characterise the material properties of the newly formed tissue, but rather to understand the load-transfer capability of the bone *ex vivo*. Additionally, the calibration phantom was not included with each specimen to be imaged; therefore, the intrinsic fluctuations of the microCT system (i.e. tube voltage level, current), which could potentially affect the grey-scale levels, were not accounted for [32]. Though, the purpose of the presented calibration was to better understand how high and low mineralised regions of bone correlated with newly formed bone as opposed to a precise determination of density measures of each specimen.

5.2.5. Conclusion

The combination of high-resolution X-ray microCT, *in situ* mechanics and DVC was used to characterise the relationships between microstructure, mineralisation and load-bearing capacity of newly formed bone induced *in vivo* in a large animal critical size bone defect following different treatments. Bone produced via BMP-2 delivery with two different carriers was compared to the gold standard procedure (autograft), providing new information on the bone healing process and the micromechanics of the regenerated bone. Independent of the applied treatment, DVC-computed strain distributions indicate that the regenerated bone structure is mechanical adapted to bear external loads from the earliest stages of the bone reparation cascade. The results of this study provide an important step towards understanding the load transfer ability of newly formed bone *in vivo*. Such information is crucial to facilitate developments in new improved bone tissue regeneration strategies designed to produce bone tissue with comparable biomechanical qualities to native bone.

Author contributions

Marta Peña Fernández: Study design, data curation, formal analysis, data interpretation; Cameron Black: Animal model; John Dawson Animal model; Janos Kanczler: Animal model; David Gibbs: Animal model; Richard O.C. Oreffo: Study design, animal mdel; Gianluca Tozzi: Study design, data interpretation, supervision.

Acknowledgments

The authors would like to acknowledge Dr. Alexander Kao for support during X-ray imaging and Dr. Enrico Dall'Ara for providing the calibration phantom. The Zeiss Global Centre (University of Portsmouth) is acknowledged for providing X-ray imaging facilities. Funding to RO from the Biotechnology and Biological Sciences Research Council (BBSRC LO21071/, BB/G010579/1, and BB/L00609X/1) and UK Regenerative Medicine Platform Hub Acellular Approaches for Therapeutic Delivery (MR/K026682/1) and University of Southampton is gratefully acknowledged.

Supplementary material S1

Evaluation of DVC uncertainties

The quantification of the level of uncertainties in the DVC measurements were computed for each pair of 'zero-strain' repeated tomograms. Ideally, null displacements are expected; however, during image acquisition displacements are affected by the inevitable unknown micromovements of the different parts of the system. Therefore, only the variability of the displacement (random errors) within each pair of tomograms was calculated. Additionally, any non-zero values of the derived strains were considered as error. Eight multi-pass schemes [50] with final sub-volume sizes ranging from 16 to 72 voxels, in steps of 8 voxels were investigated. For each sub-volume, the following parameters were computed.

- Mean absolute strain value: average of the average of the absolute values of the six components of the differential strain, similar to MAER or "accuracy", as in [73,74]
- Standard deviation of the strain value: standard deviation of the average of the absolute values of the six components of the differential strain, similar to SDER or "precision", as in [73,74].
- Random errors of the displacements: standard deviation of each displacement component, as in [75].
- Random errors of the strain components: standard deviation of each strain component, as in [75].

The random errors of each component of the displacement never exceeded 2.07 μm (0.4 voxel) (Table S1) for a final sub-volume size of 200 μm). The errors obtained for the displacements in the x direction were larger than in y (lowest random errors) and z direction. As expected from previous studies on bone [73,76], the strain uncertainties of the DVC had decreasing trends with respect to the sub-volume size, and the values of the mean value of the strain (MAER) were larger than the standard deviation (SDER) (Figure S1). The mean

MAER ranged between 1200 με and 400 με, in sub-volumes of 16 to 72 voxels (80 to 360 μm). The mean SDER ranged between 550 με and 100 με in the same sub-volumes. For a sub-volume size of 40 voxels (200 μm), the mean random errors of the displacement components remained below 2 μm (Figure S2a), whereas the mean random errors of the strain (Figure S2b) were below 360 με.

Table S1. Random errors for the three displacement components in the multi-pass schemes analysed. Median values of the six specimens are shown.

Multi-pass scheme sub-volume sizes (voxels)	Final sub-volume size (μm)	Displacement random errors (μm)		
		X	Y	Z
80-40-32-24-16	80	1.78	1.34	1.74
96-48-40-32-24	120	1.70	1.18	1.64
112-56-48-40-32	160	1.62	1.02	1.55
128-64-56-48-40	200	2.07	0.96	1.66
144-72-64-56-48	240	2.02	0.91	1.62
160-80-72-64-56	280	1.94	0.86	1.56
178-88-80-72-64	320	1.86	0.81	1.49
192-96-88-80-72	360	1.81	0.77	1.44

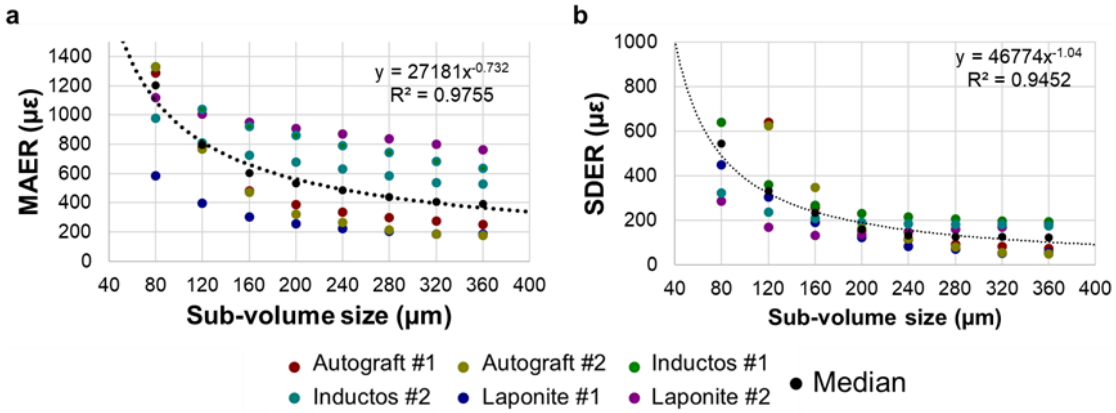

Figure S1. Relationship between (a) MAER and (b) SDER with the sub-volume size for the six specimens. Median values are also reported.

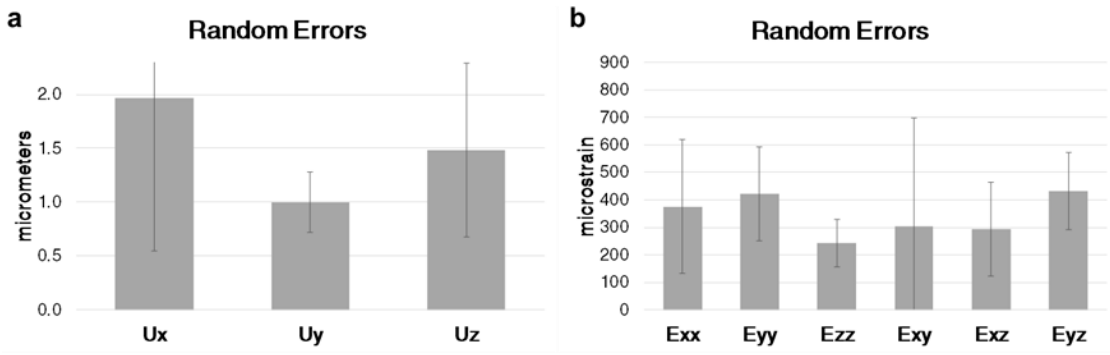

Figure S2. (a) Displacement random errors and (b) random errors of each strain component for the analysed specimens computed with a final sub-volume size of 40 voxels. Bars represent the median value, whereas error bars represent the standard deviation accounting for the total number of specimens (n = 6).

References

[1] R. Marsell, T.A. Einhorn, The biology of fracture healing, Injury. 42 (2011) 551–555. doi:10.1016/j.injury.2011.03.031.

[2] A. Oryan, S. Monazzah, A. Bigham-Sadegh, Bone injury and fracture healing biology., Biomed. Environ. Sci. 28 (2015) 57–71. doi:10.3967/bes2015.006.

[3] P. V. Giannoudis, T.A. Einhorn, D. Marsh, Fracture healing: The diamond concept, Injury. 38 (2007) 3–6. doi:10.1016/S0020-1383(08)70003-2.

[4] N.G. Lasanianos, N.K. Kanakaris, P. V. Giannoudis, Current management of long bone large segmental defects, Orthop. Trauma. 24 (2010) 149–163. doi:10.1016/j.mporth.2009.10.003.

[5] E. Roddy, M.R. DeBaun, A. Daoud-Gray, Y.P. Yang, M.J. Gardner, Treatment of critical-sized bone defects: clinical and tissue engineering perspectives, Eur. J. Orthop. Surg. Traumatol. 28 (2018) 351–362. doi:10.1007/s00590-017-2063-0.

[6] W. Wang, K.W.K. Yeung, Bone grafts and biomaterials substitutes for bone defect repair: A review, Bioact. Mater. 2 (2017) 224–247. doi:https://doi.org/10.1016/j.bioactmat.2017.05.007.

[7] F.W. Bloemers, T.J. Blokhuis, P. Patka, F.C. Bakker, B.W. Wippermann, H.J.T.M. Haarman, Autologous bone versus calcium-phosphate ceramics in treatment of experimental bone defects., J. Biomed. Mater. Res. B. Appl. Biomater. 66 (2003) 526–531. doi:10.1002/jbm.b.10045.

[8] M.K. Sen, T. Miclau, Autologous iliac crest bone graft: Should it still be the gold standard for treating nonunions?, Injury. 38 (2007) 2–7. doi:10.1016/j.injury.2007.02.012.

[9] J.E. Schroeder, R. Mosheiff, Tissue engineering approaches for bone repair: Concepts and evidence, Injury. 42 (2011) 609–613. doi:10.1016/j.injury.2011.03.029.

[10] J.C. Banwart, M.A. Asher, R.S. Hassanein, Iliac Crest Bone Graft Harvest Donor Site Morbidity: A Statistical Evaluation, Spine (Phila. Pa. 1976). 20 (1995).

https://journals.lww.com/spinejournal/Fulltext/1995/05000/Iliac_Crest_Bone_Graft_Harvest_Donor_Site.12.aspx.

[11] R. Dimitriou, G.I. Mataliotakis, A.G. Angoules, N.K. Kanakaris, P. V. Giannoudis, Complications following autologous bone graft harvesting from the iliac crest and using the RIA: A systematic review, Injury. 42 (2011) S3–S15. doi:10.1016/j.injury.2011.06.015.

[12] F.R.A.J. Rose, ore, R.O.C. Oreffo, Bone tissue engineering: Hope vs hype, Biochem. Biophys. Res. Commun. 292 (2002) 1–7. doi:10.1006/bbrc.2002.6519.

[13] A.R. Amini, C.T. Laurencin, S.P. Nukavarapu, Bone Tissue Engineering: Recent Advances and Challenges, Crit. Rev. Biomed. Eng. 40 (2012) 363–408. http://www.ncbi.nlm.nih.gov/pmc/articles/PMC3766369/.

[14] R. Agarwal, A.J. Garcia, Biomaterial strategies for engineering implants for enhanced osseointegration and bone repair., Adv. Drug Deliv. Rev. 94 (2015) 53–62. doi:10.1016/j.addr.2015.03.013.

[15] M. Mohammadi, S.A. Mousavi Shaegh, M. Alibolandi, M.H. Ebrahimzadeh, A. Tamayol, M.R. Jaafari, M. Ramezani, Micro and nanotechnologies for bone regeneration: Recent advances and emerging designs, J. Control. Release. 274 (2018) 35–55. doi:10.1016/j.jconrel.2018.01.032.

[16] T.-M. De Witte, L.E. Fratila-Apachitei, A.A. Zadpoor, N.A. Peppas, Bone tissue engineering via growth factor delivery: from scaffolds to complex matrices, Regen. Biomater. (2018) 197–211. doi:10.1093/rb/rby013.

[17] M.M. Stevens, Biomaterials for bone tissue engineering, Mater. Today. 11 (2008) 18–25. doi:https://doi.org/10.1016/S1369-7021(08)70086-5.

[18] C.J. Kowalczewski, J.M. Saul, Biomaterials for the delivery of growth factors and other therapeutic agents in tissue engineering approaches to bone regeneration, Front. Pharmacol. 9 (2018) 1–15. doi:10.3389/fphar.2018.00513.

[19] V. Martin, A. Bettencourt, Bone regeneration: Biomaterials as local delivery systems with improved osteoinductive properties, Mater. Sci. Eng. C. 82 (2018) 363–371. doi:10.1016/j.msec.2017.04.038.

[20] M. Faßbender, S. Minkwitz, C. Strobel, G. Schmidmaier, B. Wildemann, Stimulation of bone healing by sustained bone morphogenetic protein 2 (BMP-2) delivery, Int. J. Mol. Sci. 15 (2014) 8539–8552. doi:10.3390/ijms15058539.

[21] J.A. Spector, J.S. Luchs, B.J. Mehrara, J.A. Greenwald, L.P. Smith, M.T. Longaker, Expression of bone morphogenetic proteins during membranous bone healing., Plast. Reconstr. Surg. 107 (2001) 124–134.

[22] K.R. Garrison, I. Shemilt, S. Donell, J.J. Ryder, M. Mugford, I. Harvey, F. Song, V. Alt, Bone morphogenetic protein (BMP) for fracture healing in adults, Cochrane Database Syst Rev. (2010). doi:10.1002/14651858.CD006950.pub2.www.cochranelibrary.com.

[23] J.D. Boerckel, Y.M. Kolambkar, K.M. Dupont, B.A. Uhrig, E.A. Phelps, H.Y. Stevens, A.J. García, R.E. Guldberg, Effects of protein dose and delivery system on BMP-

mediated bone regeneration, Biomaterials. 32 (2011) 5241–5251. doi:10.1016/j.biomaterials.2011.03.063.

[24] M. Geiger, R.H. Li, W. Friess, Collagen sponges for bone regeneration with rhBMP-2, Adv. Drug Deliv. Rev. 55 (2003) 1613–1629. doi:10.1016/j.addr.2003.08.010.

[25] W.R. Walsh, R.A. Oliver, C. Christou, V. Lovric, E.R. Walsh, G.R. Prado, T. Haider, Critical size bone defect healing using collagen-calcium phosphate bone graft materials, PLoS One. 12 (2017) 1–21. doi:10.1371/journal.pone.0168883.

[26] A.A. El-Rashidy, J.A. Roether, L. Harhaus, U. Kneser, A.R. Boccaccini, Regenerating bone with bioactive glass scaffolds: A review of *in vivo* studies in bone defect models, Acta Biomater. 62 (2017) 1–28. doi:10.1016/j.actbio.2017.08.030.

[27] S.H. Jun, E.J. Lee, T.S. Jang, H.E. Kim, J.H. Jang, Y.H. Koh, Bone morphogenic protein-2 (BMP-2) loaded hybrid coating on porous hydroxyapatite scaffolds for bone tissue engineering, J. Mater. Sci. Mater. Med. 24 (2013) 773–782. doi:10.1007/s10856-012-4822-0.

[28] A. Ferrand, S. Eap, L. Richert, S. Lemoine, D. Kalaskar, S. Demoustier-Champagne, H. Atmani, Y. Mély, F. Fioretti, G. Schlatter, L. Kuhn, G. Ladam, N. Benkirane-Jessel, Osteogenetic properties of electrospun nanofibrous PCL scaffolds equipped with chitosan-based nanoreservoirs of growth factors, Macromol. Biosci. 14 (2014) 45–55. doi:10.1002/mabi.201300283.

[29] Z. Wang, K. Wang, X. Lu, M. Li, H. Liu, C. Xie, F. Meng, O. Jiang, C. Li, W. Zhi, BMP-2 encapsulated polysaccharide nanoparticle modified biphasic calcium phosphate scaffolds for bone tissue regeneration, J. Biomed. Mater. Res. - Part A. 103 (2015) 1520–1532. doi:10.1002/jbm.a.35282.

[30] O. Gauthier, R. Müller, D. Von Stechow, B. Lamy, P. Weiss, J.M. Bouler, E. Aguado, G. Daculsi, *In vivo* bone regeneration with injectable calcium phosphate biomaterial: A three-dimensional micro-computed tomographic, biomechanical and SEM study, Biomaterials. 26 (2005) 5444–5453. doi:10.1016/j.biomaterials.2005.01.072.

[31] M.L. Bouxsein, S.K. Boyd, B.A. Christiansen, R.E. Guldberg, K.J. Jepsen, R. M??ller, Guidelines for assessment of bone microstructure in rodents using micro-computed tomography, J. Bone Miner. Res. (2010). doi:10.1002/jbmr.141.

[32] A. Nazarian, B.D. Snyder, D. Zurakowski, R. Müller, Quantitative micro-computed tomography: A non-invasive method to assess equivalent bone mineral density, Bone. 43 (2008) 302–311. doi:10.1016/j.bone.2008.04.009.

[33] A. Nazarian, R. Müller, Time-lapsed microstructural imaging of bone failure behavior, J. Biomech. 37 (2004) 55–65. doi:10.1016/S0021-9290(03)00254-9.

[34] B.K. Bay, T.S. Smith, D.P. Fyhrie, M. Saad, Digital volume correlation: Three-dimensional strain mapping using X-ray tomography, Exp. Mech. 39 (1999) 217–226. doi:10.1007/BF02323555.

[35] B.K. Bay, Methods and applications of digital volume correlation, J. Strain Anal. Eng. Des. 43 (2008) 745–760. doi:10.1243/03093247JSA436.

[36] M. Peña Fernández, S. Cipiccia, A.J. Bodey, R. Parwani, E. Dall'Ara, G. Blunn, M. Pani, A.H. Barber, G. Tozzi, Effect of SR-microCT exposure time on the mechanical integrity of trabecular bone using *in situ* mechanical testing and digital volume correlation, J. Mech. Behav. Biomed. Mater. 88 (2018) 109–119. doi:https://doi.org/10.1016/j.jmbbm.2018.08.012.

[37] F. Gillard, R. Boardman, M. Mavrogordato, D. Hollis, I. Sinclair, F. Pierron, M. Browne, The application of digital volume correlation (DVC) to study the microstructural behaviour of trabecular bone during compression, J. Mech. Behav. Biomed. Mater. 29 (2014) 480–499. doi:10.1016/j.jmbbm.2013.09.014.

[38] D. Christen, A. Levchuk, S. Schori, P. Schneider, S.K. Boyd, R. Müller, Deformable image registration and 3D strain mapping for the quantitative assessment of cortical bone microdamage, J. Mech. Behav. Biomed. Mater. 8 (2012) 184–193. doi:10.1016/j.jmbbm.2011.12.009.

[39] G. Tozzi, V. Danesi, M. Palanca, L. Cristofolini, Elastic Full-Field Strain Analysis and Microdamage Progression in the Vertebral Body from Digital Volume Correlation, Strain. 52 (2016) 446–455. doi:10.1111/str.12202.

[40] V. Danesi, G. Tozzi, L. Cristofolini, Application of digital volume correlation to study the efficacy of prophylactic vertebral augmentation, Clin. Biomech. 39 (2016) 14–24. doi:10.1016/j.clinbiomech.2016.07.010.

[41] G. Tozzi, Q.H. Zhang, J. Tong, 3D real-time micromechanical compressive behaviour of bone-cement interface: Experimental and finite element studies, J. Biomech. 45 (2012) 356–363. doi:10.1016/j.jbiomech.2011.10.011.

[42] P.M. Arrabal, R. Visser, L. Santos-Ruiz, J. Becerra, M. Cifuentes, Osteogenic molecules for clinical applications: Improving the BMP-collagen system, Biol. Res. 46 (2013) 421–429. doi:10.4067/S0716-97602013000400013.

[43] D.M.R. Gibbs, C.R.M. Black, G. Hulsart-Billstrom, P. Shi, E. Scarpa, R.O.C. Oreffo, J.I. Dawson, Bone induction at physiological doses of BMP through localization by clay nanoparticle gels, Biomaterials. 99 (2016) 16–23. doi:10.1016/j.biomaterials.2016.05.010.

[44] M. Mousa, N.D. Evans, R.O.C. Oreffo, J.I. Dawson, Clay nanoparticles for regenerative medicine and biomaterial design: A review of clay bioactivity, Biomaterials. 159 (2018) 204–214. doi:10.1016/j.biomaterials.2017.12.024.

[45] N. Otsu, A threshold selection method from gray-level histograms, IEEE Trans. Syst. Man. Cybern. 9 (1979) 62–66. doi:10.1109/TSMC.1979.4310076.

[46] M. Doube, M.M. Klosowski, I. Arganda-Carreras, F.P. Cordelières, R.P. Dougherty, J.S. Jackson, B. Schmid, J.R. Hutchinson, S.J. Shefelbine, BoneJ: Free and extensible bone image analysis in ImageJ, Bone. 47 (2010) 1076–1079. doi:10.1016/j.bone.2010.08.023.

[47] J. Schindelin, I. Arganda-Carreras, E. Frise, V. Kaynig, M. Longair, T. Pietzsch, S. Preibisch, C. Rueden, S. Saalfeld, B. Schmid, J.-Y. Tinevez, D.J. White, V.

Hartenstein, K. Eliceiri, P. Tomancak, A. Cardona, Fiji: an open-source platform for biological-image analysis, Nat Meth. 9 (2012) 676–682. doi:10.1038/nmeth.2019.

[48] S.M. Ross, Peirce's criterion for the elimination of suspect experimental data, J. Eng. Technol. 20 (2003) 1–12. http://classes.engineering.wustl.edu/2009/fall/che473/handouts/OutlierRejection.pdf.

[49] K. Madi, G. Tozzi, Q.H. Zhang, J. Tong, A. Cossey, A. Au, D. Hollis, F. Hild, Computation of full-field displacements in a scaffold implant using digital volume correlation and finite element analysis, Med. Eng. Phys. 35 (2013) 1298–1312. doi:10.1016/j.medengphy.2013.02.001.

[50] M. Peña Fernández, A.H. Barber, G.W. Blunn, G. Tozzi, Optimisation of digital volume correlation computation in SR-microCT images of trabecular bone and bone-biomaterial systems, J. Microsc. 00 (2018) 1–16. doi:doi: 10.1111/jmi.12745.

[51] M. Palanca, L. Cristofolini, E. Dall'Ara, M. Curto, F. Innocente, V. Danesi, G. Tozzi, Digital volume correlation can be used to estimate local strains in natural and augmented vertebrae: an organ-level study, J. Biomech. 49 (2016) 3882–3890. doi:10.1016/j.jbiomech.2016.10.018.

[52] W. Friess, H. Uludag, S. Foskett, R. Biron, C. Sargeant, Characterization of absorbable collagen sponges as recombinant human bone morphogenetic protein-2 carriers, Int. J. Pharm. 185 (1999) 51–60. doi:10.1016/S0378-5173(99)00128-3.

[53] S.C. Cowin, The relationship between the elasticity tensor and the fabric tensor, Mech. Mater. 4 (1985) 137–147. doi:https://doi.org/10.1016/0167-6636(85)90012-2.

[54] P.K. Zysset, A. Curnier, An alternative model for anisotropic elasticity based on fabric tensors, Mech. Mater. 21 (1995) 243–250. doi:https://doi.org/10.1016/0167-6636(95)00018-6.

[55] X. Shi, X. Wang, G.L. Niebur, Effects of Loading Orientation on the Morphology of the Predicted Yielded Regions in Trabecular Bone, Ann. Biomed. Eng. 37 (2009) 354–362. doi:10.1007/s10439-008-9619-4.

[56] C. Öhman, M. Baleani, E. Perilli, E. Dall'Ara, S. Tassani, F. Baruffaldi, M. Viceconti, Mechanical testing of cancellous bone from the femoral head: Experimental errors due to off-axis measurements, J. Biomech. 40 (2007) 2426–2433. doi:10.1016/j.jbiomech.2006.11.020.

[57] E.F. Morgan, T.M. Keaveny, Dependence of yield strain of human trabecular bone on anatomic site, J. Biomech. 34 (2001) 569–577. doi:https://doi.org/10.1016/S0021-9290(01)00011-2.

[58] E.F. Morgan, H.H. Bayraktar, T.M. Keaveny, Trabecular bone modulus–density relationships depend on anatomic site, J. Biomech. 36 (2003) 897–904. doi:https://doi.org/10.1016/S0021-9290(03)00071-X.

[59] A. Nazarian, J. Muller, D. Zurakowski, R. Müller, B.D. Snyder, Densitometric, morphometric and mechanical distributions in the human proximal femur, J. Biomech. 40 (2007) 2573–2579. doi:10.1016/j.jbiomech.2006.11.022.

[60] F. Linde, I. Hvid, F. Madsen, The effect of specimen geometry on the mechanicla behaviour of trabecular bone specimens, J. Biomech. 25 (1992) 359–368.

[61] N.M. Harrison, P.E. McHugh, Comparison of trabecular bone behavior in core and whole bone samples using high-resolution modeling of a vertebral body, Biomech. Model. Mechanobiol. 9 (2010) 469–480. doi:10.1007/s10237-009-0188-8.

[62] K. Un, G. Bevill, T.M. Keaveny, The effects of side-artifacts on the elastic modulus of trabecular bone., J. Biomech. 39 (2006) 1955–1963. doi:10.1016/j.jbiomech.2006.05.012.

[63] P.J. Ehrlich, L.E. Lanyon, Mechanical strain and bone cell function: A review, Osteoporos. Int. 13 (2002) 688–700. doi:10.1007/s001980200095.

[64] H.H. Bayraktar, E.F. Morgan, G.L. Niebur, G.E. Morris, E.K. Wong, T.M. Keaveny, Comparison of the elastic and yield properties of human femoral trabecular and cortical bone tissue, J. Biomech. 37 (2004) 27–35. doi:10.1016/S0021-9290(03)00257-4.

[65] H.M. Frost, Wolff's Law and bone's structural adaptations to mechanical usage: an overview for clinicians, Angle Orthod. 64 (1994) 175–188.

[66] D.R. Carter, Mechanical loading history and skeletal biology, J. Biomech. 20 (1987) 1095–1109. doi:https://doi.org/10.1016/0021-9290(87)90027-3.

[67] K.T. Salisbury Palomares, R.E. Gleason, Z.D. Mason, D.M. Cullinane, T.A. Einhorn, L.C. Gerstenfeld, E.F. Morgan, Mechanical stimulation alters tissue differentiation and molecular expression during bone healing, J. Orthop. Res. 27 (2009) 1123–1132. doi:10.1002/jor.20863.

[68] D.R. Epari, G.N. Duda, M.S. Thompson, Mechanobiology of bone healing and regeneration: *In vivo* models, Proc. Inst. Mech. Eng. Part H J. Eng. Med. 224 (2010) 1543–1553. doi:10.1243/09544119JEIM808.

[69] D.C. Betts, R. Müller, Mechanical regulation of bone regeneration: Theories, models, and experiments, Front. Endocrinol. (Lausanne). 5 (2014) 1–14. doi:10.3389/fendo.2014.00211.

[70] L.E. Claes, C.A. Heigele, Magnitudes of local stress and strain along bony surfaces predict the course and type of fracture healing, J. Biomech. 32 (1999) 255–266. doi:10.1016/S0021-9290(98)00153-5.

[71] C. Öhman, E. Dall'Ara, M. Baleani, S.V.S. Jan, M. Viceconti, The effects of embalming using a 4% formalin solution on the compressive mechanical properties of human cortical bone, Clin. Biomech. 23 (2008) 1294–1298. doi:10.1016/j.clinbiomech.2008.07.007.

[72] J. Wieding, E. Mick, A. Wree, R. Bader, Influence of three different preservative techniques on the mechanical properties of the ovine cortical bone, Acta Bioeng. Biomech. 17 (2015) 137–146. doi:10.5277/ABB-00067-2014-03.

[73] M. Palanca, A.J. Bodey, M. Giorgi, M. Viceconti, D. Lacroix, L. Cristofolini, E. Dall'Ara, Local displacement and strain uncertainties in different bone types by digital volume

correlation of synchrotron microtomograms, J. Biomech. c (2017). doi:10.1016/j.jbiomech.2017.04.007.

[74] L. Liu, E.F. Morgan, Accuracy and precision of digital volume correlation in quantifying displacements and strains in trabecular bone, J. Biomech. 40 (2007) 3516–3520. doi:10.1016/j.jbiomech.2007.04.019.

[75] M. Palanca, G. Tozzi, L. Cristofolini, M. Viceconti, E. Dall'Ara, 3D Local Measurements of Bone Strain and Displacement: Comparison of Three Digital Volume Correlation Approaches., J. Biomech. Eng. 137 (2015) 1–14. doi:10.1115/1.4030174.

[76] E. Dall'Ara, M. Peña-Fernández, M. Palanca, M. Giorgi, L. Cristofolini, G. Tozzi, Precision of DVC approaches for strain analysis in bone imaged with μCT at different dimensional levels, Front. Mater. 4:31 (2017). doi:10.3389/fmats.2017.00031.

Chapter 6. Synthesis

6.1. Background

One of the largest unsolved challenges in clinical orthopaedics regards bone regeneration in critical-sized bone defects caused by trauma, infection, tumours or musculoskeletal diseases [1–3]. To repair such defects, biomaterials are used to restore both bone structure and function [4,5]. Autografts are still considered the most effective methods for bone regeneration; however, only in some specific cases, with precise indication or small defects, biomaterials can be safely and efficiently used [6]. Improvement of the osteoconductive properties of the biomaterials associated with a controlled release of osteoinductive compounds might replace the use of autograft in several clinical situations, which will result in faster, cheaper and easier surgeries, with less side effects and morbidity [4–10].

Along with the intense research in biomaterials for bone regeneration, still major limitations exist in the translation of novel biomaterials from the lab to the clinic. Especifically, the biomechanical response of newly regenerated bone in critical-sized defects after the implantation of such biomaterials remains poorly understood [11–13]. This is particular important when bone defects occur in load-bearing regions [13,14]. A detailed investigation of the biomaterial integration together with their ability to restore bone with biomechanical properties that are comparable with the native tissue is essential, as it will help to predict the overall structural response under load, as well as the internal microdamage initiation and progression, which may progress to failure. Ultimately, these findings will benefit biomaterials development and predictions of long-term bone healing following their implantation.

The introduction of high-resolution X-ray micro-computed tomography (microCT) combined with *in situ* mechanical experiments (X-ray biomechanical imaging) and the latest development on digital volume correlation (DVC) techniques provided access not only to three-dimensional (3D) bone microstructure information but also the 3D evaluation and quantification of bone deformation under different loading conditions [15–17]. However, the application of these techniques for the investigation of newly formed bone produced *in vivo* in critical-sized bone defects after biomaterial implantation has never been addressed. To a certain extent, the absence of research on that area is due to the need for a translation of DVC computation from apparent to tissue level, with the ability to provide reliable strain measurements within the bone tissue. Therefore, the main aim of this thesis was to combine high-resolution X-ray microCT biomechanical imaging and DVC to newly regenerated bone structures in order to provide a deeper insight on bone formation, mechanical competence and deformation mechanisms at tissue level. Different tissue engineering strategies promoting the healing process clearly influence the newly formed bone morphometry, mineralisaton and mechanics; thus the design of novel biomaterials will benefit from the 3D *ex vivo* characterization of such hererogeneous structures. The main research outcomes are presented in the following sections.

6.2. Full-field strain measurement at tissue level

Bone is a highly hierarchical material that is organised at the different levels to optimise its mechanical performance during life [18,19]. Therefore, its mechanical behaviour (i.e. failure load, toughness) depends on the intrinsic materials properties at the different dimensional scales as well as the structural relationships at the various levels of organisation. Specifically, to evaluate the effect of biomaterials implantation on the mechanical properties of the newly formed bone and bone healing process, where the implanted constructs need to integrate with the tissue and provide mechanical integrity to the bone structure [20,21], the mechanical properties on the different bone structural units (i.e. trabeculae) need to be accurately quantified [22]. A reliable measurement of the internal full-field distribution of local properties, such as displacement and strain, within the tissue in different loading conditions can be used to evaluate the efficacy and competence of such biomaterials during bone forming.

The main achievement of Chapter 3 was the development of a comprehensive methodological approach for full-strain investigation of bone and bone-biomaterial systems at tissue level using a local DVC approach based on SR-microCT images. Although the suitability of high-resolution SR-microCT imaging to provide reliable displacement and strain measurement in bone structures (i.e. cortical and trabecular) at tissue level has been previously addressed [22,23], the image quality was considerably improved by using longer acquisition times, shorter propagation distance and higher optical magnification. In Chapter 3, the signal-to-noise ratio (SNR) was significantly reduced in order to minimise the irradiation-induced damage by optimising imagining acquisition parameters, post-processing and DVC-settings. A detailed methodological study was conducted bringing awareness of DVC-computation at tissue level and how to relate local strain mapping into the microstructure of the tissue. This is fundamental as image correlation is sensitive to all grey-level features in the images, including noise and artefacts which can cause an overestimation of the errors. In fact, without standardized guidelines and being DVC the only experimental method that allows for 3D displacements/strain measurements, the best strategy for ensuring reliable results is a correlation based in repeated unloaded scans followed by a careful analysis of the associated residual strains [22,24,25].

6.3. Bone preservation strategies during *in situ* SR-microCT experiments.

SR-microCT possesses significant advantages over standard microCT systems. To date, SR-microCT remains the only technique that allows the acquisition of high-resolution 3D images with sufficient spatial resolution and SNR to visualise damage initiation and propagation, when coupled to *in situ* mechanics [26,27]. Additionally, scanning times are reduced enough to perform *in situ* experiments in a quasi-time-resolved manner. However, it cannot be considered as a non-invasive technique. Synchrotron radiation dose can alter the

mechanical properties of bone [28–30]; therefore, special care is needed when performing mechanical test on biological materials in combination with SR-microCT imaging. The major aim of Chapter 4 was the development of two methodological approaches aiming at preserving bone tissue structural and mechanical integrity during *in situ* SR-microCT experiments. To date, radiation doses up to 35 kGy are considered to be within the 'safe' threshold dosage for bone allograft sterilization [28,31]. However, *in situ* SR-microCT experiments usually requires longer exposure times to gain accurate information at tissue level, which consequently results in high irradiation levels. In Chapter 4.1 preservation of bone integrity was achieved by reducing the total exposure to SR radiation, which resulted in a total accumulated dose below 35 kGy after the acquisition of seven tomographic dataset; thus, allowing the translation to *in situ* mechanical tests for the assessment of damage (i.e. microcrack) initiation and progression not only in the elastic, but also beyond yield in the plastic region. Furthermore, the application of DVC to specimens deformed by a combination of both mechanical load and irradiation was addressed for the first time. Local deformations changes were analysed after increasing radiation doses and highly strained regions were found in correspondence with microdamaged regions. The proposed protocol was successfully applied in Chapter 5.1 to *in situ* SR-microCT mechanical testing of bone-biomaterial systems, in which low exposure times to SR radiation were used to minimise irradiation-induced damage in the tissue and preserve the mechanical properties of the analysed specimens. Preservation of bone integrity during *in situ* experiments is particularly important to accurately characterise the newly regenerated bone, which is less mineralised than the mature trabecular bone tissue; thus, SR radiation may have a more harmful effect.

In Chapter 4.2 bone tissue preservation was effectively attained by controlling the environmental temperature while irradiating the bone specimens. Imaging settings that in Chapter 4.1 were shown to deteriorate bone tissue were also adopted here and it was shown that decreasing the environmental temperature to 0°C promoted bone preservation. In fact, controlling the temperature allowed to prolong the exposure time during SR-microCT imaging without compromising bone integrity; thus, higher SNR could be achieved. DVC was used for the first time to quantify the deformation induced in bone due to the irradiation, showing cumulative residual strains after increasing radiation exposures, which were considerably lower with decreased temperatures. The obtained knowledge in Chapter 4.2. highlights the importance of a controlled environment during *in situ* SR-microCT experiments to retain bone tissue integrity. In addition, irradiation-induced microcracks in the tissue could be tracked using DVC, and the displacement and strain directions successfully tracked crack initiation and propagation, suggesting the potential of *in situ* SR-microCT mechanical testing and DVC to experimentally characterise the crack opening modes in bone tissue.

6.4. Full-field deformation of newly regenerated bone.

The variation in load-bearing capacity of the newly formed bone produced *in vivo* by osteoregenerative biomaterials in critical-sized defects is crucial to fully characterise the biomechanical capacity of the new tissue and enhancing novel bone regeneration approaches. Mechanical support is continuously needed as the biomaterial degrades within the defect site, until the new bone tissue can take up the load. In fact, the inability of the newly regenerated tissue to prevent further bone damage and support weight-bearing regions may jeopardise the surgical interventions, resulting in a second intervention with associated impact on patient's quality of life and costs to the national healthcare system. Additionally, it can be clinically observed that sometimes biomaterials may be too quickly fully resorbed thus leaving voids in the reconstructed bone defects. However, the conditions and the extent of how bone functional adaptation (i.e. modelling and remodelling) will lead to a replacement of the bioresorbable material with mechanically competent bone tissue remains partially understood [32]. Several numerical models have been proposed describing the biomechanical phenomena which occur in bone tissues reconstructed with biomaterials and predicting the processes of bone growth and resorption of biomaterials [32–36]. Although such models seem extremely promising for the prediction of long-term bone adaptation within the defect site, *in vivo* and *ex vivo* data is yet limited. This is mainly due to difficulties associated with experimental analysis over the healing time.

Chapter 5 detailed the investigation of the full-field deformation of bone-biomaterial systems and newly formed bone produced *in vivo* after the application of osteoconductive (Chapter 5.1) and osteoinductive (Chapter 5.2) biomaterials in an ovine critical-sized defect model. Undoubtedly, the data and results presented in Chapter 5 will allow for the refinement of the above mentioned models and consequently, to implement their use in the design of novel biomaterials as a predictive tool for a priori optimisation and long-term behaviour of such materials. In Chapter 5.1 the time point of extraction (6 weeks post-implantation) was not enough for a total resorption of the graft material; consequently, the microdamage initiation and propagation at the interface between the newly formed bone and the remnant biomaterial could be investigated. The main findings in Chapter 5.1 was the identification of microdamage accumulation in proximity or within the newly formed bone tissue. It was also shown that when the biomaterial was less resorbed, the higher gradient of stiffness at the bone-biomaterial interface resulted in a weaker interface and consequently an inefficient load transfer from the more remodeled bone towards the bone graft regions, which finally induced microdamage in the trabeculae. However, when the biomaterials are resorbed faster the newly formed bone could efficiently bear the load, although still in an immature stage of development (woven). These findings ultimately suggest that a faster resorption rate and higher osteoinduction may be more beneficial for an efficient micromechanics *in vivo* in a postoperative overloading scenario. On the other hand, the longer implantation time (10 weeks) and different nature of the biomaterials used in Chapter 5.2 allowed for their

complete resorption and therefore only newly regenerate tissue was observed. The major finding in Chapter 5.2 was the demonstration of the mechanical adaptation of bone structure since the early stages of bone healing independently on the biomaterial used for treating the bone defects. Unavoidably, the microstructure of the newly formed bone in each defect site analysed was different not only among the treatment groups, but also within the same group. However, the full-field strain distribution showed that each particular microstructure was optimised to bear and distribute the externally applied loads. These results eventually suggest that enhanced osteoinductive biomaterials offering a controlled released of BMP-2 could successfully be adopted for the treatment of critical-sized bone defects, replacing the use of autografting.

The different time point of extraction and nature of the biomaterials makes a comparison between both studies difficult. It has been shown that the level of osteoinductivity achieved with bone grafts appears to be very limited when compared to BMP. Therefore, hybrid materials incorporating BMPs for added osteoinductivity seems to indicate the strategy to follow. However, the biomaterial delivery-system has to be carefully chosen in order to provide spatial-temporal release of BMPs, otherwise, as shown in Chapter 5.2 the fast degradation of the biomaterials (i.e. collagen) does not provide structural support for an adequate time and large voids may be found within the newly formed structure. Consequently, those voids acting as strain concentrators that in the event of an overload during *in vivo* service may result in the failure of the overall structure. Other studies have shown that bone formation induced by BMPs is much faster, and it is more reproducible that that seen with bone grafts [37–39]. Accordingly, the slow bone formation together with the slow degradation of bone grafts induce a weak interface, as presented in Chapter 5.1 in which microdamage may initiate and propagate if the defect site is subjected to and excessive load *in vivo*.

6.5. Limitations and future research.

The DVC approach used in this work is a local approach, in which the sub-volumes of the undeformed and deformed images are registered independently [40]. Global approaches instead [40,41] consist of performing the registration over the entire images by superimposing a mesh (i.e. 8-noded cube elements). The displacement field is then assumed to be continuous a priori and that allows for a decrease of the displacement resolution when compared to local approaches for an equivalent spatial resolution [42]. However, the multipass scheme implemented in the local DVC approach of DaVis software allows for consistency between the deformation of adjacent sub-volumes, when more than one pass is invoked. As shown in the development of this PhD work, reliable strain measurements can be obtained with the adopted local DVC approach, which has successfully been used to track initiation and propagation of local microdamage in the tissue. Nevertheless, novel DVC methodologies, aiming at improving the measurement uncertainties by increasing/decreasing the density of sub-volumes in specific location in

order to better follow the microstructure [43,44], may result to be beneficial for tracking the deformation in such heterogeneous structures as the ones presented in this work. In fact, different sub-volumes could be defined for the newly formed bone, more remodeled trabecular and biomaterial remnants, as the image texture differs for each of those phases, and therefore, a material-specific sub-volume size might allow for a more accurate tracking of the deformation of each phase. Another important advantage of DVC is in its potential for integration with numerical simulations and mechanical problems [42]. In this perspective, both local and global approaches are valuable although the latter makes the transition of DVC measurements in finite element modelling (FEM) easier in comparison with local DVC. A full integration of DVC measurements with FEM is extremely beneficial, as DVC can be used to validate FEM predictions of both apparent and local properties [45–47]. In addition, and integrative FE-DVC approach can be used to identify the material properties of the tissue and/or the biomaterial [43], allowing a better characterisation of the micromechanics of bone regeneration following different tissue engineering strategies.

Another limitation of concerns the use of ovine animal models to characterise the effect of the implanted biomaterials. The ovine condyle defect model is a widely used preclinical model for testing tissue engineering strategies at a clinically relevant scale in musculoskeletal research [48,49]. Sheep have cancellous and cortical bone and show similar bone remodeling and turnover rate as humans [14,50-52]. As no single animal model completely resembles human bone regeneration each species provided advantages and limitations [48,49]. In fact, the ovine condyle defect model has the advantages of an adequate defect size for the targeted application in a patient [14]. Therefore, these models are intended to be used as a simplified screening tool for the selection of promising tissue engineering strategies and biomaterials before applications in a more complex scenario. Regarding the extraction time points of both studies in Chapter 5, one limitation is the absence of monitoring of bone growth within the defect previous to the retrieval of the condyles. *In vivo* radiographic analysis (if not low-dose CT) would be beneficial in future studies to control bone healing within the defect [14,53].

The present thesis has focused on the application of DVC at tissue level based on high-resolution microCT images of distinct bone structures subjected to compression load and/or high-energy irradiation. Nevertheless, the defined methodologies can be translated into other biological structures at different dimensional levels and under different loading scenarios. In that perspective, during the course of this PhD thesis, through collaboration with other institutions, the proposed approach has also been successfully implemented for the evaluation of the full-field strain distribution in other applications. At the nanoscale, the quantification of the anisotropy of the deformation of elephant dentin during quasi-static *in situ* nanoCT indentation and the relationships with the orientation of the tubules within the dentin (Figure 1) [54] was performed. Two studies have also been conducted combining time-lapse microCT and DVC; firstly, the 3D internal strains have been quantified in the

trabecular bone around lag screws, with increased levels of screw tightening in order to gain a deeper understanding on how the induced load is transferred to the surrounding bone during screw tightening (Figure 2) [55]. A second application consisted on the analysis of the full-field residual strains in the enamel-dentin interface of porcine teeth models as a result of *ex situ* brushing of teeth to better assess how the applied brushing forces may induce microdamage at the enamel-dentin interface (Figure 3) [56]. Finally, DVC has also been applied to clinical CT images to measure the deformation of lower limbs in load-bearing conditions (Figure 4) [57].

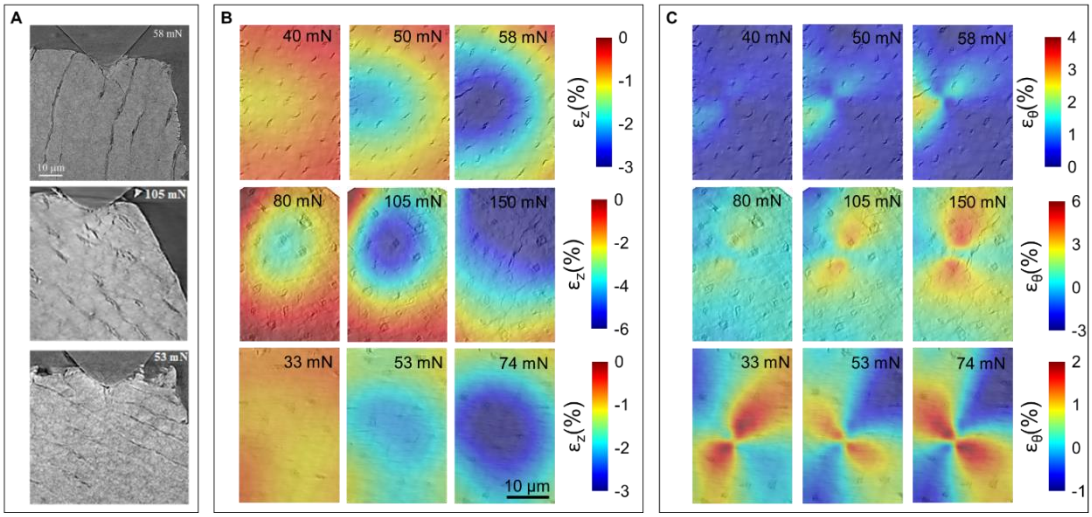

Figure 1. (A) nanoCT orthogonal slices showing the alignment of the indenter and the orientation of the tubules relative to the indenter: 0° (top), 45° (centre) and 70° (bottom). Full-field strain distribution in (B) indentation direction and (C) hoop direction as a function of the applied load for the three considered orientations. The strain in the indenting direction (A) is isotropic around the indenter tip, whereas axisymmetric in the hoop direction. Adapted from [54].

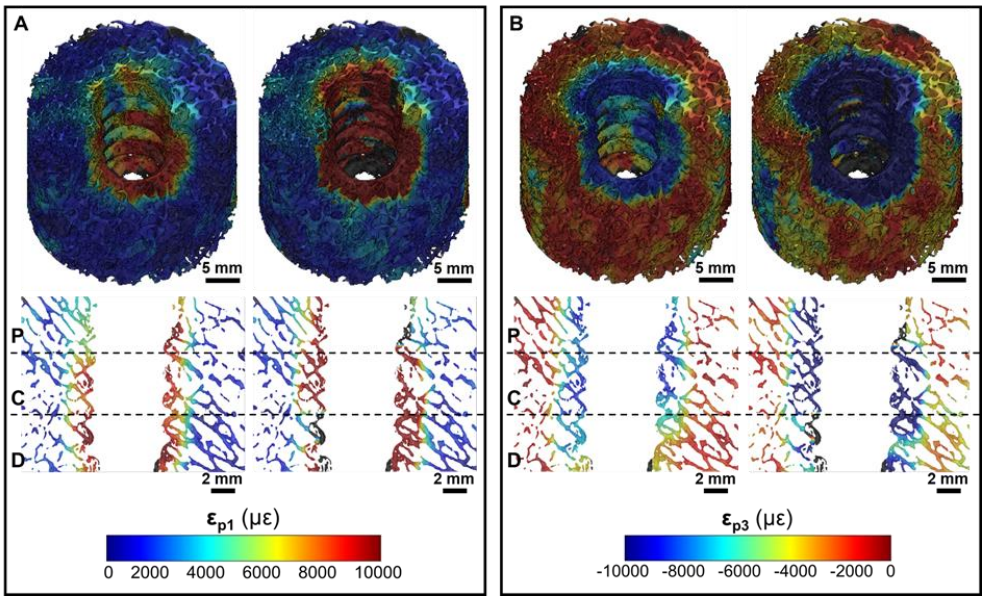

Figure 2. (A) First (ε_{p1}) and (B) third (ε_{p3}) principal strain distributions within the peri-implant bone at 60% (left) and 100% (right) of the torque between head contact and maximum torque within the volume of interest for one analysed specimen. Highly strained areas were restricted to bone within 2-3 mm from the implant interface. Lower strain magnitudes were found in the proximal (P) region compared to the central (C) or distal (D) regions. Adapted from [55].

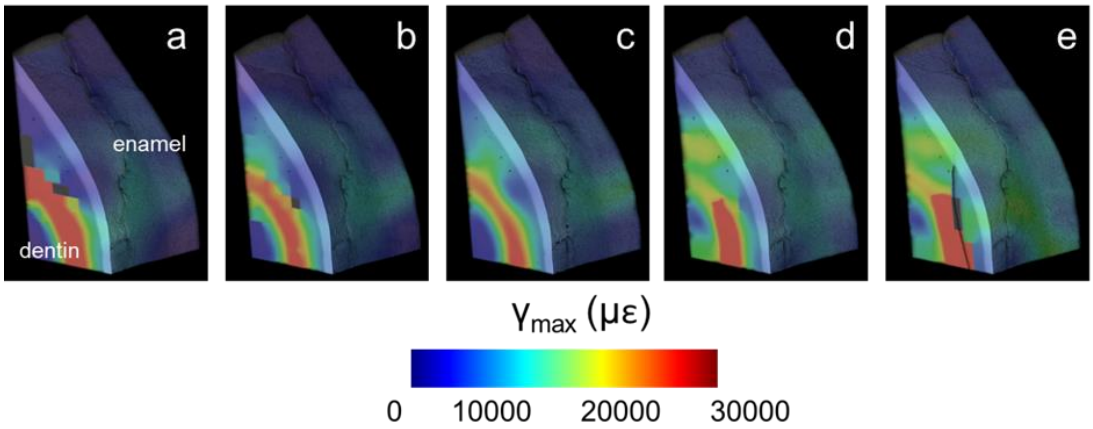

Figure 3. Full-field maximum shear strain (γ_{max}) at the enamel (exterior) and dentin (interior) interface after cumulative brushing time from (a) two minutes to (e) ten minutes. Maximum values are identified within the dentin and in correspondence with the microcrack identified after ten minutes of brushing (e) [56].

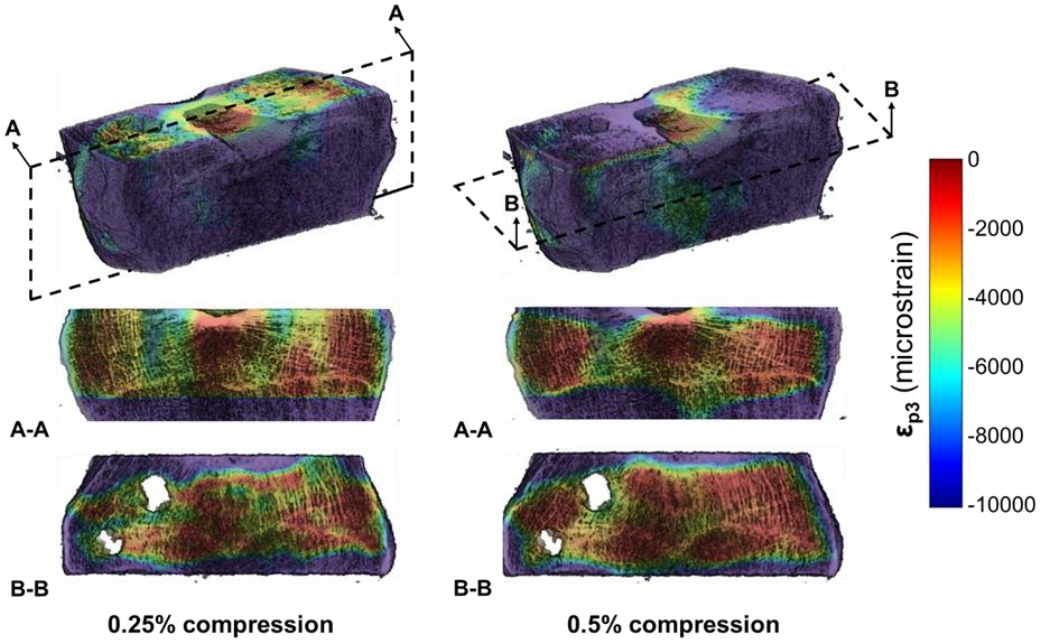

Figure 4. Full-field third principal strain (ε_{p3}) distribution in a 30-mm thick slice of distal human femur under apparent axial compression of 0.25% (left) and 0.5% (right) [57].

The recent advances in novel 3D imaging techniques, such as polarised second harmonic generation (SHG) microscopy [58,59], has allowed the extension of DVC methods to study 3D deformation at cellular levels. In fact, DVC based on SHG images has been used for the study of cell-induced extracellular matrix deformations in 3D [60,61]. Although this application is certainly new, the results seem promising for the translation into novel tissue engineering strategies. In that perspective, the full-field deformation induced during bone regeneration by bone-forming cells could be evaluated with different biomaterials, gaining a deeper insight on how cell-mechanics promote bone formation. Undoubtfully, expanding the capabilities of DVC from tissue to cellular level to the study of bone regeneration will benefit

the development of novel biomaterials by observing the temporal changes in cell-matrix and tissue mechanics during the healing process.

6.6. Conclusion

In conclusion, the presented PhD project has led to a deeper understanding of bone regeneration, mechanical competence and deformation mechanisms of newly regenerated bone structures following different tissue engineering strategies, which is essential for the development and enhancement of novel osteoregenerative biomaterials. The combination of high-resolution microCT imaging, *in situ* mechanical testing and DVC has allowed the computation of 3D full-field strain distribution in bone-biomaterial systems and newly formed bone produced *in vivo* in order to characterise the microdamage initiation and progression and load-transfer ability of such structures. This experimental approach has shown to be useful for investigating the local mechanics of bone tissue during the healing process in relation to the regeneration achieved *in vivo* for a variety of biomaterials.

References

[1] E.H. Schemitsch, Size Matters: Defining Critical in Bone Defect Size!, J. Orthop. Trauma. 31 (2017) S20–S22. doi:10.1097/BOT.0000000000000978.

[2] A. Nauth, M.D. McKee, T.A. Einhorn, J.T. Watson, R. Li, E.H. Schemitsch, Managing bone defects., J. Orthop. Trauma. 25 (2011) 462–466. doi:10.1097/BOT.0b013e318224caf0.

[3] A. Nauth, E. Schemitsch, B. Norris, Z. Nollin, J.T. Watson, Critical-Size Bone Defects, J. Orthop. Trauma. 32 (2018) S7–S11. doi:10.1097/BOT.0000000000001115.

[4] W. Wang, K.W.K. Yeung, Bone grafts and biomaterials substitutes for bone defect repair: A review, Bioact. Mater. 2 (2017) 224–247. doi:https://doi.org/10.1016/j.bioactmat.2017.05.007.

[5] T.-M. De Witte, L.E. Fratila-Apachitei, A.A. Zadpoor, N.A. Peppas, Bone tissue engineering via growth factor delivery: from scaffolds to complex matrices, Regen. Biomater. (2018) 197–211. doi:10.1093/rb/rby013.

[6] V. Martin, A. Bettencourt, Bone regeneration: Biomaterials as local delivery systems with improved osteoinductive properties, Mater. Sci. Eng. C. 82 (2018) 363–371. doi:10.1016/j.msec.2017.04.038.

[7] T. Winkler, F.A. Sass, G.N. Duda, K. Schmidt-Bleek, A review of biomaterials in bone defect healing, remaining shortcomings and future opportunities for bone tissue engineering, Bone Joint Res. 7 (2018) 232–243. doi:10.1302/2046-3758.73.BJR-2017-0270.R1.

[8] E. Garcia-Gareta, M.J. Coathup, G.W. Blunn, E. García-Gareta, M.J. Coathup, G.W. Blunn, Osteoinduction of bone grafting materials for bone repair and regeneration, Bone. 81 (2015) 112–121. doi:10.1016/j.bone.2015.07.007.

[9] C.J. Kowalczewski, J.M. Saul, Biomaterials for the delivery of growth factors and other therapeutic agents in tissue engineering approaches to bone regeneration, Front. Pharmacol. 9 (2018) 1–15. doi:10.3389/fphar.2018.00513.

[10] E. Roddy, M.R. DeBaun, A. Daoud-Gray, Y.P. Yang, M.J. Gardner, Treatment of critical-sized bone defects: clinical and tissue engineering perspectives, Eur. J. Orthop. Surg. Traumatol. 28 (2018) 351–362. doi:10.1007/s00590-017-2063-0.

[11] T. Ishimoto, T. Nakano, M. Yamamoto, Y. Tabata, Biomechanical evaluation of regenerating long bone by nanoindentation, J. Mater. Sci. Mater. Med. 22 (2011) 969–976. doi:10.1007/s10856-011-4266-y.

[12] O. Gauthier, R. Müller, D. Von Stechow, B. Lamy, P. Weiss, J.M. Bouler, E. Aguado, G. Daculsi, In vivo bone regeneration with injectable calcium phosphate biomaterial: A three-dimensional micro-computed tomographic, biomechanical and SEM study, Biomaterials. 26 (2005) 5444–5453. doi:10.1016/j.biomaterials.2005.01.072.

[13] C. Zhang, J. Wang, H. Feng, B. Lu, Z. Song, X. Zhang, Replacement of segmental bone defects using porous bioceramic cylinders: a biomechanical and X-ray diffraction

study., J. Biomed. Mater. Res. 54 (2001) 407–11. http://www.ncbi.nlm.nih.gov/pubmed/11189048.

[14] A.M. Pobloth, K.A. Johnson, H. Schell, N. Kolarczik, D. Wulsten, G.N. Duda, K. Schmidt-Bleek, Establishment of a preclinical ovine screening model for the investigation of bone tissue engineering strategies in cancellous and cortical bone defects, BMC Musculoskelet. Disord. 17 (2016) 1–12. doi:10.1186/s12891-016-0964-4.

[15] F. Gillard, R. Boardman, M. Mavrogordato, D. Hollis, I. Sinclair, F. Pierron, M. Browne, The application of digital volume correlation (DVC) to study the microstructural behaviour of trabecular bone during compression, J. Mech. Behav. Biomed. Mater. 29 (2014) 480–499. doi:10.1016/j.jmbbm.2013.09.014.

[16] D. Christen, A. Levchuk, S. Schori, P. Schneider, S.K. Boyd, R. Müller, Deformable image registration and 3D strain mapping for the quantitative assessment of cortical bone microdamage, J. Mech. Behav. Biomed. Mater. 8 (2012) 184–193. doi:10.1016/j.jmbbm.2011.12.009.

[17] G. Tozzi, V. Danesi, M. Palanca, L. Cristofolini, Elastic Full-Field Strain Analysis and Microdamage Progression in the Vertebral Body from Digital Volume Correlation, Strain. 52 (2016) 446–455. doi:10.1111/str.12202.

[18] P. Fratzl, H.S. Gupta, E.P. Paschalis, P. Roschger, Structure and mechanical quality of the collagen–mineral nano-composite in bone, J. Mater. Chem. 14 (2004) 2115–2123. doi:10.1039/B402005G.

[19] J.Y. Rho, L. Kuhn-Spearing, P. Zioupos, Mechanical properties and the hierarchical structure of bone, Med. Eng. Phys. 20 (1998) 92–102. doi:10.1016/S1350-4533(98)00007-1.

[20] V. Danesi, G. Tozzi, L. Cristofolini, Application of digital volume correlation to study the efficacy of prophylactic vertebral augmentation, Clin. Biomech. 39 (2016) 14–24. doi:10.1016/j.clinbiomech.2016.07.010.

[21] G. Tozzi, Q.H. Zhang, J. Tong, Microdamage assessment of bone-cement interfaces under monotonic and cyclic compression, J. Biomech. 47 (2014) 3466–3474. doi:10.1016/j.jbiomech.2014.09.012.

[22] E. Dall'Ara, M. Peña-Fernández, M. Palanca, M. Giorgi, L. Cristofolini, G. Tozzi, Precision of DVC approaches for strain analysis in bone imaged with μCT at different dimensional levels, Front. Mater. 4:31 (2017). doi:10.3389/fmats.2017.00031.

[23] M. Palanca, A.J. Bodey, M. Giorgi, M. Viceconti, D. Lacroix, L. Cristofolini, E. Dall'Ara, Local displacement and strain uncertainties in different bone types by digital volume correlation of synchrotron microtomograms, J. Biomech. c (2017). doi:10.1016/j.jbiomech.2017.04.007.

[24] E. Dall'Ara, D. Barber, M. Viceconti, About the inevitable compromise between spatial resolution and accuracy of strain measurement for bone tissue: A 3D zero-strain study, J. Biomech. 47 (2014) 2956–2963. doi:10.1016/j.jbiomech.2014.07.019.

[25] M. Palanca, G. Tozzi, L. Cristofolini, M. Viceconti, E. Dall'Ara, 3D Local Measurements of Bone Strain and Displacement: Comparison of Three Digital Volume Correlation Approaches., J. Biomech. Eng. 137 (2015) 1–14. doi:10.1115/1.4030174.

[26] A. Larrue, A. Rattner, N. Laroche, L. Vico, F. Peyrin, Feasibility of micro-crack detection in human trabecular bone images from 3D synchrotron microtomography, Annu. Int. Conf. IEEE Eng. Med. Biol. - Proc. (2007) 3918–3921. doi:10.1109/IEMBS.2007.4353190.

[27] A. Larrue, A. Rattner, Z.A. Peter, C. Olivier, N. Laroche, L. Vico, F. Peyrin, Synchrotron radiation micro-CT at the Micrometer scale for the analysis of the three-dimensional morphology of microcracks in human trabecular bone, PLoS One. 6 (2011). doi:10.1371/journal.pone.0021297.

[28] H.D. Barth, M.E. Launey, A.A. MacDowell, J.W. Ager, R.O. Ritchie, On the effect of X-ray irradiation on the deformation and fracture behavior of human cortical bone, Bone. 46 (2010) 1475–1485. doi:10.1016/j.bone.2010.02.025.

[29] H.D. Barth, E.A. Zimmermann, E. Schaible, S.Y. Tang, T. Alliston, R.O. Ritchie, Characterization of the effects of x-ray irradiation on the hierarchical structure and mechanical properties of human cortical bone, Biomaterials. 32 (2011) 8892–8904. doi:10.1016/j.biomaterials.2011.08.013.

[30] A. Singhal, A.C. Deymier-Black, J.D. Almer, D.C. Dunand, Effect of high-energy X-ray doses on bone elastic properties and residual strains, J. Mech. Behav. Biomed. Mater. 4 (2011) 1774–1786. doi:10.1016/j.jmbbm.2011.05.035.

[31] H. Nguyen, D.A.F. Morgan, M.R. Forwood, Sterilization of allograft bone: Effects of gamma irradiation on allograft biology and biomechanics, Cell Tissue Bank. 8 (2007) 93–105. doi:10.1007/s10561-006-9020-1.

[32] T. Lekszycki, F. Dell'Isola, A mixture model with evolving mass densities for describing synthesis and resorption phenomena in bones reconstructed with bio-resorbable materials, ZAMM Zeitschrift Fur Angew. Math. Und Mech. 92 (2012) 426–444. doi:10.1002/zamm.201100082.

[33] U. Andreaus, I. Giorgio, A. Madeo, Modeling of the interaction between bone tissue and resorbable biomaterial as linear elastic materials with voids, Zeitschrift Fur Angew. Math. Und Phys. 66 (2014) 209–237. doi:10.1007/s00033-014-0403-z.

[34] I. Giorgio, U. Andreaus, A. Madeo, The influence of different loads on the remodeling process of a bone and bioresorbable material mixture with voids, Contin. Mech. Thermodyn. 28 (2016) 21–40. doi:10.1007/s00161-014-0397-y.

[35] I. Giorgio, U. Andreaus, D. Scerrato, F. dell'Isola, A visco-poroelastic model of functional adaptation in bones reconstructed with bio-resorbable materials, Biomech. Model. Mechanobiol. 15 (2016) 1325–1343. doi:10.1007/s10237-016-0765-6.

[36] I. Giorgio, U. Andreaus, D. Scerrato, P. Braidotti, Modeling of a non-local stimulus for bone remodeling process under cyclic load: Application to a dental implant using a

bioresorbable porous material, Math. Mech. Solids. 22 (2017) 1790–1805. doi:10.1177/1081286516644867.

[37] O. Chan, M.J. Coathup, A. Nesbitt, C.Y. Ho, K.A. Hing, T. Buckland, C. Campion, G.W. Blunn, The effects of microporosity on osteoinduction of calcium phosphate bone graft substitute biomaterials, Acta Biomater. 8 (2012) 2788–2794. doi:10.1016/j.actbio.2012.03.038.

[38] A.M.C. Barradas, H. Yuan, C.A. van Blitterswijk, P. Habibovic, Osteoinductive biomaterials: current knowledge of properties, experimental models and biological mechanisms., Eur. Cell. Mater. 21 (2011) 407–429. doi:10.22203/eCM.v021a31.

[39] P. Habibovic, K. de Groot, Osteoinductive biomaterials – properties and relevance in bone repair, J. Tissue Eng. Regen. Med. 1 (2007) 25–32. doi:10.1002/term.

[40] H. Leclerc, J.-N. Périé, F. Hild, S. Roux, Digital volume correlation: what are the limits to the spatial resolution?, Mech. Ind. 13 (2012) 361–371. doi:10.1051/meca/2012025.

[41] S. Roux, F. Hild, P. Viot, D. Bernard, Three-dimensional image correlation from X-ray computed tomography of solid foam, Compos. Part A Appl. Sci. Manuf. 39 (2008) 1253–1265. doi:10.1016/j.compositesa.2007.11.011.

[42] F. Hild, A. Bouterf, L. Chamoin, H. Leclerc, F. Mathieu, J. Neggers, F. Pled, Z. Tomičević, S. Roux, Toward 4D mechanical correlation, Adv. Model. Simul. Eng. Sci. 3 (2016). doi:10.1186/s40323-016-0070-z.

[43] K. Madi, G. Tozzi, L. Courtois, J. Hummel, F. Hild, Integrated DVC approach applied to augmented vertebral bodies, (2018) 19–20.

[44] C.M. Disney, P.D. Lee, J.A. Hoyland, M.J. Sherratt, B.K. Bay, A review of techniques for visualising soft tissue microstructure deformation and quantifying strain Ex Vivo, J. Microsc. 00 (2018) 1–15. doi:10.1111/jmi.12701.

[45] M.C. Costa, G. Tozzi, L. Cristofolini, V. Danesi, M. Viceconti, E. Dall'Ara, Micro finite element models of the vertebral body: Validation of local displacement predictions, PLoS One. 12 (2017) 1–18. doi:10.1371/journal.pone.0180151.

[46] Y. Chen, E. Dall'Ara, E. Sales, K. Manda, R. Wallace, P. Pankaj, M. Viceconti, Micro-CT based finite element models of cancellous bone predict accurately displacement once the boundary condition is well replicated: A validation study, J. Mech. Behav. Biomed. Mater. 65 (2017) 644–651. doi:10.1016/j.jmbbm.2016.09.014.

[47] S. Oliviero, M. Giorgi, E. Dall'Ara, Validation of finite element models of the mouse tibia using digital volume correlation, J. Mech. Behav. Biomed. Mater. 86 (2018) 172–184. doi:10.1016/j.jmbbm.2018.06.022.

[48] A.I. Pearce, R.G. Richards, S. Milz, E. Schneider, S.G. Pearce, Animal models for implant biomaterial research in bone: A review, Eur. Cells Mater. 13 (2007) 1–10. doi:10.22203/eCM.v013a01.

[49] L.M. Wancket, Animal Models for Evaluation of Bone Implants and Devices: Comparative Bone Structure and Common Model Uses, Vet. Pathol. 52 (2015) 842–850. doi:10.1177/0300985815593124.

[50] P. Augat, K. Margevicius, J. Simon, S. Wolf, G. Suger, L. Claes, Local tissue properties in bone healing: Influence of size and stability of the osteotomy gap, J. Orthop. Res. 16 (2005) 475–481. doi:10.1002/jor.1100160413.

[51] C.P.G. Machado, S.C. Sartoretto, A.T.N.N. Alves, I.B.C. Lima, A.M. Rossi, J.M. Granjeiro, M.D. Calasans-Maia, Histomorphometric evaluation of strontium-containing nanostructured hydroxyapatite as bone substitute in sheep, Braz. Oral Res. 30 (2016) 1–11. doi:10.1590/1807-3107BOR-2016.vol30.0045.

[52] J.J. Li, A. Akey, C.R. Dunstan, M. Vielreicher, O. Friedrich, D. Bell, H. Zreiqat, Effects of material-tissue interactions on bone regeneration outcomes using baghdadite implants in a large animal model, Adv. Healthc. Mater. 1800218 (2018) 1–9. doi:10.1002/adhm.201800218.

[53] A. Malhotra, M.H. Pelletier, Y. Yu, C. Christou, W.R. Walsh, A Sheep Model for Cancellous Bone Healing, Front. Surg. 1 (2014) 1–7. doi:10.3389/fsurg.2014.00037.

[54] X. Lu, M. Peña Fernández, R.S. Bradley, S.R. Dawson, B. Hornberger, M. Leibowitz, G. Tozzi, P.J. Withers;, In Situ 3D Characterization of Crack Growth and Deformation in Elephant Dentin Using X-ray Laboratory-Based Nano-Tomography, Prep. (n.d.).

[55] M.K. Ryan, E. Perilli, M. Peña Fernández, G. Tozzi, K.J. Reynolds, Digital volume correlation of the bone-screw interface during tightening, Prep. (n.d.).

[56] M. Peña Fernández, A.P. Kao, S. Khan, A.H. Barber, G. Tozzi, Abrasion induced damaged in porcine teeth measured using digital volume correlation, Prep. (2018).

[57] M. Pani, M. Peña Fernández, G. Tozzi, E. Schileo, P. Erani, M. Baleani, DVC-based strains measurement in human distal femur unsig clinical CBCT, in: 8th World Congr. Biomech., 2018.

[58] A.C. Millard, P.J. Campagnola, W. Mohler, A. Lewis, L.M. Loew, Second harmonic imaging microscopy., Methods Enzymol. 361 (2003) 47–69.

[59] P.J. Campagnola, L.M. Loew, Second-harmonic imaging microscopy for visualizing biomolecular arrays in cells, tissues and organisms, Nat. Biotechnol. 21 (2003) 1356–1360. doi:10.1038/nbt894.

[60] A.K. Fung, J.J. Paredes, N. Andarawis-Puri, Novel image analysis methods for quantification of in situ 3-D tendon cell and matrix strain, J. Biomech. 67 (2017) 184–189. doi:10.1016/j.jbiomech.2017.11.030.

[61] Y.G. Kang, H. Jang, T.D. Yang, J. Notbohm, Y. Choi, Y. Park, B.-M. Kim, Quantification of focal adhesion dynamics of cell movement based on cell-induced collagen matrix deformation using second-harmonic generation microscopy, J. Biomed. Opt. 23 (2018) 1. doi:10.1117/1.JBO.23.6.065001.

Annexes

Curriculum Vitae

Marta Peña Fernández

Education

2015 – 2018	PhD in Bioengineering, School of Mechanical and Design Engineering, University of Portsmouth, UK.
2014 – 2015	Master in Biomedical Engineering, Université Paris-Descartes and ParisTech, France.
2006 – 2014	5-year MSc in Industrial Engineering, School of Engineering, University of Seville, Spain.

Journal papers (published)

Peña Fernández, M., Kao, A., Karali, K., Bodey, A., Dall'Ara, E., Blunn, G., Barber, A., Tozzi, G., (2018). Preservation of bone tissue mechanics with temperature control for *in situ* SR-microCT experiments. Materials, 11(11), 2155, doi: 10.3390/ma11112155.

Peña Fernández, M., Cipiccia, S., Dall'Ara, E., Bodey, A., Parwani, R., Blunn, G., Pani, M., Barber, A., Tozzi, G., (2018). Effect of synchrotron microCT radiation on the mechanical integrity of trabecular bone using *in situ* mechanical testing and digital volume correlation. JMBBM, 88, doi: 10.1016/j.jmbbm.2018.08.012

Peña Fernández, M., Blunn, G., Barber, A., Tozzi, G., (2018). Optimisation of digital volume correlation computation in SR-microCT images of trabecular bone and bone-biomaterial systems. Journal of Microscopy. doi: 10.1111/jmi.12745

De Mori, A., Peña Fernández, M., Blunn, G., Tozzi, G., Roldo, M., (2018). 3D printing and electrospinning for cartilage and bone tissue engineering. Polymers. 10, 285. doi:10.3390/polym10030285

Bottier, M., Peña Fernández, M., Pelle, G., Isabey, D., Louis, B., Grotberg, J.B., Filoche, M., (2017). A new index for characterizing micro-bead motion in a flow induced by ciliary beating: Part II, modeling. PLoS Comput Biol 13(7): e1005552. https://doi.org/10.1371/journal.pcbi.1005552

Dall'Ara, E., Peña Fernández, M., Palanca, M., Giorgi, M., Cristofolini, L., Tozzi, G., (2017). Precision of Digital Volume Correlation approaches for strain analysis in bone imaged with micro-computed tomography at different dimensional levels. Front. Mater. 4:31. doi: 10.3389/fmats.2017.00031

Journal papers (under review)

Peña Fernández, M., Dall'Ara, E., Bodey, A., Parwani, R., Blunn, G., Barber, A., Tozzi, G., (2018). Full-field strain analysis of bone-biomaterial systems produced by osteoregenerative biomaterials after *in vivo* service in an ovine model.

Peña Fernández, M., Black, C., Dawson, J., Gibbs, D., Kanczler, J., Oreffo, R., Tozzi, G., (2018). Load transfer analysis in newly formed bone induced by BMP-2 loaded hydrogels.

Journal papers (in preparation)

Ryan, M., Perilli, E., Peña Fernández, M., Tozzi, G., Reynolds, K.J., (2019). Digital volume correlation of the bone screw interface during tightening.

Lu, X., Peña Fernández, M., Bradley, R., Hornberger, B., Leibowitz, M., Tozzi, G., Whiters, P., (2019). *In situ* 3D characterization of crack growth and deformation in elephant denting by nano-tomography.

Gibbs, D., Peña Fernández, M., Black, C., Dawson, J., Kanczler, J., Tozzi, G., Oreffo, R., (2019). Comparison of bone morphogenetic protein delivery by clay nanoparticles with current clinical practice in an aged ovine femoral condyle defect.

Conference proceedings and abstracts

Peña Fernández, M., Kao, A., Karali, K., Bodey, A., Dall'Ara, E., Blunn, G., Barber, A., Tozzi, G., (2018). *Reducing bone tissue damage with temperature control for in situ SR-microCT mechanics.* 13th International Conference on Advances in Experimental Mechanics. Young Stress Analyst Competition (YSA). Southampton (UK) August 2018.

Peña Fernández, M., Black, C., Dawson, J., Gibbs, D., Kanczler, J., Oreffo, R., Tozzi, G., *Full-field strain analysis of newly formed bone induced by BMP-2 loaded hydrogels. 8th* World Congress of Biomechanics (WCB) Dublin (Ireland) July 2018.

Peña Fernández, M., Kao, A., Karali, K., Bodey, A., Dall'Ara, E., Blunn, G., Barber, A., Tozzi, G., (2018). *Reducing bone tissue damage with temperature control for in situ SR-microCT mechanics.* 8th World Congress of Biomechanics (WCB) Dublin (Ireland) July 2018.

Pani, M., Peña Fernández, M., Tozzi, G., Schileo, E., Erani, P., Baleani, M., (2018). *DVC-based strain measurement in human distal femur using clinical CBCT*. 8th World Congress of Biomechanics (WCB) Dublin (Ireland) July 2018.

Peña Fernández, M., Parwani, R., Bodey, A., Dall'Ara, E., Blunn, G., Barber, A., Tozzi, G., (2017). *Micromechanics and DVC of bone-biomaterial systems produced by osteoregenerative biomaterials.* 5th Tomography for Scientific Advancement (ToScA) symposium, Portsmouth (UK) Sept 2017.

Peña Fernández, M., Parwani, R., Bodey, A.J., Dall'Ara, E., Blunn, G., Barber, A., Tozzi, G., (2017). *Micromechanics and DVC of bone-biomaterial systems produced by osteoregenerative biomaterials.* 12th International Conference on Advances in Experimental Mechanics. Young Stress Analyst Competition (YSA). Sheffield (UK) August 2017.

Peña Fernández, M., Parwani, R., Bodey, A., Dall'Ara, E., Blunn, G., Barber, A., Tozzi, G., (2017). *Effect of SR-microCT exposure time on the damage induced on trabecular bone using DVC.* 23rd European Society of Biomechanics (ESB) congress. Seville (Spain) July 2017.

Ryan, M., Peña Ferández, M., Tozzi, G., Perilli, E., Reynolds, K.J., (2017) *Digital volume correlation of bone-screw interface at different tightening levels.* 23rd European Society of Biomechanics (ESB) congress. Seville (Spain) July 2017.

Peña Fernández, M., Pani, M., Barber, A., Tozzi, G., (2017). *Multi-material 3D printing of trabecular bone*. Orthopaedic Proceedings. Vol 99-B, (SUPP 1 34). 24th European Orthopaedic Research Society (EORS) congress. Bologna (Italy) September 2016.

Awards

- Travel Award, Tomography for Scientific Advancement (ToScA) 2018, Royal Society of Microscopy (Sept 2018)
- 1st Poster Prize, Tomography for Scientific Advancement (ToScA) 2018, Royal Society of Microscopy (Sept 2018)
- 3rd place, Young Stress Analyst Competition, British Society for Strain Measurement (Aug 2018)
- 4th Finalist, Young Stress Analyst Competition, British Society for Strain Measurement (Aug 2017)

Research proposals

- Diamond Light Source (PI: Tozzi, G.; CI: Arora, H., Peña Fernández, M., Kao, A., Bodey, A., Blunn, G.) – *"In situ real-time assessment of hard/soft tissue deformation using digital volume correlation"* – £57,600.000 in kind beam time.

Electronic data

The following data are available online at 10.6084/m9.figshare.7609835:

- **AVI_4.2.6_Troom** – First principal strain distribution over time of trabecular bone specimen imaged at room temperature.
- **AVI_4.2.6_T0** – First principal strain distribution over time of trabecular bone specimen imaged at 0°C.
- **AVI_4.2.7_Disp** – 3D displacement field around microcracked region in trabecular bone specimen imaged at room temperature over time.
- **AVI_5.1.5_Actifuse** – Third principal strain distribution under uniaxial compression in bone-Actifuse system.
- **AVI_5.1.5_ApaPore** – Third principal strain distribution under uniaxial compression in bone-ApaPore system.
- **AVI_5.1.5_StronBone** – Third principal strain distribution under uniaxial compression in bone-StronBone system.
- **AVI_5.1.5_StronBoneP** – Third principal strain distribution under uniaxial compression in bone-StronBone-P system.
- **AVI_5.1.5_Control** – Third principal strain distribution under uniaxial compression in trabecular bone control specimen.
- **AVI_5.1.6_Actifuse** – First principal strain distribution under uniaxial compression in bone-Actifuse system.
- **AVI_5.1.6_ApaPore** – First principal strain distribution under uniaxial compression in bone-ApaPore system.
- **AVI_5.1.6_StronBone** – First principal strain distribution under uniaxial compression in bone-StronBone system.
- **AVI_5.1.6_StronBoneP** – First principal strain distribution under uniaxial compression in bone-StronBone-P system.
- **AVI_5.1.6_Control** – First principal strain distribution under uniaxial compression in trabecular bone control specimen.
- **AVI_5.1.7_Actifuse** – Maximum shear strain distribution under uniaxial compression in bone-Actifuse system.
- **AVI_5.1.7_ApaPore** – Maximum shear strain distribution under uniaxial compression in bone-ApaPore system.
- **AVI_5.1.7_StronBone** – Maximum shear strain distribution under uniaxial compression in bone-StronBone system.
- **AVI_5.1.7_StronBoneP** – Maximum shear strain distribution under uniaxial compression in bone-StronBone-P system.

- **AVI_5.1.7_Control** – Maximum shear strain distribution under uniaxial compression in trabecular bone control specimen.
- **AVI_5.2.5a_Autograft#1** – Third principal strain distribution under uniaxial compression in Autograft#1 specimen.
- **AVI_5.2.5b_Autograft#1** – Third principal strain distribution under uniaxial compression in highly strained regions of Autograft#1 specimen.
- **AVI_5.2.5a_Autograft#2** – Third principal strain distribution under uniaxial compression in Autograft#1 specimen.
- **AVI_5.2.5b_Autograft#2** – Third principal strain distribution under uniaxial compression in highly strained regions of Autograft#2 specimen.
- **AVI_5.2.6a_InductOs#1** – Third principal strain distribution under uniaxial compression in InductOs#2 specimen.
- **AVI_5.2.6b_InductOs#1** – Third principal strain distribution under uniaxial compression in highly strained regions of InductOs#1 specimen.
- **AVI_5.2.6a_InductOs#2** – Third principal strain distribution under uniaxial compression in InductOs#2 specimen.
- **AVI_5.2.6b_InductOs#2** – Third principal strain distribution under uniaxial compression in highly strained regions of InductOs#2 specimen.
- **AVI_5.2.7a_Laponite#1** – Third principal strain distribution under uniaxial compression in Laponite#1 specimen.
- **AVI_5.2.7b_Laponitet#1** – Third principal strain distribution under uniaxial compression in highly strained regions of Laponite#1 specimen.
- **AVI_5.2.7a_Laponite#2** – Third principal strain distribution under uniaxial compression in Laponite#2 specimen.
- **AVI_5.2.7b_Laponitet#2** – Third principal strain distribution under uniaxial compression in highly strained regions of Laponite#2 specimen.
-

Ethical conduct of the research

FORM UPR16

Research Ethics Review Checklist

Please include this completed form as an appendix to your thesis (see the Research Degrees Operational Handbook for more information

UNIVERSITY OF PORTSMOUTH

Postgraduate Research Student (PGRS) Information				Student ID:	95849
PGRS Name:	Marta Peña Fernández				
Department:	SMDE	First Supervisor:		Dr. Gianluca Tozzi	
Start Date: (or progression date for Prof Doc students)		October 2015			
Study Mode and Route:	Part-time ☐	MPhil ☐	MD ☐		
	Full-time ☒	PhD ☒	Professional Doctorate ☐		

Title of Thesis:	X-ray biomechanical imaging and digital volume correlation of bone: from regeneration to structure
Thesis Word Count: (excluding ancillary data)	~ 50,000

If you are unsure about any of the following, please contact the local representative on your Faculty Ethics Committee for advice. Please note that it is your responsibility to follow the University's Ethics Policy and any relevant University, academic or professional guidelines in the conduct of your study

Although the Ethics Committee may have given your study a favourable opinion, the final responsibility for the ethical conduct of this work lies with the researcher(s).

UKRIO Finished Research Checklist:
(If you would like to know more about the checklist, please see your Faculty or Departmental Ethics Committee rep or see the online version of the full checklist at: http://www.ukrio.org/what-we-do/code-of-practice-for-research/)

a) Have all of your research and findings been reported accurately, honestly and within a reasonable time frame?	YES ☒ NO ☐
b) Have all contributions to knowledge been acknowledged?	YES ☒ NO ☐
c) Have you complied with all agreements relating to intellectual property, publication and authorship?	YES ☒ NO ☐
d) Has your research data been retained in a secure and accessible form and will it remain so for the required duration?	YES ☒ NO ☐
e) Does your research comply with all legal, ethical, and contractual requirements?	YES ☒ NO ☐

Candidate Statement:

I have considered the ethical dimensions of the above named research project, and have successfully obtained the necessary ethical approval(s)

Ethical review number(s) from Faculty Ethics Committee (or from NRES/SCREC):	ETHIC-2018-743

If you have *not* submitted your work for ethical review, and/or you have answered 'No' to one or more of questions a) to e), please explain below why this is so:

Marta Peña Fernández

Signed *(PGRS)*:		Date: 10th October 2018

UPR16 – April 2018

Certificate of Ethics Review

Project Title: X-ray biomechanical imaging and digital volume correlation of bone: from regeneration to structure.

Name: Marta Pena Fernandez **User ID:** 795849 **Application Date:** 29-Sep-2018 18:55 **ER Number:** ETHIC-2018-743

You must download your certificate, print a copy and keep it as a record of this review.

It is your responsibility to adhere to the University Ethics Policy and any Department/School or professional guidelines in the conduct of your study including relevant guidelines regarding health and safety of researchers and University Health and Safety Policy.

It is also your responsibility to follow University guidance on Data Protection Policy:

- General guidance for all data protection issues
- University Data Protection Policy

You are reminded that as a University of Portsmouth Researcher you are bound by the UKRIO Code of Practice for Research; any breach of this code could lead to action being taken following the University's Procedure for the Investigation of Allegations of Misconduct in Research.

Any changes in the answers to the questions reflecting the design, management or conduct of the research over the course of the project must be notified to the Faculty Ethics Committee. **Any changes that affect the answers given in the questionnaire, not reported to the Faculty Ethics Committee, will invalidate this certificate.**

This ethical review should not be used to infer any comment on the academic merits or methodology of the project. If you have not already done so, you are advised to develop a clear protocol/proposal and ensure that it is independently reviewed by peers or others of appropriate standing. A favourable ethical opinion should not be perceived as permission to proceed with the research; there might be other matters of governance which require further consideration including the agreement of any organisation hosting the research.

(A1) Please briefly describe your project:: The ultimate goal of this thesis is to combine X-ray biomechanical imaging and digital volume correlation to new regenerated bone structures in order to provide a deeper insight on bone regeneration, mechanical competence and deformation mechanisms following different tissue engineering strategies during the healing process. In short, in situ microCT mechanics and DVC will be applied, for the first time, to newly formed bone produced in vivo in critical bone defects following the implantation of osteoregenerative biomaterials. To do so, first a comprehensive methodological approach will be defined, able to determine the reliability of DVC at tissue level based on high- resolution microCT images. Additionally, experimental protocols will be defined for the application of in situ SR-microCT mechanics to bone tissue aiming to minimise the irradiation-induced damage. Finally, the defined methodological works will be used to investigate, ex vivo, the micromechanics of bone-biomaterial systems and newly formed bone.
(A2) What faculty do you belong to?: Technology
(A3) I am sure that my project requires ethical review by my Faculty Ethics Committee because it includes at least one material ethical issue.: No
(A5) Has your project already been externally reviewed?: No
(B1) Is the study likely to involve human participants?: No
(B2) Are you certain that your project will not involve human subjects or participants?: Yes
(C6) Is there any risk to the health & safety of the researcher or members of the research team beyond those that have already been risk assessed?: No
(D2) Are there risks of damage to physical and/or ecological environmental features?: No
(D4) Are there risks of damage to features of historical or cultural heritage (e.g. impacts of study techniques, taking of samples)?: No
(E1) Will the study involve the investigator and/or any participants in activities that could be considered contentious, unacceptable, or illegal, or in any other way harmful to the reputation of the University of Portsmouth?: No
(E2) Are there any potentially socially or culturally sensitive issues involved? (e.g. sexual, political, legal/criminal or financial): No
(F1) Does the project involve animals in any way?: No
(F2) Could the research outputs potentially be harmful to third parties?: No
(G1) Please confirm that you have read the University Ethics Policy and have considered the implications for your project.: Confirmed
(G2) Please confirm that you have read the UK RIO Code of Practice for Research and will conduct your project in accordance with it.: Confirmed
(G3) The University is committed to The Concordat to Support Research Integrity.: Confirmed
(G4) Submitting false or incorrect information is a breach of the University Ethics Policy and may be considered as misconduct and be subject to disciplinary action. Please confirm you understand this and agree that the information you have entered is correct.: Confirmed

“That you are here — that life exists, and identity;
That the powerful play goes on, and you may contribute a verse.”
Walt Withman, 1892